

DISSERTATION

THE INFLUENCE OF VARIATIONS IN PENETRATING SOLAR RADIATION ON
THE DIURNAL AND INTRASEASONAL STRUCTURE OF THE OCEANIC
BOUNDARY LAYER

Submitted by

Luke P. Van Roekel

Department of Atmospheric Science

In partial fulfillment of the requirements

For the Degree of Doctor of Philosophy

Colorado State University

Fort Collins, Colorado

Summer 2010

COLORADO STATE UNIVERSITY

JULY 7 , 2010

WE HEREBY RECOMMEND THAT THE DISSERTATION PREPARED UNDER OUR SUPERVISION BY LUKE PATRICK VAN ROEKEL ENTITLED THE INFLUENCE OF VARIATIONS IN PENETRATING SOLAR RADIATION ON THE DIURNAL AND INTRASEASONAL STRUCTURE OF THE OCEANIC BOUNDARY LAYER BE ACCEPTED AS FULFILLING IN PART REQUIREMENTS FOR THE DEGREE OF DOCTOR OF PHILOSOPHY.

Committee on Graduate Work

Takamitsu Ito

Michael Kirby

A. Scott Denning

Advisor: David A. Randall

Acting Department Head: Christian D. Kummerow

ABSTRACT OF DISSERTATION

THE INFLUENCE OF VARIATIONS IN PENETRATING SOLAR RADIATION ON THE DIURNAL AND INTRASEASONAL STRUCTURE OF THE OCEANIC BOUNDARY LAYER

The upper portion of the ocean is fairly well mixed and turbulent. The turbulence within the ocean boundary layer (OBL) is regulated by many mechanisms. One process that is receiving a renewed interest is the effect of penetrating component of surface shortwave radiation on ocean dynamics. The influence of solar radiation has been parameterized in two ways. A limited set of models force all the incoming solar radiation to be absorbed in the top model layer. The second parameterization assumes that the irradiance (light) at a given level follows a multiple term exponential. Most commonly it is assumed that shortwave radiation is absorbed in two bands: visible and near infrared. The strength of the infrared absorption is assumed to be fixed. For the visible band, absorption depends on water clarity. Until recently, water clarity could take six different values (Jerlov water types).

On climate scales, spatial and temporal variations in water clarity, based on surface chlorophyll, have a strong impact on the simulated ocean temperature, salinity,

and momentum. For example, the sea surface temperature (SST) in the cold tongue is reduced. In addition, the strength of the Walker circulation is increased. However, this response is not consistent among different models and parameterizations.

When chlorophyll is predicted, the influence of vertically variable water clarity on the thermodynamic and dynamic fields of the ocean can be examined. Studies that have incorporated an ecosystem model find minimal changes relative to using observed surface chlorophyll.

Previous research has focused on longer climate time scales and most models do not consider vertical variations in water clarity. In this study the response of the ocean to diurnal and intraseasonal variations of water clarity is examined. The sensitivity to vertical variations in water clarity is also considered.

To study the impact of variable solar radiation a model that accurately represents upper ocean physics is required. A new ocean mixing model is proposed that addresses some of the known deficiencies in previous models. The new model predicts entrainment based on turbulence at the OBL base, unlike other ocean models. An over prediction of the vertical heat flux in previous mixed layer models is avoided. The model framework discussed can be easily extended to any coordinate system. Further, this model can be coupled to an ocean biological model, which would determine the water clarity with depth, in a natural way.

An evaluation of the new model against observations and a newly developed vector vorticity large eddy simulation (LES) model has shown that the new model performs as well or better than previous OBL models in certain circumstances. This is

especially with low vertical resolution. Since this version of the new model is local, it does not perform as well in pure convective simulations as OBL models with non-local forcing

In this new model and K-Profile Parameterization (KPP), the temperature and velocity is very sensitive to variations in water clarity. Trapping more heat near the surface increases the temperature near the surface and confines daytime momentum input to a shallow layer. In addition, the depth of the thermocline is reduced as water clarity decreases.

The simulated temperature and velocity fields are insensitive to subsurface variations in water clarity. The responses of the new model and KPP are similar when the turbidity of the column is taken as the near surface average.

Two-dimensional simulations examining the influence of spatially variable turbidity lead to a slightly deeper thermocline and weaker near surface velocity relative to simulations with a zonally constant water clarity.

It is found that models must allow solar radiation to penetrate beyond the top model level. Further, water clarity should be diagnosed from observed or predicted surface chlorophyll instead of the six Jerlov water types.

Luke P. Van Roekel
Department of Atmospheric Science
Colorado State University
Fort Collins, CO 80523
Summer 2010

ACKNOWLEDGEMENTS

I am very grateful for the guidance and support of my advisor, Dr. David A. Randall. This dissertation would not be possible without his encouragement and willingness to pursue a topic of my choosing that was a little “far of field”. I also thank Dr. Randall for the opportunity to travel the world, learning and presenting my research to others in the community. I would also like to thank Dr. Takamitsu Ito, A. Scott Denning, and Michael Kirby for their invaluable help as members of my committee. I am also very grateful for the flexibility of Dr. Randall and the committee with regards to the accelerated timeline of the dissertation.

I am indebted to the Randall Research group, especially Don Dazlich and Dr. Celal Konor for many stimulating discussions about model issues. I also thank Cindy Carrick, Connie Hale, and Karrie Butler for coordinating travel and other purchases. I am also grateful to Tak Yamaguchi, Jim Benedict, and Erica McGrath-Spangler for a willingness to talk through different aspects of my research and providing many useful suggestions. Special thanks is also given to Drs. Alistair Adcroft, Laurent White, Vittorio M. Canuto, and Armando Howard for providing assistance with various aspects of this work.

None of this would be possible without the love and support of my wonderful wife and family. Their encouragement, willingness to proofread and ability to put up with me during this process was essential.

This project was supported by Department of Energy Scientific Discovery through Advanced Computing cooperative agreement with Colorado State University no. DE-FC02-06ER64302.

TABLE OF CONTENTS

SIGNATURE PAGE	ii
ABSTRACT OF DISSERTATION	iii
ACKNOWLEDGEMENTS.....	vi
TABLE OF CONTENTS.....	viii
LIST OF TABLES	xii
LIST OF FIGURES	xiii
Chapter 1: The Dynamics of the Upper Ocean	1
1.1 Penetrating Shortwave Radiation.....	3
1.1.1 Influence of Penetrating Shortwave Radiation	6
1.2 Past OBL Models	8
1.2.1 OBL Model Evaluations	15
1.3 Vertical Coordinates.....	16
1.4 Where do we go from here?.....	18
Chapter 2: A Vector Vorticity Large Eddy Simulation Model.....	21
2.1 Model Equations	21

2.1.1 Sub-grid Scale Mixing.....	27
2.2 VVM-Aqua Evaluation.....	29
2.2.1 Bubble in a Sheared Flow.....	34
2.2.2 Wind Driven Mixed Layer.....	35
2.2.3 LC Simulation.....	37
2.3 Conclusions.....	52
Chapter 3: A New Vertical Mixing Model with Explicit Entrainment.....	54
3.1 Computation of the Entrainment Rate.....	54
3.2 Prediction of the Vertical Velocity Variance and Turbulence Kinetic energy	64
3.2.1 Third order moments.....	66
3.3 Virtual Mass Flux.....	70
3.3.1 PPM vs. PCM.....	74
3.3.2 Detrainment.....	75
3.4 Discretization.....	75
3.4.1 Vertical staggering.....	76
3.4.2 Time discretization.....	78
3.5 Summary.....	81
Chapter 4: Model Evaluation.....	83
4.1 Formation of a Mixed Layer.....	91
4.2 Established Mixed Layer.....	97
4.2.1 Convectively driven simulation.....	102
4.3 Conclusions.....	106

Chapter 5: The Effect of Turbidity on the Diurnal Cycle of the Ocean Boundary Layer.....	108
5.1 Large Scale Forcing.....	113
5.2 Baseline Simulation	115
5.2.1 Resolution comparisons	120
5.3 Sensitivity Tests	122
5.3.1 Resolution dependence.....	132
5.4 Conclusions.....	135
5.4.1 Caveats and future work	138
Chapter 6: Two-Dimensional Simulations	140
6.1 Two-Dimensional Framework	141
6.1.1 Pressure gradient force.....	142
6.2 Simple Tests of the Pressure Gradient Force	147
6.3 More Realism.....	150
6.3.1 Diurnal cycle.....	155
6.3.2 Sensitivity to monthly varying surface chlorophyll.....	159
6.4 Conclusions.....	161
Chapter 7: Regulation of Intraseasonal SST Variability in the East Pacific Warm Pool by Vertical Mixing	164
7.1 Introduction.....	164
7.2 Model Details.....	167
7.2.1 GCM tendencies.....	168

7.3 Results.....	168
7.4 Sensitivity Tests	173
7.4.1 Sensitivity to model design.....	182
7.5 Conclusions.....	186
Chapter 8: General Conclusions and Future Work.....	189
8.1 Future Work.....	194
APPENDIX A: Derivation of the Vorticity Equations with CLII Forcing.....	198
APPENDIX B: Higher Order Moments	201
B.1 Second Moment Equations.....	201
B.2 Simplifying Assumptions	209
B.3 Third Order Moments.....	212
APPENDIX C: Model Parameters.....	222
APPENDIX D: Two-Dimensional Equations	225
APPENDIX E: Equation Predicting the Inversion Layer Thickness.....	230
APPENDIX F: Structure Functions	232
APPENDIX G: Implicit Treatment of the Discretized TKE Equation	234
REFERENCES.....	238

LIST OF TABLES

TABLE 2.1: Operations performed to derive the vorticity equations in VVM-Aqua.....	25
TABLE 2.2: Summary of parameters relevant to the simulation.....	38
TABLE 3.1: Summary of the key features of the two model frameworks that have been developed. The down gradient model is the simplified framework.....	82
TABLE 4.1: Summary of the five initial test cases. The initial temperature and velocity profiles are given in Figure 4.1. For salinity, there is no vertical variation and the initial value is 35 PSU.....	84
TABLE 6.1: Thicknesses of model layers used in the simulations conducted in this chapter.....	151
TABLE B.1: Operations performed to derive the cross correlations	207
TABLE B.2: Tensor forms of functions introduced in equations (B.35) - (B.44)	211
TABLE B.3: Operations performed to derive the third order moments	213

LIST OF FIGURES

Figure 1.1: Cartoon of temperature profile. Turbulence extends to the thermocline, mixing the top 50 - 100 meters. Taken from <http://www.onrglobal.navy.mil/focus/ocean/images/water/temp.jpg>..... 1

Figure 1.2: Cartoon schematic of a subset of the phenomena influencing the OBL (Taken from pmel.noaa.gov). Incoming shortwave radiation can influence the entire boundary layer and part of the abyssal ocean (blue arrow). The OBL is also influence by the net imbalance of downwelling longwave radiation and surface longwave radiation (green arrows). Sensible (Yellow) and Latent (Purple) heat fluxes also influence the OBL. Finally we must also consider the entrainment of waters from the abyssal ocean (Orange) and water that is detrained from the OBL (red). 2

Figure 1.3: Sensitivity of annually averaged OBL depths to penetrating shortwave radiation. (a) Depth of the OBL base when sunlight is allowed to penetrate below the first model layer and (b) depth of the OBL base when all the sunlight is absorbed in the first model layer, which is 15 meters thick. Taken from Schneider and Zhu, their Figure 7..... 7

Figure 1.4: Schematic illustrating the boundary layer depth interpolation routine. In this one-dimensional example, all quantities are computed at layer center. The differences are defined at model edges. This suggests that the Richardson number should also be defined at layer edges. The green dot represent the critical Richardson number (e.g. 0.65 from PWP)..... 9

Figure 1.5: Illustrations of (a) non-local mixing in the upper ocean and down gradient mixing below. The result of this mixing is shown in (b). 11

Figure 1.6: Sensitivity to the boundary layer depth interpolation routine in CCSM3. HBL is determined by Equation (2), and HMXL is the depth of the maximum buoyancy gradient (thermocline). In this plot, thicker lines represent quadratic interpolation and thin lines are linear interpolation. Taken from Danabasoglu et al. (2006), their Figure A.2..... 13

Figure 1.7: Horizontal mean temperature error for three different GFDL ocean models. CM2G, which is the isopycnal model is Black. CM2.1 and CM2M, which are two different z-coordinate models are Red and Blue respectively. Taken from Hallberg and Adcroft (2009). 17

Figure 2.1: Schematics to illustrate the CLII mechanism. (a) Evidence of Langmuir Cells on a lake. The white lines are called windrows and are the convergence zone of two Langmuir Cells, taken from www.umaine.edu/waterresearch/FieldGuide/onthewater.htm (b) illustration of the wave induced (Stokes) drift (Taken from http://commons.wikimedia.org/wiki/File:Deep_water_wave.gif). (c)

Resulting force from the interaction of the Stokes drift and zonal velocity perturbation (adapted from Leibovich 1983).....	22
Figure 2.2: Variable discretization for VVM-Aqua. The red levels are considered model centers and the black layers are model edges. At the surface, all quantities are assumed to be zero, which is the rigid lid approximation.....	26
Figure 2.3: Slice through the center of the domain of a negatively buoyant bubble placed at the top of the domain through time for third order advection (Left column) and 5th order advection (right column). The times of the slice are given between the two columns.....	30
Figure 2.4: As in Figure 2.3, but for doubled resolution	31
Figure 2.5: Plots of the normalized temperature variance. The dashed lines are for the high resolution simulations. The red lines are for fifth order advection and the black are for third order advection.....	32
Figure 2.6: Snapshots of a slice through the center of the domain of perturbation temperature (a-c) and η (d-f). In the plots of the y-component of vorticity the contour interval is $0.003 \text{ kg m}^{-3}\text{s}^{-1}$, we have shaded vertical velocities less than -0.1 ms^{-1} in gray and values larger than 0.1 ms^{-1} are black. The times are as in Figure 2.3.....	33
Figure 2.7: Temperature (a) and Zonal Velocity (b) profiles through time for the wind induced mixed layer deepening simulation. In both plots, the black plot is hour one, red is hour three, and blue is hour six.	36

Figure 2.8: Vertical velocity variance normalized by the surface friction velocity through time for the Langmuir turbulence run (a), and the surface momentum forcing only run (b). Note the difference in color scale. In (a) the contour interval is 0.213 and is 0.07 in (b).39

Figure 2.9: Horizontal slices of vertical velocity at two meters depth for the run with LC forcing (a) and the run without (b). The color scale is identical in both plots..... 39

Figure 2.10: Plot of horizontally averaged temperature relative to the initial temperature for the run with LC (a), and without (b). The contour interval in (a) is 0.02 K and is 0.0013 in (b). 40

Figure 2.11: Identical LC test as shown in Figure 2.9a, but here the domain size has been doubled. 41

Figure 2.12: Effect of averaging interval on the profile of normalized heat flux. In this plot, green is the instantaneous heat flux. The black line is averaged over one hour, the red curve is averaged over two hours, and the blue curve is averaged over six hours. 42

Figure 2.13: Time and domain averaged zonal velocity plots for VVM-Aqua (a) and M97 (b). In both plots, the dashed line includes LC forcing, the solid line does not. In (a), the dashed blue line is the small domain (S/0.3 in M97) and the red line is the extended domain (E/0.3 in M97). 42

Figure 2.14: As in Figure 2.13, but for the v -component of velocity..... 43

Figure 2.15: Time averaged profiles of the normalized turbulent flux of u for VVM-Aqua (a) and M97 (b). The line styles and colors are as in Figure 2.13.....	44
Figure 2.16: As in Figure 2.15, but for $\overline{v'w'}/u_*^2$	45
Figure 2.17: As in Figure 2.15, but for $\overline{w'\theta'}/w'\theta'_{sfc}$	46
Figure 2.18: As in Figure 2.15, but for $\overline{w'\theta'}/w'\theta'_{sfc}$	48
Figure 2.19: Horizontally and time averaged profiles of $\overline{u'w'}/u_*^2$ (a) and $\overline{v'w'}/u_*^2$ (b). In these plots, the blue line is the small domain LC run with one meter resolution and the dashed blue line uses 0.5 meter resolution.....	49
Figure 2.20: As in Figure 2.19, but for the normalized heat flux.....	50
Figure 2.21: As in Figure 2.19, but for $\overline{w'^2}/u_*^2$	51
Figure 3.1: Grid arrangement of the new model framework discussed here and in Chapter 6.....	56
Figure 3.2: Plots of modeled $\overline{w'^4}$ and $3\overline{w'^2}$ (a) is from the test of Andre and Lacarrere (1985) and (b) is from the LC forcing run described in Chapter 2. The blue box in both figures represents the inversion layer. The thickness of this layer is bounded by the positions where $\overline{\theta'^2}$ falls to 5% of its maximum value.....	62

- Figure 3.3:** Schematics illustrating when the down gradient approximation fails (a) and when it works (b). In both plots, the TKE is plotted in black, and the arrows indicate the direction of the down gradient forcing. (a) is convectively dominated and (b) is shear dominated. 67
- Figure 3.4:** Schematic to illustrate the virtual mass flux. The original depths at the interfaces are given by unprimed z 's. Entrainment occurs at the layer three interface. After some Δt , the model interfaces move to the red lines (primed z 's). The new properties within the layer result from a combination of the original layer value, and those between the black and red lines. 71
- Figure 3.5:** Two possible representations of the sub-grid scale distribution of temperature. The original profile is black, a piecewise constant representation is green, and the piecewise parabolic representation is red. 72
- Figure 3.6:** Profiles of temperature after one remapping cycle using the PCM (black) and PPM (blue) methods. The observed temperature is red. 74
- Figure 3.7:** Vertical discretization used in the new model framework. 76
- Figure 4.1:** Initial temperature and velocity profile from AL85. (a) Temperature and (b) zonal velocity. Below 15 meters, the stratification is constant ($0.04 \text{ }^\circ\text{Cm}^{-1}$) and the zonal velocity is zero. 83
- Figure 4.2:** Temperature (a) and mixed layer depth (b). For Case 1. In (a), the black curves are at two minutes. The blue curves are after 10 hours and the red curves are after 15 hours. At each time, the solid line is VVM-Aqua, the dashed line is

<p>KPP, the dashed line is the second order model, and the circle line is the TKE based model. In (b), the dashed line is VVM-Aqua, the black line is KPP, the red line is the SOC model, and the blue line is the TKE based model.</p>	85
Figure 4.3: As in Figure 4.2, but for Case 2.....	86
Figure 4.4: Temperature (a), salinity (b), and mixed layer depths (c) for Case 3. In (a) and (b), the colors and line styles are as in Figure 4.2a. In (c), the colors are as in Figure 4.2b	87
Figure 4.5: As in Figure 4.4, but for surface freshening (Case 4)	88
Figure 4.6: Temperature (a) and simulated mixed layer depths (b). In (a), the defined line styles are as in the previous temperature profiles, but the black lines are 15 hours, the blue lines are 22 hours, and the red lines are 30 hours. The colors in (b) are as in Figure 4.2b.....	89
Figure 4.7: Mixed layer depths simulated by the TKE model (blue) and the SOC model (black) forced as in Case 2, but the simulation length is increased by a factor of ten.	90
Figure 4.8: Temperature (ab) and Zonal Velocity (cd) profiles for the no initial mixed layer, wind-driven, run. In all these plots black lines are from VVM-Aqua, blue lines are from KPP, and the red lines are from the TKE model. The solid lines are at two hours, the dashed lines are from six hours, and the circle dashed lines are from 12 hours. The vertical resolution for VVM-Aqua is 0.5 meters. In (a) and (c), the initial vertical resolution for the TKE model and KPP is one meter. The resolution is increased to five meters in (b) and (d).....	91

Figure 4.9: Colors and line styles are as in Figure 4.8. (a) one meter resolution, (b) five meter resolution, and (c) 11 meter resolution. 92

Figure 4.10: Test of the influence of non-local forcing in KPP. The line style is as in Figure 4.9. The blue line is the result from Figure 4.9. The black line removes the non-local forcing. (a) one meter resolution, (b) five meter resolution, and (c) 11 meter resolution..... 95

Figure 4.11: Time averaged profiles of zonal velocity (a), meridional velocity (b), $\overline{u'w'}/u_*^2$, and (c) $\overline{v'w'}/u_*^2$. In these figures, the black line is from VVM-Aqua, red is KPP and blue is the TKE model. The results are plotted in a normalized depth coordinate (as in Chapter 2). 96

Figure 4.12: Time averaged profiles of normalized vertical heat flux. The colors are as in Figure 4.11. 97

Figure 4.13: Impact of changing vertical resolution on (ab) u , (cd) v , (ef) $\overline{u'w'}/u_*^2$, and (gh) $\overline{v'w'}/u_*^2$. In these plots, the black line is one-meter resolution, the blue line is five meter resolution, and the red line is 11 meter resolution. The left column is the TKE model and the right column is from KPP..... 99

Figure 4.14: As in Figure 4.13, but for $\overline{w'\theta'}/w'\theta'_{sfc}$ 101

Figure 4.15: Temperature change relative to the initial temperature through time for (a) VVM-Aqua, (b) TKE model, and (c) KPP. In (a) and (c), the contour interval is 0.008°C and is 0.006°C in (b). 103

Figure 4.16: Mixed layer depths through time for three different resolutions. (a) one meter resolution, (b) five meter resolution, and (c) 11 meter resolution. In all the plots, black is VVM-Aqua, red is KPP, and blue is the TKE model..... 104

Figure 5.1: Annual composite (2009) of surface chlorophyll observed by SeaWIFS. Green colors are high chlorophyll and blue is low chlorophyll. Figure is taken from oceancolor.nasa.gov..... 109

Figure 5.2: Temperature of water in the Equatorial undercurrent for different strengths of chlorophyll forcing. Taken from GA09, their Figure 6c..... 109

Figure 5.3: Observed chlorophyll distributions. The left figure is near the Southern California coast, the middle is from the Scotian shelf, and the right profile is taken near the Azores. Figure taken from Lewis et al. (1983), their Figure 4 111

Figure 5.4: Initial profiles of (a) zonal velocity, (b) temperature, (c) large scale vertical velocity, (d) divergence, (e) large scale pressure gradient (solid line) and eddy forcing term in the zonal momentum equation (dashed line), and (f) eddy forcing for the temperature equation. Taken from Wang et al. (1998) their Figure 1. ... 114

Figure 5.5: Temperature profiles through time from LES output of W98 (a), the new model (b), and KPP (c). The contour interval in every plot is 0.1°C. The plots

have been sized and offset such that the length of the run in W98 matches that conducted here. 116

Figure 5.6: Zonal velocity profiles through time from LES output of W98 (a), the new model (b), and KPP (c). The contour interval in every plot is 0.05 ms⁻¹. The plots have been sized and offset such that the length of the run in W98 matches that conducted here. 117

Figure 5.7: $\frac{\overline{u'w'}}{u_*^2}$ profiles from day six from LES output of W98 (a), the new model (b), and KPP (c). The contour interval in every plot is 0.2. 119

Figure 5.8: Time-depth profiles of temperature for the new model (a) and KPP (b). Zonal velocity for the new model (c) and KPP (d), and Normalized momentum flux for the new model (e) and KPP (f). The results from the new model are interpolated to a uniform grid and KPP is not, this accounts for the white space in the plots in the right column. 121

Figure 5.9: Profiles of Chlorophyll normalized by their respective maximums (a) and their resulting irradiance profiles (b). In these figures, the black line is from observations, and the dashed line is constructed. In (b) we have plotted the irradiance profile resulting from a constant $k_{VIS} = 0.05 \text{ m}^{-1}$ 124

Figure 5.10: Profiles of simulated temperature anomalies (°C) relative to the four meter resolution control run for (a) low k , (b) high k , (c) Chlorophyll II, and (d) top simulations. The Chlorophyll I anomalies are very small and are not plotted... 125

Figure 5.11: As in Figure 5.10, but for zonal velocity 127

Figure 5.12: As in Figure 5.10, but for KPP.....	128
Figure 5.13: As in Figure 5.11, but for KPP.....	130
Figure 5.14: Profiles of simulated temperature anomalies (a) and velocity (b) at ten meter resolution relative to the ten meter control run for the top test.....	132
Figure 5.15: As in Figure 5.14, but for KPP.....	133
Figure 6.1: Schematic of the contour interval to be evaluated in the model pressure gradient force. The solid curved lines represent constant σ surfaces. This figure has been adapted from SW03, their Figure 7.....	144
Figure 6.2: Longitude-Depth plots of Temperature at seven meter resolution (a) and 2.5 meter resolution (b). Plotted in (c) is the zonal velocity at seven meter resolution. In (d) is the zonal velocity at 2.5 meter resolution. The contour intervals for the temperature plots is 1°C and is 0.05 ms^{-1} for velocity.	148
Figure 6.3: Sea surface height in the coarse resolution simulation (a) and the simulation with 2.5 meter resolution (b). In both models, the black line is one quarter the way through the run, the red line is one half through the run, blue is three quarters through the run, and green is at the end of the run.....	149
Figure 6.4: (a) Annually averaged temperature from LB94 at the equator. (b) the initial temperature profile used in the simulations, which is a zonal average of (a).....	150
Figure 6.5: Levitus (1994) SST along the section in Figure 6.4a (solid black), and the restoring function used in the model simulations (blue line).....	152

Figure 6.6: Time averaged longitude-depth profiles of temperature (a) and zonal velocity (b) for the baseline Levitus simulation. On both plots, the modeled boundary layer depth is plotted as a dashed line. As in the previous plots, the output from the model has been interpolated to a uniformly spaced vertical grid. The contour intervals are as in Figure 6.2..... 153

Figure 6.7: Surface height predicted by the new model at 2.5 years (black), 5 years (red), 7.5 years (blue), and 10 years (green). 154

Figure 6.8: Time averaged (year 10) latitude-depth plots of temperature (a) and zonal velocity (b). The contour intervals are as in Figure 6.2. 155

Figure 6.9: Surface height predicted by the model in the run with constant coefficient solar forcing. The colors of the curves are as in Figure 6.7. 157

Figure 6.10: Time averaged (year 10) latitude-depth plots of the change in temperature (a) and zonal velocity (b) relative to the previous simulation (Figure 6.8). The contour interval in (a) is 0.25°C and is 0.05 ms⁻¹ in (b). 158

Figure 6.11: Attenuation coefficients resulting from the GA09 optical parameterization. The chlorophyll is from a SeaWIFS monthly climatology. 159

Figure 6.12: Time averaged (year 10) latitude-depth plots of the change in temperature (a) and zonal velocity (b) due to the addition of surface chlorophyll relative to the previous simulation (Figure 6.8). The contour interval in (a) is 0.5°C and is 0.05 ms⁻¹ in (b). 160

Figure 7.1: Surface forcing derived from observations at the 8°N 95°W TAO buoy from 2002. (a) Surface heat flux (Black) and Surface Shortwave radiation (Red). (b) Zonal (red) and Meridional (blue) wind stress. (c) Precipitation..... 166

Figure 7.2: Raw (a) and 59-day running mean filtered SST (b) for TAO data (dashed red), KPP (blue), and the new model (Black). In this plot and all others, the Day refers to days since January 1, 2002. 169

Figure 7.3: (a) MLD predicted by the new model (red) versus observations (black) (b) MLD predicted by KPP (red) versus observations (black) 170

Figure 7.4: Sensitivity to a minimum mixing coefficient in the new model. The simulated SST anomaly is in black. The result from Figure 7.2b has been replotted (blue). Again the TAO observation is the dashed red line. 171

Figure 7.5: Sensitivity of the simulated SST anomalies to advective tendencies diagnosed from CCoSM. (a) New model framework, (b) KPP. In (a)-(b), the baseline result is plotted in black, the run with advective tendencies in blue, and the dashed red line is from the TAO buoy. (c) OML depths simulated in the new model and (d) KPP. In (c)-(d), the observations are plotted in black, the control simulation is dashed gray, and the sensitivity test is in red..... 172

Figure 7.6: Sensitivity to fixing the surface heat flux (Sensible plus Latent) to the summer time average. (a) SST anomaly, (b) OML depths simulated by the new model, (c) OML depths simulated by KPP. The colors are as in Figure 7.5..... 174

Figure 7.7: Sensitivity to fixing the surface shortwave radiation to the summer time average. (a) SST anomaly, (b) OML depths simulated by the new model, (c) OML depths simulated by KPP. The colors are as in Figure 7.5. 175

Figure 7.8: Sum of SST changes due to fixing all fluxes to the summertime average (black). The blue line is the sum of SST changes due to fixing the surface heat flux and shortwave radiation to the summer average. 176

Figure 7.9: Sensitivity to increasing the absorption of the visible component of shortwave radiation ($k = 5m^{-1}$). (a) SST anomaly, (b) OML depths simulated by the new model, (c) OML depths simulated by KPP. The colors are as in Figure 7.5..... 177

Figure 7.10: Profiles of TKE near day 200 for (a) Baseline simulation, (b) and increased absorption test. The units are m^2s^{-2} 178

Figure 7.11: Sensitivity to fixing the surface wind stress to the summer time average. (a) SST anomaly, (b) OML depths simulated by the new model, (c) OML depths simulated by KPP. The colors are as in Figure 7.5..... 179

Figure 7.12: Modeled viscosity for the baseline run (a) and (c) and the sensitivity test fixing wind stress to the summertime average (b) and (d). The top row is for KPP and the bottom is the new model framework. The units are m^2s^{-1} 181

Figure 7.13: Sensitivity to fixing the artificially increasing the diffusivity in the top model layer. (a) SST anomaly, (b) OML depths simulated by the new model, (c) OML depths simulated by KPP. The colors are as in Figure 7.5. 183

Figure 7.14: Evaluation of the impact of non-local effects on KPP simulated SST.

Black is the control run and Blue is the result from the test. 184

Figure 7.15: SST anomalies simulated by a slab model. The black line is for a constant

mixed layer depth. The blue line allows the mixed layer to vary according to the

value given by the Monterrey and Levitus dataset. 185

Figure 8.1: Layer thicknesses, of the top 15 layers, adjacent to the western boundary for

the baseline two dimensional run. The black circles are the initial thicknesses and

the blue circles are thicknesses at the end of the ten year run. 195

Figure C.1: Plot of functions from Canuto et al. (2008) (a) π_1 , (b) π_4 , and (c) π_2 . In

all of the plots, the constant value assumed in Canuto et al. (2002) is signified by

a blue dot. 224

Figure G.1: Four different cases of a cubic function defined by equation G.1. 236

Chapter 1:

The Dynamics of the Upper Ocean

The top few hundred meters of the ocean is characterized by strong turbulence. It is directly involved in the communication of fluxes (latent heat, sensible heat, and momentum) to the atmosphere and abyssal ocean. Although upper ocean turbulence may end at the base of the ocean mixed layer (OML), it is possible for it to extend beyond this depth. Figure 1.1 shows a schematic of ocean temperature with depth. Turbulence extends to the thermocline. This depth may not be identical to the depth of the OML base.

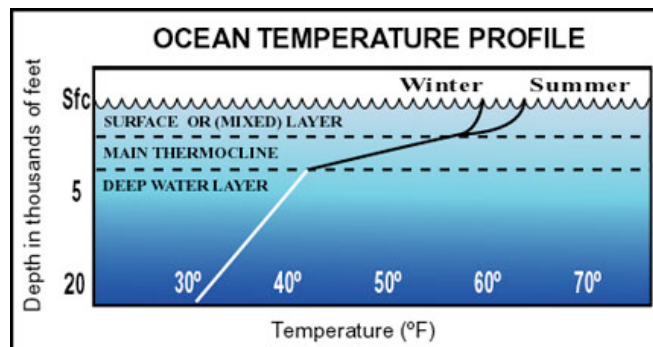


Figure 1.1 - Cartoon of temperature profile. Turbulence extends to the thermocline, mixing the top 50 - 100 meters. Taken from <http://www.onrglobal.navy.mil/focus/ocean/images/water/temp.jpg>

Though the terms mixed layer and boundary layer tend to be used interchangeably, we define the near surface turbulent layer as the ocean boundary layer (OBL) and the well mixed region of the OBL as the OML.

The OBL is essential for many processes such as the meridional overturning circulation (Mohammad and Nilsson 2004), El Niño Southern Oscillation, and hurricanes. Many physical processes regulate the thermodynamic and momentum fields

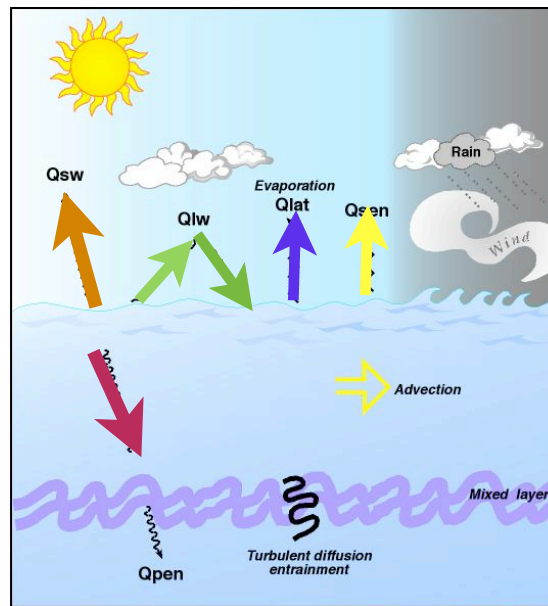


Figure 1.2 - Cartoon schematic of a subset of the phenomena influencing the OBL (Taken from pmel.noaa.gov). Incoming shortwave radiation can influence the entire boundary layer and part of the abyssal ocean (blue arrow). The OBL is also influence by the net imbalance of downwelling longwave radiation and surface longwave radiation (green arrows). Sensible (Yellow) and Latent (Purple) heat fluxes also influence the OBL. Finally we must also consider the entrainment of waters from the abyssal ocean (Orange) and water that is detrained from the OBL (red).

of the upper ocean. A few of these processes are illustrated in Figure 1.2. There are two essential ingredients that models of upper ocean must consider. First, a parameterization of entrainment across the OBL base is needed. As the mixed layer expands, abyssal water is entrained into the upper ocean and can then be influenced by surface fluxes.

When the OBL shoals, the water that has been modified by surface fluxes becomes part of the deep ocean.

Second, models must correctly incorporate the influence of atmospheric forcing. In this work, we pay particular attention to how surface shortwave radiation influences the OBL.

1.1 Penetrating Shortwave Radiation

There are two ways to parameterize the remaining shortwave radiation. The first approach is to absorb all the radiation in the top model level. When shortwave radiation is allowed to penetrate beyond the top layer, the depth dependence is assumed to follow

$$I(z) = I_o \left(I_{IR} e^{-k_{ir}z} + I_{VIS} e^{-k_{vis}z} \right). \quad (1.1)$$

Here, I_o is the surface irradiance, I_{IR} and I_{VIS} are the percentage of irradiance absorbed in the infrared and visible bands respectively, and k_{ir} and k_{vis} are the attenuation coefficients. For many years, k_{VIS} was assumed to coincide with one of five different water types (Jerlov 1968, Paulson and Simpson 1977). Instead of assuming a priori water types, calculating irradiance based on modeled quantities is desirable (Ohlmann et al. 1998).

Morel (1988), Morel and Antoine (1994), and Morel and Maritorena (2001) suggested that the extinction coefficient should be dependent upon the in situ chlorophyll concentration. These studies propose that the extinction should be computed as $k_{VIS}(\lambda) = K_w(\lambda) + \chi_c(\lambda)C^{e(\lambda)}$. Here K_w is the attenuation of clear water and C is the

chlorophyll-a concentration. The functions $\chi_c(\lambda)$ and $e(\lambda)$ are determined by fitting the proposed equation to data.

The resulting parameterization is a function of wavelength and chlorophyll. It is not feasible for ocean general circulation models to predict irradiance across all wavelengths. Instead, this parameterization is usually integrated across two bands to mirror the form of Paulson and Simpson (1977). Manizza et al. (2005) proposed the following

$$\begin{aligned}
 I(z) &= I_o \left(0.5e^{-k_{IR}z} + 0.5e^{-k_{chl}z} \right) \\
 k_{IR} &= 2m^{-1} \\
 k_{chl} &= 0.0232 + 0.074C^{0.674}.
 \end{aligned}
 \tag{1.2}$$

The chlorophyll concentration in the parameterization of k_{chl} is most often assumed to be a surface value. Therefore, the extinction coefficient is taken to be horizontally and temporally variable, but there is no change with depth. To allow extinction to vary with depth phytoplankton, which can be taken as a proxy for chlorophyll, must be predicted.

It should be noted that this parameterization is just one of a large number previously proposed in the literature. For example, Ohlmann et al. (1998,2000) proposed a parameterization that has two more terms than equation (1.2). Ohlmann et al. (1998,2000) proposed a relationship that depends on cloud fraction and solar zenith angle in addition to the chlorophyll concentration.

Despite extensive efforts to parameterize the relationship between visible light extinction and chlorophyll, some have questioned (Siegel et al. 2005) if the extinction of visible light should depend solely on the chlorophyll concentration. In addition to

chlorophyll, colored dissolved organic matter strongly absorbs solar radiation in the visible band and other particles scatter incident visible light. This implies that use of surface chlorophyll measurements may not be sufficient in determining the influence of penetrating solar radiation on ocean dynamics.

Even if we were to include other particles in a parameterization of visible light extinction the standard continuum approximation is invoked. This may be a poor assumption when considering phytoplankton. In a given parcel of water, a wide variety of phytoplankton species coexist. Siegel (1998) argues that this paradox, where many species of phytoplankton coexist in a small space, is due to a highly discrete (i.e. non-continuous) distribution within a parcel. Siegel (1998) states that the separation between individual phytoplankton is large enough to allow different species to coexist in a parcel and the continuum approximation should not be invoked for even the largest observed phytoplankton concentrations.

If we are forced to abandon the continuum approximation for ocean biomass (e.g. phytoplankton), the interaction of solar radiation, biology, and ocean dynamics becomes exponentially more complex. Regions of water within a GCM grid box will not absorb solar radiation at a constant rate. This implies that knowledge of the sub-grid distribution of biomass would be required to accurately parameterize solar heating. In spite of the results presented by Siegel (1998), we utilize the continuum approximation in this work.

To low order, phytoplankton attempts to maximize light and nutrients. The vertical distribution of phytoplankton could have an important influence on the profile of solar heating. The flow of nutrients into the OBL is controlled by two mechanisms.

McGillicuddy et al. (1998, 2007) propose that lifting due to mesoscale eddies is a large contributor to the nutrient budget in many regions of the ocean. In addition, the entrainment of cold abyssal waters can move nutrient-replete waters into the upper ocean. In the simulations presented in this work, which are one- and two-dimensional, we cannot simulate the influence of mesoscale eddies. However, the importance of the second mechanism confirms our belief that a model must accurately predict entrainment at the base of the boundary layer.

1.1.1 Influence of Penetrating Shortwave Radiation.

The influence of allowing shortwave radiation to penetrate beyond the first layer is dramatic. Schneider and Zhu (1998, SZ98) conducted a simulation where all the shortwave radiation is absorbed in the top model layer (15 m) and another using equation (1.1) with $k_{vis}=15 \text{ m}^{-1}$. The resulting OML depths for the sunlight penetration and no sunlight penetration runs are shown in Figure 1.3a and 1.3b respectively.

The rough pattern of OML depths in Figure 1.3b is as expected. The boundary layer is deeper in the extra-tropics and polar regions and shallower in the tropics. When sunlight is allowed to penetrate beyond the first layer, the change is dramatic. A realistic east-west tilt of the tropical OML is now evident, and in general, the modeled mixed layer depths are deeper nearly everywhere.

When all of the sunlight is confined to the top layer, the static stability is increased, prohibiting vertical mixing. The overestimated seasonal cycle amplitude in the run where the sunlight is confined to the top layer is reduced when the sunlight is allowed

to penetrate, due to the increased OML depth, which increases the thermal inertia of the ocean.

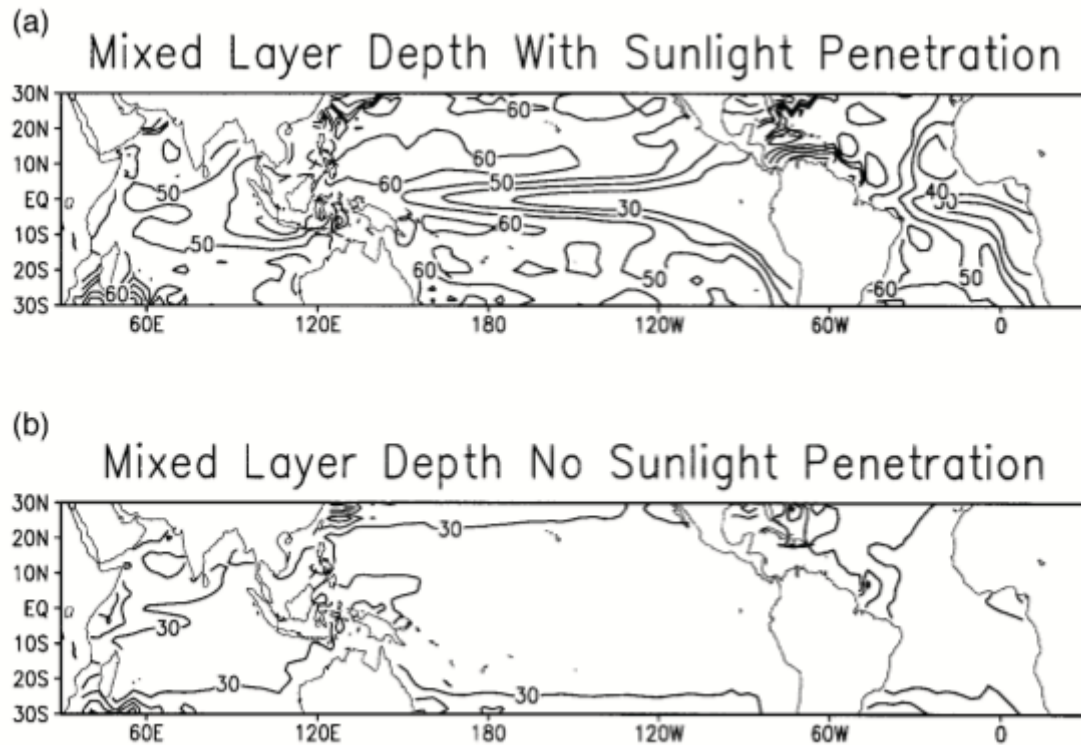


Figure 1.3 - Sensitivity of annually averaged OBL depths to penetrating shortwave radiation. (a) Depth of the OBL base when sunlight is allowed to penetrate below the first model layer and (b) depth of the OBL base when all the sunlight is absorbed in the first model layer, which is 15 meters thick. Taken from Schneider and Zhu, their Figure 7.

The influence of k_{vis} on the observed (or modeled) chlorophyll is not completely understood. Many (e.g. Manizza et al. 2005; M05, Anderson et al. 2007, Gnanadesikan and Anderson 2009; GA09, Anderson et al. 2009) find that the eastern tropical Pacific (cold tongue) sea surface temperature (SST) cools and the Walker circulation strengthens. A few others (e.g. Murtugudde et al. 2002 and one simulation from M05) find the opposite result.

To study the influence of penetrating shortwave radiation on the upper ocean, a model is required. Therefore, a survey of previous vertical mixing models is conducted

to determine what is desirable in a model. We also address why a new model is developed rather than using a previous mixing scheme.

1.2 Past OBL Models

Modeling of the OBL began with the pioneering work of Kraus and Turner (1967; hereafter KT). KT (and other works utilizing the type of model developed by Kraus and Turner 1967) assume that the upper ocean is a perfectly mixed slab. To predict the position of the OBL base, KT considered an integrated turbulence kinetic energy (TKE) equation. Further, KT assumed that buoyant production of TKE is due to temperature fluxes only (no salinity). This model was later extended by Niiler and Kraus (1977), Gaspar (1988), and numerous others. Advances include the incorporation of salinity and refinement of the parameterizations of the integrated TKE production terms.

The model of Deardorf (1983) follows KT, but neglects the time change term in the integrated turbulence kinetic energy equation. The resulting entrainment rate is proportional to three different diagnostic quantities. These quantities depend on shear across the boundary layer base, and surface buoyancy and momentum forcing.

Modeling of the OBL moved in a different direction with the work of Price et al. (1986; hereafter PWP). In this model, the mixing of properties is assumed to be

proportional to a given function of the bulk Richardson number $\left(Ri = \frac{g\Delta\rho H}{\rho_o(\Delta V)^2} \right)$ and the

base of the OBL is determined as the location where $Ri = 0.65$. This critical Richardson

number was determined by comparing model output to observations of OBL deepening due to two storms near the Florida coast (Price et al. 1978).

The method for determining the boundary layer depths in these models is

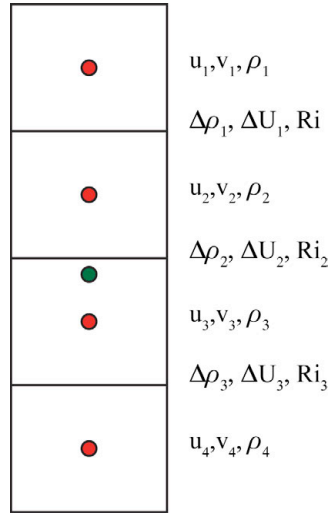


Figure 1.4 - Schematic illustrating the boundary layer depth interpolation routine. In this one-dimensional example, all quantities are computed at layer center. The differences are defined at model edges. This suggests that the Richardson number should also be defined at layer edges. The green dot represent the critical Richardson number (e.g. 0.65 from PWP).

illustrated in Figure 1.4. The critical Richardson number is given as the green dot. Let us also assume that the density is equal in the top two layers. In one-dimension, it is assumed that the velocities and densities are co-located. This implies that the natural location for $\Delta\rho = \rho_2 - \rho_1$ and $\Delta U = U_2 - U_1$ is the layer interface. Beginning at the first interface, the Richardson number is calculated (Ri_1 in the figure). Since the value has not yet exceeded the critical Richardson number ($\Delta\rho = 0$), the Richardson Number is calculated at the second model interface. In this example we have assumed that the Richardson number calculated at the second interface is slightly smaller than the PWP

critical value. When we calculate the Richardson number at the third interface, the value will exceed 0.65, therefore, we must use interpolation to find the depth of the boundary layer. To the best of our knowledge, models similar to PWP use linear interpolation. This assumption becomes tenuous as the resolution coarsens.

To this point, a perfectly uniform mixed layer has been assumed (for all predicted quantities), which implies an infinite efficiency of mixing. Further, the assumption of a uniform OBL is contradicted by observations from the Tropical Oceans Global Atmosphere Coupled Ocean-Atmosphere Response Experiment (TOGA-COARE; Webster and Lukas 1992).

Vertical structure in the salinity and theta fields in the upper ocean can still result in a fairly well mixed layer in density. Anderson et al. (1996) find that the depth of the constant salinity (isohaline) layer can deviate from that of the isothermal layer by as much as 30 meters. A large precipitation event can create a shallow isohaline layer. The influence on the temperature field would be minimal. The resulting mixed layer would lie between the isothermal and isohaline layers. Bulk mixed layer models cannot correctly predict the depth of the OML base in this situation.

To address some of these assumptions, Large et al. (1994), following on previous atmospheric modeling research (e.g. Troen and Mahrt 1986 and Holtslag et al. 1990), proposed K-profile parameterization (KPP). KPP does not assume a well mixed upper ocean. In KPP, a polynomial profile of diffusivity is fit to match Monin-Obukhov similarity theory at the surface and the model predicted diffusivity at the OML base.

KPP also included a non-local forcing. The non-local term assumes a well mixed upper ocean and hence a linear flux profile that is related to the surface heat flux, convective velocity scale, and mixed layer depth is implemented in KPP. Large et al. (1994) did not propose a non-local momentum flux, however, one has recently been suggested by Smyth et al. (2002).

The non-local forcing is schematically illustrated in Figure 1.5. As the surface fluxes change the temperature and salinity, these changes can be communicated to the deeper ocean by two mechanisms. When convection occurs (cooling or increasing salinity), an unstable gradient is created (temperature increasing with depth or salinity decreasing with depth). This forcing needs to be communicated across very weak (or unstable) gradients to the mixed layer base (illustrated in the top portion of Fig. 1.5a). Inclusion of non-local mixing can be important to correctly simulating the diurnal cycle

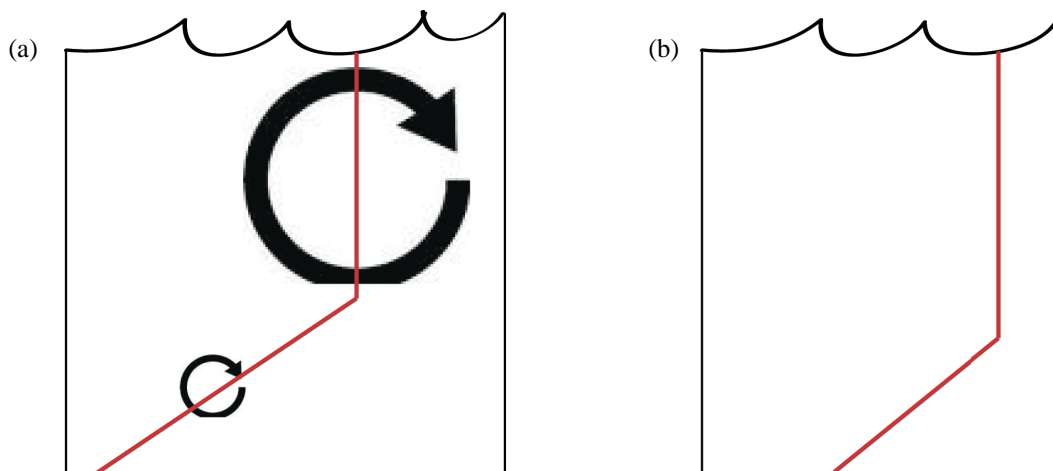


Figure 1.5 - Illustrations of (a) non-local mixing in the upper ocean and down gradient mixing below. The result of this mixing is shown in (b).

of the OBL.

Mixing in the absence of convection is usually down-gradient (bottom portion of Figure 1.5a). The result of these two types of mixing is schematically illustrated in Figure 1.5b.

Despite advances in the model predicted diffusivity, KPP still determines the depth of the OML by a Richardson number criterion. In KPP, the Richardson number is defined as

$$Ri = \frac{(B_r - B(h))h}{|V_r - V(h)|^2 + V_t^2(h)}; V_t^2(h) = \frac{C_v (-\beta_T)^{1/2}}{Ri_c K^{2/3}} (c_s \epsilon)^{-1/6} h N w^*. \quad (1.3)$$

In this definition, the turbulent velocity shear squared (V_t^2) is not only dependent on the boundary layer depth (h), stratification (N), and the convective velocity scale, but it also depends on a critical Richardson number (Ri_c). In the original model, a value of 0.3 is proposed, which was chosen to match a high resolution KPP run. Danabasoglu and Large (2003) suggest that this value should increase as resolution coarsens.

This critical Richardson number is also used to determine the boundary layer depth. The same methodology described in reference to Figure 1.4 is used in this model. However, the current version of KPP has abandoned linear interpolation for a second order polynomial fit. This change was implemented in the third version of the Community Climate System Model (Danabasoglu et al. 2006).

The influence of changing the accuracy of interpolation is shown in Figure 1.6, where the results have been zonally averaged. In this plot, HBL is the quantity determined by equation (1.3). HMXL is the depth of the maximum buoyancy gradient

(thermocline), which is opposite of what is defined in this work. The thick lines are the result of using quadratic interpolation and thin lines result from linear interpolation. At all latitudes, the zonally averaged HBL and HMXL are deeper when using quadratic interpolation. The systematic shallow bias noted in Appendix C of Large et al. (1994) is

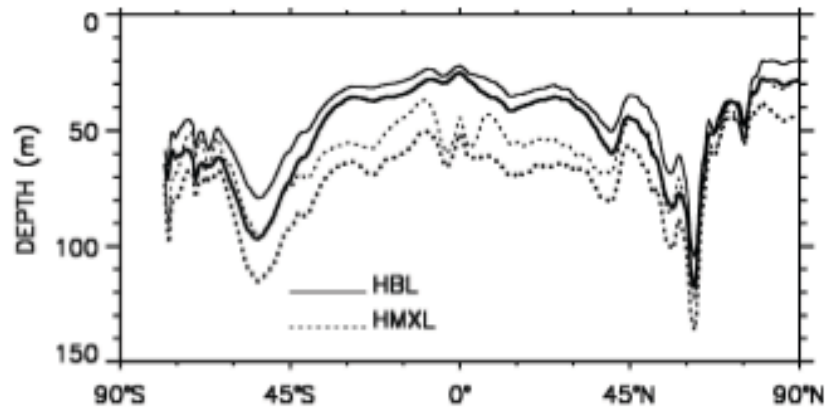


Figure 1.6 - Sensitivity to the boundary layer depth interpolation routine in CCSM3. HBL is determined by Equation (2), and HMXL is the depth of the maximum buoyancy gradient (thermocline). In this plot, thicker lines represent quadratic interpolation and thin lines are linear interpolation. Taken from Danabasoglu et al. (2006), their Figure A.2.

partially remedied by using quadratic interpolation.

Although KPP is an improvement over previous OBL models, there are many shortcomings, the most glaring is the internal mixing algorithm. Below the OML the mixing is simply proportional to the Richardson number. A number of papers (e.g. Jackson et al. 2008 and Zaron and Moum 2009) have noted that the dimensional coefficients in this parameterization yield unrealistically large heat fluxes (Zaron and Moum 2009). Since the predicted mixing at the base of the OML affects the profile of diffusivity in the OBL, this problem could propagate through the entire upper ocean.

The last common option for modeling of OBL processes are k - ε (TKE - dissipation) models. These models will predict TKE (k) and the dissipation of TKE (ε).

Once these quantities are predicted, the diffusivity is parameterized as $K_h = \frac{2k^2}{\varepsilon} S_h$. In

this equation, S_h is referred to as a structure function (see for example, Canuto et al. 2001, 2002, 2008).

In this framework, it is assumed that the third order moments and time tendency terms of the second order moment equations are small compared to other terms. For example, consider the potential temperature variance ($\overline{\theta'^2}$) equation, which is given by (see Appendix B)

$$\frac{\partial \overline{\theta'^2}}{\partial t} + \frac{\partial \overline{w'\theta'^2}}{\partial z} = -2\overline{w'\theta'} \frac{\partial \theta}{\partial z} - \frac{2\overline{\theta'^2}}{\tau_\theta}.$$

Here, the second term on the left-hand side is the non-locality and τ_θ is an eddy turnover time-scale. If we assume the the left-hand side is zero, the potential temperature variance is given by $\overline{\theta'^2} = -2\overline{w'\theta'} \tau_\theta \frac{\partial \theta}{\partial z}$. If we make this assumption in the other second moment

equations, we have a coupled set of linear equations. All of the second order moment equations are satisfied, assuming the time change and non-local terms are small. This type of model is sometimes referred to as an algebraic Reynolds stress model and follows on the early work of Rodi (1976) and Gibson and Launder (1976).

The solution of the system equations is very complex. The resulting fluxes are proportional to mean quantities (e.g. shear, N^2), TKE, and dissipation. Most of the terms are grouped into the structure functions for simplicity.

Burchard et al. (1998) find that the use of a differential equation for dissipation led to an under prediction of TKE dissipation. Thus, many k - ε models have abandoned the equation for dissipation and have chosen to determine the dissipation from different parameterizations (most commonly $\varepsilon = k^{3/2} / l$, where l is the turbulent length scale, which can be diagnosed or predicted).

1.2.1 OBL Model Evaluations

KPP and KT type models have been tested in many situations. van Eijk (1998) tested a bulk (KT like) model and non-local diffusion (KPP) model in the Hamburg Ocean model. The non-local diffusion model outperformed the bulk model in most simulations. The only noted advantage of the KT model was speed.

In a study using Argo floats to verify predicted OML depths, Acreman and Jeffery (2007) found that KPP simulated mixed layer depths well, provided the vertical resolution was fine enough. KPP did well at 2m resolution and outperformed KT and a two equation (k - ε) model at 0.5m resolution. As the resolution degrades (their Fig. 3), KPP is unable to correctly simulate the deepening phase of the annual cycle of the mixed layer depth.

Models following KT assume that the top model level is the mixed layer. In summer months, the mixed layer depths are shallower and the model can respond quickly to atmospheric forcing. In the winter, when the mixed layer is thicker, the models

following KT are not able to respond to atmospheric forcing as rapidly as KPP. The model predicted OML is closer to observations in the summer than in winter in bulk mixed layer models (Acreman and Jeffery 2007).

In a study of the response of the upper ocean to three separate hurricanes, Jacob et al. (2006) found that the level 2.5 model of Mellor and Yamada (1982), which is a two equation turbulence model, outperformed bulk models when compared to observations. In one of the three hurricanes, KPP performed on par with the two equation mixing models.

In general, models following KT tended to be too warm and exhibit too little entrainment. Some improvement was found by adjusting some of the constants in the parameterizations of the production terms in the layer integrated TKE equation. Jacob et al. (2000) argue that the under prediction of entrainment rate in bulk mixed layer models can be linked to not considering the effect of shear across the OML base.

1.3 Vertical Coordinates

In addition to model physics, discretization can impact the fidelity of model solutions. The first ocean models (e.g. Bryan 1969) were discretized on a cartesian (i.e. z-level) grid. It is relatively easy to formulate a model on a cartesian grid, but the model can be prone to spurious diapycnal mixing (Griffies et al. 2000). This can degrade the representation of key physical processes, such as overflows. Cool waters in the far North Atlantic spill over the Greenland-Scotland Ridge. These overflowing waters fill much of the abyssal ocean. As they descend, entrainment occurs, modifying the volume and

density of the overflow. Accurate simulation of these waters and the corresponding entrainment is essential.

Hallberg and Adcroft (2009) have developed a new version of the GFDL ocean

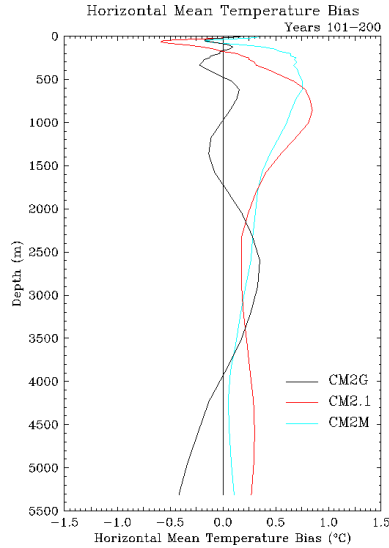


Figure 1.7: Horizontal mean temperature error for three different GFDL ocean models. CM2G, which is the isopycnal model is Black. CM2.1 and CM2M, which are two different z-coordinate models are Red and Blue respectively. Taken from Hallberg and Adcroft (2009).

model that uses an isopycnal coordinate. This model is nearly identical to the previous GFDL ocean model, except for the mixing schemes (a bulk model is used in the isopycnal model, where KPP is used for the cartesian model). This allows for a cleaner examination of the influence of chosen vertical coordinate. Figure 1.7, which is taken from Hallberg and Adcroft (2009), shows the horizontal mean temperature bias relative to observations from the World Ocean Circulation Experiment (WOCE). Particularly in the mode water regions of the upper ocean, the errors in the density coordinate model (CM2G, black line in Figure 1.7) are much smaller than the other two GFDL z-coordinate models.

Although density coordinate models eliminate numerical diffusion in adiabatic conditions, the resolution is degraded in regions of low stratification. This is especially problematic in the OML and the far northern and southern oceans. There are two possible remedies. First, we could simply add more model layers.

The second option is to blend different types of vertical coordinates, creating a hybrid vertical coordinate. The hybrid coordinate ocean model (HYCOM, Halliwell et al. 1998) utilizes a density coordinate in the stably stratified, adiabatic interior, a z-coordinate in the OBL and weakly stratified interior, and a terrain following coordinate in shallow coastal regions.

In this study, we operate under the assumption that z-coordinate model should be avoided. Therefore, an OBL model that is easily adapted to other coordinate systems is required. Bulk models and those similar to Canuto et al. (2001, 2002, 2008) can be adapted, where KPP is specifically designed for height based coordinates¹.

1.4 Where do we go from here?

The previous section leads us to the conclusion that there are many nice aspects of present OBL models. However, we believe that there are areas for improvement. The non-locality of KPP is important to many regions of the ocean. On the other hand, the interior mixing scheme is undesirable². Further, KPP is not easily adaptable to hybrid coordinates.

¹ Hybrid models that use KPP transform back to height coordinates when this routine is called.

² Alternate interior mixing algorithms for KPP have been proposed in Zaron and Moum (2009) and Jackson et al. (2008).

Bulk models and two-equation turbulence models can be easily derived in any coordinate. However, both of these models lack the non-local terms in KPP. In addition, two equation turbulence models do not explicitly consider the OBL depth. Bulk models do predict an entrainment rate, but base this prediction on mixed layer integrated TKE.

The design of a new model involves a series of choices. In our design, the choices are primarily informed by two goals. First, we wish to be able to include biology in a natural way. Phytoplankton is dependent on the nutrient supply in the OBL. The amount of nutrients in the upper ocean is primarily controlled by the entrainment rate of abyssal waters. The model proposed here will explicitly predict entrainment based on energy at the base of the OBL. This new model is ideal for coupling to an ecosystem model.

Second, the model should be easily adaptable to other coordinate systems. However, we must mention that inclusion of fully interactive biology and hybrid coordinates is well beyond the scope of this dissertation. But, the work done to this point is well along the road leading to these goals. We have also avoided the problems associated with the internal mixing scheme of KPP and the interpolation issues associated with determining the depth of the boundary layer.

As in-situ data is scarce for the ocean, we use a Large Eddy Simulation (LES) model as a means of model evaluation. Chapter two will describe the LES model used in this study. Chapter three will provide the details of the new model. Particular attention is paid to the prediction of entrainment and the vertical coordinate. Chapter four will present initial comparisons of the new model to LES and KPP. In chapter five, we

examine the response of the diurnal cycle in the western tropical Pacific to variations in shortwave penetration. The influence of spatially varying penetrating shortwave radiation is discussed in Chapter six. In Chapter seven we attempt to find the mechanisms that govern intraseasonal SST variability in the eastern Pacific warm pool (EPWP). Finally, Chapter eight presents some concluding remarks and proposals for future work.

Chapter 2:

A Vector Vorticity Large Eddy

Simulation Model

Due to the relative sparseness of in situ oceanographic data, we were unable to find a standard test case to evaluate the model framework developed in this work. Therefore, we have chosen to utilize a high resolution, Large Eddy Simulation (LES) . The model is cast in a vector vorticity framework. We have dubbed it VVM-Aqua. It follows the work of Jung and Arakawa (2008).

Our focus is on the upper ocean. This is a region of very active turbulence. Since vorticity is fundamental to an understanding of turbulence, we have adopted the Vector Vorticity Model (VVM) developed by Jung and Arakawa (2008) as a benchmark in this study. VVM should more accurately represent the vortices associated with turbulence than other momentum predicting LES models.

2.1 Model Equations

To convert the model described in Jung and Arakawa (2008) for use in the ocean, a number of changes were necessary. For example, the equation of state was altered to

include the effects of salinity. We also wish to include the influence of Langmuir Circulation (Langmuir, 1938), which is modeled by the CLII mechanism (Craik 1977, Leibovich 1977, described below). Langmuir cells are counter-rotating vortices, which are active in the upper ocean. The middle of the two vortices is visible as windrows on a lake (Figure 2.1a).

Mathematically, the CLII mechanism is the cross product of the Stokes (or wave induced) drift with the three dimensional vorticity. For very small waves, particle trajectories are closed ellipses. As the waves grow in amplitude, the trajectories no

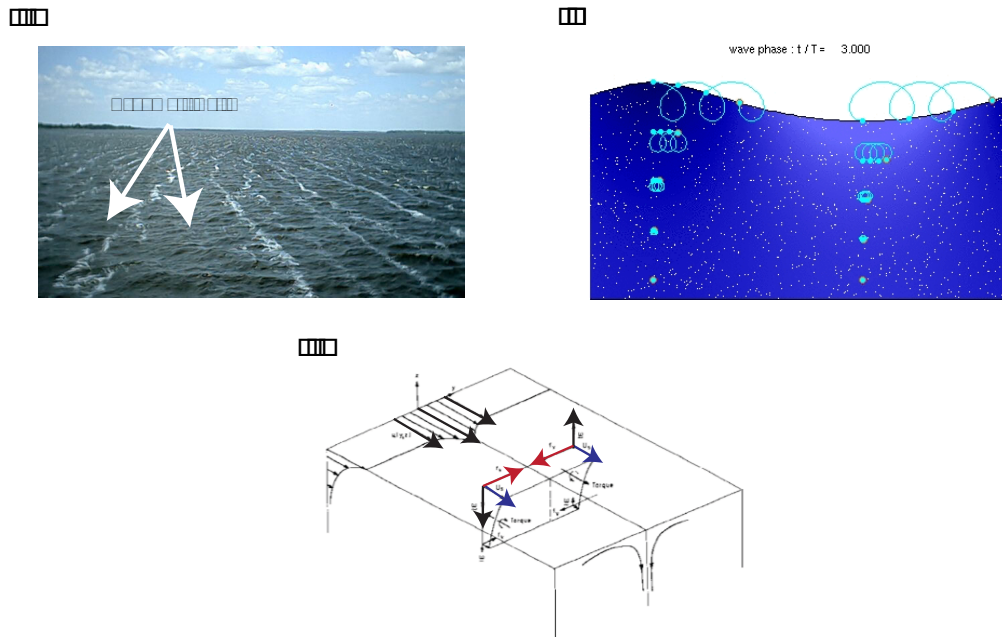


Figure 2.1 - Schematics to illustrate the CLII mechanism. (a) Evidence of Langmuir Cells on a lake. The white lines are called windrows and are the convergence zone of two Langmuir Cells, taken from www.umaine.edu/waterresearch/FieldGuide/onthewater.htm (b) illustration of the wave induced (Stokes) drift (Taken from http://commons.wikimedia.org/wiki/File:Deep_water_wave.gif). (c) Resulting force from the interaction of the Stokes drift and zonal velocity perturbation (adapted from Leibovich 1983).

longer close and the particle begins to move with the wave (Figure 2.1b). This is the Stokes drift.

Now let us imagine a small perturbation in surface zonal velocity (center of Figure 2.1c). A zonal Stokes drift is also imposed (Blue arrows in Figure 2.1c). To the north of the velocity perturbation, the vertical vorticity $\left(-\frac{\partial u}{\partial y}\right)$ is positive (black arrows in Figure 2.1c). Conversely, the vorticity is negative to the south of the velocity maximum. If the Stokes drift (blue) is crossed with the vorticity (black), the resulting force, which is depicted as red arrows in Figure 2.1c, points toward the velocity maximum. By continuity, there must be a downward velocity (i.e. sinking) at this position. Away from the zonal velocity perturbation, the force vectors diverge, which signifies upward motion. The spacing and depth of these rolls are dependent upon wind speed and stratification (e.g. Pluedemann et al 1996).

When the CLII mechanism is included, the equations of motion in momentum space are written as

$$\frac{Du}{Dt} - f(v + v_s) = -\frac{\partial \pi}{\partial x} - \frac{\partial \overline{u'u'}}{\partial x} - \frac{\partial \overline{u'v'}}{\partial y} - \frac{\partial \overline{u'w'}}{\partial z} + v_s \zeta \quad (2.1)$$

$$\frac{Dv}{Dt} + f(u + u_s) = -\frac{\partial \pi}{\partial x} - \frac{\partial \overline{u'v'}}{\partial x} - \frac{\partial \overline{v'v'}}{\partial y} - \frac{\partial \overline{v'w'}}{\partial z} - u_s \zeta \quad (2.2)$$

$$\frac{Dw}{Dt} = -g \frac{\rho}{\rho_o} - \frac{\partial \pi}{\partial x} - \frac{\partial \overline{u'w'}}{\partial x} - \frac{\partial \overline{v'w'}}{\partial y} - \frac{\partial \overline{w'w'}}{\partial z} + u_s \eta - v_s \xi \quad (2.3)$$

$$\frac{D\theta}{Dt} = -\frac{\partial \overline{u'\theta'}}{\partial x} - \frac{\partial \overline{v'\theta'}}{\partial y} - \frac{\partial \overline{w'\theta'}}{\partial z} + \frac{1}{\rho_o C_p} \frac{\partial I(z,t)}{\partial z} \quad (2.4)$$

$$\frac{DS}{Dt} = -\frac{\partial \overline{u'S'}}{\partial x} - \frac{\partial \overline{v'S'}}{\partial y} - \frac{\partial \overline{w'S'}}{\partial z} \quad (2.5)$$

$$\nabla \cdot \mathbf{u} = 0 \quad (2.6)$$

$$\rho = \rho_o \left(1 - \alpha (\theta - \theta_o) + \beta (S - S_o) \right). \quad (2.7)$$

In these equations, u_s and v_s are the Stokes (or wave) drift in the zonal and meridional directions respectively. The function I is the irradiance (i.e. light). Finally, π is the modified pressure, which is given (following McWilliams et al. 1997; M97) as

$$\pi = p / \rho_o + \frac{1}{2} \left[|\mathbf{u} + \mathbf{u}_s|^2 - |\mathbf{u}|^2 \right].$$

In VVM-Aqua, the zonal, meridional, and vertical components of vorticity are defined (following Jung and Arakawa, 2008) as

$$\xi = \frac{\partial w}{\partial y} - \frac{\partial v}{\partial z}; \eta = \frac{\partial u}{\partial z} - \frac{\partial w}{\partial x}; \zeta = \frac{\partial v}{\partial x} - \frac{\partial u}{\partial y}.$$

In these definitions we have used the Boussinesq approximation where Jung and Arakawa (2008) use the Anelastic approximation.

To derive the vorticity equations for VVM-Aqua, we perform the operations given in Table 2.1³.

³ A derivation of the equation describing the x-component of vorticity is presented in Appendix A (the other two derivations are similar).

Equation	Operation Performed
ξ	$\frac{\partial}{\partial y}(2.3) - \frac{\partial}{\partial z}(2.2)$
η	$\frac{\partial}{\partial x}(2.3) - \frac{\partial}{\partial z}(2.1)$
ζ	$\frac{\partial}{\partial x}(2.2) - \frac{\partial}{\partial y}(2.1)$

Table 2.1 - Operations performed to derive the vorticity equations in VVM-Aqua.

The resulting vorticity equations are

$$\frac{\partial \xi}{\partial t} + \frac{\partial u_* \xi}{\partial x} + \frac{\partial v_* \xi}{\partial y} + \frac{\partial w \xi}{\partial z} + \eta \frac{\partial u_*}{\partial y} - \zeta \frac{\partial u_*}{\partial z} - \xi \frac{\partial u_*}{\partial x} = \frac{\partial B}{\partial y} + f \frac{\partial u_*}{\partial z} + \frac{\partial F_w}{\partial y} - \frac{\partial F_u}{\partial z} \quad (2.8)$$

$$\frac{\partial \eta}{\partial t} + \frac{\partial u_* \eta}{\partial x} + \frac{\partial v_* \eta}{\partial y} + \frac{\partial w \eta}{\partial z} - \eta \frac{\partial v_*}{\partial y} + \xi \frac{\partial v_*}{\partial x} + \zeta \frac{\partial v_*}{\partial z} = -f \frac{\partial v_*}{\partial z} + \frac{\partial B}{\partial x} + \frac{\partial F_w}{\partial x} - \frac{\partial F_u}{\partial z} \quad (2.9)$$

$$\frac{\partial \zeta}{\partial t} + \frac{\partial u_* \zeta}{\partial x} + \frac{\partial v_* \zeta}{\partial y} + \frac{\partial w \zeta}{\partial z} + \eta \frac{\partial w}{\partial y} - \xi \frac{\partial w}{\partial x} - \zeta \frac{\partial w}{\partial z} = -f \left(\frac{\partial u_*}{\partial x} + \frac{\partial v_*}{\partial y} \right) + \frac{\partial F_v}{\partial x} - \frac{\partial F_u}{\partial y} \quad (2.10)$$

$$\frac{\partial \xi}{\partial x} + \frac{\partial \eta}{\partial y} + \frac{\partial \zeta}{\partial z} = 0 \quad (2.11)$$

In these equations, we have defined

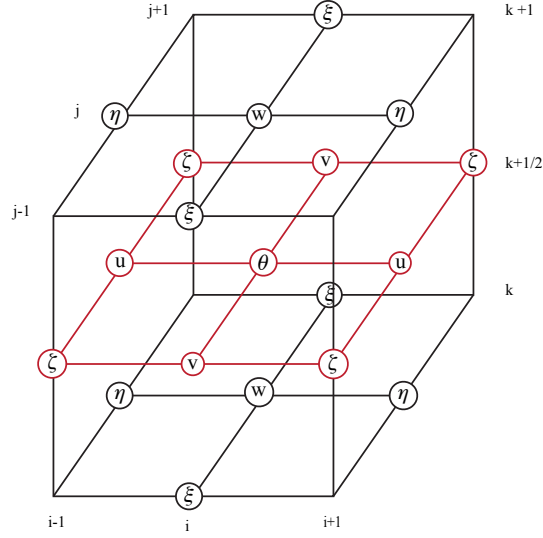


Figure 2.2 - Variable discretization for VVM-Aqua. The red levels are considered model centers and the black layers are model edges. At the surface, all quantities are assumed to be zero, which is the rigid lid approximation.

$$u_* \equiv u + u_s$$

$$v_* \equiv v + v_s$$

$$F_u \equiv -\frac{\partial \overline{u'u'}}{\partial x} - \frac{\partial \overline{u'v'}}{\partial y} - \frac{\partial \overline{u'w'}}{\partial z}$$

$$F_v \equiv -\frac{\partial \overline{u'v'}}{\partial x} - \frac{\partial \overline{v'v'}}{\partial y} - \frac{\partial \overline{v'w'}}{\partial z}$$

$$F_w \equiv -\frac{\partial \overline{u'w'}}{\partial x} - \frac{\partial \overline{v'w'}}{\partial y} - \frac{\partial \overline{w'w'}}{\partial z}$$

$$F_\theta \equiv -\frac{\partial \overline{u'\theta'}}{\partial x} - \frac{\partial \overline{v'\theta'}}{\partial y} - \frac{\partial \overline{w'\theta'}}{\partial z}$$

$$F_s \equiv -\frac{\partial \overline{u'S'}}{\partial x} - \frac{\partial \overline{v'S'}}{\partial y} - \frac{\partial \overline{w'S'}}{\partial z}$$

$$B \equiv g \frac{\rho}{\rho_o}$$

The model is discretized on the grid illustrated in Figure 2.2. The salinity and density is located at θ points.

Even though we can write an equation for the vertical vorticity (ζ) at every level, the vertical vorticity is predicted at one layer only. After the vertical vorticity is predicted at the bottom layer, Equation (2.11) is used to obtain ζ at the remaining levels. If we were to predict ζ at every level, there is no guarantee that equation (2.11) could be satisfied.

2.1.1 Sub-grid Scale Mixing

Although VVM-Aqua is run at a resolution that captures most turbulent motions, we still require a sub-grid mixing parameterization. We have chosen to follow an adaptation of the Smagorinsky scheme presented by Noh et al. (1999). In this scheme, the friction terms in (2.8) - (2.10) are written as

$$\begin{aligned} F_u &\equiv -\nabla \cdot (v_T \nabla u) \\ F_v &\equiv -\nabla \cdot (v_T \nabla v) \\ F_w &\equiv -\nabla \cdot (v_T \nabla w) \\ F_\theta &\equiv -\nabla \cdot (\kappa_T \nabla \theta) \\ F_S &\equiv -\nabla \cdot (\kappa_T \nabla S) \end{aligned}$$

where the viscosity (v_T) is parameterized as $v_T \equiv C_s l^2 f(Ri) \sqrt{2S_{ij}S_{ij}}$. In this equation,

C_s is a constant, l is a length scale, and S_{ij} is the strain rate tensor $S_{ij} \equiv \left(\frac{\partial u_i}{\partial x_j} + \frac{\partial u_j}{\partial x_i} \right)$. In

the simulations presented in this work, C_s is set to 0.17, following Noh et al. (1999).

Frequently the length scale is defined as $l \equiv (\Delta x \Delta y \Delta z)^{1/3}$. Mason (1989)

proposed a modification of the length scale to include the effects of buoyancy. The resulting length scale, which is used in Noh et al. (1999) and VVM-Aqua, is

$$l = \min\left[\left(\Delta x \Delta y \Delta z\right)^{1/3}, \phi \kappa \left(z + z_o\right)\right].$$

Here κ is von Karman's constant, z_o is the surface roughness, and $\phi \equiv (1 - 4\gamma Ri)^{1/4}$,

where γ is an adjustable constant.

Finally, we have added a function of Richardson number that cuts off mixing whenever $Ri > 0.25$. The explicit form of this function is

$$f(Ri) = \begin{cases} 1 & Ri < 0 \\ \sqrt{1 - 4Ri} & 0 \leq Ri \leq 0.25 \\ 0 & Ri > 0.25 \end{cases}.$$

Throughout this thesis, we assume that $\kappa_T = \nu_T$.

When discretized on the grid in Figure 2.2, the mixing coefficients are located with the tracers. The coefficients are then interpolated to locations that facilitate the computation of frictional tendencies in momentum space. For example, using Figure 2.2, we discretize the frictional term for zonal momentum as

$$\begin{aligned} -\frac{\partial}{\partial x}\left(\nu_T \frac{\partial u}{\partial x}\right) - \frac{\partial}{\partial y}\left(\nu_T \frac{\partial u}{\partial y}\right) - \frac{\partial}{\partial z}\left(\nu_T \frac{\partial u}{\partial z}\right) = & -\frac{1}{\Delta x}\left(\nu_{T_{i,j,k+1/2}}\left\{u_{i+1,j,k+1/2} - u_{i,j,k+1/2}\right\} - \right. \\ & \left. \nu_{T_{i-1,j,k+1/2}}\left\{u_{i,j,k+1/2} - u_{i-1,j,k+1/2}\right\}\right) - \frac{1}{\Delta y}\left(0.25\left\{\nu_{T_{i,j,k+1/2}} + \nu_{T_{i,j+1,k+1/2}} + \nu_{T_{i-1,j,k+1/2}} + \nu_{T_{i-1,j+1,k+1/2}}\right\}\right. \\ & \left.\left\{u_{i,j+1,k+1/2} - u_{i,j-1,k+1/2}\right\} - 0.25\left\{\nu_{T_{i,j,k+1/2}} + \nu_{T_{i,j-1,k+1/2}} + \nu_{T_{i-1,j,k+1/2}} + \nu_{T_{i-1,j-1,k+1/2}}\right\}\left\{u_{i,j+1,k+1/2} - u_{i,j-1,k+1/2}\right\}\right) \\ & - \frac{1}{\Delta z}\left(0.25\left\{\nu_{T_{i,j,k+1/2}} + \nu_{T_{i,j,k+1/2}} + \nu_{T_{i-1,j,k+3/2}} + \nu_{T_{i-1,j,k+3/2}}\right\}\left\{u_{i,j,k+3/2} - u_{i,j,k+1/2}\right\} - \right. \\ & \left. 0.25\left\{\nu_{T_{i,j,k-1/2}} + \nu_{T_{i,j,k-1/2}} + \nu_{T_{i-1,j,k+1/2}} + \nu_{T_{i-1,j,k+1/2}}\right\}\left\{u_{i,j,k+1/2} - u_{i,j,k-1/2}\right\}\right). \end{aligned}$$

After computing the tendencies at momentum points, we take the curl to obtain the frictional forcing at the vorticity points.

2.2 VVM-Aqua Evaluation

After conversion of the original VVM to VVM-Aqua, the initial test was a negatively buoyant bubble near the top of the domain. The background state is at rest and is isothermal and isohaline. The domain is 3.2 km x 3.2 km in the horizontal and is 2.4 km deep. Initially, we use a isotropic resolution of 50 meters. The number of grid points is $n_x = n_y = 64$ and $n_z = 55$. The shape of the bubble is defined by (equation 27 of Jung and Arakawa, 2008)

$$\Delta\theta = \begin{cases} 0 & \text{if } L > 1 \\ \Delta\theta_{\max} (1-L) & \text{if } L \leq 1 \end{cases}$$

$$\text{where } \Delta\theta_{\max} = -0.5K, \quad L \equiv \text{sqrt} \left[\left(\frac{x-x_c}{x_r} \right)^2 + \left(\frac{y-y_c}{y_r} \right)^2 + \left(\frac{z-z_c}{z_r} \right)^2 \right], \quad x_c = y_c = 1.5875$$

km, $x_r = y_r = z_r = 200$ m, and $z_c = -300$ m.

The model is run for a short time (10 minutes) with the position of the bubble fixed to allow the motion fields to spin up. Diffusion is not included in these simulations. The buoyant bubble is simply advected. Therefore, any reduction in the domain variance of potential temperature should be due to numerical diffusion. The default advection scheme is third order accurate, but there is an option for a fifth order accurate scheme.

Figure 2.3 shows vertical cross sections of the temperature perturbation

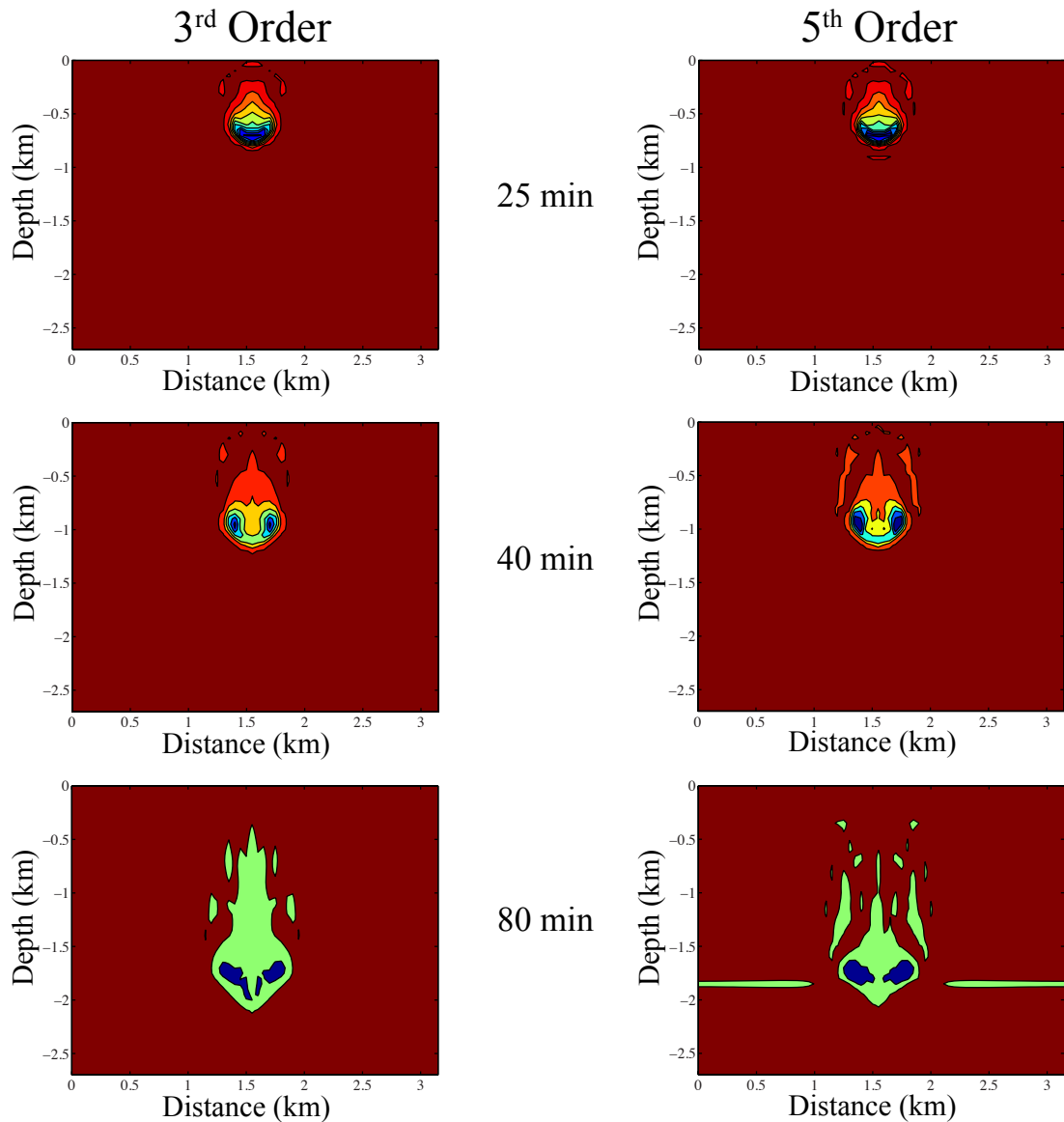


Figure 2.3 - Slice through the center of the domain of a negatively buoyant bubble placed at the top of the domain through time for third order advection (Left column) and 5th order advection (right column). The times of the slice are given between the two columns.

$(\theta - \theta_{Background})$ in time for the third (left column) and fifth order (right column) advection

schemes at three different times. The initial contour is zero and the interval is -0.05 K.

At this resolution, there are eight grid points across the diameter of the bubble.

At 25 and 40 minutes, there is more variance in the 5th order simulation (note the darker blues evident after 40 minutes of the fifth order plot especially). However, after

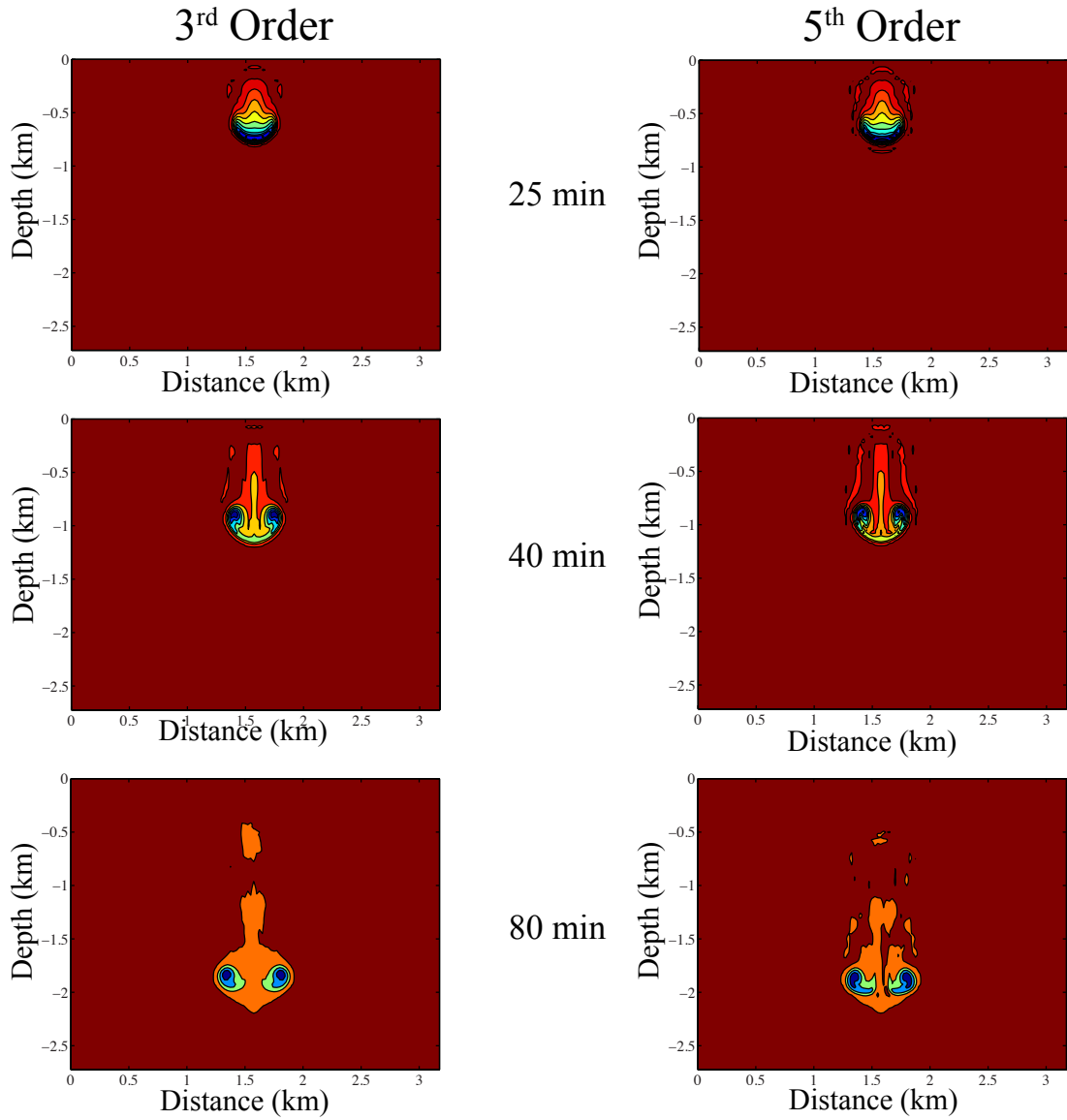


Figure 2.4 - As in Figure 2.3, but for doubled resolution.

80 minutes the variance in both the third and fifth order simulations is greatly reduced.

As previously mentioned, ζ is obtained by integration of equation (2.11). The numerical implementation of the equation (2.11) is second order accurate. Therefore, we expect that there will be more numerical diffusion in VVM-Aqua at coarser resolutions when compared to other oceanic LES models.

Figure 2.4 is identical to Figure 2.3, but the resolution is doubled in every direction. We now have 128 x 128 x 110 points, which is equivalent to $\Delta x = \Delta y = \Delta z = 25$ meters.

As expected, doubling the resolution improves the simulation of the descending bubble. The maximum magnitude of the fifth order, high resolution, bubble is -0.25 at 80 minutes compared to -0.1 K for the corresponding low resolution bubble.

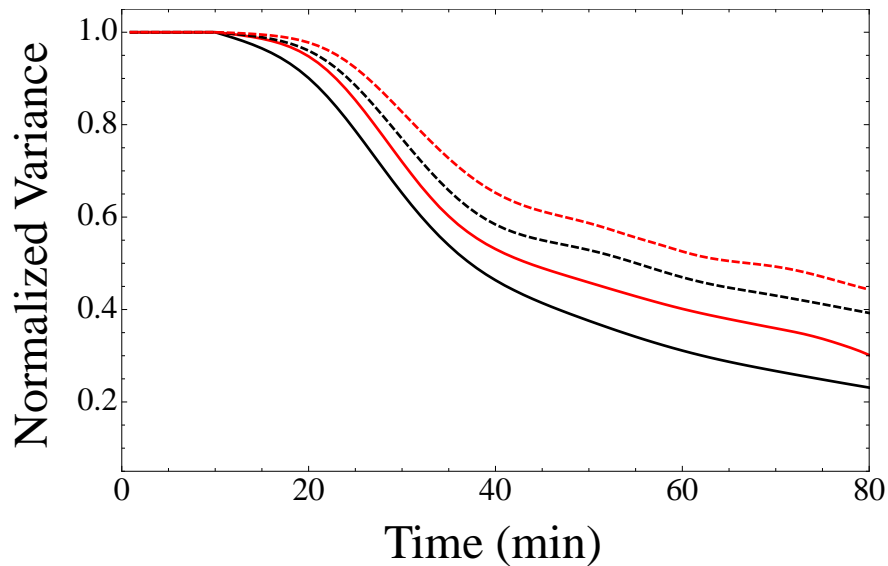


Figure 2.5 - Plots of the normalized temperature variance. The dashed lines are for the high resolution simulations. The red lines are for fifth order advection and the black are for third order advection.

Figure 2.5 shows the variance, which has been normalized by the initial variance, in time for the four simulations. Since sub-grid diffusion is not used in this simulation,

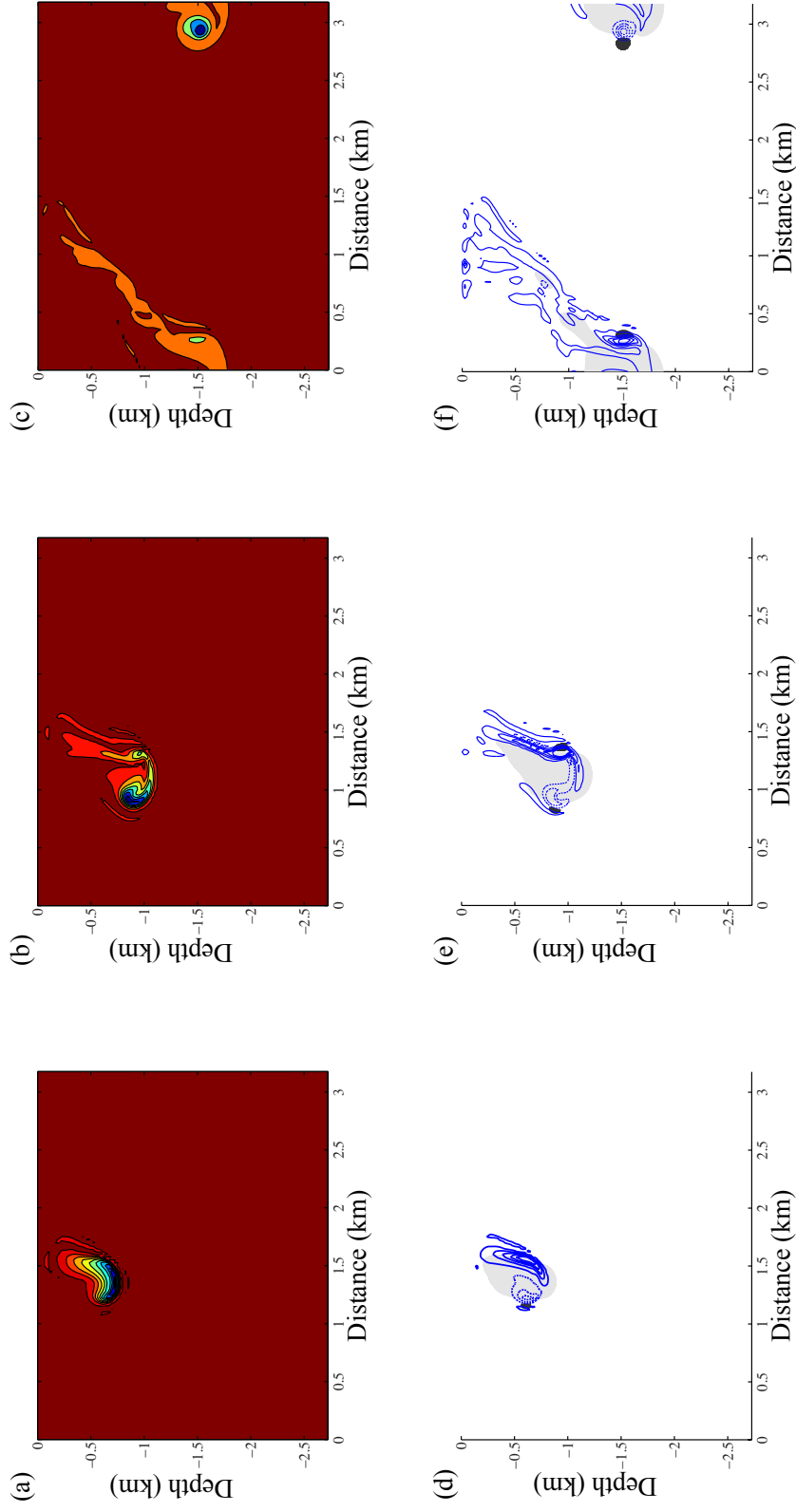


Figure 2.6 - Snapshots of a slice through the center of the domain of perturbation temperature (a-c) and η (d-f). In the plots of the y-component of vorticity the contour interval is $0.003 \text{ kg m}^{-3}\text{s}^{-1}$, we have shaded vertical velocities less than -0.1 ms^{-1} in gray and values larger than 0.1 ms^{-1} are black. The times are as in Figure 2.3.

all the diffusion results from the numerical discretization. In Figure 2.5, the red lines are for fifth order advection, the black lines are third order advection, and the dashed lines are the high resolution runs. There is a noted improvement when moving from third to fifth order advection, but the increase in resolution, given the same advection scheme has a greater impact on the numerical diffusion.

Overall these initial tests offer nothing surprising and simply serve as a sanity check after converting the VVM for oceanic use.

2.2.1 Bubble in a Sheared Flow

As noted above and in Appendix A, the CLII mechanism is easily incorporated in a vorticity framework. In VVM-Aqua, the CLII mechanism acts as an additional background flow. Prior to a Langmuir simulation, with heat fluxes and wind stress, we conduct the high resolution, fifth order, simulation with a simple background flow. The background flow is horizontally homogenous with a constant vertical shear. The velocity is zero at the surface and linearly increases to -0.5 ms^{-1} at the bottom of the model. In this simulation, the Smagorinsky sub-grid mixing scheme is enabled.

Three time snapshots of the perturbation temperature field are shown in Figure 2.6a-c. In Figure 2.6d-f the y-component of vorticity (η) multiplied by a reference density is plotted in contours, the gray shaded region corresponds to vertical velocities less than -0.1 ms^{-1} and regions where the vertical velocity exceeds 0.1 ms^{-1} is black. The contours of $\rho_o \eta$ run from $-0.015 \text{ kg m}^{-3} \text{ s}^{-1}$ to $0.015 \text{ kg m}^{-3} \text{ s}^{-1}$ by 0.003 intervals. Figures 2.6a and 2.6d are at 25 minutes, Figures 2.6b and 2.6e are at 40 minutes, and Figures 2.6c and 2.6f are at 80 minutes.

As time increases, the density perturbation now translates with the background flow, which is moving from right to left in each plot. Additionally, the temperature perturbation bows into the background flow (Figure 2.6a). Near the end of the simulation without background shear, the temperature perturbation becomes concentrated in two regions connected by a thin filament-like structure. This is the result of an increase in radius of the vortex ring that is advecting the bubble downward. When background shear is included, the upwind portion of the vortex (solid lines) is stretched vertically, and the downwind vortex (dashed lines) is compressed. These results are qualitatively similar to those obtained in a similar simulation conducted by Jung and Arakawa (2008).

2.2.2 Wind Driven Mixed Layer

The final essential ingredient in any Langmuir cell (LC) simulation is wind driven mixing. In VVM-Aqua, we implement the effect of surface wind on vorticity by first computing the tendency at momentum points in the first model layer and then taking the curl.

In this test, the surface temperature is set to 293.15 K and the stratification is $4 \times 10^{-2} \text{ Km}^{-1}$. The zonal wind stress is set to 0.037 Nm^{-2} (there is no meridional wind stress). There is no initial flow. The model domain 80 m x 80 m x 30 m. There are 30 points in the x- and y-directions and 60 points in the vertical.

In addition to the Smagorinsky sub-grid mixing scheme, we have also included a sponge layer in the bottom third of the domain. This layer is designed to relax properties back to their instantaneous horizontal average to minimize wave reflection. Finally, a

small white noise forcing is added to the surface momentum forcing for the first thirty

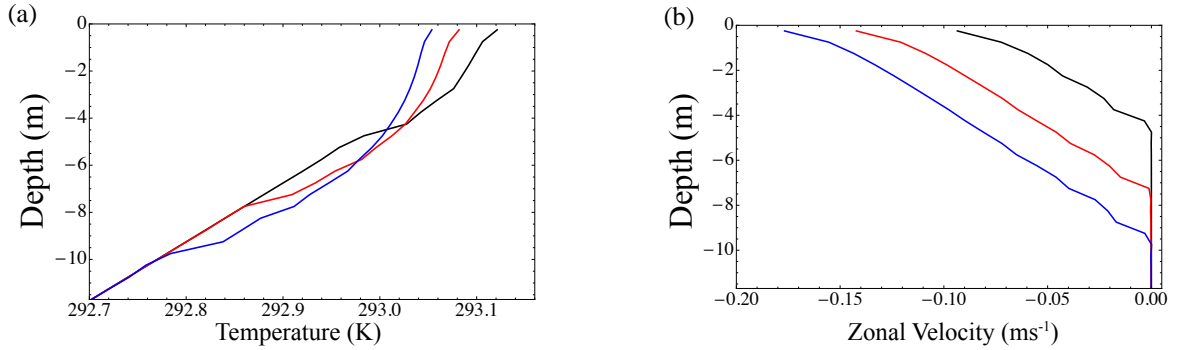


Figure 2.7 - Temperature (a) and Zonal Velocity (b) profiles through time for the wind induced mixed layer deepening simulation. In both plots, the black plot is hour one, red is hour three, and blue is hour six.

minutes of the simulation to initiate turbulent motions.

The model was run for six hours. The temperature and zonal momentum fields are shown in Figure 2.7 for three times (black is hour one, red is hour three, and blue is hour six). It is encouraging that the wind is successfully mixing the temperature field. The question is whether or not the simulated amount of mixing is appropriate. We can get an analytic estimate from Denman (1973).

Denman (1973) was able to obtain an analytic solution under the assumption of no heat exchange between the atmosphere and ocean, no dissipation, and no vertical velocity. Further, it is assumed that once the mixed layer forms it remains well mixed. Using these assumptions, the mixed layer depth is given by (equation 33 of Denman, 1973)

$$h(t) = \left(\frac{12G}{\frac{\partial\theta}{\partial z}} \right)^{1/3} t^{1/3}.$$

In this equation, t is the time and G is the energy input by the wind. In bulk mixed models $G = g\alpha m_3 u_*^3$, where m_3 is a constant (Denman 1973 and Gaspar 1988 choose a value of 0.3) and α is the coefficient of thermal expansion. Using the parameters in this test, $h_{hour1} = 3.35m$, $h_{hour3} = 4.83m$, and $h_{hour6} = 6.08m$.

From Figure 2.7 it is evident that the bulk mixed layer assumption is tenuous. However, if we use the threshold criterion of Montegut et al. (2004) to determine a mixed layer depth and proceed with the comparison to the Denman (1973) estimate, we find fairly good agreement ($h_{hour1} = 3.33m$, $h_{hour3} = 4.32m$, and $h_{hour6} = 4.51m$).

With the individual pieces tested, we assemble everything in an often used LC simulation.

2.2.3 LC Simulation

The tests conducted to this point, although simple, suggest that VVM-Aqua is behaving appropriately. We now turn our attention to a more “real world” problem. The LC simulation we conduct is quite common (e.g. Skyllingstad and Denbo 1995, M97, Li et al. 2005, Polton et al. 2008, Harcourt and D’Asaro 2008). The mixed layer is 33 meters deep and below the mixed layer the stratification is set to 0.01 Km^{-1} . There is no initial motion field. Although VVM-Aqua has salinity, among other passive tracers built-in, we assign a constant salinity throughout the run.

The Stokes drift is parameterized as the result of a monochromatic surface wave. In addition, the Stokes drift is assumed to be horizontally homogeneous. Using this assumption, the depth dependence of the Stokes drift ($U_s(z)$) is given as

$U_s(z) = U_s(0)e^{-kz}$, where k is the wavenumber. The surface Stokes drift is specified by

the turbulent Langmuir number, which is defined (following M97) as $La_t = \sqrt{\frac{u_*}{U_s(0)}}$.

Therefore, specification of La_t and the surface friction velocity will give

Parameter	Value
u_*^2	$3.721 \times 10^{-5} \text{ m}^2 \text{ s}^{-2}$
La_t	0.3
k	0.105 m^{-1}
$U_s(0)$	0.068 m s^{-1}
$\overline{w'\theta'}_{sfc}$	$1.22 \times 10^{-6} \text{ m K s}^{-1}$
$\overline{w'S'}_{sfc}$	0 m PSU s^{-1}
f	10^{-4} s^{-1}

Table 2.2 - Summary of parameters relevant to this simulation.

the surface Stokes drift. The simulation parameters are summarized in Table 2.2.

The sub-grid mixing scheme is included, as is the sponge layer scheme described in Section 2.2.2. Finally, we note that white noise is added to the heat flux for the first hour to initiate turbulence.

In this section, we conduct two nearly identical simulations, in the first, we omit the CLII mechanism ($U_s(z) = 0$). In the second, LC is included. In these initial

simulations, we choose $\Delta x = \Delta y = 5\text{m}$ and $\Delta z = 1\text{m}$. The initial number of grid points is $32 \times 32 \times 90$.

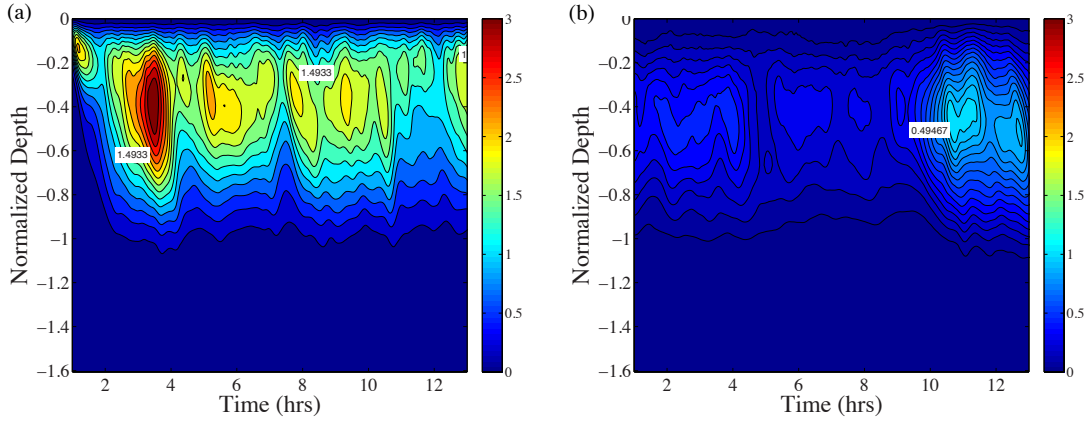


Figure 2.8 - Vertical velocity variance normalized by the surface friction velocity through time for the Langmuir turbulence run (a), and the surface momentum forcing only run (b). Note the difference in color scale. In (a) the contour interval is 0.213 and is 0.07 in (b).

In these simulations, we have changed to a normalized depth coordinate, which is

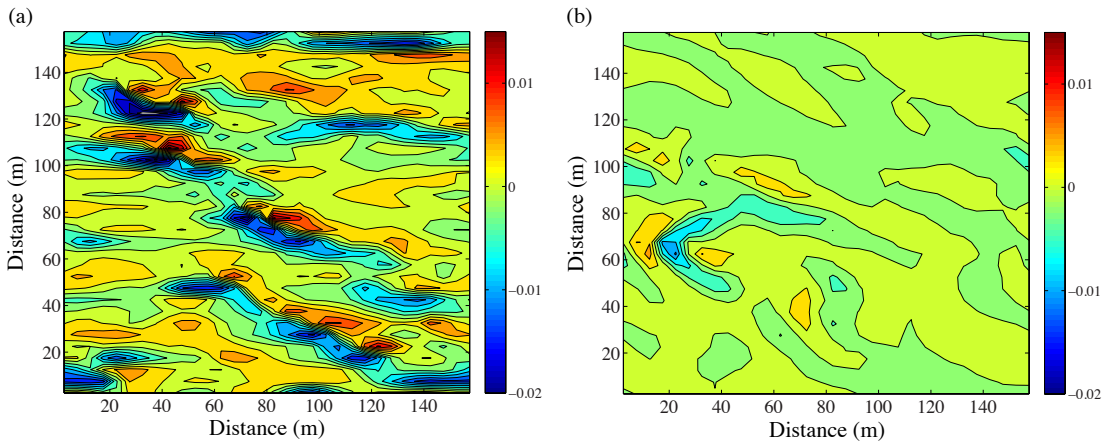


Figure 2.9 - Horizontal slices of vertical velocity at two meters depth for the run with LC forcing (a) and the run without (b). The color scale is identical in both plots.

given as the actual depth divided by the initial mixed layer depth (z_i). In Figure 2.8, the

vertical velocity variance (normalized by u_*^2) is plotted as a function of time for both

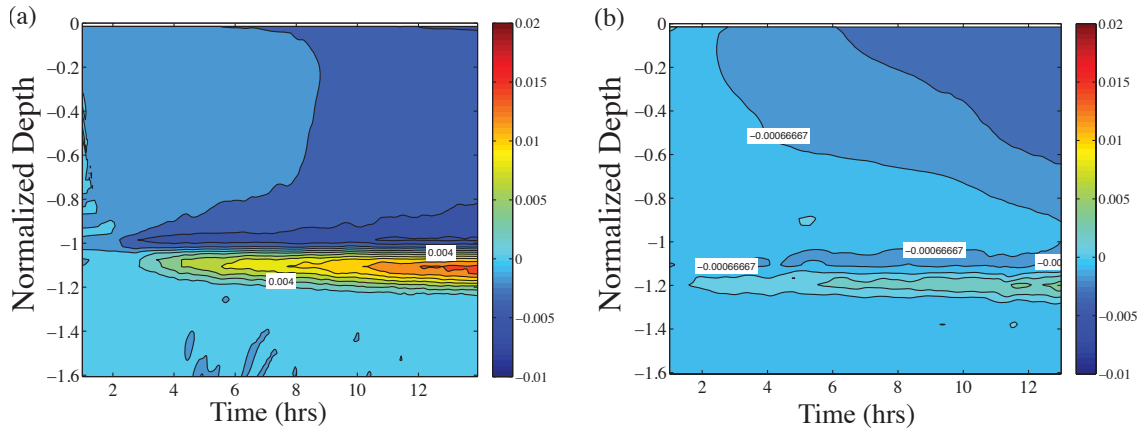


Figure 2.10 - Plot of horizontally averaged temperature relative to the initial temperature for the run with LC (a), and without (b). The contour interval in (a) is 0.02 K and is 0.0013 in (b).

runs. When the CLII mechanism (Figure 2.8a) is included, $\overline{w'^2}$ increases by nearly a factor of three when compared to the run without LC (Figure 2.8b).

Horizontal slices of predicted vertical velocity at two meters depth for the run with LC forcing and no LC forcing are shown in Figures 2.9ab respectively. The most apparent difference is the increase of coherent structures in the LC run. The overturning cells, which are deflected to the right of the surface momentum forcing due to the Coriolis force, appear as neighboring regions of rising and sinking motion. When the LC forcing is omitted (Figure 2.9b), the cells are no longer visible, and the magnitude of w is reduced. These results are expected from the argument given in Section 2.1.

In Figure 2.10 the horizontally averaged change in temperature from the initial profile is shown for the run with LC and without LC in Figures 2.10a and 2.10b respectively. The inclusion of Langmuir Cells increases the entrainment at the mixed

layer base. This is evident from the increased warming below the mixed layer and

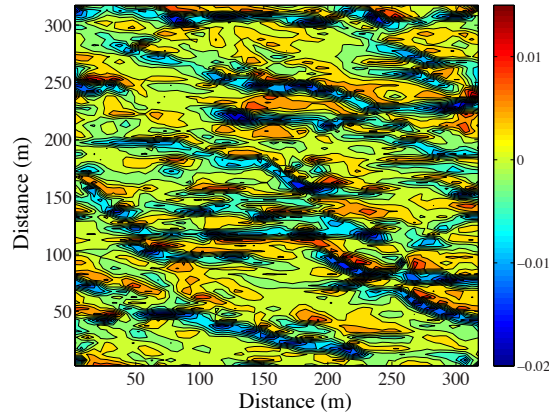


Figure 2.11 - Identical LC test as shown in Figure 2.9a, but here the domain size has been doubled.

cooling directly above in Figure 2.10a.

Two key questions remain. First, is our chosen domain large enough? As can be seen in Figure 2.9a, the number of LCs present may not constitute a sample size large enough to obtain meaningful turbulence statistics. Second, is the increase in the magnitude of $\overline{w'^2}$ correct?

To address the first question, we have conducted a simulation identical to the LC run shown here, but the domain size has been doubled ($n_x = n_y = 64$, $n_z = 90$, $\Delta x = \Delta y = 5$, and $\Delta z = 1$). Doubling the domain size does increase the number of LCs in the domain (compare Figure 2.9a to Figure 2.11), but to examine the effect on turbulent statistics further analysis is required.

In M97, the turbulent quantities are averaged over many eddy turnover times. Here, the eddy turnover time scale is defined as the eddy length divided by a velocity scale. Mathematically, the time scale can be written as $\tau = \frac{l_{eddy}}{\sqrt{2e}}$. For these tests, the

denominator is on the order of 1 cm s^{-1} . If the eddy fills half of the initial mixed layer

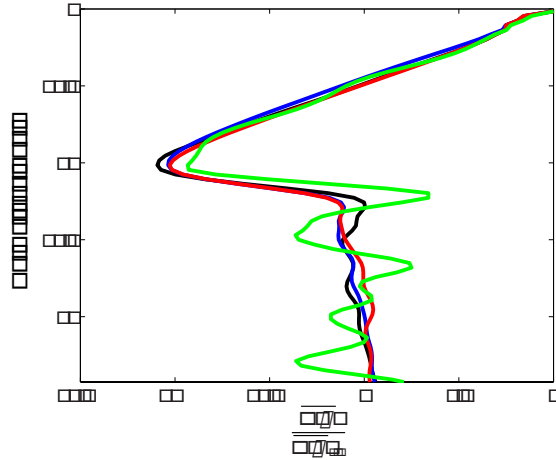


Figure 2.12 - Effect of averaging interval on the profile of normalized heat flux. In this plot, green is the instantaneous heat flux. The black line is averaged over one hour, the red curve is averaged over two hours, and the blue curve is averaged over six hours.

depth, the eddy turnover timescale is about 30 minutes. Even though we can define an eddy turnover timescale, the use of *many* in M97 is ambiguous. Therefore, we examine the influence of the averaging time period on the vertical heat flux, which has been normalized by the surface flux, in Figure 2.12. In this figure, the green line is the

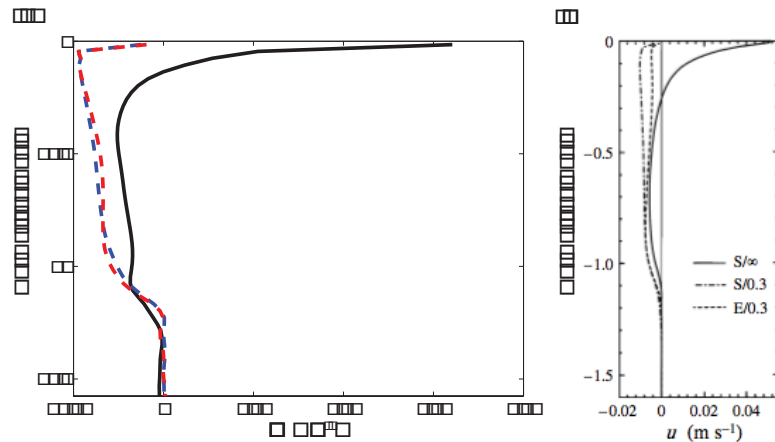


Figure 2.13 - Time and domain averaged zonal velocity plots for VVM-Aqua (a) and M97 (b). In both plots, the dashed lines include LC forcing, the solid line does not. In (a), the dashed blue line is the small domain (S/0.3 in M97) and the red line is the extended domain (E/0.3 in M97).

normalized heat flux at a given instant. We see strong wiggles below the mixed layer.

The result of averaging over 1 hour is given in black. Most of the oscillations seen in the green curve below the mixed layer have averaged out. However, a few remain. The result of averaging over two hours is the red curve. Most of the flux profile in the upper portion of the domain has remained the same, and the overshoot near -1.4 is diminished. Finally, the blue curve is the result of a six hour average. The blue and red curves are

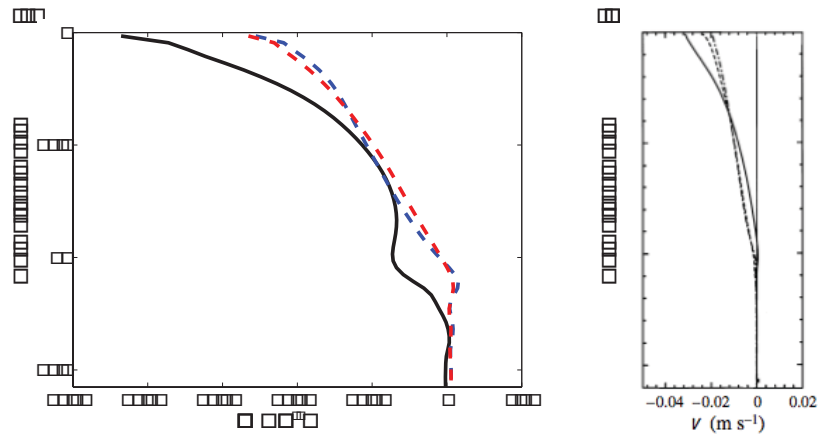


Figure 2.14 - As in Figure 2.13, but for the v -component of velocity.

nearly identical. For the following analysis, we will choose to average over a three hour window.

The time and horizontally averaged zonal velocity for the no LC, small domain LC, and large domain LC runs are shown in Figure 2.13a. The corresponding result from M97 is shown in Figure 2.13b. In the following comparisons, the solid black line in the figures from M97 corresponds to the solid black line in our figures. The dot dashed line corresponds to our dashed blue line (small domain), and the dashed line corresponds to the dashed red line (large domain).

The averaged zonal velocity profiles compare well. As in M97, the inclusion of LC results in a well mixed layer of easterly momentum, although it is better mixed in

M97. Without LC, the surface velocity is positive. The surface value is stronger in VVM-Aqua (0.065 ms^{-1} compared to 0.052 ms^{-1} in M97). In our runs, the differences in the time and spatially averaged zonal velocity between the small and large domain runs (red and blue dashed lines) is similar to what is observed in M97.

The v-component of velocity is shown in Figure 2.14ab for VVM-Aqua and M97 respectively. The profiles for the run without LC forcing match fairly well. Again the surface v-velocity is stronger in VVM-Aqua than in M97. Within the mixed layer, the

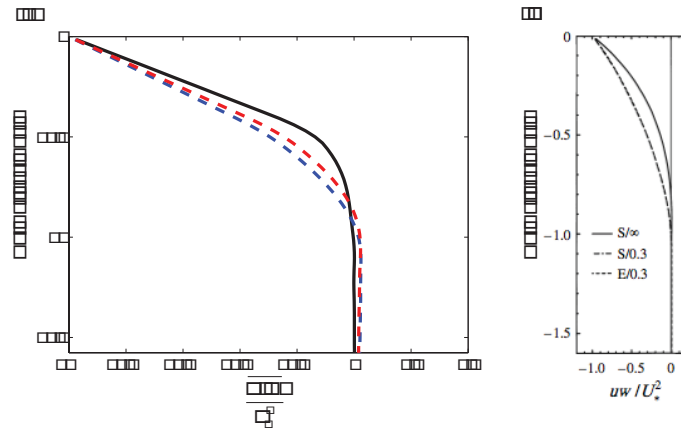


Figure 2.15 - Time averaged profiles of the normalized turbulent flux of u for VVM-Aqua (a) and M97 (b). The line styles and colors are as in Figure 2.13.

profiles remain similar.

Near the bottom of the mixed layer, the v-velocity decreases to zero in M97, but remains slight positive in VVM-Aqua. Below the mixed layer base, the velocity decreases to zero rapidly in VVM-Aqua. We believe that this may be related to the averaging interval. Since Figure 2.14b is time averaged in addition to being horizontally averaged, the length of the averaging and the end points of the averaging window will alter the profiles in Figure 2.14ab (and Figure 2.13ab), due to the Coriolis force. If we

move the averaging window and alter the length, the structure below the mixed layer in Figure 2.14a disappears (not shown).

The magnitudes of zonal and meridional velocity are weaker in the LC run relative to the run without LC forcing. The vertical profiles are also more mixed in the Langmuir turbulence runs.

The zonal momentum flux is shown in Figure 2.15 for VVM-Aqua and M97. The two models agree well. The profile of $\overline{u'w'}/u_*^2$ for the run including Langmuir turbulence

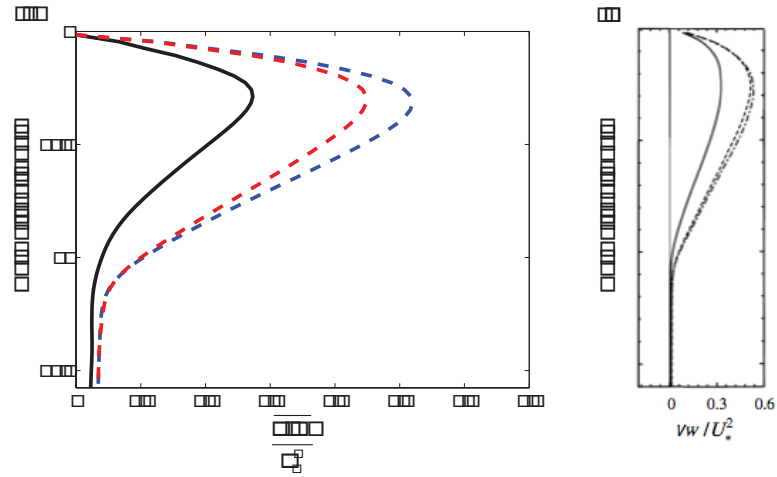


Figure 2.16 - As in Figure 2.15, but for $\overline{v'w'}/u_*^2$

is slightly stronger at depth when compared to the run without LC forcing. If we think of the Stokes drift as an additional source of shear, it is logical that the zonal momentum flux is stronger at depth in the run with LC included.

The aspect ratios of Figure 2.15ab are different making it seem that the profiles of $\overline{u'w'}/u_*^2$ are quite different in VVM-Aqua compared to M97. However, the values

through depth are similar. For example, in the middle of the mixed layer, the zonal momentum flux is approximately -0.3 in both runs.

Figure 2.16 displays $\overline{v'w'}/u_*^2$ for the two models. The comparison is quite good

between VVM-Aqua and M97. The increase in meridional momentum flux in the run with Langmuir turbulence is due to the Coriolis vortex term, as an increase in zonal velocity at depth will also increase the southward velocity at depth (see Figure 2.14). An increase in the vertical shear of the meridional current would increase the value of

$$\overline{v'w'}/u_*^2.$$

There are two primary differences between the results of our simulations and

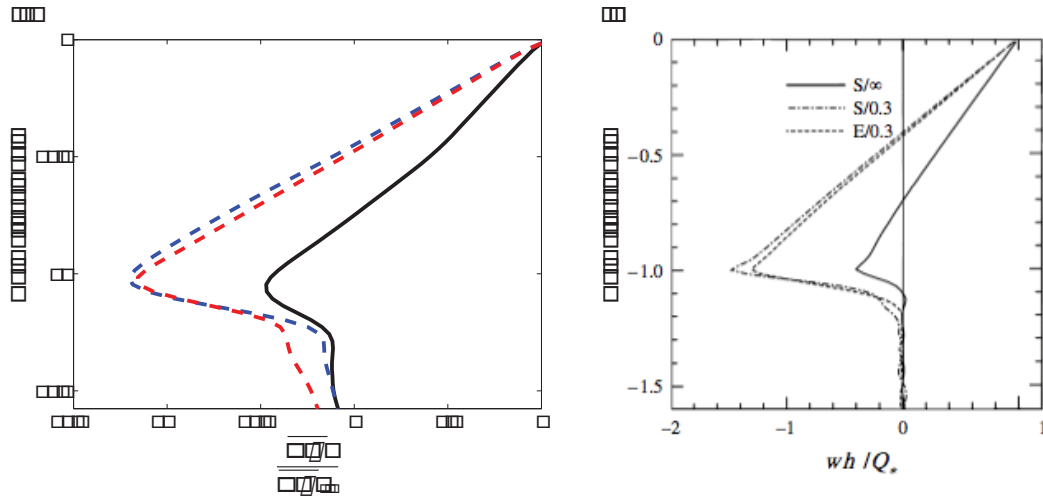


Figure 2.17 - As in Figure 2.15, but for $\overline{w'\theta'}/\overline{w'\theta'}_{sfc}$

those of M97. First, we observe a greater difference between the small and large domain runs than that seen in M97. Second, the vertical flux of meridional momentum is

stronger, albeit only slightly, below the mixed layer in our Langmuir turbulence simulation.

The vertical heat flux, normalized by the surface heat flux, for VVM-Aqua and M97 are given in Figures 2.17a and 2.17b respectively. Inclusion of the CLII forcing increases the upward heat flux in the lower portion of the mixed layer, confirming the increased entrainment due to LC observed in Figure 2.10a. The VVM-Aqua fluxes are similar to those obtained in M97, except there is a slight upward heat flux near a normalized depth of -1.5, which is absent in M97. The increase in the magnitude of the vertical heat flux through much of the mixed layer suggests there will be a larger value of eddy diffusivity associated with LC.

McWilliams and Sullivan (2000) have suggested that the mixing due to LC can be included in the KPP model by modifying the turbulent velocity scale to include a factor given by $(1 + 0.08La_t^{-4})^{1/2}$. This factor is derived from scalings from LES output that relate $\overline{w'^2}$ and the turbulent Langmuir number. The scaling that leads to the proposal of McWilliams and Sullivan (2000) is not conclusive. For example, Harcourt and D'Asaro (2008), using LES output from Li et al. (2005), found that the best fit for the mixed layer average of normalized vertical velocity variance scales as $(1 + 0.098La_t^{-2})$. This is consistent with McWilliams and Sullivan (2000) for large values of turbulent Langmuir number, but diverge as this number decreases, which is when the CLII forcing becomes important.

It is important to note that these scalings are for a very specific circumstance, and there is yet no agreement. Grant and Belcher (2009) have recently proposed that the correct scaling is $(u_*^2 u_{s0})^{1/3}$, where u_{s0} is the surface Stokes drift.

Despite the lack of conclusive evidence on which scaling is physically correct, M97 uses the same set up and forcing as Li et al. (2005) and McWilliams and Sullivan

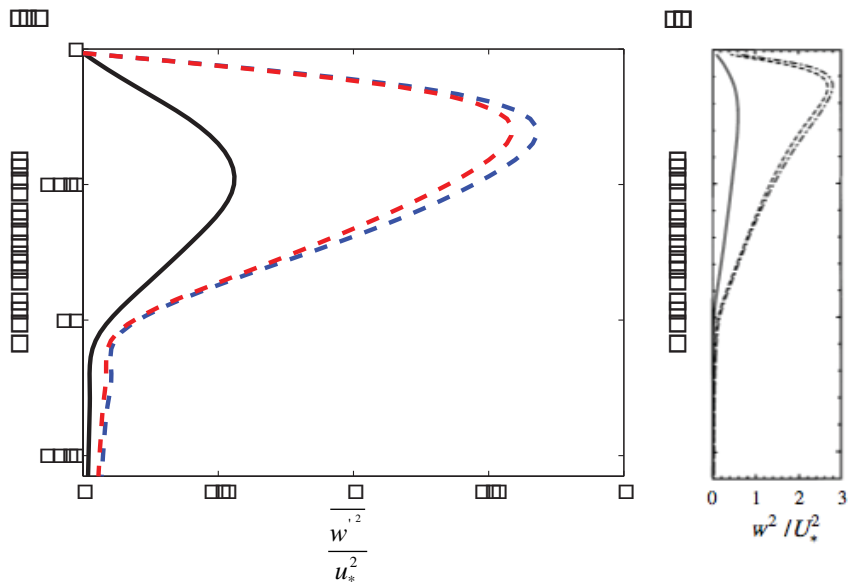


Figure 2.18 - As in Figure 2.15, but for $\frac{\overline{w^2}}{u_*^2}$

(2000). We have more faith in the scaling of Li et al. (2005). The coefficients in the scaling proposed by McWilliams and Sullivan (2000) are chosen for mathematical elegance and are not fit to LES results.

In this simulation, $La_t = 0.3$, implying that $\overline{w_{ML}^{\prime 2}} / u_*^2 = 1.3$. The VVM-Aqua output

for the small and large domain runs is approximately 1.1, which is close to the Li et al. (2005) scaling.

The smaller magnitude of the mixed layer average of normalized $w^{\prime 2}$ in VVM-

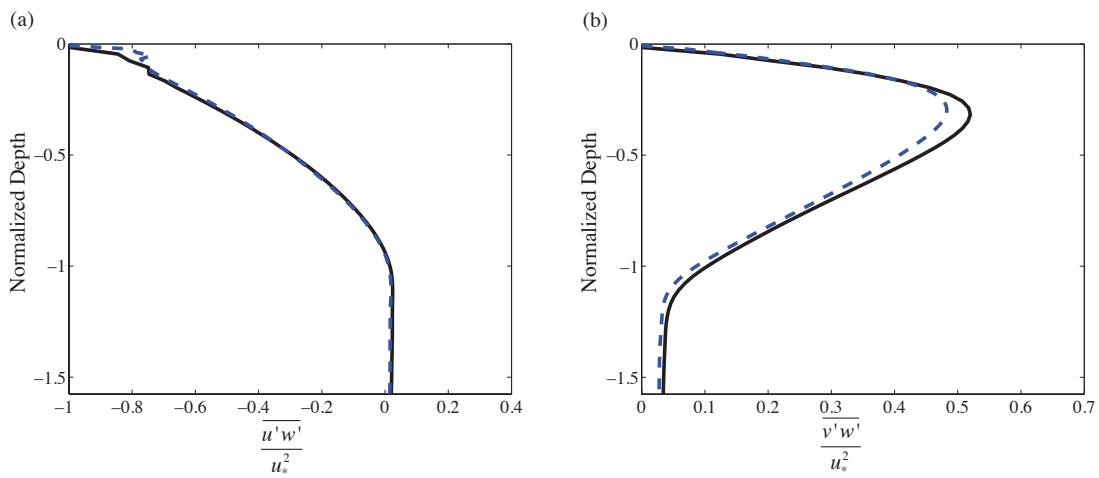


Figure 2.19 - Horizontally and time averaged profiles of $\overline{u'w'}/u_*^2$ (a) and $\overline{v'w'}/u_*^2$ (b). In these plots, the blue line is the small domain LC run with one meter resolution and the dashed blue line uses 0.5 meter resolution.

Aqua can be further elucidated by comparing the vertical profile of $w^{\prime 2}$ in VVM-Aqua (Figure 2.18a) to M97 (Figure 2.18b). As expected from Figure 2.8, the time averaged vertical velocity variance is much stronger when LC forcing is included than the run driven by surface forcing alone. The peak in $w^{\prime 2}$ for the black curve in Figure 2.18a (no LC) is similar to the M97 result (0.57 for VVM-Aqua, compared to 0.6 for M97).

The differences are much larger for the Langmuir turbulence runs. The peak value of $\overline{w'^2}/u_*^2$ for the small domain VVM-Aqua run is 1.69 and is 1.61 for the large domain run. In M97 the peak values for the small and large domain runs are

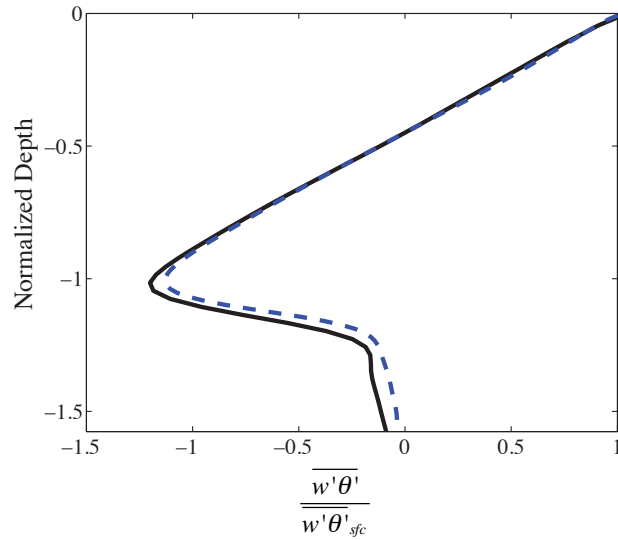


Figure 2.20 - As in Figure 2.19, but for the normalized heat flux.

approximately 2.8 and 2.6 respectively. This is a non-negligible difference. In addition, the maximum of $\overline{w'^2}/u_*^2$ occurs at a deeper level in VVM-Aqua compared to M97 and other similar simulations (e.g. Skillingstad and Denbo 1995 or Grant and Belcher 2009). In addition, it seems as though the profile is more diffuse, i.e. the fall off from the peak value is more gentle in VVM-Aqua than in M97.

The difference in vertical velocity variance simulated by VVM-Aqua compared to M97 is not understood. A detailed examination of LC simulated by VVM-Aqua and that simulated by other momentum predicting LES models is left for future work.

We have conducted a simulation identical to our LC simulations, except that the

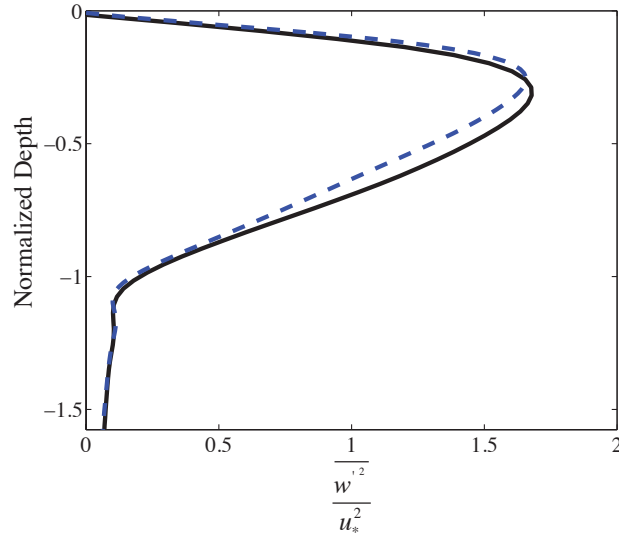


Figure 2.21 - As in Figure 2.19, but for $\frac{\overline{w'^2}}{u_*^2}$

resolution is doubled ($dz = 0.5$). The profiles of the vertical fluxes of u and v momentum, which are again normalized by the surface friction velocity, are shown in Figure 2.19. In these resolution comparisons, the solid black curve is the small domain Langmuir turbulence result, and the blue dashed line is from a high vertical resolution, small domain, run. The profile of $\frac{\overline{u'w'}}{u_*^2}$ in the low and high resolution simulations are

very similar, except near the surface. The maximum magnitude of $\overline{v'w'}/u_*^2$ is slightly less in the high resolution simulation when compared to the lower resolution run.

The normalized heat flux is given in Figure 2.20. Through most of the boundary layer, the heat fluxes are nearly identical. Below the boundary layer, the small positive heat flux evident in the lower resolution simulation is reduced at the finer resolution.

Finally, the vertical velocity variances for the high and low resolution runs are shown in Figure 2.21. The maximum in normalized $\overline{w'^2}$ has shifted toward the surface in the high resolution simulation. The general shape now better resembles that in M97 (Figure 2.18b). However, the maximum magnitude is still approximately half of that observed in M97.

2.3 Conclusions

We have successfully converted an atmospheric vector vorticity model (Jung and Arakawa 2008) to an ocean model. Temperature, salinity, and two passive tracers are included. The model utilizes a linear equation of state (equation 2.7). We have implemented a fifth order accurate advection scheme, and the sub-grid mixing scheme follows Noh et al. (1999).

Initial testing of the model shows that VVM-Aqua behaves as expected. Simple tests of the formation of a mixed layer by wind stress agree with the analytic estimate of Denman (1973). More rigorous testing, following M97, shows that VVM-Aqua seems to be slightly more diffusive than other LES models.

The run with surface momentum forcing only compares well to M97. Many of the VVM-Aqua simulated turbulent quantities for the run simulating Langmuir turbulence are similar to M97. However, the variances $\left(\overline{w'^2} \text{ and } \overline{\theta'^2}\right)$ tend to be weaker in VVM-Aqua. Further, the location in the maximum of normalized vertical velocity variance is shifted downward from M97. We have found that increasing the vertical resolution eases this bias.

The differences in the maximum simulated value of $\overline{w'^2}/u_*^2$ in VVM-Aqua compared to M97 is not fully understood. The large domain run with LC forcing is identical to M97 (except the vertical resolution is coarser), and many turbulent statistics are very similar, yet the maximum value of $\overline{w'^2}/u_*^2$ is much smaller in VVM-Aqua.

We have also examined the sensitivity to doubling the horizontal resolution in addition to doubling the vertical resolution. The maximum in $\overline{w'^2}/u_*^2$ does increase, but only to 1.9 (recall in M97 the normalized vertical velocity variance was nearly three) and the mixed layer average increases to 1.2. The increased resolution does improve the result relative to M97, but it seems as though something else is missing.

Despite this unanswered question, we are encouraged by the comparison between VVM-Aqua and M97 in the simulation without LC forcing.

Chapter 3:

A New Vertical Mixing Model with Explicit Entrainment

As previously mentioned, the model described in this chapter is designed with two guiding principles. First, we desire a model that explicitly predicts the entrainment rate. Second, we want the model to be easily adaptable to hybrid coordinates.

The entrainment rate could be predicted via a layer integrated TKE equation, as in bulk models (e.g. KT, Gaspar 1988). This assumes that the vertical profiles of the mean and turbulent quantities within the upper ocean are well mixed. Instead we expect that entrainment at the OBL base should be based on local turbulent fluctuations.

To predict the entrainment rate based upon properties at the OBL base we follow the work of Lappen et al. (2010, L10).

3.1 Computation of the Entrainment Rate

L10 have recently modified the Assumed Distribution Higher Order Closure (ADHOC3) model to include a prognostic PBL top. ADHOC3 parameterizes

entrainment by considering the budgets of $\overline{w'^2}$ and $\overline{w'w'w'}$ near the PBL top. These turbulent moments are predicted by assuming a top-hat distribution within a grid cell.

In this model, we write the budget equations for $\overline{w'^2}$ and $\overline{w'w'w'}$ in a general (η) coordinate as⁴

$$\frac{\partial m \overline{w'^2}}{\partial t} + \nabla \cdot \left(m \mathbf{v} \overline{w'^2} \right) + \frac{\partial m \dot{\eta} \overline{w'^2}}{\partial \eta} + \frac{\partial \overline{w'^3}}{\partial \eta} \frac{\partial \eta}{\partial z} = \left(\frac{1}{3} c_1 - c_2 \right) \left(\overline{u'w'} \frac{\partial \overline{u}}{\partial \eta} \frac{\partial \eta}{\partial z} + \overline{v'w'} \frac{\partial \overline{v}}{\partial \eta} \frac{\partial \eta}{\partial z} \right) + \frac{4g}{3} \left(\alpha \overline{w'\theta'} - \beta \overline{w'S'} \right) + \varepsilon - 2\tau_{pv}^{-1} \overline{w'^2} \quad (3.1)$$

$$\frac{\partial m \overline{w'^3}}{\partial t} + \nabla \cdot \left(m \mathbf{v} \overline{w'^3} \right) + \frac{\partial m \dot{\eta} \overline{w'^3}}{\partial \eta} + \frac{\partial \overline{w'^4}}{\partial \eta} \frac{\partial \eta}{\partial z} = -\frac{2c_8}{\tau} \overline{w'^3} + 3g(1-c_{11}) \left\{ \alpha \overline{w'^2 \theta'} - \beta \overline{w'^2 S'} \right\} \quad (3.2)$$

In these equations, $\dot{\eta}$ is the vertical velocity in our general coordinate and m is the

pseudo-density $\left(m \equiv \frac{1}{g} \left| \frac{\partial p}{\partial \eta} \right| \right)$. The remaining constants are defined in Appendix C.

Since we are predicting the entrainment rate, the model layers will expand and contract. This implies that cartesian coordinates would be a very poor choice.

Most of the interior oceanic flows are adiabatic and thus an isopycnal coordinate is logical. However, in weakly stratified regions, isopycnal models lose resolution. A few ocean models, such as HYCOM, seek to combine the best qualities of different coordinate systems. HYCOM uses a cartesian coordinate in the mixed layer, an isopycnal coordinate in the adiabatic interior, and a terrain following (σ) coordinate in

⁴ See Appendix B for a derivation of these moments, and Appendix D for a derivation of the two-dimensional equations

shallow coastal regions. This allows the model to maintain high resolution in weakly

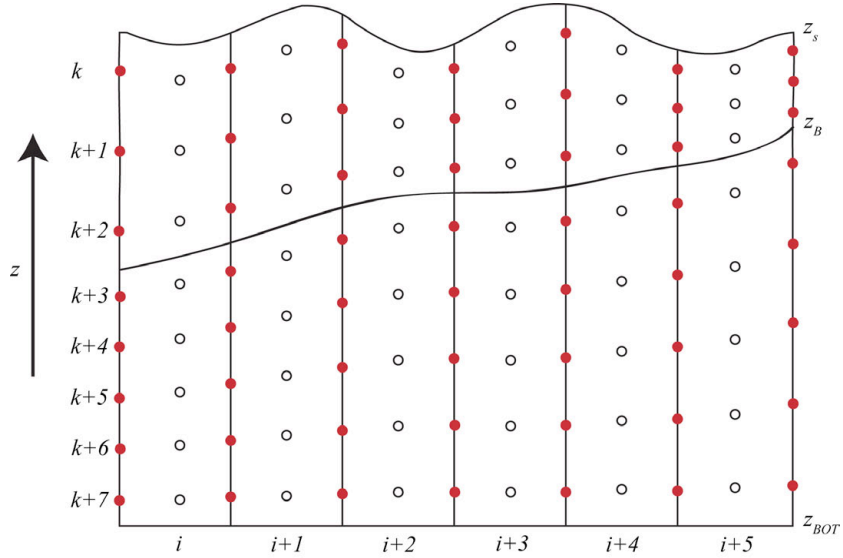


Figure 3.1 - Grid arrangement of the new model framework discussed here and in Chapter 6.

stratified and coastal regions. Further, HYCOM avoids the spurious diffusion associated with advection in z-coordinate models (Griffies et al. 2000).

The end goal for this model is a hybrid coordinate. In the first version of the model, the chosen vertical coordinate is a normalized height coordinate. The grid levels are schematically illustrated in Figure 3.1. In the model, height (z) increases upward. Therefore, as we move down in a column, z becomes more negative. In Figure 3.1, the dots signify the position of the mean quantities (u, v, T, S, m, ρ) . In one-dimensional simulations, all of the mean quantities are predicted at open circles. When the model is extended to two dimensions in Chapter 6, the grid is staggered and the velocities will be predicted at the red circles.

In this example, the OBL depth (z_B) decreases from left to right. This implies the

thickness of the layers in the OBL is larger on the left side of the domain than on the right. The opposite is true in the deep ocean. In Figure 3.1, we have assumed that the coordinate surfaces are equally spaced within each layer, however, this not required.

The mathematical form of our chosen coordinate is given by

$$\sigma \equiv \begin{cases} \frac{z_s - z}{z_s - z_B} & \text{for } z_s \geq z > z_B \\ \frac{z_B - z}{z_B - z_{BOT}} + 1 & \text{for } z_B \geq z \geq z_{BOT}. \end{cases} \quad (3.3)$$

Where $z_s, z_B,$ and z_{BOT} are as defined in Figure 3.1. The pseudodensity (m) can now be written as

$$m = \begin{cases} \rho(z_s - z_B) & \text{for } z_s \geq z > z_B \\ \rho(z_B - z_{BOT}) & \text{for } z_B \geq z > z_{BOT}. \end{cases}$$

In this definition, the hydrostatic approximation has been used. We can now rewrite equations (3.1) and (3.2) as

$$\frac{\partial m \overline{w}^{\cdot 3}}{\partial t} + \nabla_{\sigma} \cdot (m \mathbf{v} \overline{w}^{\cdot 3}) + \frac{\partial m \dot{\sigma} \overline{w}^{\cdot 3}}{\partial \sigma} + \rho \frac{\partial \overline{w}^{\cdot 4}}{\partial \sigma} = -\frac{2c_8}{\tau} m \overline{w}^{\cdot 3} + 3mg(1 - c_{11}) \{ \alpha \overline{w}^{\cdot 2} \overline{\theta}^{\cdot} - \beta \overline{w}^{\cdot 2} \overline{S}^{\cdot} \} \quad (3.4)$$

$$\begin{aligned} \frac{\partial m \overline{w}^{\cdot 2}}{\partial t} + \nabla_{\sigma} \cdot (m \mathbf{v} \overline{w}^{\cdot 2}) + \frac{\partial m \dot{\sigma} \overline{w}^{\cdot 2}}{\partial \sigma} + \rho \frac{\partial \overline{w}^{\cdot 3}}{\partial \sigma} &= -2\tau_{pv}^{-1} m \overline{w}^{\cdot 2} + \frac{4mg}{3} \{ \alpha \overline{w}^{\cdot} \overline{\theta}^{\cdot} - \beta \overline{w}^{\cdot} \overline{S}^{\cdot} \} \\ - m \overline{u} \overline{w}^{\cdot} \frac{\partial \overline{u}}{\partial z} - m \overline{v} \overline{w}^{\cdot} \frac{\partial \overline{v}}{\partial z} + m \varepsilon. & \end{aligned} \quad (3.5)$$

As a next step, it is useful to present these equations in a very general form as

$$\frac{\partial mA}{\partial t} + \nabla_{\sigma} \cdot (m \mathbf{v} A) + \frac{\partial m \dot{\sigma} A}{\partial \sigma} + \rho \frac{\partial F_A}{\partial \sigma} = m S_A.$$

In this equation, A is some quantity to be predicted, F_A is the turbulent flux of A , and S_A represents the sources and sinks of A . If we now take the special case of $A=1$, we recover the continuity equation, which for the coordinate defined in equation (3.3) is given by

$$\frac{Dm}{Dt} = -m\nabla_{\sigma} \cdot \mathbf{v} - m \frac{\partial \dot{\sigma}}{\partial \sigma}. \quad (3.6)$$

Where the material derivative for the σ – coordinate is defined as

$$\frac{D}{Dt} \equiv \frac{\partial}{\partial t} + \mathbf{v} \cdot \nabla + \dot{\sigma} \frac{\partial}{\partial \sigma}.$$

If we introduce the OBL definition of the pseudodensity, we can rewrite equation (3.6) as

$$\begin{aligned} \frac{D}{Dt}(\rho(z_s - z_B)) &= -\rho(z_s - z_B) \left\{ \nabla \cdot \mathbf{v} + \frac{\partial \dot{\sigma}}{\partial \sigma} \right\} \\ \rho \frac{D}{Dt}(z_s - z_B) + (z_s - z_B) \frac{D\rho}{Dt} &= -\rho(z_s - z_B) \left\{ \nabla \cdot \mathbf{v} + \frac{\partial \dot{\sigma}}{\partial \sigma} \right\}. \end{aligned}$$

Since ocean water is nearly incompressible, we can neglect the second term on the left hand side. Therefore, the final form of the model continuity equation is given as

$$\begin{aligned} \frac{\partial \pi}{\partial t} + \nabla \cdot \{\pi \mathbf{v}\} + \frac{\partial}{\partial \sigma} \left\{ \pi \dot{\sigma} \right\} &= 0 \\ \pi &\equiv \begin{cases} z_s - z_B & \text{for } z_s \geq z \geq z_B \\ z_B - z_{BOT} & \text{for } z_B \geq z \geq z_{BOT} \end{cases}. \end{aligned}$$

If the continuity equation is integrated from the surface to the OBL base, we obtain

$$\frac{\partial \pi}{\partial t} + \nabla \cdot \int_0^1 \pi \mathbf{v} d\sigma = - \left(\pi \dot{\sigma} \right)_B + \left(\pi \dot{\sigma} \right)_S.$$

Here, $\left(\pi \dot{\sigma} \right)_B$ and $\left(\pi \dot{\sigma} \right)_S$ are the fluxes of mass across the OBL base and surface BS

respectively. The mass flux across the surface could be non-zero for precipitation and evaporation. In this work, this term is neglected. The mass flux across the OBL base is due to the entrainment rate.

To obtain the entrainment rate, we integrate equations (3.4) and (3.5) across a small layer centered on the OBL base (following Lilly 1968). The result, with the additional assumption that the dissipation and restoring terms are small relative to the other terms, is

$$\int_{\sigma_B - \varepsilon}^{\sigma_B + \varepsilon} \frac{\partial}{\partial t} \overline{m w^{i,3}} d\sigma + \int_{\sigma_B - \varepsilon}^{\sigma_B + \varepsilon} \nabla \cdot \left(m \mathbf{v} \overline{w^{i,3}} \right) d\sigma + \int_{\sigma_B - \varepsilon}^{\sigma_B + \varepsilon} \frac{\partial m \dot{\sigma} \overline{w^{i,3}}}{\partial \sigma} d\sigma + \int_{\sigma_B - \varepsilon}^{\sigma_B + \varepsilon} \rho \frac{\partial \overline{w^{i,4}}}{\partial \sigma} d\sigma = \int_{\sigma_B - \varepsilon}^{\sigma_B + \varepsilon} m S_{\overline{w^{i,3}}} d\sigma$$

$$\int_{\sigma_B - \varepsilon}^{\sigma_B + \varepsilon} \frac{\partial}{\partial t} \overline{m w^{i,2}} d\sigma + \int_{\sigma_B - \varepsilon}^{\sigma_B + \varepsilon} \nabla \cdot \left(m \mathbf{v} \overline{w^{i,2}} \right) d\sigma + \int_{\sigma_B - \varepsilon}^{\sigma_B + \varepsilon} \frac{\partial m \dot{\sigma} \overline{w^{i,2}}}{\partial \sigma} d\sigma + \int_{\sigma_B - \varepsilon}^{\sigma_B + \varepsilon} \rho \frac{\partial \overline{w^{i,3}}}{\partial \sigma} d\sigma = \int_{\sigma_B - \varepsilon}^{\sigma_B + \varepsilon} m S_{\overline{w^{i,2}}} d\sigma.$$

Following Randall (2010), we can rewrite these equations as

$$\overline{E w_B^{i,2}} = \overline{\rho w_B^{i,3}} + \int_{z_B - \varepsilon}^{z_B + \varepsilon} \rho S_{\overline{w^{i,2}}} dz$$

and

$$\overline{E w_B^{i,3}} = \overline{\rho w_B^{i,4}} + \int_{z_B - \varepsilon}^{z_B + \varepsilon} \rho S_{\overline{w^{i,3}}} dz$$

These equations assume that the turbulent moments vanish below the OBL base.

Plugging in the definitions of the source/sink terms (assuming that the dissipation terms are small near the OBL base), the preceding equations become

$$\overline{Ew_B^{i3}} = \overline{\rho w_B^{i4}} + \int_{z_B - \varepsilon}^{z_B + \varepsilon} \rho \left\{ 3g(1 - c_{11}) \left\{ \overline{\alpha w^{i2} \theta^i} - \overline{\beta w^{i2} S^i} \right\} \right\} dz. \quad (3.7)$$

$$\overline{Ew_B^{i2}} = \overline{\rho w_B^{i3}} + \int_{z_B - \varepsilon}^{z_B + \varepsilon} \rho \left(\frac{4g}{3} \left\{ \overline{\alpha w^i \theta^i} - \overline{\beta w^i S^i} \right\} - \overline{u^i w^i} \frac{\partial \overline{u}}{\partial z} - \overline{v^i w^i} \frac{\partial \overline{v}}{\partial z} \right) dz. \quad (3.8)$$

To proceed, we must manipulate the buoyancy terms in the $\overline{w^{i3}}$ equation to obtain a closed form equation. In this model, we invoke the assumption used in L10 and Canuto and Dubovikov (1998) that the buoyancy terms can be written as

$$\overline{w^i \theta^i} = DAF (1 - DAF) (w_d - w_u) (\theta_d - \theta_u).$$

Where DAF is the area of the downward moving plume and subscript d signifies the quantity associated with downward moving plumes and u represents the values associated with upward moving plumes. Mathematically, this is the top-hat distribution. Using this assumption, the source and sink term of $\overline{w^{i3}}$ can be written as

$$3g(1 - c_{11}) \left\{ \overline{\alpha w^{i2} \theta^i} - \overline{\beta w^{i2} S^i} \right\} = 3g(1 - c_{11}) \frac{\overline{w^{i3}}}{\overline{w}} \left\{ \overline{\alpha w^i \theta^i} - \overline{\beta w^i S^i} \right\}.$$

Using this relation, equations (3.7) and (3.8) become

$$\overline{Ew_B^{i3}} = \overline{\rho w_B^{i4}} + \int_{z_B - \varepsilon}^{z_B + \varepsilon} 3\rho g(1 - c_{11}) \overline{w^i b^i} \frac{\overline{w^{i3}}}{\overline{w}} dz \quad (3.9)$$

$$E\overline{w_B'^2} = \overline{\rho w_B'^3} + \int_{z_B-\varepsilon}^{z_B+\varepsilon} \rho \left(\frac{4g}{3} \overline{w'b'} - \overline{u'w'} \frac{\partial \overline{u}}{\partial z} - \overline{v'w'} \frac{\partial \overline{v}}{\partial z} \right) dz \quad (3.10)$$

For simplicity, we have defined $\overline{w'b'} = g \left(\alpha \overline{w'\theta'} - \beta \overline{w'S'} \right)$ where b is the buoyancy. After

partial evaluation of the integrals, the equations become

$$\begin{aligned} E\overline{w_B'^3} &= \overline{\rho w_B'^4} + 3(1 - c_{11}) E \Delta b \frac{\overline{w_B'^3}}{\overline{w_B'^2}} \delta z \\ E\overline{w_B'^2} &= \overline{\rho w_B'^3} + \frac{4}{3} \delta z E \Delta b - \rho E \Delta \overline{u} \int_{z_B-\varepsilon}^{z_B+\varepsilon} \frac{\partial \overline{u}}{\partial z} dz - \rho E \Delta \overline{v} \int_{z_B-\varepsilon}^{z_B+\varepsilon} \frac{\partial \overline{v}}{\partial z} dz \\ &= \overline{\rho w_B'^3} + \frac{4}{3} \delta z E \Delta b - E \left(\Delta u^2 + \Delta v^2 \right) \end{aligned}$$

In these equations, the Δ operator is defined as $\Delta x \equiv x_{B+} - x_{B-}$, and δz is the inversion thickness (2ε), which will be defined later.

To solve for the entrainment rate, we must decide on a closure for the fourth order moment term $\left(\overline{w'^4} \right)$. The current incarnation of the model uses the quasi-normal

approximation (QNA), $\overline{w'^4} = 3\overline{w'^2}^2$ (e.g. Andre et al. 1976). To test this approximation, a test case combining convection and shear forcing is conducted following Andre and LaCarrere (1985). The plot of $\overline{w'^4}$ and $3\overline{w'^2}^2$ diagnosed from VVM-Aqua, which was described and evaluated in Chapter 2, is shown in Figure 3.2a. A similar plot from the Langmuir Circulation run described in the previous chapter is shown in Figure 3.2b. In both of these plots, the blue shaded box signifies the inversion layer, which is

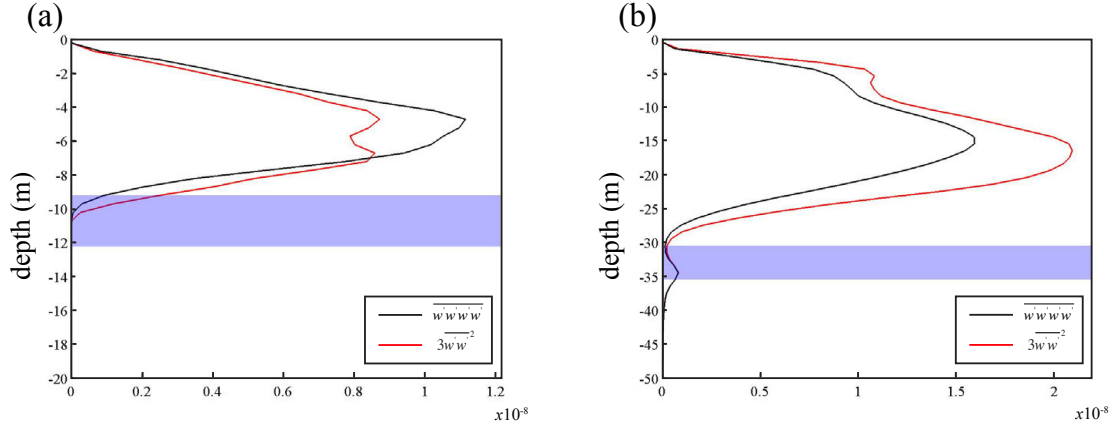


Figure 3.2 - Plots of modeled $\overline{w'w'w'}$ and $3\overline{w'^2}$ (a) is from the test of Andre and Lacarrere (1985) and (b) is from the LC forcing run described in Chapter 2. The blue box in both figures represents the inversion layer. The thickness of this layer is bounded by the positions where $\overline{\theta'^2}$ falls to 5% of its maximum value.

bounded by the positions where the value of $\overline{\theta'^2}$ falls to 5% of its maximum value. In

both cases, the QNA holds well within the diagnosed inversion layer.

When the QNA is used in equation (3.9) we obtain

$$E\overline{w_B'^3} = 3\rho\overline{w_B'^2} + 3\rho(1 - c_{11})E\Delta b \frac{\overline{w_B'^3}}{\overline{w_B'^2}} \delta z$$

We can solve for the entrainment rate (E) by solving this equation and equation (3.10) for

$\overline{w_B'^3}$. This operation yields

$$\overline{w_B'^3} = \frac{3\rho\overline{w_B'^2}^3}{\left(E\overline{w_B'^2} - 3(1 - c_{11})E\Delta b\delta z\right)} \quad (3.11)$$

$$\overline{w_B'^3} = \frac{E\overline{w_B'^2} - \frac{4}{3}\delta z E\Delta b - \left(\frac{1}{3}c_1 - c_2\right)E(\Delta u^2 + \Delta v^2)}{\rho} \quad (3.12)$$

If we equate (3.11) and (3.12) we obtain

$$3\rho^2 \overline{w'^2}^3 = E^2 \left\{ \overline{w'^2} - 3(1 - c_{11}) \Delta b \delta z \right\} \left\{ \overline{w'^2} - \frac{4}{3} \Delta b \delta z - \left(\frac{1}{3} c_1 - c_2 \right) (\Delta u^2 + \Delta v^2) \right\}.$$

The final entrainment rate equation is

$$E = \frac{\sqrt{3} \rho \overline{w'^2}^{3/2}}{sqr t \left(\left\{ \overline{w'^2} - 3(1 - c_{11}) \Delta b \delta z \right\} \left\{ \overline{w'^2} - \frac{4}{3} \Delta b \delta z - \left(\frac{1}{3} c_1 - c_2 \right) (\Delta u^2 + \Delta v^2) \right\} \right)}. \quad (3.13)$$

Prior to using equation (3.13) in a model, we must parameterize the inversion thickness (δz). L10 assume that the entrainment rate equation must reduce to the parameterization used in the Colorado State University GCM. The current version of the model follows this lead and we force equation (3.13) to be equal to the commonly used bulk mixed layer model entrainment parameterization of Gaspar (1988), which is given by

$$E_G = \frac{m_1 k_{avg} \sqrt{\overline{w'^2}_{avg}}}{h \Delta b}$$

The subscript *avg* denotes an average over the depth of the boundary layer. If we set this expression equal to equation (3.13) we can derive an expression for the inversion thickness (δz). The general functional form is $\delta z = f(\Delta b, \Delta u, \Delta v, k_{avg}, \overline{w'^2}_{avg}, \overline{w'^2})$. The complete expression is not simple and is given in Appendix E.

The parameterized inversion layer thickness used here and in L10 is not completely satisfying. There is no physical reason to expect our entrainment rate

parameterization to be equivalent to one based on boundary layer integrated quantities, but the dependence on quantities like the shear at the OBL base and buoyancy jump is expected. Despite our dissatisfaction, we will use this parameterization.

In VVM-Aqua, the inversion layer is diagnosed as the position where $\overline{\rho'^2}$ falls to 5% of its maximum value. If we were to predict $\overline{\theta'^2}$, $\overline{S'^2}$, and hence $\overline{\rho'^2}$, which is discussed in Chapter 8, the inversion layer thickness could be diagnosed as in VVM-Aqua.

3.2 Prediction of the Vertical Velocity Variance and Turbulence Kinetic Energy.

Equation (3.13) requires a method to determine $\overline{w'^2}$ and to determine the inversion layer thickness, we must predict k . It is nothing more than an algebraic exercise to write the predictive equations for these two moments (see Appendix B). When this is done we introduce many other second order moments and higher order moments. There are two possible solutions to this problem.

First, we could predict all of the second order moments (a total of 15 equations) and their respective third order moments (a total of 35 equations). The advantage is the inclusion of non-local effects. The major disadvantage is the computational burden (increased storage and computations).

The other option is to follow the recent work of Canuto et al. (2008, CEA08). CEA08 write the necessary equations for the second order moments (see equations B.80 - B.95) and assume that the time change and non-local terms of all the second order moments (except k and $\overline{w'^2}$) are small compared to the terms on the right hand side. This yields a system of 13 equations, where $\overline{w'^2}$ and k are treated as known quantities.

Solution of this matrix problem yields

$$\overline{u'w'} = -\tau \overline{w'^2} A_m \frac{\partial \overline{u}}{\partial z} \quad (3.14)$$

$$\overline{v'w'} = -\tau \overline{w'^2} A_m \frac{\partial \overline{v}}{\partial z} \quad (3.15)$$

$$\overline{w'\theta'} = -\tau \overline{w'^2} A_h \frac{\partial \overline{\theta}}{\partial z} \quad (3.16)$$

$$\overline{w'S'} = -\tau \overline{w'^2} A_s \frac{\partial \overline{S}}{\partial z} \quad (3.17)$$

The functions A_m , A_h , and A_s are given in Appendix F.

The advantages and disadvantages of this simplified system are flipped from those mentioned in relation to predicting every second order moment. We now neglect the non-local effects (third moments), but the computational burden is smaller. Although model speed is important, fewer computations does not necessarily make one model superior to another. Even though this model neglects the third order moments, a number of studies (e.g. Canuto et al. 2004, Halliwell 2004, Durski et al. 2004, Jacob et al. 2006) have found that models similar to Canuto et al. (2008) perform as well as or better than KPP. For initial testing, we retain both options for the prediction of k and $\overline{w'^2}$.

Two tasks remain to complete the new model framework. We must predict or parameterize the dissipation and third order moments. When a predictive equation is used for dissipation, the result is often too weak (e.g. Burchard et al. 1998). Burchard et al. (1998) propose a minimum value of TKE to prevent this under-prediction. Instead we choose to follow Canuto et al. (2002) and Jackson et al. (2008) and write the dissipation as $\varepsilon = k^{3/2} \Lambda^{-1}$. The length scale is given by $\Lambda \equiv 2^{-3/2} B_1 l$, where

$$l = \min \left(0.53 \frac{\sqrt{2k}}{N}, \frac{1}{4} \frac{\sqrt{2k}}{\Sigma}, \frac{0.17h\kappa z}{0.17h + \kappa z} \right)$$

Here, N is the Brunt-Väisälä frequency, $\Sigma \equiv \text{sqr}t \left(\frac{\partial \bar{u}^{-2}}{\partial z} + \frac{\partial \bar{v}^{-2}}{\partial z} \right)$ and κ is von Karman's

constant.

With a chosen parameterization of dissipation, the final task is to parameterize the third order moments.

3.2.1 Third order moments

There are a few choices for the parameterization of the third order moments (TOMs). We could completely neglect the equations for the third order moments and invoke the down gradient closure of Mellor and Yamada (1982). The relevant TOMS become

$$\overline{\dot{u}_i \dot{u}_j \dot{u}_k} = \frac{3}{5} S_q l \sqrt{2e} \left(\frac{\partial \overline{\dot{u}_i \dot{u}_j}}{\partial x_k} + \frac{\partial \overline{\dot{u}_j \dot{u}_k}}{\partial x_i} + \frac{\partial \overline{\dot{u}_i \dot{u}_k}}{\partial x_j} \right) \quad (3.18)$$

$$\overline{u_i u_k \theta'} = -S_q l \sqrt{2e} \left(\frac{\partial \overline{u_i \theta'}}{\partial x_k} + \frac{\partial \overline{u_k \theta'}}{\partial x_i} \right) \quad (3.19)$$

$$\overline{u_i u_k S'} = -S_q l \sqrt{2e} \left(\frac{\partial \overline{u_i S'}}{\partial x_k} + \frac{\partial \overline{u_k S'}}{\partial x_i} \right) \quad (3.20)$$

$$\overline{u_i \theta'^2} = -S_q l \sqrt{2e} \frac{\partial \overline{\theta'^2}}{\partial x_i} \quad (3.21)$$

$$\overline{u_i S'^2} = -S_q l \sqrt{2e} \frac{\partial \overline{S'^2}}{\partial x_i} \quad (3.22)$$

This approximation is sufficient in certain circumstances and very poor in others.

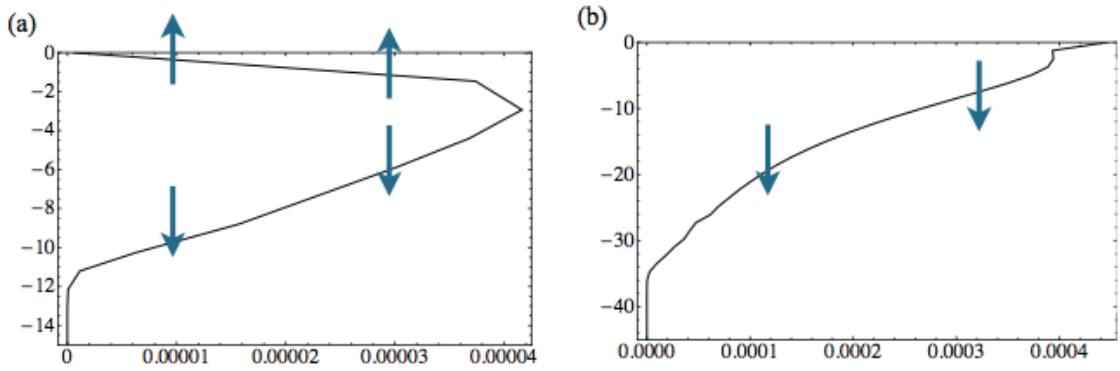


Figure 3.3 - Schematics illustrating when the down gradient approximation fails (a) and when it works (b). In both plots, the TKE is plotted in black, and the arrows indicate the direction of the down gradient forcing. (a) is convectively dominated and (b) is shear dominated.

Consider Figure 3.3. We have plotted the TKE profile for a convective dominated run (Figure 3.3a) and a wind driven simulation (Figure 3.3b). The arrows placed on the figure depict the effect of the down gradient approximation given above. Physically, we would expect the TOMs to transport energy from the surface to near the bottom of the boundary layer. Under the down gradient approximation a portion of the energy is transported from the center of the domain to the surface in convective regimes (Figure 3.3a). In wind driven flows, the down gradient approximation behaves as expected.

The other option is to predict some form of the TOMs. In doing so, we must parameterize the fourth order moments. The fourth order moments are often parameterized using the QNA, which in its most general form is

$$\overline{a'b'c'd'} \equiv \overline{a'b'c'd'} + \overline{a'c'b'd'} + \overline{a'd'b'c'}.$$

The quasi-normal approximation is subject to two different problems in convective regimes. When the background density profile is unstable the algebraic TOMs can grow rapidly. Andre et al. (1976) proposed a clipping condition to remedy this problem, which we would prefer to avoid.

Under stable conditions, the mean gradient terms in the TOMs can cause spurious oscillations near the top of the boundary layer (Moeng and Randall 1984). To alleviate these problems, Cheng et al. (2005, CEA05) write the fourth order moments as

$$\frac{\partial}{\partial z} \overline{a'b'c'd'} \equiv \frac{\partial}{\partial z} \overline{a'b'c'd'} \Big|_{QNA} + \frac{\partial}{\partial z} \overline{a'b'c'd'} \Big|_{NG}.$$

Here, the second term is a non-gaussian contribution. CEA05 also assumed that the time change of the TOMs are negligible compared to other terms. The non-gaussian terms are defined in such a way as to eliminate the mean gradient terms in the TOM equations, remedying the second problem associated with the QNA. The resulting expressions are given in equations (B.66) - (B.79).

In the model described here, we make an additional approximation. Since the eddy decay time scale $\left(\tau \equiv 2k/\varepsilon\right)$, in particular the turbulent dissipation, is a relatively

uncertain quantity, we neglect terms proportional to τ^3 and greater. For example, the

original form of $\overline{w'^3}$ is

$$\begin{aligned} \overline{w'^3} = & - \left(\frac{3\overline{w'^2}}{f_1} + \frac{3\lambda_\theta \overline{w'\theta'}}{f_1 f_{26}} - \frac{3\lambda_s \overline{w'S'}}{f_1 f_{20}} \right) \frac{\partial \overline{w'^2}}{\partial z} \\ & - \left(\frac{6\lambda_\theta \overline{w'^2}}{f_1 f_{26}} + \frac{12\lambda_\theta^2 \overline{w'\theta'}}{f_1 f_{11} f_{26}} - \frac{6g\alpha\lambda_s \overline{w'S'}}{f_1 f_{14} f_{20}} - \frac{6g\beta\lambda_\theta \overline{w'\theta'}}{f_1 f_{14} f_{26}} \right) \frac{\partial \overline{w'\theta'}}{\partial z} \\ & - \left(-\frac{6\lambda_s \overline{w'^2}}{f_1 f_{20}} + \frac{12\lambda_s^2 \overline{w'S'}}{f_1 f_8 f_{20}} - \frac{6g\alpha\lambda_s \overline{w'\theta'}}{f_1 f_{14} f_{20}} - \frac{6g\beta\lambda_\theta \overline{w'\theta'}}{f_1 f_{14} f_{26}} \right) \frac{\partial \overline{w'S'}}{\partial z} \\ & - \left(\frac{6\lambda_\theta^2 \overline{w'^2}}{f_1 f_{11} f_{26}} + \frac{18\lambda_\theta^3 \overline{w'\theta'}}{f_1 f_{11} f_{16} f_{26}} - \frac{6g\beta\lambda_\theta^2 \overline{w'S'}}{f_1 f_{11} f_{17} f_{26}} \right) \frac{\partial \overline{\theta'^2}}{\partial z} \\ & - \left(\frac{6\lambda_s^2 \overline{w'^2}}{f_1 f_8 f_{20}} + \frac{6g\alpha\lambda_s^2 \overline{w'\theta'}}{f_1 f_8 f_{20} f_{23}} - \frac{18\lambda_\theta^3 \overline{w'\theta'}}{f_1 f_8 f_{15} f_{20}} \right) \frac{\partial \overline{S'^2}}{\partial z} \\ & - \left(\frac{12g\alpha\lambda_s^2 \overline{w'S'}}{f_1 f_8 f_{20} f_{23}} - \frac{12g\beta\lambda_\theta^2 \overline{w'\theta'}}{f_1 f_{11} f_{17} f_{26}} - \frac{6g\alpha\lambda_s \overline{w'^2}}{f_1 f_{14} f_{20}} - \frac{6g\beta\lambda_\theta \overline{w'^2}}{f_1 f_{14} f_{26}} \right) \frac{\partial \overline{\theta'S'}}{\partial z}. \end{aligned}$$

In this equation, $f_x \equiv c_x / \tau$. Our assumption neglects any term with three or more f 's in

the denominator. The third order moment in the equation for $\overline{w'^2}$ used in the model is

$$\overline{w'^3} = - \left(\frac{3\overline{w'^2}}{f_1} + \frac{3\lambda_\theta \overline{w'\theta'}}{f_1 f_{26}} - \frac{3\lambda_s \overline{w'S'}}{f_1 f_{20}} \right) \frac{\partial \overline{w'^2}}{\partial z} - \frac{6\lambda_\theta \overline{w'^2}}{f_1 f_{26}} \frac{\partial \overline{w'\theta'}}{\partial z} + \frac{6\lambda_s \overline{w'^2}}{f_1 f_{20}} \frac{\partial \overline{w'S'}}{\partial z}.$$

The cautionary comment is that we have neglected a portion of the non-locality. This may have a non-negligible influence on the simulations.

When all of the second order moments are predicted, use of the down-gradient approximation offers little advantage. When we use the algebraic Reynolds stress model, we choose to invoke the down-gradient approximation for the turbulent transport of TKE and $\overline{w'^2}$.

We could use equations (B.66) - (B.68), but since only two second moments are predicted, the TOMs derived following Cheng et al. (2005) can be rewritten as down-gradient. All of the second moments in the equation for $\overline{w'^3}$ are directly proportional to TKE. Therefore the new TOMs are essentially down-gradient in the simplified framework.

Use of the new TOMs could inform the choice of the diffusion coefficient in equations (3.16) - (3.20). Mellor and Yamada (1982), and other authors who invoke this closure (e.g. Kantha and Clayson 1994, 2004), assume that Sq is a constant. The original value of 0.2 was chosen to match a few different simulations. The TOMs we have derived could make this choice more general, but initial tests have shown that simulations using equations (B.66) - (B.68) are similar to tests conducted with a fixed Sq . The two models are summarized in Table 3.1 at the end of this chapter.

3.3 Virtual Mass Flux

We next consider the virtual mass flux, which is schematically illustrated in Figure 3.4. There are six interfaces and the initial positions are black. In this simple example, we assume that when there is entrainment into the ocean boundary layer (OBL). The thicknesses of the top three layers are and remain equal. We also assume that the

thicknesses of the layers in the deep ocean are equal. This means that the layers in the upper ocean expand like the bellows of an accordion, while those below contract. The

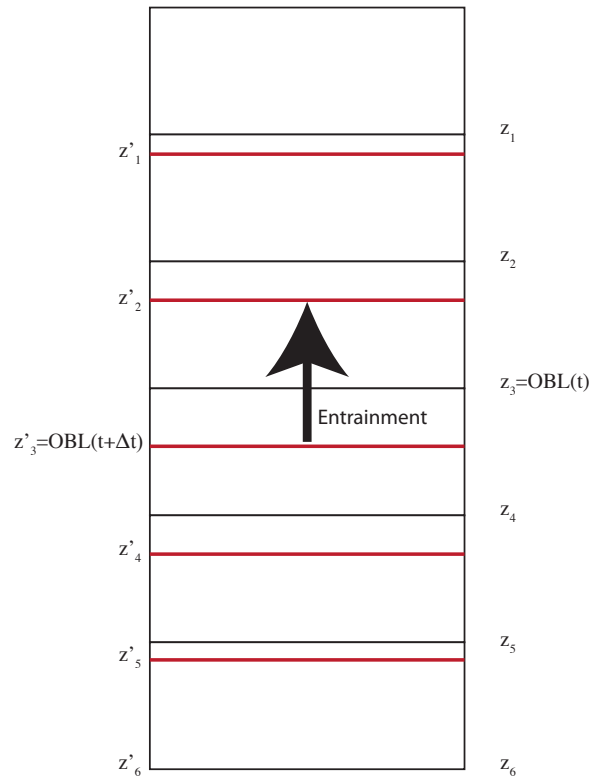


Figure 3.4 - Schematic to illustrate the virtual mass flux. The original depths at the interfaces are given by unprimed z 's. Entrainment occurs at the layer three interface. After some Δt , the model interfaces move to the red lines (primed z 's). The new properties within the layer result from a combination of the original layer value, and those between the black and red lines.

positions of the interfaces after entrainment are shown by the red lines. Although the top three layers move different vertical distances, the thicknesses remain equal.

The movement of these layers implies a corresponding mass flux. Take the first layer as an example. After the coordinate interface has moved, the original mass of layer one is combined with the mass between the depths z'_1 and z_1 to form a new layer one. The properties in this smaller region are combined with those in the original layer one. This is the virtual mass flux.

The transfer of mass implies that we must compute new values of layer properties (e.g. temperature, salinity, and momentum). To do this, we must make assumptions about the profile of a given property within a grid cell. Consider the following example profile illustrated in Figure 3.5. Here we have plotted an observed temperature profile from the eastern tropical Pacific (black). On top of this profile, we have plotted two possible representations of the sub-grid scale temperature distribution.

The simple choice is to assume that the distribution is piecewise continuous (green lines). Using this assumption, we only consider one value in the box. The new temperature is determined by the following sequence of equations

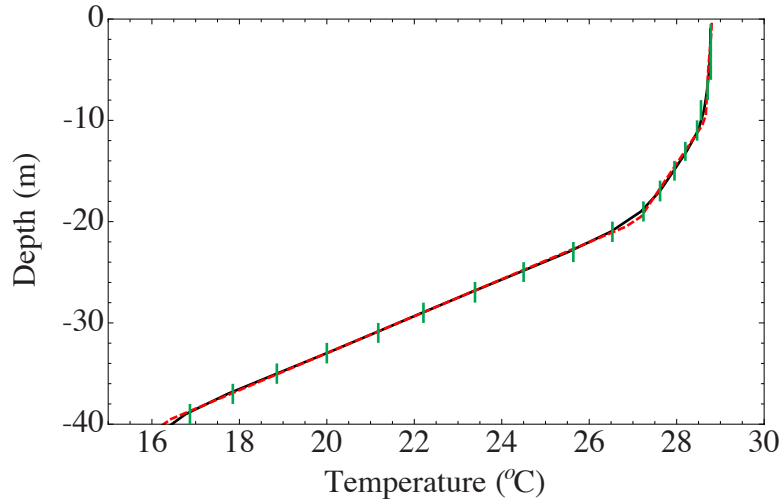


Figure 3.5 - Two possible representations of the sub-grid scale distribution of temperature. The original profile is black, a piecewise constant representation is green, and the piecewise parabolic representation is red.

$$(\rho\theta)_1^{new} = \frac{(z_1 - z_{sfc})\rho_1\theta_1 + (z_1' - z_1)\rho_2\theta_2}{(z_1' - z_{sfc})}$$

$$\rho_1^{new} = \frac{(z_1 - z_{sfc})\rho_1 + (z_1' - z_1)\rho_2}{(z_1' - z_{sfc})}$$

$$\theta_1^{new} = \frac{(\rho\theta)_1^{new}}{\rho_1^{new}}. \quad (3.23)$$

This can be repeated for all layer quantities.

The primary drawback of this approach has been discussed in the context of how KPP determines the boundary layer depth (Chapter 1). This method relies on linear interpolation, which may not be appropriate as the resolution degrades since this method is subject to strong numerical diffusion. This can be seen by recasting the remapping problem as an advection problem. The corresponding equations are

$$\frac{\partial \rho\theta}{\partial t} = \frac{\partial \rho E\theta}{\partial z}$$

$$\frac{\partial \rho}{\partial t} = \frac{\partial \rho E}{\partial z}$$

This is consistent with equation (3.23), when the above equations are discretized with the first order upstream method. Since the upstream method is highly diffusive, we can expect equation (3.23) to be subject to similar diffusion.

The second option considered is the piecewise parabolic method (PPM; Colella and Woodward 1984). The resulting reconstruction, which utilizes the limiter described in White et al. (2009), is plotted as the red dashed line. It is obvious that this is a much more faithful representation of the temperature profile and is third order accurate (Colella and Woodward 1984). Use of PPM requires more computations relative to the piecewise constant method (PCM) to ensure monotonicity and positive definiteness. It is possible to reduce the number of computations by using a hybrid of these two schemes. When the model is entraining, the interfaces do not move rapidly over large distances, and the

numerical diffusion associated with the first order scheme is fairly minimal. The interfaces move rapidly over large distances when the boundary layer collapses and the diffusion associated with the first order scheme is large. We could therefore use PPM for shoaling and and PCM for entrainment to minimize both diffusion and the number of calculations. For simplicity we choose either PPM or PCM depending on the simulation.

3.3.1 PPM vs. PCM

We have conducted two tests to illustrate the numerical diffusion associated with the PCM and PPM methods. The temperature profile shown in Figure 3.5 is discretized on a vertical grid with two-meter resolution. We assume that six layers are in the OBL. The boundary layer thickness is doubled (12 m to 24 m). The thickness of the top six

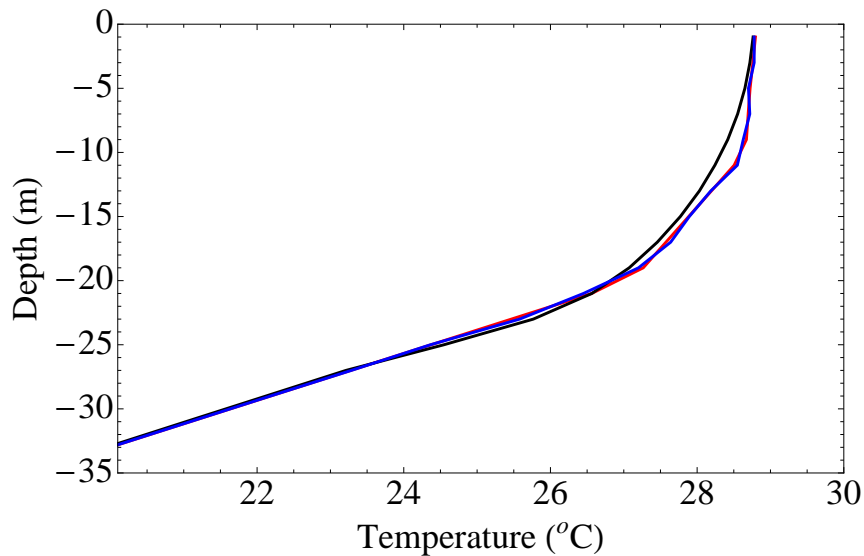


Figure 3.6 - Profiles of temperature after one remapping cycle using the PCM (black) and PPM (blue) methods. The observed temperature is red.

layers becomes four meters and the remaining layers thin to 1.82 m. The boundary layer is then collapsed back to the original value. The final PCM and PPM profiles are shown in Figure 3.6. Here, PCM is the black line, PPM is blue, and observed is red. With no

forcing, the profile should not change, despite the change in boundary layer depth. After the cycle of entrainment and collapse, the PPM profile remains similar to the observed profile. Near the thermocline, the PCM profile is diffused relative to observations and PPM.

3.3.2 Detrainment

Equation (3.13) is only applicable to an entraining boundary layer. We must parameterize boundary layer shoaling. In many regions of the extratropical ocean, the diurnal cycle is small and the boundary layer may or may not collapse. This suggests that we cannot let the modeled boundary layer collapse whenever the surface buoyancy forcing becomes positive. Instead, we propose a somewhat ad hoc condition. When the predicted value of $\overline{w'^2}$ at the boundary layer falls below a chosen threshold and the surface buoyancy forcing is positive, the boundary layer collapses to a depth given by the method in Montegut et al. (2004). This threshold was determined by experimentation. For two separate simulations, we began with a large (ocean) value of $10^{-5} \text{ m}^2\text{s}^{-2}$ and reduced this value until the simulated boundary layer depth did not change. These experiments led us to choose a threshold of $10^{-6} \text{ m}^2\text{s}^{-2}$.

3.4 Discretization

We have laid out the conceptual pieces of two vertical mixing models. Both will predict an entrainment rate given by equation (3.13). One will predict all of the second order moments (equations B.80 - B.93), where the third order moments are given by a

simplified form of equations (B.66) - (B.79). The other model will only predict TKE and

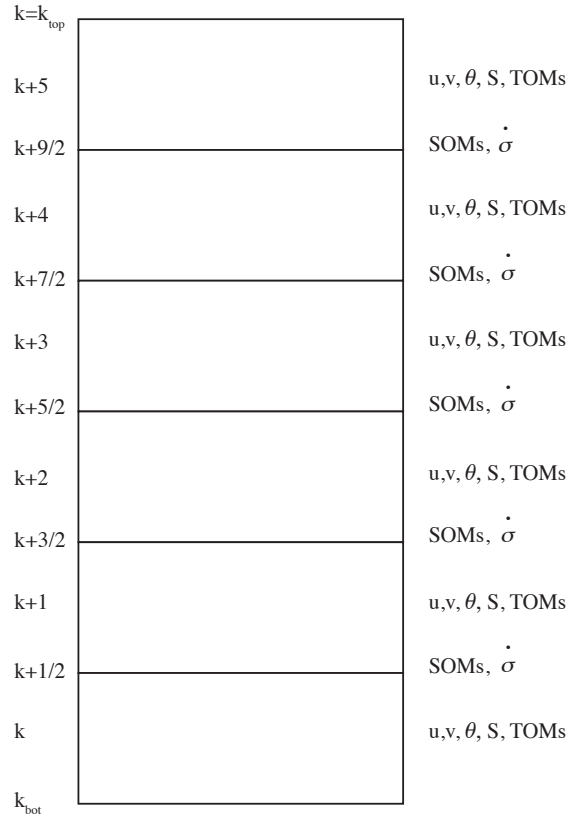


Figure 3.7 - Vertical discretization used in the new model framework.

$\overline{w'^2}$. In this case, the TOMs of TKE and $\overline{w'^2}$ are assumed to be down-gradient (equation 3.18). Finally, both models use a normalized height coordinate (equation 3.3). We now discuss the numerical details of each model.

3.4.1 Vertical staggering

For the mean variables there are two primary vertical grids, the Charney-Phillips (CP) and the Lorenz (L) grids. The difference between the two grids is in the placement of the tracer variables (e.g. θ and S). The tracer variables are located at cell interfaces on the CP grid and at cell centers on the L grid. The L grid is susceptible to a computational mode due to the extra degree of freedom in determining the vertical fluxes of temperature

and salinity (Arakawa and Konor 1996). Despite this shortcoming, we have chosen the

L grid. Mean quantities and the TOMs reside at cell centers and the vertical velocity $\left(\dot{\sigma}\right)$

and second order moments live at the interfaces (Figure 3.6). The L grid allows the

equations for the mean quantities and second order moments to be discretized in a

straight forward manner. Consider the one-dimensional u momentum equation

$$\frac{\partial \bar{u}}{\partial t} = f\bar{v} + \frac{\partial \overline{u'w'}}{\partial z}.$$

For layer $k + 1$ on the L grid, this equation is discretized in space as

$$\frac{\partial \bar{u}_{k+1}}{\partial t} = f\bar{v}_{k+1} + \frac{\overline{u'w'}_{k+3/2} - \overline{u'w'}_{k+1/2}}{z_{k+3/2} - z_{k+1/2}} \quad (3.24)$$

The corresponding equation for the vertical momentum flux (B.82) is discretized as

$$\begin{aligned} \frac{\partial \overline{u'w'}_{k+3/2}}{\partial t} + \frac{\overline{u'w'^2}_{k+2} - \overline{u'w'^2}_{k+1}}{z_{k+2} - z_{k+1}} &= \frac{1}{2} \frac{\bar{u}_{k+2} - \bar{u}_{k+1}}{z_{k+2} - z_{k+1}} \left[(c_1 + c_2 - 2) \overline{w'^2}_{k+3/2} + (c_1 - c_2) \overline{u'^2}_{k+3/2} + 4 \left(\frac{1}{5} - \frac{c_1}{3} \right) k_{k+3/2}^n \right] \\ \overline{u'v}_{k+3/2} \frac{c_1 - c_2}{2} \frac{\bar{v}_{k+2} - \bar{v}_{k+1}}{z_{k+2} - z_{k+1}} + \frac{g}{2} \left(\overline{\alpha u \theta'}_{k+3/2} - \overline{\beta u s'}_{k+3/2} \right) &- 5 \tau_{k+3/2}^{-1} \overline{u'w'}_{k+3/2}. \end{aligned}$$

The remaining mean quantities and second order moments are discretized in a similar

manner. In the simplified framework, the previous equation becomes

$$\overline{u'w'}_{k+3/2}^n = \frac{1}{2} \tau_{k+3/2}^n \epsilon_{k+3/2}^n S_{m_{k+3/2}}^n \frac{u_{k+2}^n - u_{k+1}^n}{z_{k+2} - z_{k+1}}. \quad (3.25)$$

3.4.2 Time discretization

To discretize the model in time, we begin by defining a diffusion coefficient

$\left(v_{k+3/2}^n \equiv \frac{1}{2} \tau_{k+3/2}^n \mathcal{E}_{k+3/2}^n S_{n_{k+3/2}}^n \right)$. Using this definition, we insert (3.25) into (3.24) to obtain

$$\frac{\bar{u}_{k+1}^{-n+1} - \bar{u}_{k+1}^{-n}}{\Delta t} = f \bar{v}_{k+1}^{-n} + \frac{v_{k+3/2}^n}{(z_{k+3/2} - z_{k+1/2})(z_{k+2} - z_{k+1})} \left(\bar{u}_{k+2}^{-n} - \bar{u}_{k+1}^{-n} \right) - \frac{v_{k+1/2}^n}{(z_{k+1/2} - z_{k_{bot}})(z_{k+1} - z_k)} \left(\bar{u}_{k+1}^{-n} - \bar{u}_k^{-n} \right)$$

This equation can be written implicitly, where all the terms on the right hand side except the Coriolis term are taken at time $n+1$. Performing this operation yields

$$\begin{aligned} \bar{u}_{k+1}^{-n+1} & \left(\frac{1}{\Delta t} + \frac{v_{k+3/2}^{n+1}}{(z_{k+3/2} - z_{k+1/2})(z_{k+2} - z_{k+1})} + \frac{v_{k+1/2}^{n+1}}{(z_{k+1/2} - z_{k_{bot}})(z_{k+1} - z_k)} \right) \\ & - \bar{u}_k^{-n+1} \left(\frac{v_{k+1/2}^{n+1}}{(z_{k+1/2} - z_{k_{bot}})(z_{k+1} - z_k)} \right) \\ & - \bar{u}_{k+2}^{-n+1} \left(\frac{v_{k+3/2}^{n+1}}{(z_{k+3/2} - z_{k+1/2})(z_{k+2} - z_{k+1})} \right) = \frac{\bar{u}_{k+1}^{-n}}{\Delta t} + f \bar{v}_{k+1}^{-n} \end{aligned} \quad (3.26)$$

This has been written in such a way to suggest that when similar equations are written for all grid points in the vertical, we obtain a tri-diagonal system of equations. All the equations for the mean quantities can be written in a similar manner. Thus, we are able to increase the *implicitness* of the model in the simplified framework.

We still must discretize the TKE and vertical velocity variance equations for the simplified framework. We assume that the prediction of TKE can be done in two steps. The first step considers the buoyant and shear production and dissipation. In the second step we apply the TOMs to the updated TKE and $\overline{w'^2}$.

In the simplified framework, the TKE equation is discretized semi-implicitly as

$$\frac{k_{k+3/2}^{n+1} - k_{k+3/2}^n}{\Delta t} = - \left(\overline{u'w'} \frac{\overline{u}_{k+2}^n - \overline{u}_{k+1}^n}{z_{k+2} - z_{k+1}} + \overline{v'w'} \frac{\overline{v}_{k+2}^n - \overline{v}_{k+1}^n}{z_{k+2} - z_{k+1}} \right) - g \left(\overline{\alpha w' \theta}_{k+3/2}^n - \overline{\beta w' S}_{k+3/2}^n \right) - \frac{k_{k+3/2}^{3/2^{n+1}}}{\Lambda}.$$

It seems that this equation is not tractable. We have a $k_{3/2}$ and k at time level $n+1$ to consider. If we instead predict the square root of TKE ($q \equiv \sqrt{k}$), we can rewrite the

previous equation as

$$\left(q_{k+3/2}^3 \right)^{n+1} + \frac{\Lambda}{\Delta t} \left(q_{k+3/2}^2 \right)^{n+1} - \frac{\Lambda k_{k+3/2}^n}{\Delta t} + \Lambda \left(\overline{u'w'} \frac{\overline{u}_{k+2}^n - \overline{u}_{k+1}^n}{z_{k+2} - z_{k+1}} + \overline{v'w'} \frac{\overline{v}_{k+2}^n - \overline{v}_{k+1}^n}{z_{k+2} - z_{k+1}} \right) + \Lambda g \left(\overline{\alpha w' \theta}_{k+3/2}^n - \overline{\beta w' S}_{k+3/2}^n \right).$$

Cardano's formula can now be used to obtain the roots of this equation, but we have three possible answers. To solve for the TKE, we must devise a method to choose the appropriate root. This procedure is discussed in Appendix G.

Once the TKE is updated, the vertical velocity variance is updated following

$$\begin{aligned} \overline{w'^2}_{k+3/2}^{n+1} \left(\frac{1}{\Delta t} + 5\tau_{k+3/2}^{-1} \right) - \left(\frac{1}{3}c_1 - c_2 \right) \frac{\overline{u}_{k+1}^n - \overline{u}_k^n}{z_{k+1} - z_k} \overline{u'w'}_{k+3/2}^{n+1} - \left(\frac{1}{3}c_1 - c_2 \right) \frac{\overline{v}_{k+1}^n - \overline{v}_k^n}{z_{k+1} - z_k} \overline{v'w'}_{k+3/2}^{n+1} \\ - \frac{4g\alpha}{3} \overline{w'\theta}_{k+3/2}^{n+1} + \frac{4g\beta}{3} \overline{w'S}_{k+3/2}^{n+1} = \frac{\overline{w'^2}_{k+3/2}^n}{\Delta t} + \epsilon_{k+3/2}^n \end{aligned}$$

After this equation is invoked, the TOMs are applied. The TOMs are discretized in a manner similar to equation (3.26).

Making the complete second order model more implicit is not straightforward.

We can no longer write equation (3.24) as a tridiagonal matrix since the vertical momentum flux is predicted. It is possible to make the system of equations (B.80) - (B.

93) more implicit by writing them in matrix form. For example, equations (B.80) - (B.

82) can be written (without the TOMs) in discrete form as

$$\begin{aligned} \frac{\overline{u}_{k+3/2}^{\cdot,2}{}^{n+1} - \overline{u}_{k+3/2}^{\cdot,2}{}^n}{\Delta t} &= \left(\frac{1}{3}c_1 + c_2 - 2 \right) \frac{\overline{u}_{k+1}^{\cdot,2}{}^{n+1} - \overline{u}_k^{\cdot,2}{}^{n+1}}{z_{k+1} - z_k} - \frac{2}{3}c_1 \frac{\overline{v}_{k+1}^{\cdot,2}{}^{n+1} - \overline{v}_k^{\cdot,2}{}^{n+1}}{z_{k+1} - z_k} \\ &+ \frac{g}{3} \left(\overline{\alpha w \theta}_{k+3/2}^{\cdot,2}{}^{n+1} - \overline{\beta w S}_{k+3/2}^{\cdot,2}{}^{n+1} \right) + \varepsilon_{k+3/2}^n - 5\tau_{k+3/2}^{-1} \overline{u}_{k+3/2}^{\cdot,2}{}^{n+1} \end{aligned} \quad (3.27)$$

$$\begin{aligned} \frac{\overline{w}_{k+3/2}^{\cdot,2}{}^{n+1} - \overline{w}_{k+3/2}^{\cdot,2}{}^n}{\Delta t} &= \left(\frac{1}{3}c_1 - c_2 \right) \left(\frac{\overline{u}_{k+1}^{\cdot,2}{}^{n+1} - \overline{u}_k^{\cdot,2}{}^{n+1}}{z_{k+1} - z_k} + \frac{\overline{v}_{k+1}^{\cdot,2}{}^{n+1} - \overline{v}_k^{\cdot,2}{}^{n+1}}{z_{k+1} - z_k} \right) \\ &+ \frac{4g}{3} \left(\overline{\alpha w \theta}_{k+3/2}^{\cdot,2}{}^{n+1} - \overline{\beta w S}_{k+3/2}^{\cdot,2}{}^{n+1} \right) + \varepsilon_{k+3/2}^n - 5\tau_{k+3/2}^{-1} \overline{w}_{k+3/2}^{\cdot,2}{}^{n+1} \end{aligned} \quad (3.28)$$

$$\begin{aligned} \frac{\overline{u w}_{k+3/2}^{\cdot,2}{}^{n+1} - \overline{u w}_{k+3/2}^{\cdot,2}{}^n}{\Delta t} &= \frac{1}{2} \frac{\overline{u}_{k+1}^{\cdot,2}{}^n - \overline{u}_k^{\cdot,2}{}^n}{z_{k+1} - z_k} \left[(c_1 + c_2 - 2) \overline{w}_{k+3/2}^{\cdot,2}{}^{n+1} + (c_1 - c_2) \overline{u}_{k+3/2}^{\cdot,2}{}^{n+1} + \right. \\ &4 \left(\frac{1}{5} - \frac{c_1}{3} \right) k_{k+3/2}^{n+1} \left. \right] + \frac{c_1 - c_2}{2} \frac{\overline{v}_{k+1}^{\cdot,2}{}^{n+1} - \overline{v}_k^{\cdot,2}{}^{n+1}}{z_{k+1} - z_k} \\ &+ \frac{g}{2} \left(\overline{\alpha u \theta}_{k+3/2}^{\cdot,2}{}^{n+1} - \overline{\beta u S}_{k+3/2}^{\cdot,2}{}^{n+1} \right) - 5\tau_{k+3/2}^{-1} \overline{u w}_{k+3/2}^{\cdot,2}{}^{n+1}. \end{aligned} \quad (3.29)$$

Equations (3.27) - (3.29) can be arranged to

$$\begin{aligned} \overline{u}_{k+3/2}^{\cdot,2}{}^{n+1} \left(\frac{1}{\Delta t} + 5\tau_{k+3/2}^{-1} \right) - \left(\frac{1}{3}c_1 + c_2 - 2 \right) \frac{\overline{u}_{k+1}^{\cdot,2}{}^{n+1} - \overline{u}_k^{\cdot,2}{}^{n+1}}{z_{k+1} - z_k} + \frac{2}{3}c_1 \frac{\overline{v}_{k+1}^{\cdot,2}{}^{n+1} - \overline{v}_k^{\cdot,2}{}^{n+1}}{z_{k+1} - z_k} \\ - \frac{g\alpha}{3} \overline{w \theta}_{k+3/2}^{\cdot,2}{}^{n+1} + \frac{g\beta}{3} \overline{w S}_{k+3/2}^{\cdot,2}{}^{n+1} = \varepsilon_{k+3/2}^n + \frac{\overline{u}_{k+3/2}^{\cdot,2}{}^n}{\Delta t} \end{aligned} \quad (3.30)$$

$$\begin{aligned} \overline{u w}_{k+3/2}^{\cdot,2}{}^{n+1} \left(\frac{1}{\Delta t} + 5\tau_{k+3/2}^{-1} \right) - \frac{1}{2} \frac{\overline{u}_{k+1}^{\cdot,2}{}^n - \overline{u}_k^{\cdot,2}{}^n}{z_{k+1} - z_k} (c_1 + c_2 - 2) \overline{w}_{k+3/2}^{\cdot,2}{}^{n+1} - \frac{1}{2} \frac{\overline{u}_{k+1}^{\cdot,2}{}^n - \overline{u}_k^{\cdot,2}{}^n}{z_{k+1} - z_k} (c_1 - c_2) \overline{u}_{k+3/2}^{\cdot,2}{}^{n+1} \\ 2 \frac{\overline{u}_{k+1}^{\cdot,2}{}^n - \overline{u}_k^{\cdot,2}{}^n}{z_{k+1} - z_k} \left(\frac{1}{5} - \frac{c_1}{3} \right) k_{k+3/2}^{n+1} - \frac{c_1 - c_2}{2} \frac{\overline{v}_{k+1}^{\cdot,2}{}^n - \overline{v}_k^{\cdot,2}{}^n}{z_{k+1} - z_k} \overline{u w}_{k+3/2}^{\cdot,2}{}^{n+1} - \frac{g\alpha}{2} \overline{u \theta}_{k+3/2}^{\cdot,2}{}^{n+1} + \\ \frac{g\beta}{2} \overline{u S}_{k+3/2}^{\cdot,2}{}^{n+1} = \frac{\overline{u w}_{k+3/2}^{\cdot,2}{}^n}{\Delta t}. \end{aligned} \quad (3.31)$$

$$\begin{aligned}
\overline{u w}_{k+3/2}^{n+1} \left(\frac{1}{\Delta t} + 5\tau_{k+3/2}^{-1} \right) - \frac{1}{2} \frac{\overline{u}_{k+1} - \overline{u}_k}{z_{k+1} - z_k} (c_1 + c_2 - 2) \overline{w}_{k+3/2}^{n+1} - \frac{1}{2} \frac{\overline{u}_{k+1} - \overline{u}_k}{z_{k+1} - z_k} (c_1 - c_2) \overline{u}_{k+3/2}^{n+1} \\
+ \frac{2}{z_{k+1} - z_k} \frac{\overline{u}_{k+1} - \overline{u}_k}{5 - \frac{c_1}{3}} k_{k+3/2}^{n+1} - \frac{c_1 - c_2}{2} \frac{\overline{v}_{k+1} - \overline{v}_k}{z_{k+1} - z_k} \overline{u v}_{k+3/2}^{n+1} - \frac{g\alpha}{2} \overline{u \theta}_{k+3/2}^{n+1} + \quad (3.32) \\
\frac{g\beta}{2} \overline{u S}_{k+3/2}^{n+1} = \frac{\overline{u w}_{k+3/2}^n}{\Delta t}.
\end{aligned}$$

The remaining second order moment equations can be written in this manner⁵. The result is a 15 x 15 matrix that is easily solvable. Once we obtain the new second order moments, the influence of the third order moments (equations B.66 - B.79) is computed. Finally, the vertical momentum, heat, salinity, and passive tracer fluxes are plugged into the mean equations.

3.5 Summary

In this chapter we have laid out the framework of two models, which are summarized in Table 3.1. The first model predicts all of the second order moments and compute TOMs following Cheng et al. (2005). The most important aspects of these models are the ease of adaptability to any coordinate system and the explicit prediction of entrainment rate. The latter will be especially important if this model is coupled to a ocean biology model. The second order model does retain some non-local effects, although a portion of these effects have been neglected (Section 3.2.1). The simpler model is currently completely local.

⁵ We can gain a slight increase in time step by writing the diffusion term as $\mathcal{E}_{k+3/2}^n = \frac{k_{k+3/2}^{n+1} \sqrt{k_{k+3/2}^n}}{\Lambda}$, which follows Kalnay and Kanamitsu (1988). However, this introduces noise to the solution. Due to this noise, we choose to use the dissipation at time level n.

	Second Order	Down Gradient
Predicted Second Order Moments	Equations (B.80) - (B.93)	k and $\overline{w'^2}$
Diagnosed Second Order Moments	None	$\overline{u'w'}$, $\overline{v'w'}$, $\overline{w'\theta'}$, $\overline{w'S'}$, and $\overline{w'P'}$
TOMs	Simplified versions of Equations (B.66) - (B.79)	Down Gradient (equation 3.18; Mellor and Yamada 1982)
Dissipation	$\varepsilon = \frac{k^{3/2}}{\Lambda}$	Same
Length Scale	$\Lambda = 2^{-3/2} B_1 l$ $l = \min\left(0.53 \frac{\sqrt{2k}}{N}, \frac{1}{4} \frac{\sqrt{2k}}{\Sigma}, \frac{0.17h\kappa z}{0.17h + \kappa z}\right)$	Same
Entrainment Rate	Equation (3.13)	Same
Vertical Coordinate	Equation (3.3)	Same

Table 3.1 - Summary of the key features of the two model frameworks that have been developed. The down gradient model is the simplified framework.

We now turn our attention to an evaluation of these two models. In our initial testing, the models described here will be compared against VVM-Aqua results and a single column version of KPP from the most recent version of the Community Climate System Model.

Chapter 4:

Model Evaluation

The initial evaluation of the two models described in the previous chapter follows case B of Andre and Lacarrere (1985, AL85). AL85 conducted simple simulations of the

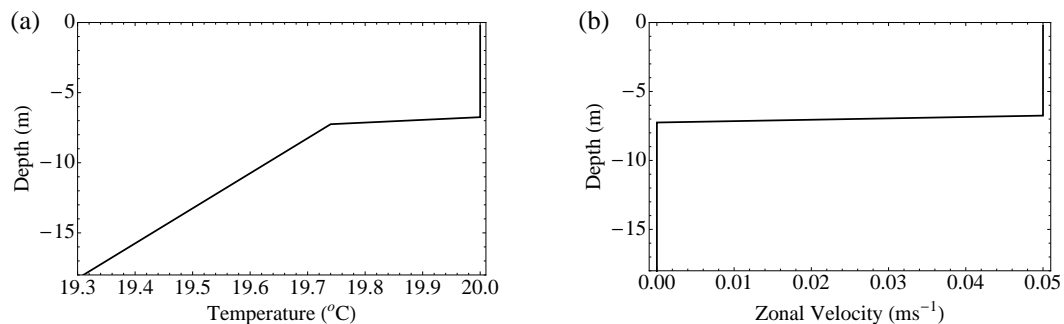


Figure 4.1 - Initial temperature and velocity profile from AL85. (a) Temperature and (b) zonal velocity. Below 15 meters, the stratification is constant ($0.04\text{ }^{\circ}\text{Cm}^{-1}$) and the zonal velocity is zero.

OML with a third order, one-dimensional mixing model. The model domain is 30 meters deep and the vertical resolution is 0.5 meters. The initial profiles of temperature and zonal velocity are shown in Figures 4.1a and 4.1b respectively. AL85 does not consider salinity. In all of our simulations, the initial salinity profile is held fixed.

The initial zonal velocity profile suggests an issue in using this set-up for model evaluation. If we intend to compare our new model at varying resolutions to VVM-Aqua at 0.5 m resolution, the strength of the initial shear changes with the resolution. To

address this concern, we will conduct additional simulations without the background zonal velocity. Although the initial strength of the shear changes with resolution, this test allows us to compare the TKE based mixing model and the full second order closure model proposed in the previous chapter. In these initial tests, we utilized the PCM method for the virtual mass flux.

We have conducted five simulations with the initial conditions shown in Figure 4.1. The remaining parameters for the initial simulations are summarized in Table 4.1.

	Heat Flux	Salinity Tendency	Resolution	Solar Radiation
Case 1	-200 W m ⁻²	0	1m	None
Case 2	-200 W m ⁻²	0	2.5 m	None
Case 3	-200 W m ⁻²	3.5 x 10 ⁻⁶ PSU s ⁻¹	2.5 m	None
Case 4	-200 W m ⁻²	-3.5 x 10 ⁻⁶ PSU s ⁻¹	2.5 m	None
Case 5	-200 W m ⁻²	0	2.5 m	None for first 15 hours then 450 Wm ⁻² in the second 15 hours

Table 4.1 - Summary of the five initial test cases. The initial temperature and velocity profiles are given in Figure 4.1. For salinity, there is no vertical variation and the initial value is 35 PSU.

The temperature profiles at two minutes (black), 10 hours (blue) and 15 hours (red) are shown in Figure 4.2a. In these initial tests, the solid line is from VVM-Aqua, the long dashed line is KPP, the line with open circles is the TKE based model, and the dot-dashed line is the SOC model. The agreement among the models is good, which is not incredibly surprising at such a fine resolution. The SOC model mixes more than KPP and the TKE model. In this test, KPP seems to mix the least.

This is confirmed in a comparison of model mixed layer depths, which is defined as the location where the density changes (compared to the value at 2.5 meters depth) by 0.01 kg m^{-3} (Figure 4.2b). In the initial comparisons of MLD, the TKE model is blue, KPP is black, the SOC model is red, and VVM-Aqua is dashed. The MLDs agree well, with KPP being shallowest and the SOC model being the deepest.

Since this simulation is only driven by surface cooling, we would expect that the

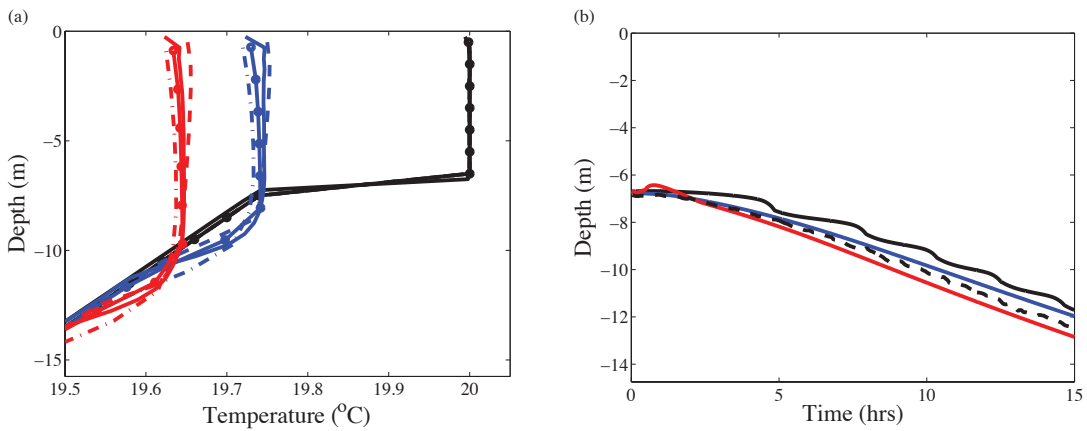


Figure 4.2 - Temperature (a) and mixed layer depth (b). For Case 1. In (a), the black curves are at two minutes. The blue curves are after 10 hours and the red curves are after 15 hours. At each time, the solid line is VVM-Aqua, the dashed line is KPP, the dashed-dot line is the second order model, and the circle line is the TKE based model. In (b), the dashed line is VVM-Aqua, the black line is KPP, the red line is the SOC model, and the blue line is the TKE based model.

SOC model and KPP to simulate the temperature profile and MLD better than the TKE model, which is down-gradient. We believe that the TKE model is able to do a good job in this case due to the background shear included in this test (Figure 4.1b). It seems as though the background shear is more effective at generating sub-surface mixing than the surface fluxes.

When the resolution is decreased, the resulting temperature profiles and MLDs are shown in Figure 4.3a and 4.3b respectively. The temperature profiles for the SOC and TKE models are not as well mixed at this coarser resolution. Consistent with this

result, the mixed layer depth is slightly shallower. It is also interesting that the KPP temperature profiles match VVM-Aqua better at a coarser resolution.

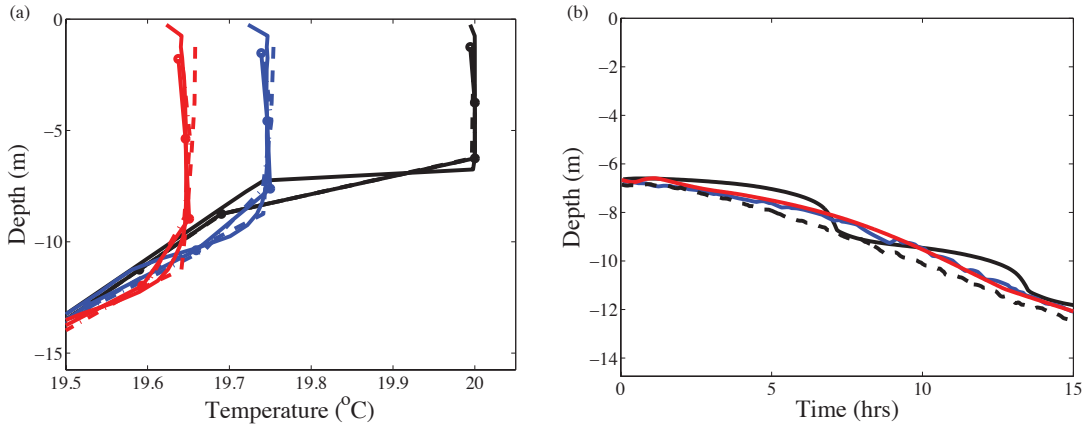


Figure 4.3 - As in Figure 4.2, but for Case 2.

If surface evaporation is included (Case 3), we would expect the strength of convection to increase and the simulated mixed layer depths to be deeper. The profiles of temperature (Figure 4.4a) are similar in this run compared to Case 2 (Figure 4.3a). The profiles of salinity (Figure 4.4b) simulated by the TKE model and KPP are similar. KPP mixes salinity better than the TKE model and is closer to the VVM-Aqua result. This is most likely due to the non-local flux of salinity included in the KPP model.

The salinity profile simulated by the SOC model is more mixed than the other models. It is possible that some of the timescales built into the TKE model (described in Appendix C) are better suited to the simulation of salinity than those in the SOC model (the timescales defined for the TKE model in Appendix C are fixed in the SOC model, as in Canuto et al., 2007).

The mixed layer depths simulated by the models deepens faster than in the first two tests, as we expected. The MLD simulated by the TKE and SOC models are nearly

identical. This result implies that the mixed layer depth is not the only model evaluation metric. The mixed layer depth can be consistent among models, but the temperature and/

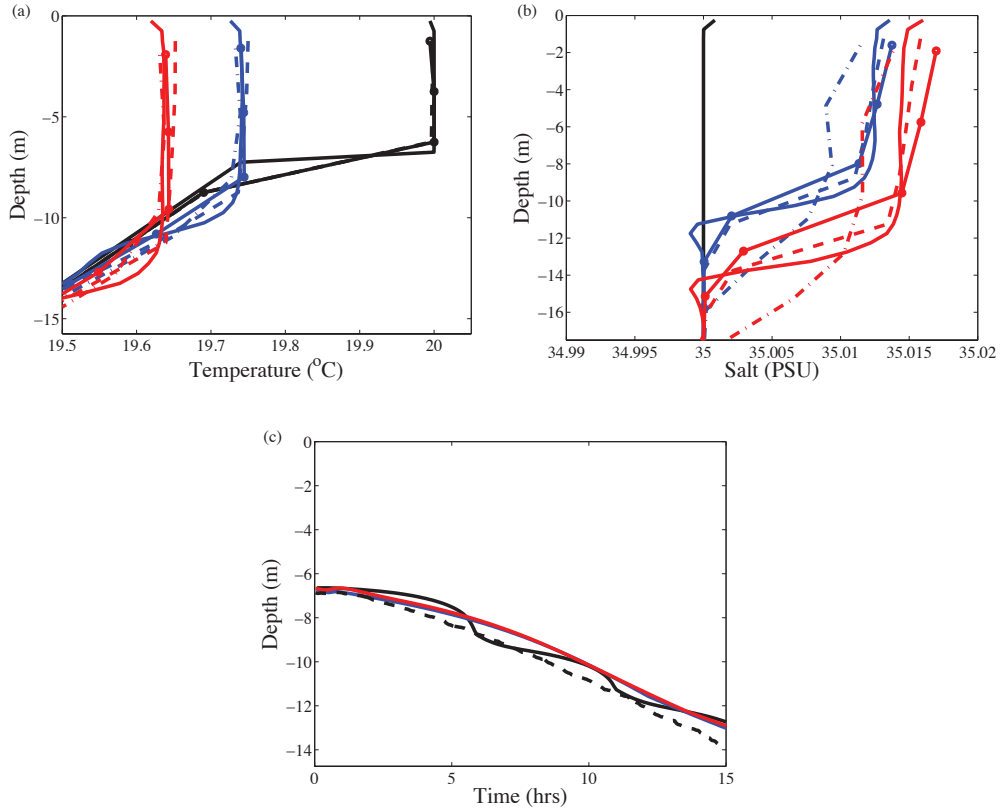


Figure 4.4 - Temperature (a), salinity (b), and mixed layer depths (c) for Case 3. In (a) and (b), the colors and line styles are as in Figure 4.2a. In (c), the colors are as in Figure 4.2b

or salinity profiles can be different due to compensating density effects.

If we now freshen the surface, the simulated mixed layer depth should be shallower. The profiles of temperature, which are shown in Figure 4.5a, are less mixed than in the previous cases. The simulated salinity profiles (Figure 4.5b) are similar for the TKE model, KPP, and VVM-Aqua. Again, the SOC result is the least like the other three models. In this stabilizing situation it does not mix enough, where in the convective situation it mixes too much. In this run, the KPP and TKE model result is similar to

VVM-Aqua throughout the model column. Since the surface salinity forcing is stabilizing, the strength of the non-local transport is reduced.

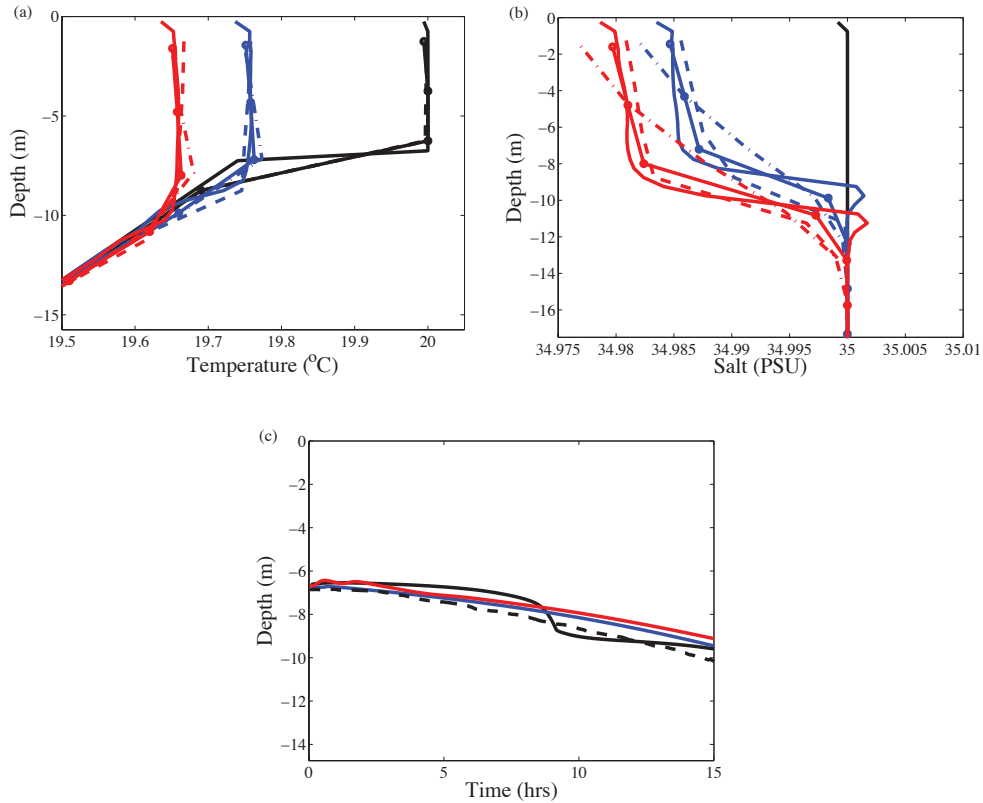


Figure 4.5 - As in Figure 4.4, but for surface freshening (Case 4).

The next case implements an incredibly simple diurnal cycle. There is no solar forcing for the first 15 hours of the simulation, and then the sun is immediately up for the next 15 hours. The surface solar radiation is 450 Wm^{-2} , which represents a daily mean solar forcing. Throughout this simulation, a -200 Wm^{-2} is included.

Since the first half of the simulation is identical to Case 1 and Case 2, we plot the temperature in Figure 4.6a at 15 hours (black), 22 hours (blue), 30 hours (red). The line styles are as in the previous figures. KPP and the new TKE model agree fairly well with the VVM-Aqua output. At 22 hours (blue lines Figure 4.6a), KPP is slightly warmer at

the surface and through the upper ocean. The SOC model is even warmer than KPP at

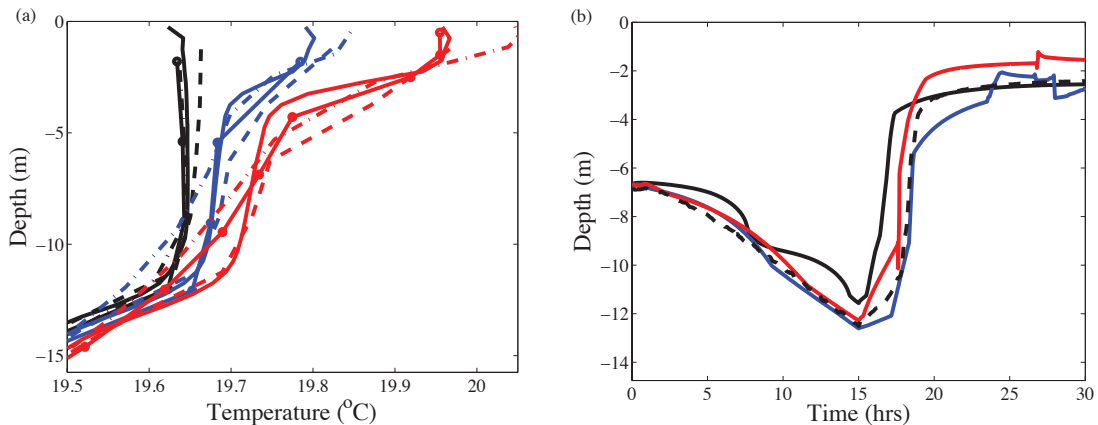


Figure 4.6 - Temperature (a) and simulated mixed layer depths (b). In (a), the defined line styles are as in the previous temperature profiles, but the black lines are 15 hours, the blue lines are 22 hours, and the red lines are 30 hours. The colors in (b) are as in Figure 4.2b.

the surface, but the temperature near the OML base agrees well with VVM-Aqua.

Below the surface, the ghost mixed layer is not as visible in the new models as in KPP and VVM-Aqua. By 22 hours, the mixed layer depth (Figure 4.6b) has decreased dramatically in all the models. Simulating this large and quick movement in the depth of the mixed layer using the PCM induces a large amount of numerical diffusion, which weakens the strong temperature gradient near three and 12 meters depth.

At 30 hours, the surface temperature in KPP now agrees well with VVM-Aqua. In addition, the temperature profile simulated by the TKE model in the upper few meters matches VVM-Aqua as well. The general agreement between VVM-Aqua, KPP, and the TKE model is good. The SOC model has a surface temperature that is much too warm.

To this point, it seems that the SOC model offers no advantage over the TKE based model. We believe the simulated salinity could be improved in the SOC model by allowing the timescales in the model equations to vary with the Richardson number and

the density ratio $\left(\frac{\beta S_z}{\alpha T_z}\right)$. We are not convinced that this change will improve the

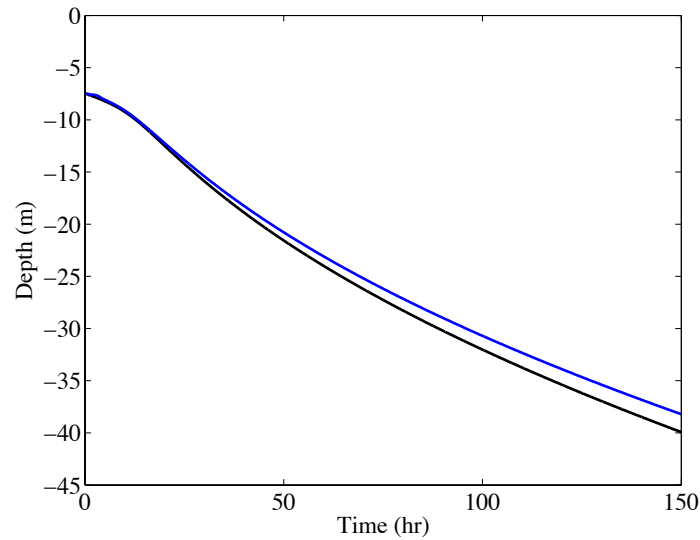


Figure 4.7 - Mixed layer depths simulated by the TKE model (blue) and the SOC model (black) forced as in Case 2, but the simulation length is increased by a factor of ten.

SOC result enough to warrant the additional computational burden associated with this model. Prior to dismissing this model, we have extended the Case 2 simulation to 150 hours.

The mixed layer depths simulated by each model are given in Figure 4.7 (Black is the SOC model and Blue is the TKE model). The difference even after 150 hours is minimal. We have also conducted a test without the background shear (i.e. pure convection), but again, the improvement in the SOC model is minimal (not shown). It seems that the algebraic third order moments derived in Appendix B are not completely capturing the non-local aspects of convection.

The results of these tests lead us to the conclusion that the TKE model behaves nearly as well in surface cooling simulations, but better when salinity is included, than

the SOC model. Therefore, throughout the rest of this work, we will only use the TKE based model.

4.1 Formation of a Mixed Layer

The next set of simulations have no initial mixed layer. We have also eliminated the initial background shear. The surface temperature is set to 20°C and the stratification

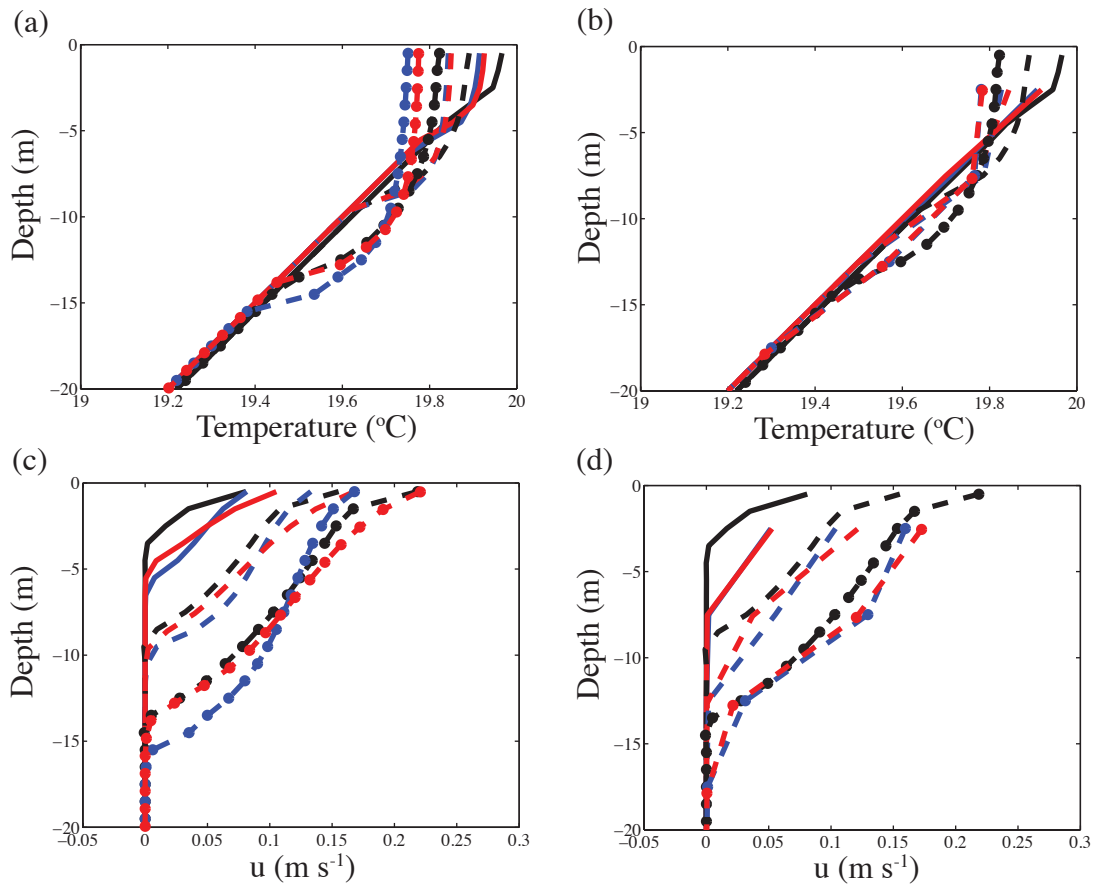


Figure 4.8 - Temperature (ab) and Zonal Velocity (cd) profiles for the no initial mixed layer, wind-driven, run. In all these plots black lines are from VVM-Aqua, blue lines are from KPP, and the red lines are from the TKE model. The solid lines are at two hours, the dashed lines are from six hours, and the circle dashed lines are from 12 hours. The vertical resolution for VVM-Aqua is 0.5 meters. In (a) and (c), the initial vertical resolution for the TKE model and KPP is one meter. The resolution is increased to five meters in (b) and (d).

is $0.04 \text{ } ^\circ\text{C m}^{-1}$. In the first test, the wind stress is 0.037 Nm^{-2} . KPP and the TKE model are run at one, five, and 11 meter resolutions.

The temperature and velocity profiles for the two one-dimensional models and

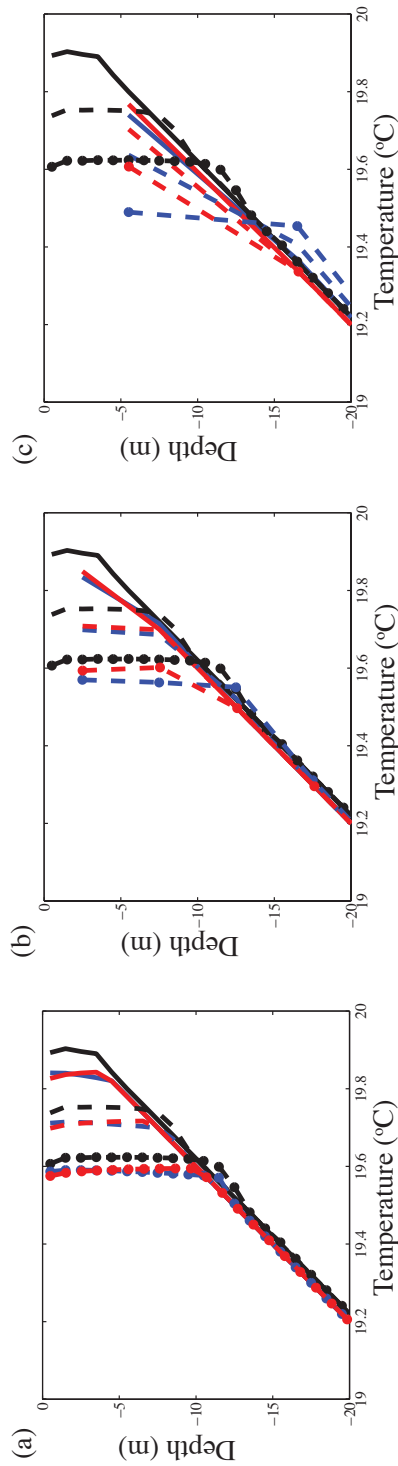


Figure 4.9 - Colors and line styles are as in Figure 4.8. (a) one meter resolution, (b) five meter resolution, and (c) 11 meter resolution.

VVM-Aqua are given in Figure 4.8. In these figures, VVM-Aqua is black, KPP is blue,

and the new TKE model is red. The solid lines are the profiles at two hours, the dashed lines are at six hours and the dashed line with circles is 12 hours.

At one-meter resolution (Figures 4.8a and 4.8c), both one-dimensional models mix more strongly than VVM-Aqua. The temperature at depth in the new TKE-based model agrees with VVM-Aqua better than KPP. The profiles of zonal momentum from VVM-Aqua and the TKE model match quite well (Figure 4.8c). The velocity profiles from KPP tend to be more strongly mixed. It is possible that this is related to the deficient interior mixing scheme.

At five meter resolution, the difference in the temperature of the top model level of KPP and the new model and the corresponding temperature in VVM-Aqua is small (Figure 4.8b). However, the agreement near the base of the mixed layer is not as good at this resolution. Neither KPP or the TKE model mix as deeply as VVM-Aqua.

The zonal momentum profile simulated by KPP is now closer to VVM-Aqua than the corresponding 1-meter resolution result (Figure 4.8d). The results here are the beginning of what will become a recurring theme. For a given shear, KPP predicts too much mixing.

At five meter resolution, the agreement between the zonal momentum profiles in the new model and VVM-Aqua is good. The visual deviation between the red dashed and black dashed lines near 10 meters depth is a result of linearly joining two data points. The zonal velocity predicted by the TKE model goes to zero prior to hitting the next model level. At 11-meter resolution the change in the temperature and velocity fields below layer one is minimal (not shown).

The next test imposes a constant cooling of -200 Wm^{-2} and ignores the surface stress. The remaining initial conditions are the same as in the previous test.

The temperature profiles at the three different resolutions are shown in Figure 4.9. At one-meter resolution (Figure 4.9a), the one-dimensional models mix rapidly near the beginning of the run, but then the LES model seems to catch up and the profiles at 12 hours agree well.

When the resolution coarsens to five meters (Figure 4.9b), the upper ocean temperature in KPP and the TKE model are cooler than VVM-Aqua. The temperature profile simulated by the TKE model is not as well mixed as VVM-Aqua or KPP.

At the coarsest resolution (Figure 4.9c), the KPP simulated temperature profile at 12 hours is much cooler than VVM-Aqua or the new mixing model. It is also interesting to note that the thickness of the well mixed layer in the KPP model is approximately equal to that in VVM-Aqua, except that the KPP result is shifted downward. We believe that this is due to the design of KPP.

In KPP, the shape of diffusivity is assumed to be a cubic polynomial and is fit to the diffusivity predicted by the interior mixing scheme as well as the gradient of diffusivity across the OML base. At the surface the profile of diffusivity matches similarity theory. Therefore, the diffusivity predicted by KPP is critically dependent on the mixed layer depth determined by the model. At 11-meter resolution, the mixed layer depth is much deeper than what is predicted by the model at higher resolution. This leads to a diffusivity profile that is spread out over a greater depth than in the higher resolution runs. At this resolution, quadratic interpolation may be inadequate and is causing a deep

bias. It is also possible that, as argued by Danabasoglu and Large (2003), the critical

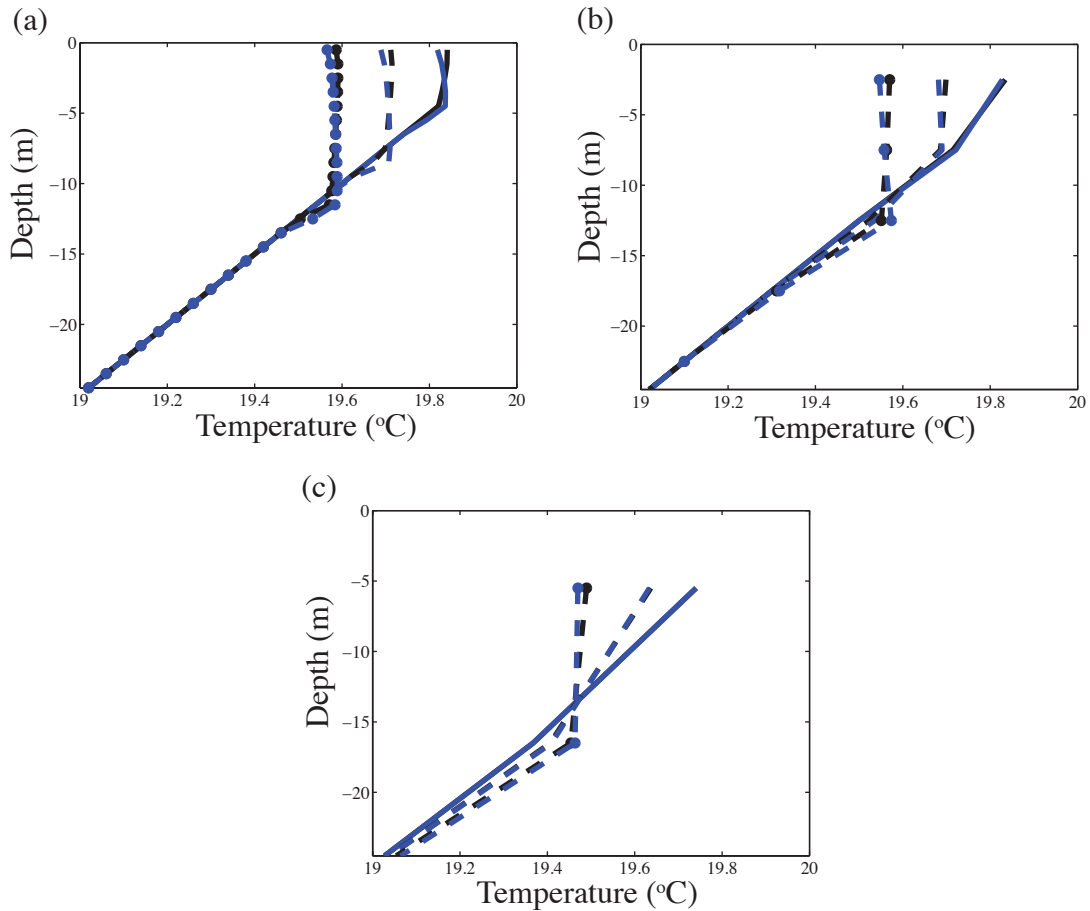


Figure 4.10 - Test of the influence of non-local forcing in KPP. The line style is as in Figure 4.9. The blue line is the result from Figure 4.9. The black line removes the non-local forcing. (a) one meter resolution, (b) five meter resolution, and (c) 11 meter resolution.

Richardson number used to determine the depth of the boundary layer should change with resolution.

Prior to leaving this test we assess the influence of the non-local transport term in KPP. Figure 4.10 shows the influence of this term on the temperature profile at each resolution. In each figure, the black line is the result from Figure 4.9, the blue line is the companion simulation with the non-local forcing removed. The general pattern is that once a mixed layer is formed, the non-local terms keep the temperature field well mixed

(as expected). Without the counter-gradient flux, there is a slight temperature instability (although there is no static instability). This is similar to what is seen in the TKE model (e.g. Figure 4.2a), which is a down-gradient model. At the coarsest resolution (Figure 4.10c), we notice that the non-local term is not responsible for the overly deep and cold mixed layer seen in Figure 4.9c.

The results of this test suggest caution is needed when using KPP at coarse

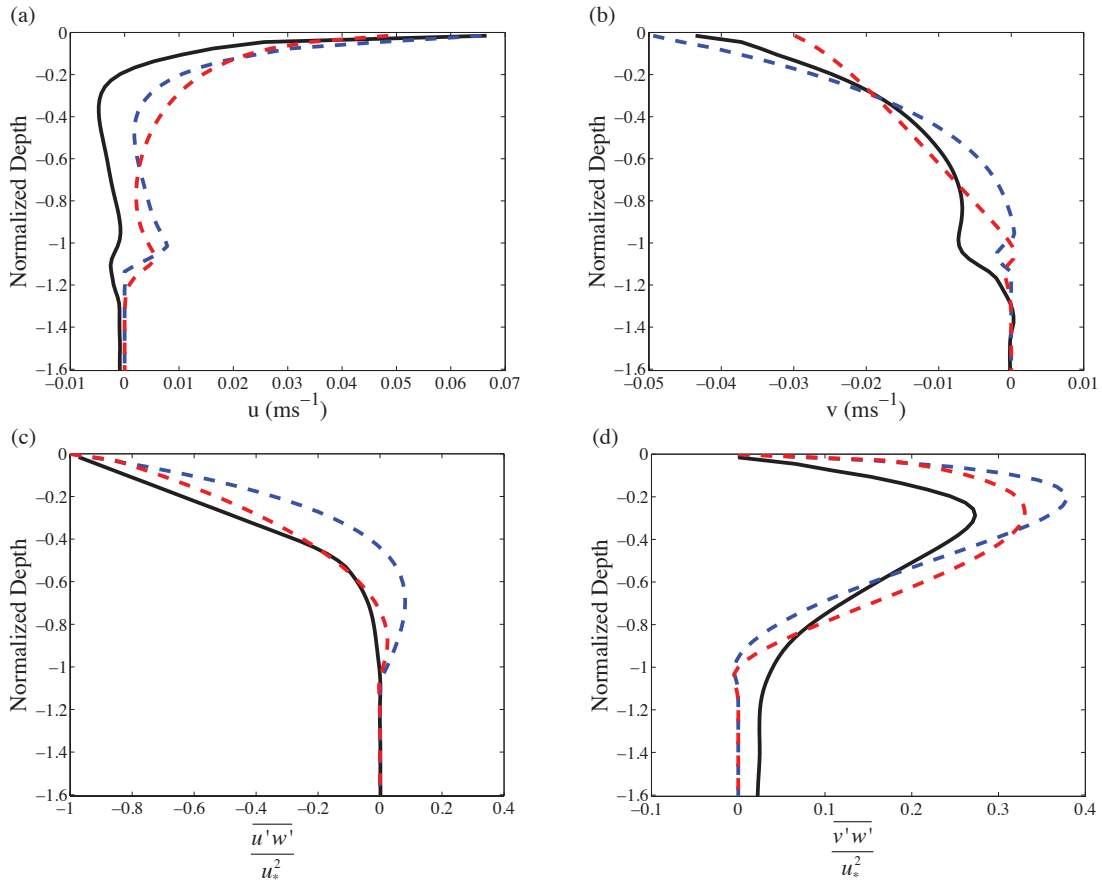


Figure 4.11 - Time averaged profiles of zonal velocity (a), meridional velocity (b), $\overline{u'w'}/u_*^2$, and (c) $\overline{v'w'}/u_*^2$. In these figures, the black line is from VVM-Aqua, red is KPP and blue is the TKE model. The results are plotted in a normalized depth coordinate (as in Chapter 2).

resolutions for regions of the ocean with shallow boundary layer depths.

4.2 Established Mixed Layer

The next series of evaluations utilizes the initial conditions of the M97 test described in Chapter 2. Although a few parameterizations of LC have been proposed in the literature for KPP (e.g. Li and Garrett 1997 and McWilliams and Sullivan 2000) none has yet been widely accepted. Here we will repeat the M97 simulation driven by surface stress with KPP and the TKE model, but not the Langmuir turbulence run.

The time averaged velocities (averaged over the same interval as in Chapter 2) and the corresponding momentum fluxes are shown in Figure 4.11. In this figure, the black line is the VVM-Aqua solution, the blue line is the new TKE model and red is from KPP. The resolution for all three models is one meter. At high resolution (Figure 4.11a),

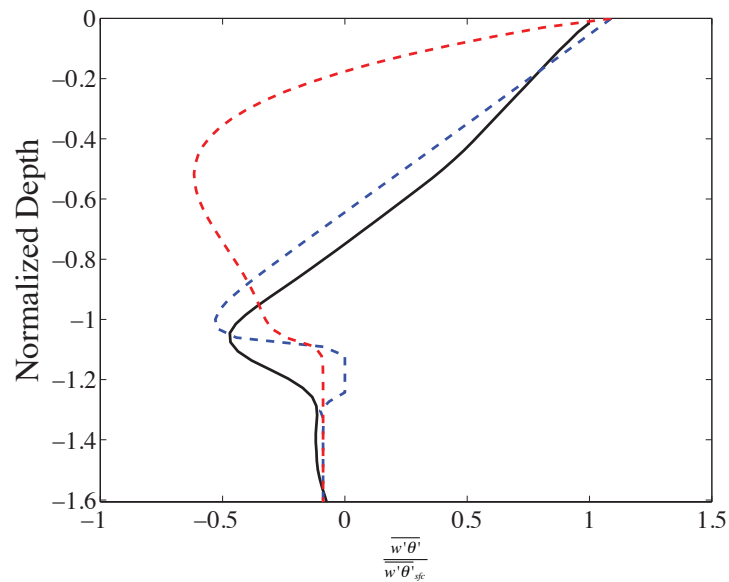


Figure 4.12 - Time averaged profiles of normalized vertical heat flux. The colors are as in Figure 4.11.

the profiles of zonal momentum for all models agree pretty well, although the zonal

velocity becomes slightly negative at lower depths in VVM-Aqua, when the KPP and TKE models do not. The profiles of v-velocity in the new model and VVM-Aqua, which are shown in Figure 4.11b, match fairly well. Near the surface, the v-velocity from the TKE model is slightly too strong. The meridional momentum profile simulated by KPP is more mixed than the TKE model. This follows the previous observation that for a given level of shear, KPP appears to mix too much.

The zonal momentum flux for VVM-Aqua and KPP match quite well (Figure 4.11c). The profile from the TKE model is too weak in the upper portion of the mixed layer and changes sign about halfway through the mixed layer. The simulated profiles of

$\overline{v'w'}/u_*^2$ for all three models have a similar structure (Figure 4.11d). Near a normalized

depth of -1, the simulated fluxes in the one-dimensional models become zero and it remains slightly positive in VVM-Aqua. Within the mixed layer, the vertical gradient of

$\overline{v'w'}/u_*^2$ from the TKE model is sharper than both KPP and VVM-Aqua. The peak value

is also slightly stronger than the other models. Visual inspection of Figure 3 from M97

suggests that the KPP profile of $\overline{v'w'}/u_*^2$ is close to the correct result, but is slightly to

strong.

The normalized vertical heat flux is given in Figure 4.12. Immediately we notice the large difference in heat flux profile simulated by KPP compared to the other models.

The positive heat flux near the surface in KPP changes sign quickly, signifying an upward

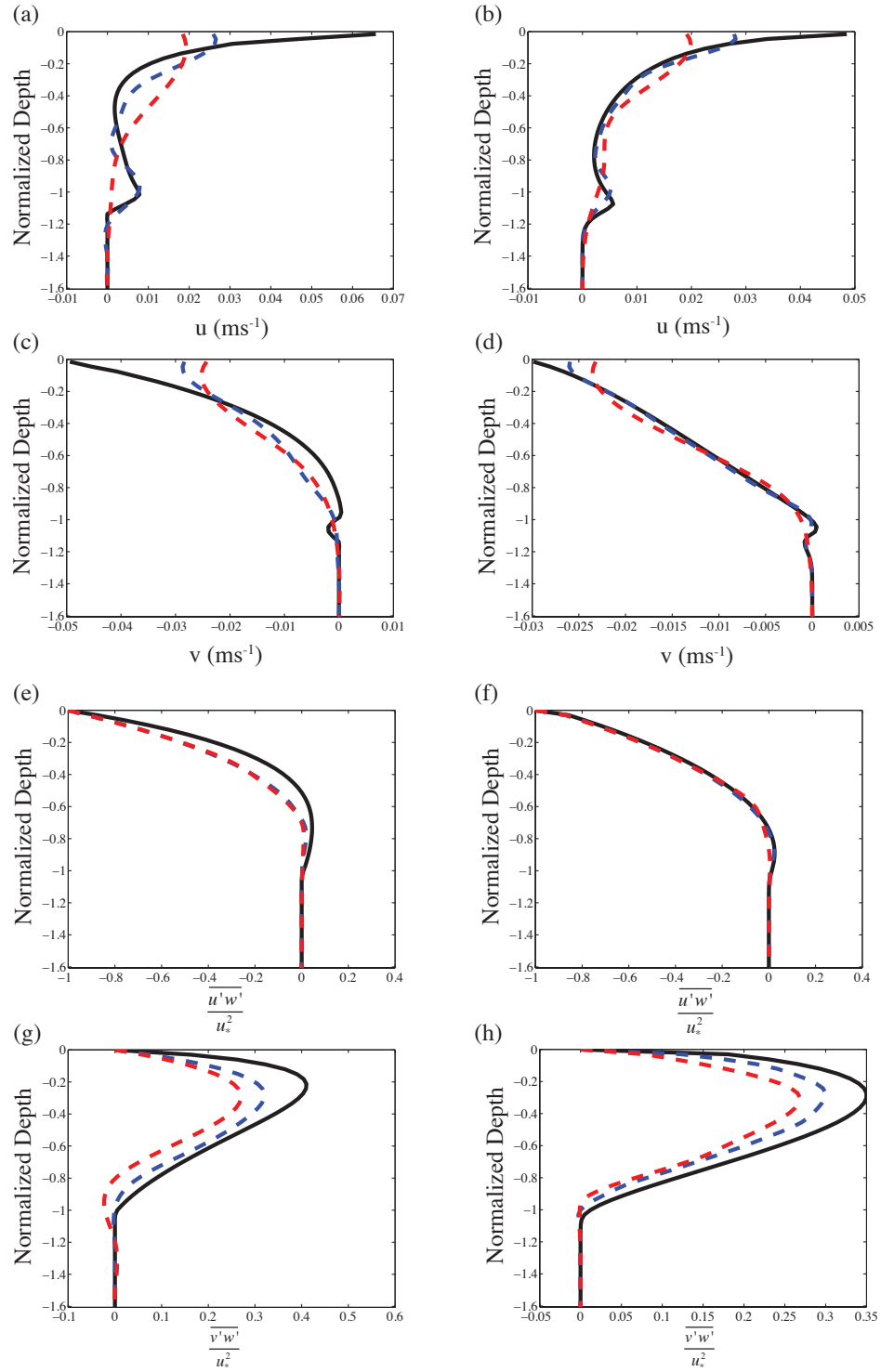


Figure 4.13 - Impact of changing vertical resolution on (ab) u , (cd) v , (ef) $\frac{\overline{u'w'}}{u_*^2}$, and (gh) $\frac{\overline{v'w'}}{u_*^2}$.

In these plots, the black line is one-meter resolution, the blue line is five meter resolution, and the red line is 11 meter resolution. The left column is the TKE model and the right column is from KPP.

movement of cold water, or a stronger entrainment rate in KPP when compared to the other two models (and M97).

The influence of vertical resolution on the time averaged quantities is given in Figure 4.13. Here the simulation with one meter resolution is black, the five meter resolution is dashed blue, and the 11-meter resolution is dashed red. The left column is output from the TKE model and the right column is from KPP.

Overall, the change in zonal momentum is minor below the surface (Figures 4.13ab). The surface zonal velocity in KPP and the new TKE model becomes weaker as the resolution decreases (Figures 4.13 ab).

With a weaker surface u-velocity, we expect, and observe (Figures 4.13 cd), a weaker y-component of velocity. In the TKE model, the decrease in v-velocity between the one and five meter resolution runs is much stronger than that observed in KPP (compare Figure 4.13c and 4.13d). The change from five to eleven meter resolution in the TKE model is much smaller.

The changes in the normalized u-momentum flux from KPP as the resolution coarsens are minimal (Figure 4.13f), but the change is noticeable in the TKE model (Figure 4.13e). The vertical momentum flux penetrates through a deeper layer at the coarser resolutions in the TKE model than in the high resolution run. This is not an expected result. As the resolution is increased, the simulation should approach “the truth”. In the TKE model, the simulation at five meters compares with VVM-Aqua better than the one meter run. This occurs in the momentum fluxes from this simulation only, which makes the conundrum even more difficult to understand. It is possible that the

coarser resolution is creating an extra transport of TKE that is physically important but is not simulated in the TKE model.

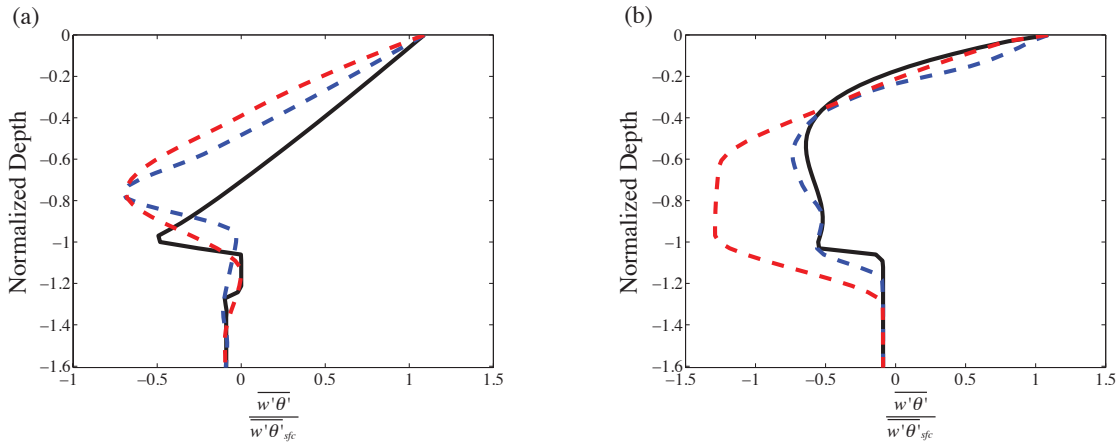


Figure 4.14 - As in Figure 4.13, but for $\frac{\overline{w'\theta'}}{\overline{w'\theta'}_{sfc}}$

Figure 4.13gh show that the normalized $\overline{v'w'}$ for the new model and KPP behave similarly as the resolution decreases. The general behavior is for the flux to weaken as the resolution becomes more coarse. Again, the five meter simulation of the TKE model is closer to the VVM-Aqua result (and M97) than the one meter simulation (Figure 4.12g).

The effect of changing resolution on the vertical heat flux is shown in Figure 4.14. In the new model, the heat flux definitely gets worse as the resolution gets more coarse (Figure 4.14a). The minimum in the profile of normalized heat flux shifts toward the surface at coarser resolution. This region corresponds to where the momentum flux increases as well (4.13e). Even though the vertical heat flux simulated by the new model degrades with coarser resolution, the change in the KPP heat flux is larger (Figure 4.14b).

At five meter resolution (blue dashed line in Figure 4.14b) the change compared

to one meter resolution is not very big. However, when the resolution is cut in half again, the vertical heat flux is greatly magnified at depth. Again we see that KPP tends to be more sensitive to resolution than the TKE model and others (e.g. Acreman and Jeffery 2007).

4.2.1 Convectively driven simulation

We now use the same initial conditions as in the previous test, but we omit the surface wind stress and increase the heat flux from -5 Wm^{-2} to -200 Wm^{-2} . In this test we would expect that KPP will outperform the new model, as non-local effects are included. This simulation is run for 15 hours.

Figure 4.15 shows the change of temperature relative to the initial time. This figure is constructed as in Figure 2.10. The VVM-Aqua result is Figure 4.15a, the new model is 4.14b, and KPP is 4.15c. The contour interval in 4.15a and 4.15b is 0.008°C and is 0.012°C in 4.15c.

The surface temperature change at the end of the simulation is similar among the three models. The profiles at specific times (not shown) for the new model resemble the blue line in Figure 4.10a, which is the KPP result without non-local forcing. It is also similar to the profile seen in the very first test conducted in this chapter (the only difference is that in this run, the mixed layer depth is nearly five times greater).

Although the temperature change near the surface seen in the three models is comparable, the rate of mixed layer deepening is different. The entrainment velocity in Figure 4.15(a-c) can be diagnosed by the area of warming water directly below the mixed layer. A visual comparison between VVM-Aqua and the new model shows that the TKE

based model under-predicts the entrainment rate in this convective simulation. The width

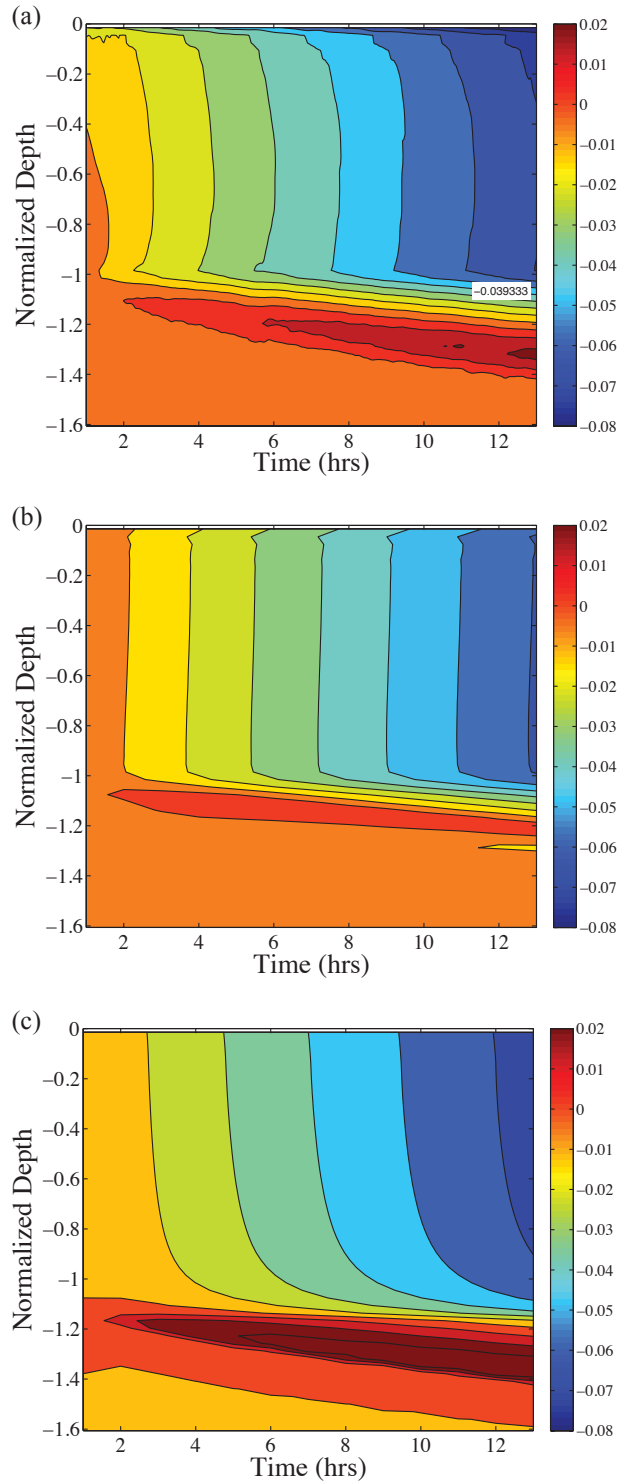


Figure 4.15 - Temperature change relative to the initial temperature through time for (a) VVM-Aqua, (b) TKE model, and (c) KPP. In (a) and (b), the contour interval is 0.008°C and is 0.012°C in (c).

of the warming region is smaller in the TKE model and it does not slope downward as much as VVM-Aqua. The entrainment rate for KPP is closer to what is seen in VVM-

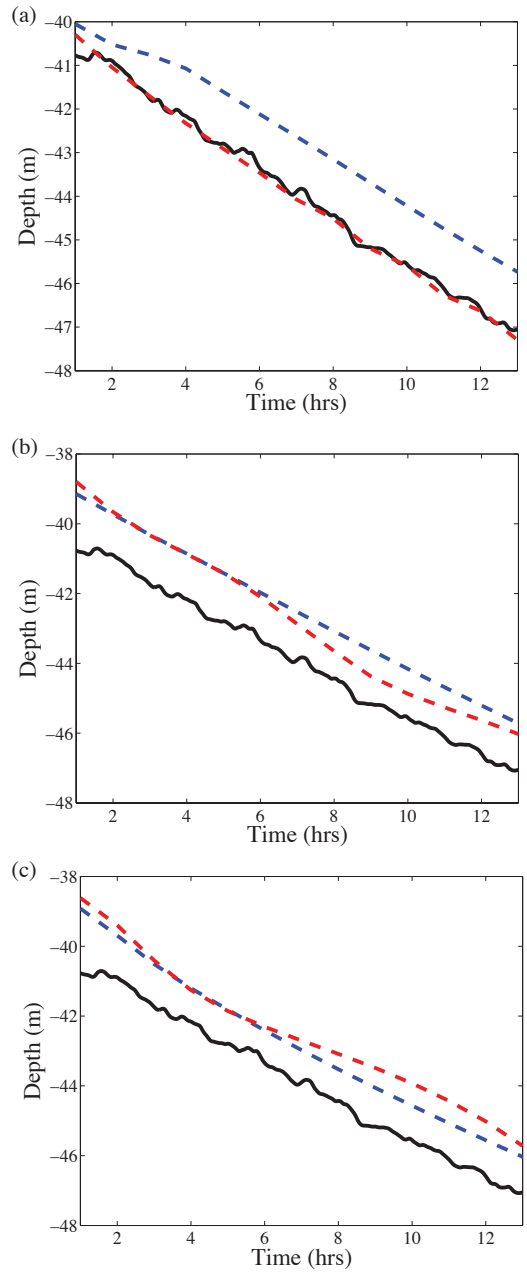


Figure 4.16 - Mixed layer depths through time for three different resolutions. (a) one meter resolution, (b) five meter resolution, and (c) 11 meter resolution. In all the plots, black is VVM-Aqua, red is KPP, and blue is the TKE model.

Aqua than the TKE model.

The better agreement between KPP and VVM-Aqua evident in Figure 4.15a and 4.15c is definitely due to the non-local term built into KPP. This term takes a portion of the energy associated with the surface heat flux and communicates it to the bottom of the boundary layer, allowing the mixed layer to deepen more rapidly than the TKE model.

These observations are confirmed in a plot of the mixed layer depths, which for this high resolution simulation are plotted in Figure 4.16a. Here, the black line is VVM-Aqua, the blue line is the TKE model, and KPP is the red line. The KPP and VVM-Aqua MLDs agree nearly perfectly, while the output from the new model is too shallow, but does seem to deepen at a fairly similar rate. When the resolution is decreased to 5 meters (Figure 4.16b), the KPP and LES MLDs no longer agree. The one-dimensional models now agree well, but are too shallow when compared to VVM-Aqua. A similar story is seen at the coarsest resolution (Figure 4.16c). In fact, the change between 4.16b and 4.16c is minimal.

The three profiles of the normalized averaged heat flux agree well within the boundary layer (not shown). At the bottom of the well mixed region, the heat flux in KPP and VVM-Aqua changes sign (similar to Figure 4.13a). The new model does not. In a down-gradient model (such as our new TKE-based model), the heat flux is given as $\overline{w'\theta'} = \kappa \partial\theta/\partial z$. Therefore, a positive heat flux occurs where there is mixing (κ) and a positive (i.e. stable) temperature gradient. Below the mixed layer, a positive temperature gradient is present in the TKE model, but there is no mixing due to the lack of TKE.

Since the vertical heat flux is counter-gradient, we expect the TKE at the base of the OML to be generated non-locally.

As we coarsen the resolution, the heat flux in the new model barely changes. The KPP simulated flux changes dramatically. This change is similar to what happened in the shear driven case. Unlike the test with no initial mixed layer, the predicted boundary layer depth in KPP is similar at all three resolutions in this test and in the previous test. Further, the profiles of diffusivity and non-local source term are very similar at the differing resolution (not shown). Thus for a given gradient, there is less change in the temperature profile at coarse resolutions. Near a normalized depth of -0.5, there is a temperature gradient at coarser resolution. As the resolution increases, the temperature profile becomes more mixed. When we compute the heat flux $\left(\overline{w'\theta'} \equiv \kappa(\theta_z - \gamma)\right)$, it is larger near a normalized depth of -0.5 at coarser resolutions due to the presence of a temperature gradient.

4.3 Conclusions

At this point, we are able to draw three primary conclusions. First, the model proposed in the previous chapter seems to work well. There are a few caveats, such as the assumption of down-gradient fluxes and the slight under prediction of TKE at depth in high resolution simulations. Second, KPP seems to be more sensitive to changes in the vertical resolution than the new model. When the resolution becomes coarse in regions of very shallow mixed layer depths, KPP mixes much more than VVM-Aqua.

Finally, KPP outperforms the new TKE based model at high resolution in convective regimes, as we would expect. For shear driven regimes, it seems as though the new model proposed here works as well, if not better than KPP.

We believe that non-local effects can be included in the new model in a manner similar to that suggested by Kantha and Clayson (1994) or Cheng et al. (2002). This will be discussed later and implemented in a future version of the model.

Overall, the tests conducted in this chapter lead us to the conclusion that both models work well, with advantages and disadvantages to each. Therefore, we now turn our attention to an examination of how penetrating shortwave radiation influences the diurnal variability of the mixed layer. In the remainder of this work, we use the one-dimensional models exclusively, but will compare to previous studies and observations whenever possible.

Chapter 5:

The Effect of Turbidity on the Diurnal Cycle of the Ocean Boundary Layer.

As alluded to briefly in Chapter 1, the influence of variations in the penetration depth of shortwave radiation on the interseasonal ocean has been studied extensively in one-dimensional models (e.g. Denman 1973, Martin 1985, Kirk 1988, Simonot et al. 1988, Ohlmann et al. 1998, Strutton and Chavez 2004) and three-dimensional models (e.g. Schneider and Zhou 1998). These studies have used the two band exponential profile of irradiance (equation 1.1), with fixed coefficients.

There has been a movement away from fixed extinction coefficients in the past decade. The extinction coefficients are assumed to be functions of the spatial and temporal distribution of chlorophyll (e.g. Morel and Maritorena 2001, Manizza et al. 2005, M05).

Nakamoto et al. (2001) and Murtugudde et al. (2002) were the first to simulate the

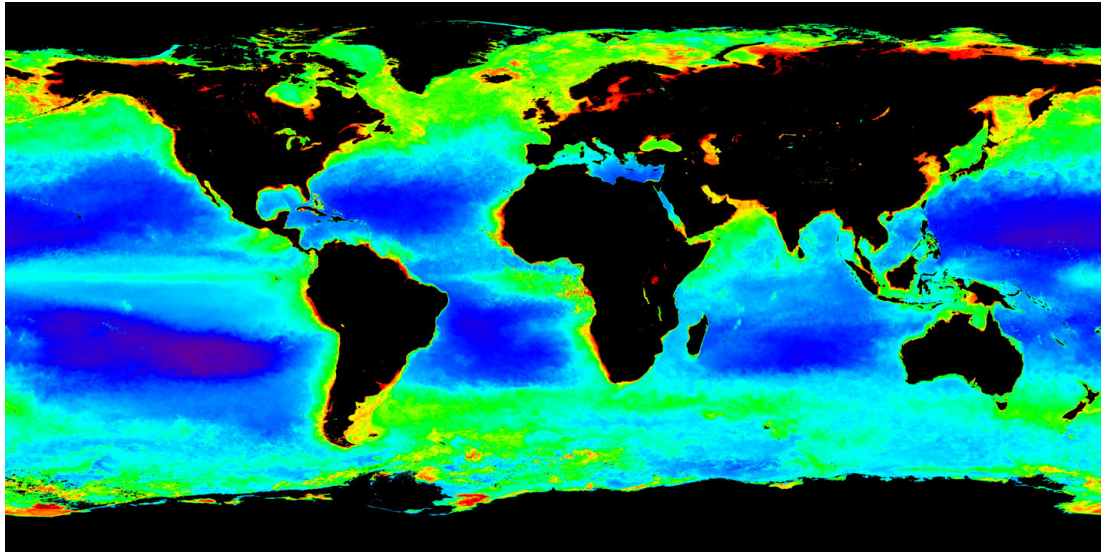


Figure 5.1 - Annual composite (2009) of surface chlorophyll observed by SeaWiFS. Green colors are high chlorophyll and blue is low chlorophyll. Figure is taken from oceancolor.nasa.gov

influence of surface chlorophyll on SST, surface salinity, and momentum. Using a very

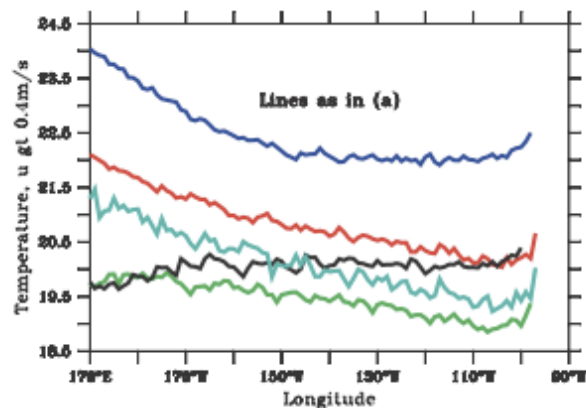


Figure 5.2 - Temperature of water in the Equatorial undercurrent for different strengths of chlorophyll forcing. Taken from GA09, their Figure 6c.

simple regional three-dimensional model, Nakamoto et al. (2001; N01) found that the eastern tropical Pacific cools when surface chlorophyll is included in the model (a result confirmed by Manizza et al. 2005 and Gnanadesikan and Anderson 2009; GA09). This is

a counter-intuitive result. The cool eastern Pacific SST is caused by upwelling of cold, nutrient rich water. Therefore, this region is fairly high in chlorophyll (see Figure 5.1).

In a region of high chlorophyll the direct effect is warming, yet many find surface cooling. The cooling observed in N01, M05, and GA09 is understood by Figure 5.2, which is taken from GA09 (their Figure 6c). This figure plots the temperature in the Equatorial undercurrent (EUC) for many different chlorophyll tests. We are focusing on the blue curve, which is the test that excludes chlorophyll, and the full chlorophyll run (green curve). When chlorophyll is included, the temperature in the EUC is much colder than in the run with fixed penetration depths. The colder water in the EUC eventually upwells on the eastern boundary, causing a cold anomaly relative to the clear run. Most interestingly, the temperature of waters in the EUC is most dependent on penetration depths in the relatively clear subtropical gyres (Anderson et al. 2009).

The cooling of the eastern tropical Pacific observed in N01, M05, and GA09 is not robust. Murtugudde et al. (2002) using a similar ocean model as N01, but a simpler atmospheric model found a warming in the eastern tropical Pacific. It is possible that the simple regional simulation of Murtugudde et al. (2002) is not correctly simulating the water flowing into the EUC. In M05 it is briefly mentioned that use of a different irradiance parameterization results in a warmer tropical Pacific.

The irradiance parameterizations used in N01, M05, and GA09 can be used to allow the extinction coefficient to vary vertically as well, but an ecosystem model is required for simulations longer than a few weeks. Even with predicted phytoplankton (M05), which can be used as a chlorophyll proxy, the result is similar to GA09.

Although vertical distributions of chlorophyll had a limited impact on the interseasonal variability of currents, temperature, and salinity, it is possible that an effect could be seen on shorter time scales.

Lewis et al. (1983) argued that phytoplankton distributions can cause a distribution of shortwave heating that could create static instability. The observed vertical distribution of phytoplankton has a subsurface maximum (Figure 5.3). If this

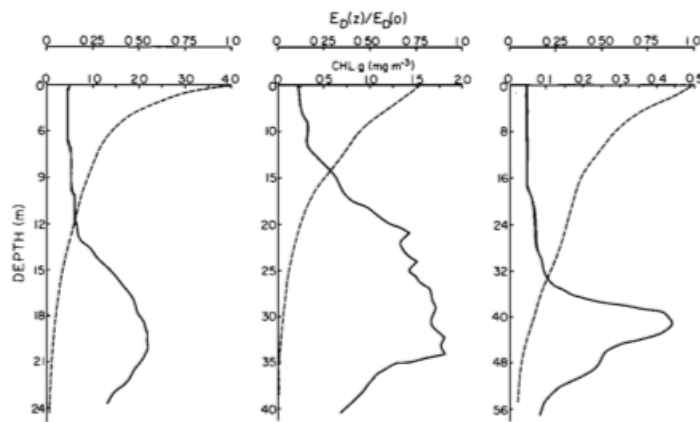


Figure 5.3 - Observed chlorophyll distributions. The left figure is near the Southern California coast, the middle is from the Scotian shelf, and the right profile is taken near the Azores. Figure taken from Lewis et al. (1983), their Figure 4

maximum is close enough to the surface, and the waters above the maximum are optically clear, unstable stratification can result. In other words, the shortwave radiation passes through the top portion of the ocean with minimal heating, and then encounters the chlorophyll maximum, creating a strong local heating. If the distribution persists long enough, the surface layer could become cooler than the water below.

Despite some uncertainty in the influence of chlorophyll on the ocean circulation, we can draw two conclusions from previous research. First, variations, both in space and

time, of penetrating shortwave radiation are important to the climate system. Second, models are sensitive to the specific parameterization of attenuation.

A detailed re-examination of how the climate responds to variations in shortwave radiation penetration is beyond the scope of this research. However, previous literature has only briefly examined the response of the ocean to variations in turbidity on intraseasonal time-scales. Denman (1973) only examined changes in mixed layer depths and SST for two different Jerlov water types over a few days. Simonot et al. (1988) simulated the SST and MLD for OWS Romeo and Papa over a two year period. To the best of our knowledge, no studies have examined how profiles of turbulence and mixing change for differing strengths of turbidity. Further, studies that have considered the spatial variability of turbidity only consider climate time scales. The diurnal to intraseasonal response has not been examined in detail.

In this chapter, the simulations will use the one-dimensional model developed in this work and KPP. Even though the model we have developed is particularly well suited for the simulation of nutrient flow into the boundary layer (recall that nutrient flow is dominated by the entrainment rate), the inclusion of a moderately simple NPZD (Nutrient-Phytoplankton-Zooplankton-Detritus) model is beyond the scope of this work. This is why we only consider a short one week run.

The final complication of using a one-dimensional model to study the influence of penetrating shortwave radiation on the tropical Pacific is the lack of an equatorial undercurrent (EUC). Prior to presenting the results of our tests, we discuss how the EUC is maintained in the one-dimensional models.

5.1 Large Scale forcing

In two and three dimensional simulations driven by surface wind stress, a surface zonal pressure gradient is balanced at the equator by a strong return current at depth. To include the equatorial undercurrent in our one-dimensional model and KPP, we utilize the large scale forcing terms derived for the studies of Wang et al. (1998; W98) and Large and Gent (1999; LG99). The forcing terms are derived from a combination of observations and model output (for details, see W98). The equations for the one-dimensional models become

$$\begin{aligned}\frac{\partial u}{\partial t} &= -\frac{\partial \overline{u'w'}}{\partial z} + G_u \\ \frac{\partial v}{\partial t} &= -\frac{\partial \overline{v'w'}}{\partial z} + G_v \\ \frac{\partial \theta}{\partial t} &= -\frac{\partial \overline{w'\theta'}}{\partial z} + H_T.\end{aligned}$$

The large scale terms are given by G_u, G_v , and H_T . Their explicit functional forms are given as

$$\begin{aligned}G_u &= -uU_x - wU_z - P_x + F_u \\ G_v &= -vV_y - wV_z \\ H_T &= -uT_x - wT_z + F_T.\end{aligned}$$

In these three equations, lowercase values are model predicted quantities and uppercase are large scale terms. In these simulations (and those in W98) salinity is fixed in the vertical and in time.

The initial conditions of zonal velocity and temperature, which are typical of the western tropical Pacific, are shown in Figure 5.4a and 5.4b respectively. The profiles of

the components of the large scale forcing terms are shown in Figures 5.4c-f. In these

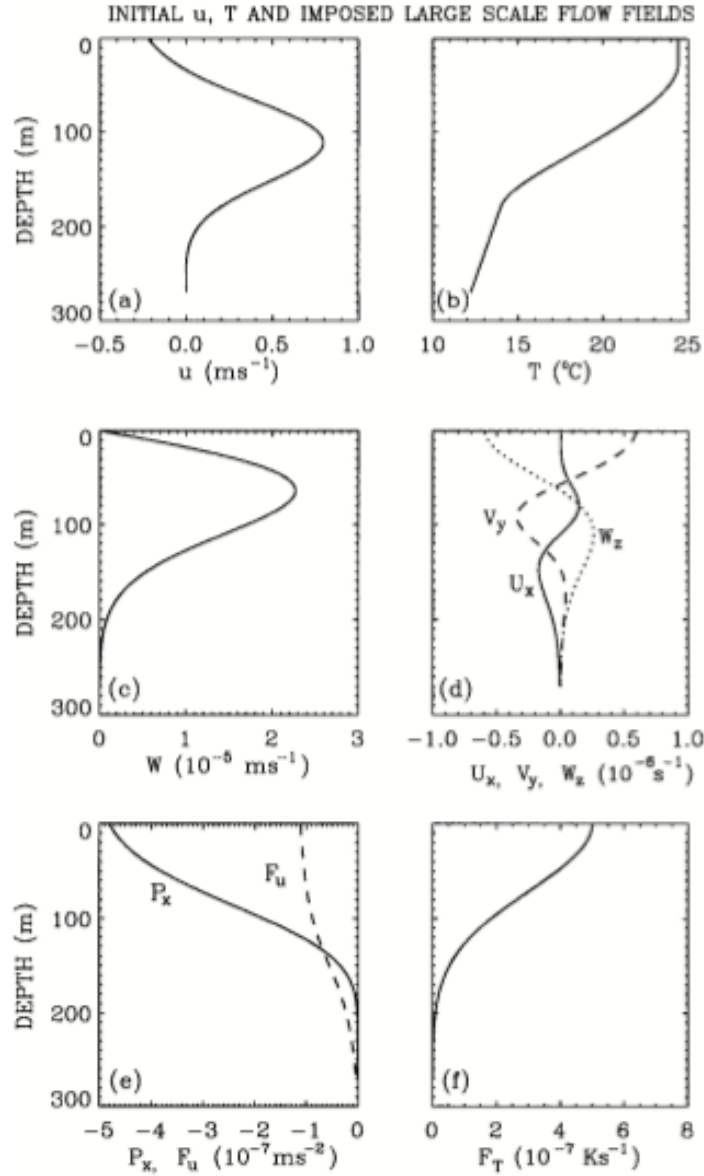


Figure 5.4 - Initial profiles of (a) zonal velocity, (b) temperature, (c) large scale vertical velocity, (d) divergence, (e) large scale pressure gradient (solid line) and eddy forcing term in the zonal momentum equation (dashed line), and (f) eddy forcing for the temperature equation. Taken from Wang et al. (1998) their Figure 1.

figures, and in the definition of the large scale forcing terms, F_u and F_T are the eddy fluxes of momentum and temperature due to the large scale flow.

In these test cases, the model is run for seven days. A constant cooling (-200 Wm^{-2}) and surface friction velocity ($u_* = 0.0064 \text{ ms}^{-1}$) is included, which is close to observed values (Moum et al. 1989). The diurnal cycle of shortwave radiation is given by

$$I_S(t) = 776 \sin[(2t - 0.5)\pi] H[\sin[(2t - 0.5)\pi]],$$

where H is the Heaviside function. The depth profile of irradiance is written as

$$I(z, t) = I_S(t) \{0.6e^{-z} + 0.4e^{-k_{vis}z}\}.$$

In the different tests, k_{vis} will be varied. The simulations will be conducted at 10 meter resolution and 4 meter resolution, which can be thought of as a practical upper bound for the vertical resolution of a large scale ocean model.

We have conducted sensitivity tests that alter the partitioning of infrared and visible radiation in the irradiance equation within the bounds given in Paulson and Simpson (1977) and found minimal differences.

5.2 Baseline Simulation

In this run, k_{vis} is set to $1/17 \text{ m}^{-1}$. The temperature profiles through time for the new model, KPP, and the result from W98 (their Figure 2) are given in Figure 5.5⁶. The LES result is plotted in Figure 5.5a, the result from the new model⁷ and KPP are presented in 5.5b and 5.5c respectively.

⁶ Our runs are seven days and W98 only ran for six days, hence the offset in the three figures.

⁷ In the rest of this chapter, the output from the new model is interpolated to a uniform grid using a spline routine from Matlab.

The initial observation is that the large scale forcing terms derived in W98 are not perfect at balancing the energy input at the surface. The thermocline continues to deepen,

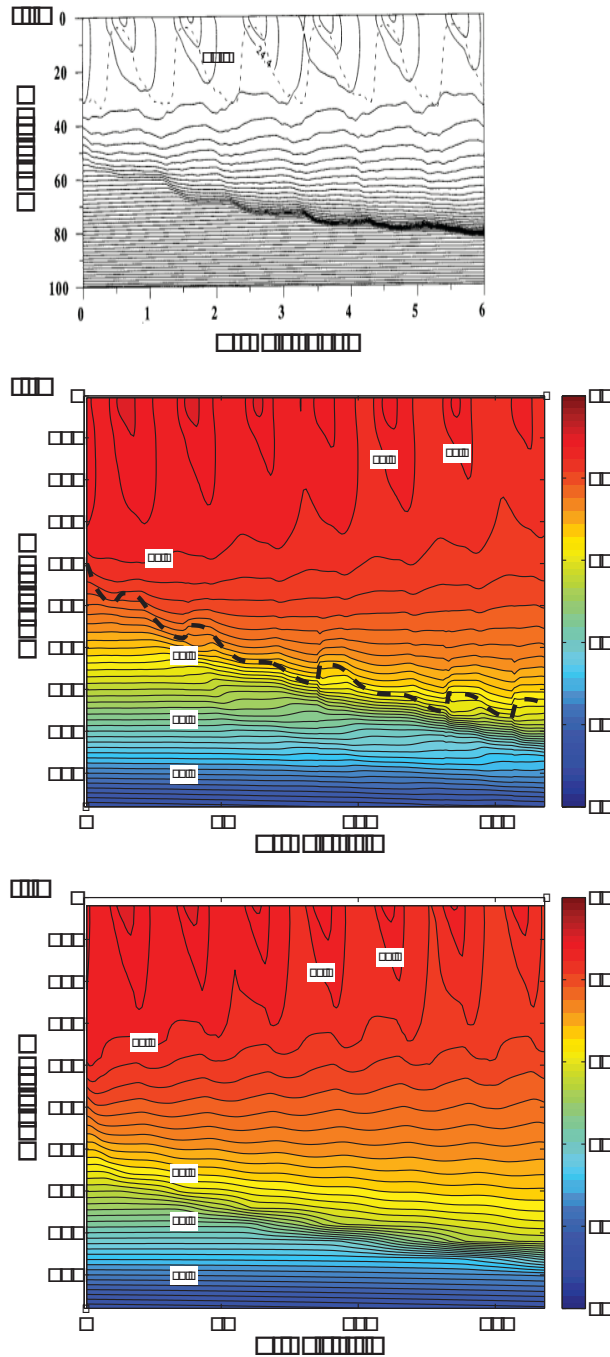


Figure 5.5 - Temperature profiles through time from LES output of W98 (a), the new model (b), and KPP (c). The contour interval in every plot is 0.1°C . The plots have been sized and offset such that the length of the run in W98 matches that conducted here.

even at the end of the sixth day of the LES run. However, the rate of deepening has

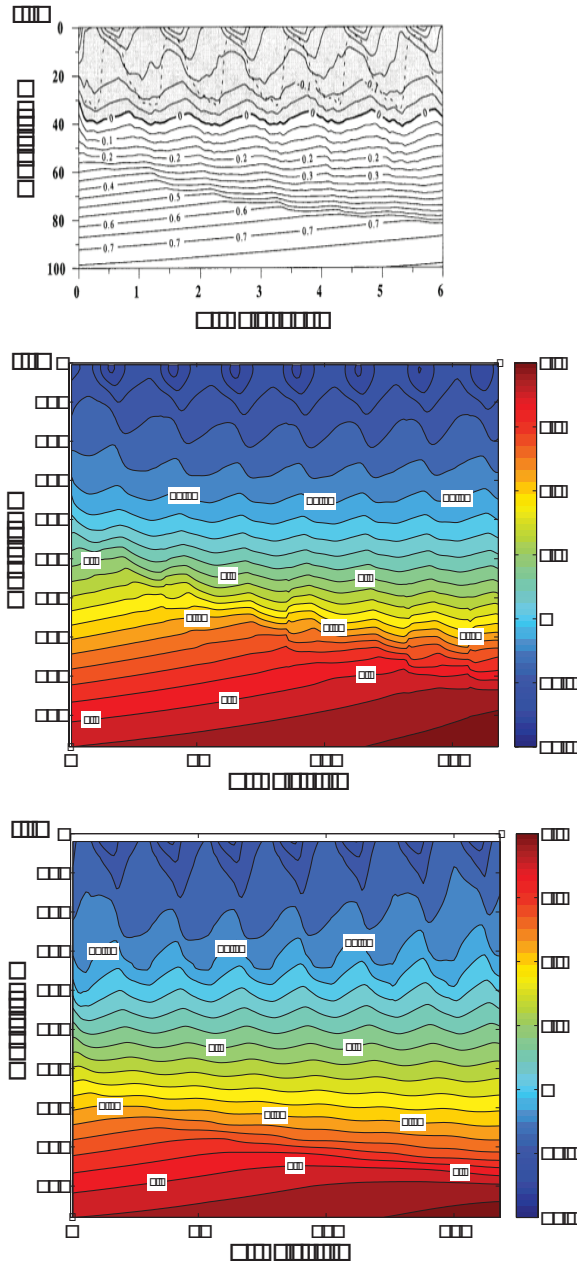


Figure 5.6 - Zonal velocity profiles through time from LES output of W98 (a), the new model (b), and KPP (c). The contour interval in every plot is 0.05 ms^{-1} . The plots have been sized and offset such that the length of the run in W98 matches that conducted here.

slowed and the mixed layer exhibits a regular diurnal cycle (dashed line in Figure 5.5a).

In Figure 5.5b, we have plotted the depth of the boundary layer predicted by the new model (dashed black line). This line is slightly shallower than the thermocline

predicted by the new model (and the thermocline predicted by LES). This highlights the difference between the boundary layer depth and mixed layer depth. The mixed layer is much shallower, oscillating between 30 meters and 5 meters depth for this run, while the boundary layer continues to deepen. Thus as previously argued, the model framework laid out in Chapter 3 predicts the depth of the boundary layer, and not the depth of the mixed layer (unless they are equal).

In a general sense, the comparison between the three models is good. The depth of the thermocline at the end of day 6 (hour 144) in KPP and the new model nearly match LES. In the upper ocean, KPP is predicting more mixing, and thus cooler temperatures than the other models. The 24.3°C isotherm surfaces during the nighttime cooling phase of day four in W98 and the new model, while in KPP it surfaces the previous day. The new model predicts a weaker mixing of temperature when compared to the other models. If we again examine the 24.3°C isotherm, but on day three in the new model (Figure 5.5b) and LES (Figure 5.5a), the isotherm is deeper in the new model compared to W98.

The zonal velocity profiles through time are shown in Figure 5.6. The LES result is Figure 5.6a, the new model is Figure 5.6b, and KPP is 5.6c. By the end of day six, the zonal velocity near the core of the EUC (~100 meters) has increased to slightly over 0.8 ms^{-1} in all models. In all the models, the zonal velocity has a strong diurnal cycle in the upper 30 meters. During the day, turbulence decreases and the surface momentum input is confined near the surface. Once convection begins, the strong stratification near the surface erodes, and this region couples to the fossil mixed layer below. This allows the momentum to be rapidly mixed.

It seems that the new model is doing a slightly better job at simulating the velocity field than KPP. The 0.75 ms^{-1} isotach approaches 85 meters depth at the end of

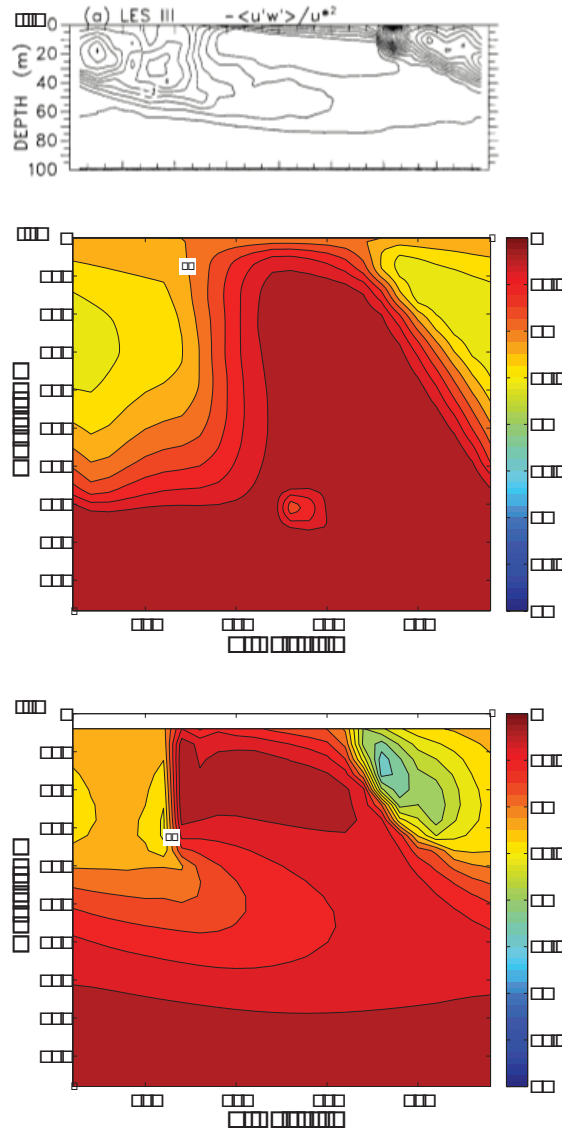


Figure 5.7 - $\overline{u'w'}/u_*^2$ profiles from day six from LES output of W98 (a), the new model (b), and KPP (c).

The contour interval in every plot is 0.2.

day 6 in W98 and the new model but in KPP it is at 90 meters depth.

The momentum flux, which has been normalized by u_*^2 , is plotted in Figure 5.7.

In general, the KPP flux (Figure 5.7c) is closer to the LES result (Figure 5.7a) than the

new model (Figure 5.7b). During the daytime (hours 126 - 138), KPP simulates the momentum flux at depth better than the new model. The TKE predicted by the new model (not shown) is nearly zero at depth during the daytime, which implies that the momentum flux is also zero. It seems that the TKE is overly dissipated at depth in the new model. This suggests that the dissipation length scale used in the new model may have to be reevaluated. When the solar heating ceases, KPP simulates the rapid mixing seen in the LES, while the new model does not do as well. This discrepancy may be due to unrepresented processes in the one-dimensional model. Gravity and internal waves are simulated in the LES model. Since there is a shear layer near the thermocline, these waves could break and increase the momentum and heat flux at depth. Even though KPP has this slow decay of turbulence at depth, it may be the right answer for the wrong reason. This could be anomalously strong mixing that looks similar to the LES result. We are running the W98 simulation in VVM-Aqua to analyze the structure of the momentum and heat fluxes in more detail.

Despite these shortcomings, the new model solution is better than KPP in certain areas. For example, during the transition from night to day, the new model maintains the momentum flux in the upper ocean longer than KPP. In addition, even though the momentum flux does not become very strong as the sun sets, it spins up a flux that becomes stronger and closer to LES at the end of the day than KPP.

These observations hold true for the heat flux as well (not shown). It seems that the new model is slower at spinning up fluxes than KPP and LES, but maintains fluxes more effectively in the transition from night to day than KPP.

5.2.1 Resolution comparisons

Figure 5.8 shows the result from an identical simulation as that conducted in the

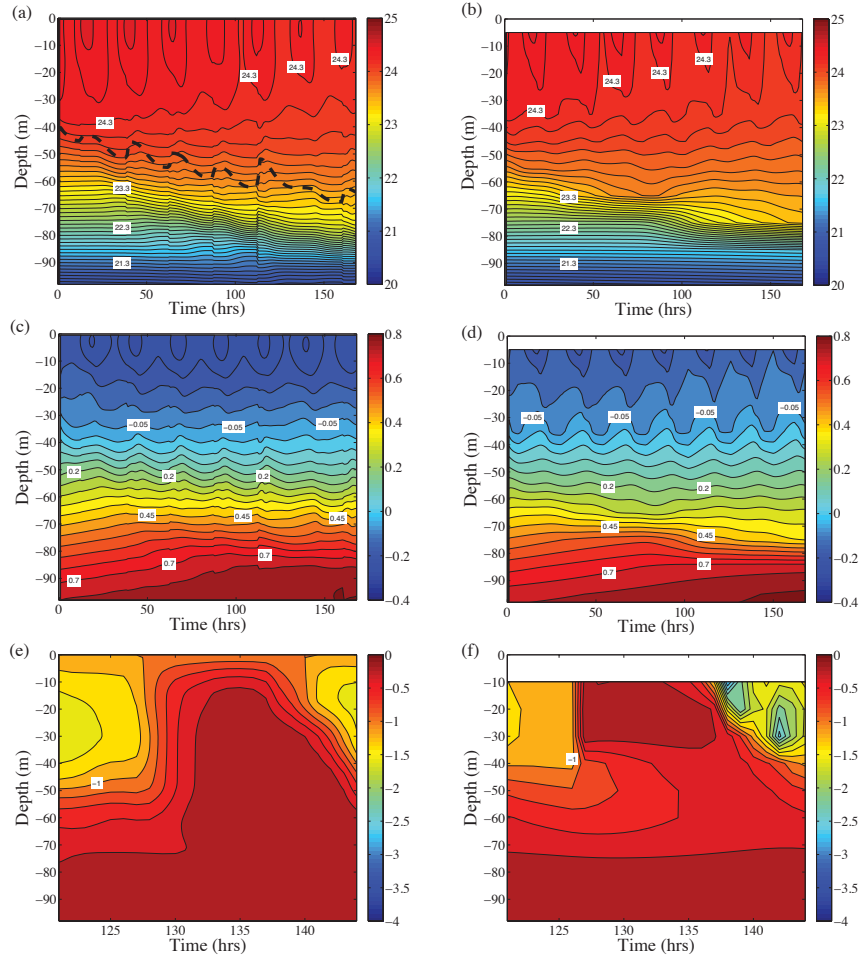


Figure 5.8 Time-depth profiles of temperature for the new model (a) and KPP (b). Zonal velocity for the new model (c) and KPP (d), and Normalized momentum flux for the new model (e) and KPP (f). The results from the new model are interpolated to a uniform grid and KPP is not, this accounts for the white space in the plots in the right column.

previous section, but at 10 meter resolution. Here the left column is the new model and the right is from KPP. The results for the temperature field are similar to those seen in Figure 5.4bc. Again, the upper ocean temperature in KPP (Figure 5.8b) is overly mixed, while the new model is less mixed (Figure 5.8a). The boundary layer depth at this resolution (dashed line in Figure 5.8a) is slightly shallower (by about five meters) than

that simulated at four meter resolution at the end of day seven. The thermocline in both models at day seven is near a depth of 80 meters.

The zonal velocity profile for KPP (Figure 5.8d) below the surface is similar to that in Figure 5.6c. Near the surface, the velocity is weaker in both models. As in the previous test, the momentum is more mixed in the new model (Figure 5.8c) than KPP.

The momentum fluxes for the new model (Figure 5.8e) and KPP (Figure 5.9f) are fairly similar to those at four meter resolution. Again, the new model does not have the fluxes at depth during the daytime that are seen in KPP. The strong fluxes that occur as the layer influenced by the diurnal cycle rejoins the mixed layer from the previous night are again absent in the new model. We believe that this is due to the lack of non-local effects. During the daytime, mixing is down-gradient (the turbulent eddies are small), but once the upper ocean couples with the fossil mixed layer, the eddies are large and non-local effects become important.

LG99 conducted identical runs to W98 with an older version of KPP and a down-gradient mixing scheme described in Gent (1991), which is a modified form of Pacanowski and Philander (1981). When the down-gradient, Richardson number based, scheme is used the large fluxes at the onset of convection are absent (see Figure 4c or 5c of LG99). This is similar to what is seen in the new model.

5.3 Sensitivity Tests

Although the diagnosed fluxes from the new model are weaker than KPP and LES, the model temperature and velocity fields are similar. With a base state in hand, we move on to examine how the simulated fields change as the parameterization of

penetrating shortwave radiation changes. In all of our tests, the irradiance at depth is governed by the dual band exponential form discussed in previous chapters.

The key parameter we vary in these tests is $k_{VIS}(z,t)$. In particular, we examine three parameterizations for this extinction coefficient. In the first set of tests, k_{VIS} is fixed to a constant value. The second parameterization, which follows GA09 and M05, is given as $k_{VIS}(z,t) = 0.0232 + 0.074Chl(z,t)^{0.674}$ where Chl is the Chlorophyll concentration (mg L^{-1}).

The third parameterization is $k_{VIS}(z,t) = 0.025 + 0.101Chl(z,t)^*$. In this equation, Chl^* is a normalized passive tracer, which can be taken as Chlorophyll. This parameterization is a linear fit through the five Jerlov water types (Jerlov 1968, Paulson and Simpson 1977). When the normalized tracer is zero, the resulting extinction coefficient is equal to very clear water ($k_{VIS}^{-1} = 40m$), as the normalized tracer goes to one, k_{VIS} approaches Jerlov type III water. This parameterization will cause the strongest response for a given level of passive tracer.

These two parameterizations require an input profile of chlorophyll. For the GA09 formulation, we use a tropical Pacific profile of chlorophyll from the 2005 World Ocean Atlas data set (Boyer et al., 2006). For the latter parameterization, we construct a very simplified profile that is zero at the surface, moves to a normalized value of one at a depth of eight meters and returns to zero at 30 meters. This profile is designed to test the

assertion of Lewis et al. (1983) that certain profiles of chlorophyll can cause unstable

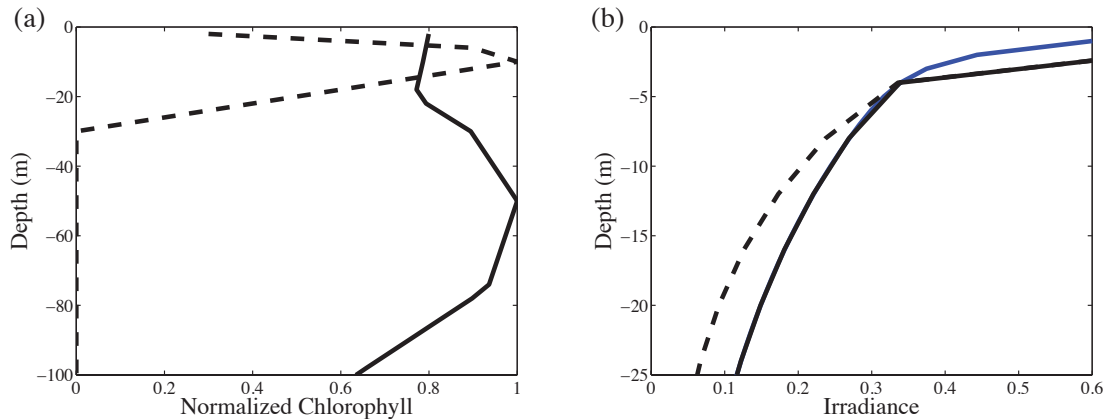


Figure 5.9 - Profiles of Chlorophyll normalized by their respective maximums (a) and their resulting irradiance profiles (b). In these figures, the black line is from observations, and the dashed line is constructed. In (b) we have plotted the irradiance profile resulting from a constant $k_{VIS} = 0.05 \text{ m}^{-1}$.

stratification.

The two normalized profiles of chlorophyll are shown in Figure 5.9a (the observed profile is Black, and the constructed profile is dashed). The resulting irradiance profile, computed from their respective equations, is shown in Figure 5.9b. In this figure, we have included another curve (blue) that results from fixing the visible extinction coefficient to 0.05 m^{-1} .

There are still some ocean GCMs that assume that all of the incident surface shortwave radiation is absorbed in the top layer. Therefore, the final sensitivity test conducted invokes this assumption. In Section 5.2.1 we found that the model result at four meter resolution is not very different from that at ten meter resolution.

All the sensitivity tests we discuss in this Chapter are conducted at four meter resolution. The one exception is this final test. There is a non-negligible difference between a run with all of the shortwave radiation being absorbed in the top four meters than one with the radiation being absorbed in the top 10 meters.

In Figure 5.10, we plot the change in temperature from a given sensitivity test to the baseline simulation for the new model. In Figure 5.10a, the coefficient of extinction for the visible band is fixed to 40 m^{-1} (hereafter referred to as low k). In the top 40 meters, the temperature is cooler when the extinction coefficient is reduced. Since we allow heating to penetrate to deeper depths, there is less heating near the surface. When the sun sets convection begins sooner and lasts longer due to the decreased stratification.

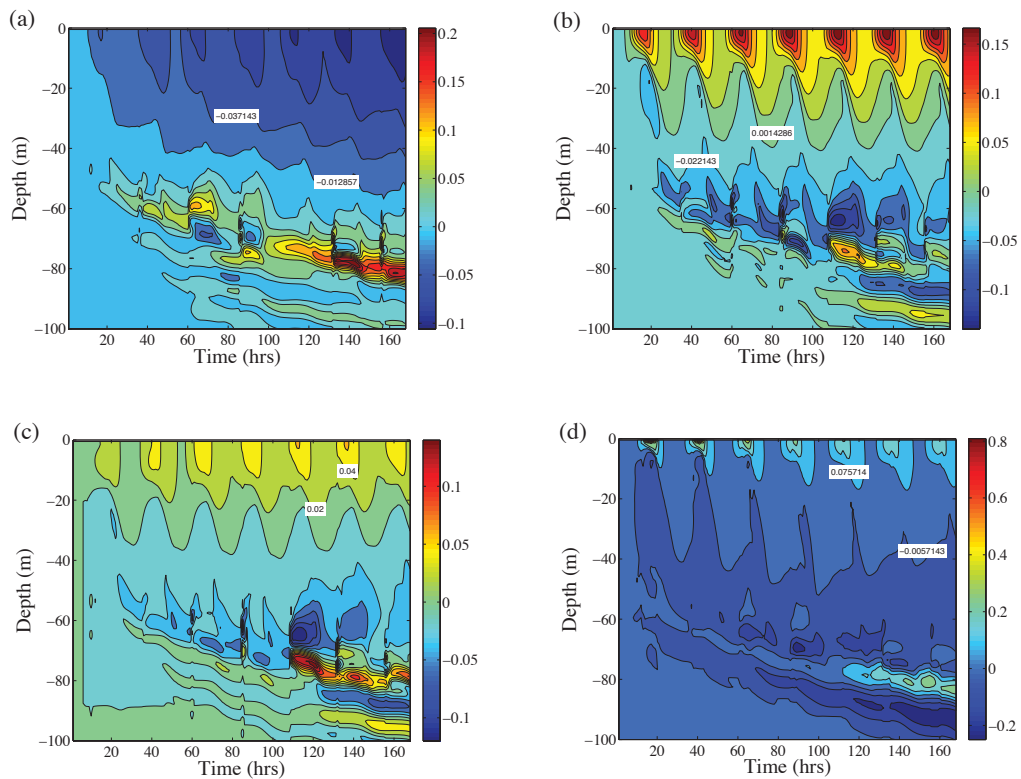


Figure 5.10 - Profiles of simulated temperature anomalies ($^{\circ}\text{C}$) relative to the four meter resolution control run for (a) low k , (b) high k , (c) Chlorophyll II, and (d) top simulations. The Chlorophyll I anomalies are very small and are not plotted.

This results in the negative anomalies near the surface.

At slightly deeper depths, there is a warm anomaly that deepens throughout the length of the run. This is related to the position of the top of the thermocline in the low k

simulation versus the depth in the control run. If the thermocline is deeper in this run, warmer temperatures exist at deeper levels than in the control simulation.

When the extinction coefficient is increased to 5m^{-1} (hereafter high k), the resulting temperature anomalies (Figure 5.10b) are essentially the opposite of Figure 5.10a. Now we are confining much more heating to the surface, which results in a positive anomaly. The penetration of heat to deeper depths is the result of the nighttime cooling, which will mix out a portion of the increased surface heating. The cold anomalies increasing with depth are what would be expected from a shallower thermocline. However, the slight warm anomalies near hour 110 are unusual. Near hour 100, the boundary layer depth from the high k simulation is slightly greater than that from the control run. This could explain the warm anomaly. The overlying cold anomaly could be a result of the decreased heating at this depth. It is also possible that the virtual mass flux scheme is causing some of the anomalies, where differing entrainment/detrainment rates cause different amounts of numerical diffusion.

The temperature anomalies from the Chlorophyll II test relative to the control run are shown in Figure 5.10c. The basic picture is very similar to what is shown for the high k test. This test suggests that the vertical profile of chlorophyll does not have a significant impact on the temperature profiles.

In this simulation, we again see the warm anomalies near 80 meters depth and hour 110. Despite the unusual anomalies at depth, the basic picture is that when the extinction coefficient is increased. More heat is trapped near the surface and the thermocline is shallower.

When the solar radiation is confined to the top model level (hereafter top simulation), the surface temperature is much warmer ($\sim 0.8^\circ\text{C}$) and the thermocline depth

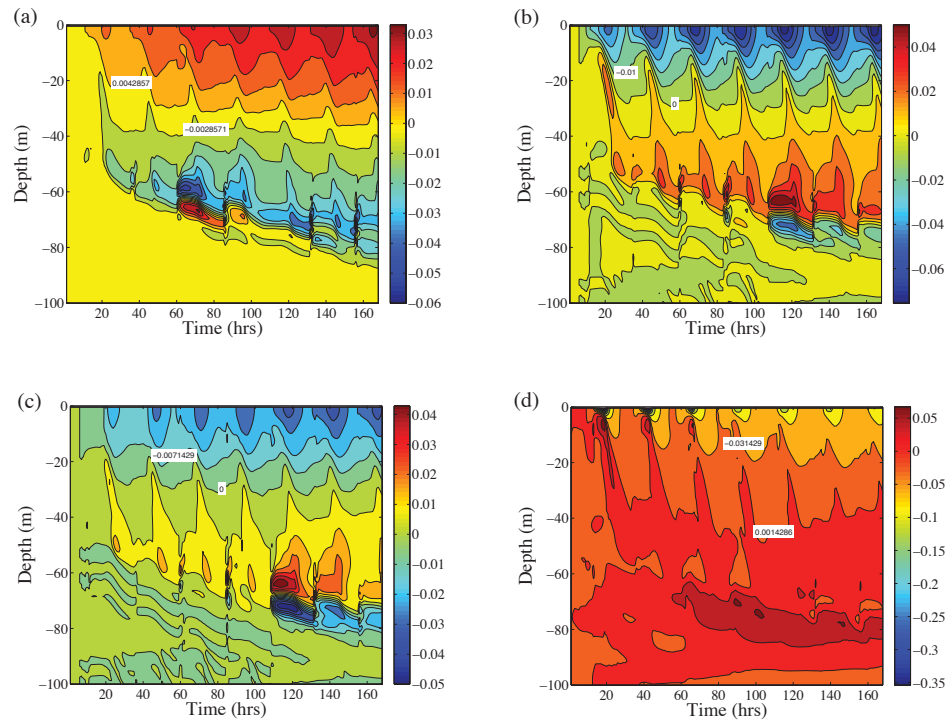


Figure 5.11 - As in Figure 5.10, but for zonal velocity

is much shallower in this test.

The change in temperature and velocity in the Chlorophyll I simulation from the control is very small and is not plotted.

The change in zonal velocity for the sensitivity tests relative to the control simulation is shown in Figure 5.11. In the low k simulation (Figure 5.11a), the near surface velocity is greater than in the control run. The surface momentum input, which is negative, is not as effective in balancing the imposed large scale pressure gradient. The momentum near the surface is easier to mix in the vertical due to the decreased stratification. The pressure gradient dominates the wind forcing.

Near the thermocline, the velocity anomalies become negative. This is due to the decreased stratification in the low k simulation. During the daytime, the mixing is stronger in the low k simulation. This causes the negative anomaly in the region of the thermocline.

In the high k test, the picture is reversed. Now the velocity near the surface is more easterly. Increased surface stratification and decreased mixing traps more negative momentum near the surface. At depth, the velocity is stronger in the high k run than in the control simulation. With less mixing during the daytime, the zonal velocity is dominated by the large scale forcing, which is positive. Therefore, the zonal velocity is more westerly in the high k test.

As seen in the temperature field, the velocity anomalies from the Chlorophyll II test relative to the control run behave similar to the high k test, although the response is weaker. The irradiance profile in Figure 5.9b (dashed line) does not exactly behave like a constant exponential, but a best fit constant coefficient profile is achieved for $k_{vis} = 0.1 \text{ m}^{-1}$.

The top simulation has the strongest surface anomalies of all the sensitivity tests. As in the temperature fields, the surface anomalies weaken during the length of the run. This is due to the deepening of the predicted boundary layer depth. Recall that as the boundary layer deepens, the thicknesses of the model layers within the upper ocean expand and the shortwave radiation is absorbed over a larger layer.

The temperature anomalies relative to the KPP control run are shown in Figure

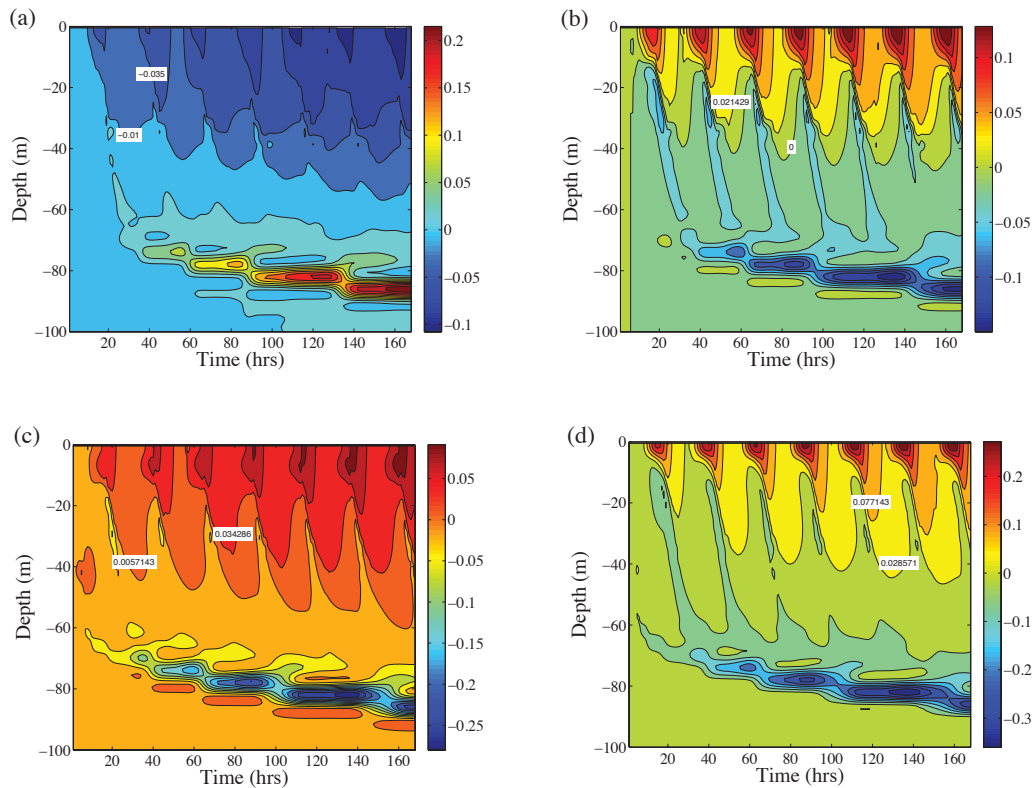


Figure 5.12 - As in Figure 5.10, but for KPP.

5.12. Again, we have not plotted the response from the Chlorophyll I simulation, as the resulting anomalies were very small.

The basic response for decreasing the extinction coefficient (low k , Figure 5.12a) is similar to what was seen in the new model. The temperature is cooler near due to the increased penetration of shortwave radiation. The warm anomalies at depth are again caused by a deeper thermocline compared to the baseline result.

In Figures 5.12bc, which are the high k and Chlorophyll II anomalies respectively, the near surface temperature is warmer than the control and the temperature near the thermocline is colder. This was seen in the new model framework, except we do not see the warm anomalies beneath the cold anomalies present in Figures 5.12bc. The vertical

variation of observed chlorophyll has a minimum impact in KPP, as we have seen in the new model result.

In the KPP top simulation (Figure 5.12d), the response behaves similarly to what

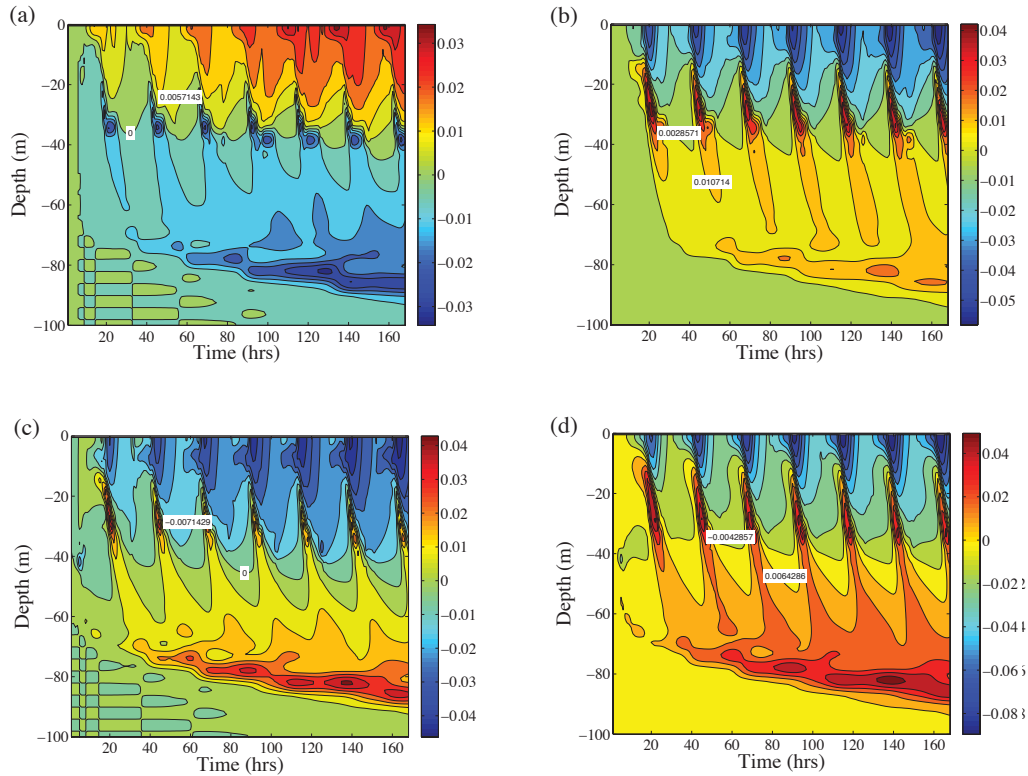


Figure 5.13 - As in Figure 5.11, but for KPP.

is seen in Figure 5.12b and 5.12c. The response is weaker than that observed in the new model. This is due to the collapse of the boundary layer in the new model top test. When the boundary layer collapses, the surface is strongly heated. Despite the differences in the magnitude of the new model and KPP responses, the general picture is similar for the two models. The surface is warmer and the thermocline is shallower than in the control simulation.

The zonal velocity anomalies for the sensitivity tests in KPP are shown in Figure 5.13. In the low k test (Figure 5.13a), the zonal velocity anomaly is positive near the

surface and negative at depth, which is what was seen in the companion simulation conducted in the new model. One difference seen in Figure 5.13a, which is partially evident in Figure 5.11a, is the extension of the negative velocity anomalies at depth toward the surface. These fingers are evidence of the joining of the surface layer and the decoupled mixed layer. With a weaker near surface stratification at sunset in the low k run convection occurs sooner than in the control simulation. The easterly momentum input at the surface mixes downward earlier in the day than in the control simulation, which decreases the momentum at depth when compared to the baseline simulation.

The opposite occurs when the extinction coefficient is increased (Figure 5.13b). The stronger stratification near the surface allows static stability to remain longer into the night. This results in the positive anomalies at mid depths (approximately 20 to 50 m) in the three remaining runs. The increased strength of these structures compared to the new model result is most likely due to the non-local forcing in KPP.

Near the surface, the velocity anomaly is negative during the daytime in the high k , Chlorophyll II (Figure 5.13c), and top (Figure 5.13d) simulations due to the strong surface stratification. The anomalies at depth in these simulations are the result in the differences in the depth of the thermocline in the sensitivity test and the control run.

The general result is that decreasing the penetration depth of solar radiation limits the thermocline depth, warms the surface, and the zonal velocity becomes more easterly. Further, we have seen a very limited dependence of the temperature and velocity fields on the vertical distribution of chlorophyll.

5.3.1 Resolution dependence

In this section we examine the influence of coarsening the resolution in the Top sensitivity test. We expect that the resolution will influence the temperature and velocity fields respective to the baseline simulation. If we coarsen the resolution to 10 meters, the surface shortwave radiation is distributed over more than double the thickness as that in the original top simulation.

In this section, the anomalies are computed relative to the baseline simulation run at 10 meter resolution (Figure 5.8). The resulting temperature and velocity anomalies for

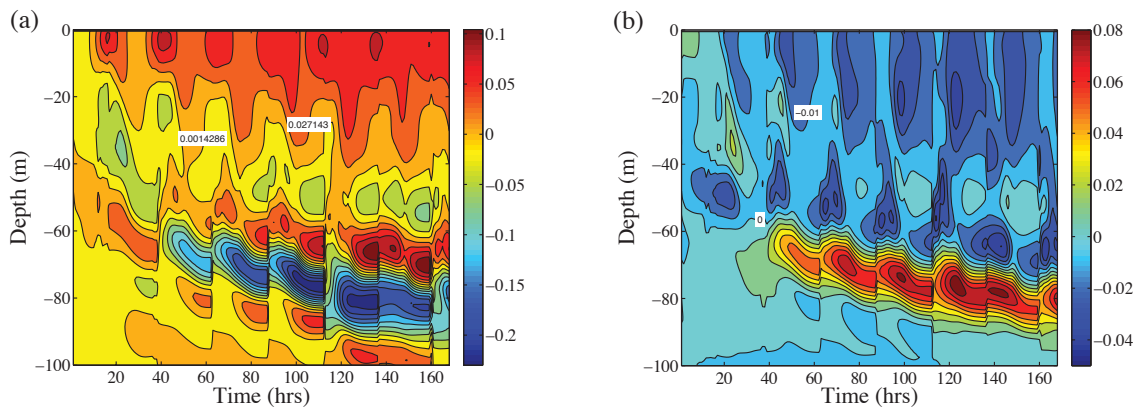


Figure 5.14 - Profiles of simulated temperature anomalies (a) and velocity (b) at ten meter resolution relative to the ten meter control run for the top test.

the new model are shown in Figures 5.14a and 5.14b respectively.

The temperature anomalies near the surface (Figure 5.14a) are not as positive as the top test at four meter resolution (Figure 5.10d). This is an expected result.

The temperature anomalies at depth are not as similar to what is seen in Figure 5.10d. We now see a tri-polar structure (warm anomalies under cold anomalies under a different warm anomaly). The lowest temperature anomaly is very weak (less than 0.05 °C), but the overlying anomalies are of order 0.1°C.

A close examination of the raw fields show that the thermocline deepens in the baseline simulation sooner than in the top simulation. The deepening of the thermocline brings warmer water to greater depths. This creates a negative temperature anomaly in Figure 5.14a. When the thermocline deepens in the top simulation, the upper ocean water that moves downward is warmer than in the baseline simulation, which leads to the

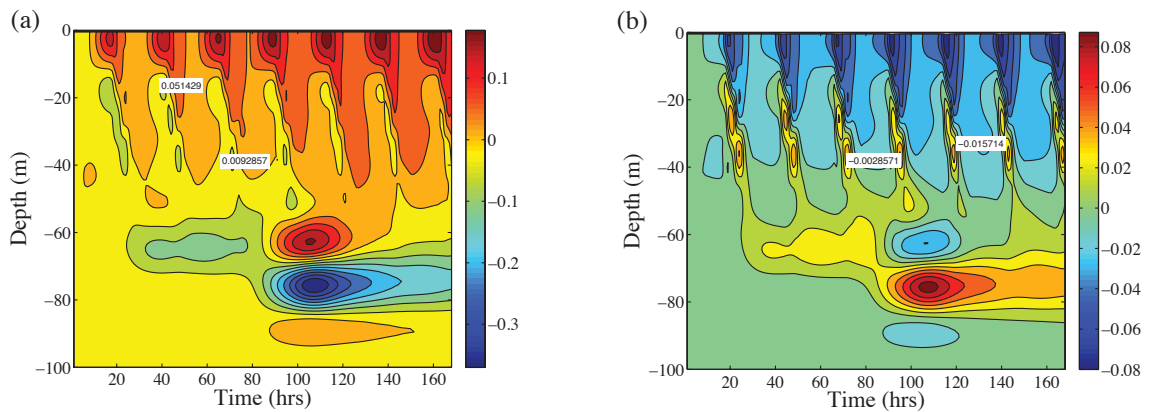


Figure 5.15 - As in Figure 5.14, but for KPP.

positive anomalies at a given depth.

The zonal velocity anomalies, which are shown in Figure 5.14b, are similar to Figure 5.11d near the surface (with a smaller magnitude). We now have a slightly different behavior at depth when compared to Figure 5.11d. In the raw fields, we see that stronger westerly momentum from the EUC diffuses upward more than in the baseline simulation. As the thermocline deepens, the positive velocity anomaly is pushed downward. The thermocline deepens sooner in the baseline run than in the sensitivity test. This causes the positive anomalies in Figure 5.14b. When the thermocline deepens in the top simulation, the negative anomalies mix downward.

The final structure to address are the strong vertical lines that appear to be discontinuities in Figure 5.14. We believe that this could be an artifact of our

interpolation to a uniform grid. Use of a different interpolation method reduced the magnitude of these drastic shifts in the anomalies. Since large shifts in the boundary layer depths occur at the same time as these vertical lines in Figure 5.14 the grid is highly non-uniform. This magnifies any problems associated with interpolation.

The KPP anomalies for this simulation are shown in Figure 5.15. The qualitative result is the same as in the new model. It is important to recall that we cannot make a direct comparison to Figure 5.14 as the layer thicknesses are changing in the new model, but are nearly constant in KPP.

As in the top simulation at four meter resolution, the temperature anomaly (Figure 5.15a) near the surface is warmer in this test than in the control run. At depth we see the same qualitative pattern seen in Figure 5.14a. Near the beginning of the run at about 60 meters depth, the temperature anomaly is negative and then becomes positive. This is again caused by the thermocline depth simulated in each test. The thermocline deepens sooner in the baseline simulation than in the sensitivity test, which was also seen in the new model.

The zonal velocity anomalies, which are plotted in Figure 5.15b, are similar to Figure 5.13d, but with a smaller magnitude. In the upper 50 meters, the anomalies have the same structure seen in Figure 5.13d. Near the thermocline, the structure is similar to Figure 5.15a. The reason for the deep structure in the velocity anomalies is the same as discussed in relation to Figure 5.14b.

5.4 Conclusions

In this chapter we have used KPP and the new model framework to reproduce the results of W98 and LG99. As seen in LG99, down gradient models, such as the model developed here, do not accurately simulate the fluxes associated with the surface layer mixes joining the fossil mixed layer. However, the model constructed here better simulates the heat flux than the control model (Gent 1991) of LG99. In addition, certain portions of the momentum flux simulated by the new model are closer to the LES result of W98 than KPP. In these simulations, similar to what we have seen throughout this work, KPP tends to over-mix when compared to LES and the new model tends to under predict mixing, which is most likely attributable to the lack of counter gradient mixing.

The resolution dependence of the baseline simulation is relatively minor. In both models, the depth of the thermocline is slightly shallower in the coarser resolution simulation.

The primary influence of changing the penetration depth of shortwave radiation is a change in the depth of the thermocline. An increase in the surface stratification will decrease the time of active convection, which will decrease the energy at the boundary layer base available for entrainment. For this reason, it was not terribly surprising that the tests with the largest extinction coefficients have the shallowest thermocline depths.

The results presented here suggest that shortwave radiation must be allowed to penetrate beyond the top model layer. If the top model layer is 10 meters thick, forcing all the radiation to absorb in this layer is equivalent to an extinction coefficient of 2 m^{-1} , or Jerlov Mud (Jerlov, 1968). In this run, the upper ocean is much warmer than all the

other cases, but the thermocline depth is not as strongly impacted. The thermocline deepens to a depth similar to the control run, but the deepening happens at a later time. This result is consistent in both the new model and KPP.

If a model is designed with constant extinction coefficients for the visible spectrum, they must be chosen carefully to match the local water properties. This is a similar conclusion reached by Ohlmann et al. (1998), where it was argued that the extinction coefficients should be calculated from in situ water mass properties.

In the spirit of the argument presented in Ohlmann et al. (1998), we have conducted a few tests with differing optical parameterizations and chlorophyll profiles. When we use the parameterization of GA09 along with a profile of chlorophyll typical of the western tropical Pacific, the resulting temperature and velocity profiles are nearly the same as the baseline simulation. Since the observed profile of chlorophyll has very limited variability in the upper ocean, this test case is essentially a constant extinction coefficient case. In addition, the observed chlorophyll in the upper ocean results in a value of k_{VIS} that is nearly identical to that used in the baseline run. This is seen in the irradiance profiles in Figure 5.9b.

The second chlorophyll test is designed to maximize the potential response of the mean fields to variations in penetrating shortwave radiation. The profile is also designed to test the assertion of Lewis et al. (1983) that certain profiles of chlorophyll can create unstable stratification. The chlorophyll II test behaves very similar to tests with a stronger extinction of shortwave radiation in the upper ocean. We were able to find no evidence that this profile created an unstable stratification. Further, this test was repeated

at various resolutions to see if the degree to which the profile is resolved in the vertical changes the result seen at four meter resolution. Even at 10 meter resolution, when the maximum in chlorophyll is not resolved, the change relative to the baseline is similar to that at higher resolutions.

Lewis et al. (1983) assumed that the radiation penetrated following a single exponential, instead of the dual band exponential formulation we have used. The resulting instability condition for a single band exponential profile is given by equation (6) of Lewis et al. (1983). If we input our profile of chlorophyll there should be instability near $z = 6.5$ m.

The single band assumption is the critical difference that explains why we see no static instability. To understand the difference, we begin with the equation for temperature forced by solar radiation only, which is written as

$$\frac{\partial \theta}{\partial t} = -\frac{I_o}{\rho C_p} \frac{\partial}{\partial z} \left(0.6e^{-z} + 0.4e^{-z(0.025+0.013467z)} \right). \quad (5.1)$$

For instability to result, the necessary (but not sufficient) condition is $\frac{\partial^2 \theta}{\partial t \partial z} > 0$. The

vertical derivative of equation (5.1) is

$$\frac{\partial^2 \theta}{\partial t \partial z} = -\frac{I_o}{\rho C_p} \left\{ 0.6e^{-z} + 0.4e^{-z(0.025+0.013467z)} \left(0.000725z^2 + 0.001347z - 0.026308 \right) \right\}.$$

It is not possible to analytically determine if the term on the right hand side could result in an instability. If it is graphed (not shown), we see that the right hand side never becomes positive. Even if we change the coefficient for the attenuation of infrared

radiation to 2 m^{-1} the conclusion remains the same. Therefore, the absorption of infrared radiation prevents the change in sign of the right hand side.

5.4.1 Caveats and future work

In these tests, we have assumed a one way interaction between the large scale forcing terms and the vertical mixing models. This may not hold for a change in the surface temperature and velocity. For example, if the tropical Pacific experiences different levels of surface heating (due to spatially variable chlorophyll), the surface pressure gradient would be affected. The most difficult, but most effective, method to address the interaction question is to conduct these sensitivity tests in a three-dimensional domain.

Since the leap from one-dimension to three is very large, we next move to an intermediate two-dimensional framework. Two-dimensional models have been widely used for the tropical atmosphere (e.g. Bretherton and Sobel 2002, Sobel et al. 2004) and for various regions of the ocean (e.g. Bleck et al. 1988, and Walker and Holland 2007). We can use a two-dimensional framework to examine the sensitivity to spatial variations of surface chlorophyll and can abandon the large scale terms necessary for these one-dimensional runs. In the following simulations we are unable to study the impact of vertical variations of chlorophyll. The spin-up necessary in the 2-D model will be long enough that biological sources and sinks would be important. Therefore, we discuss the two-dimensional model in the next chapter and leave an examination of the influence of

vertically varying chlorophyll on the two- and three-dimensional temperature and momentum fields for future work.

Chapter 6:

Two-Dimensional Simulations

In this chapter we turn our attention to how the variability in space (and time) of penetrating shortwave radiation can influence the diurnal to intraseasonal structure of the OBL. As discussed in the previous chapter, the ocean circulation (and the atmosphere) is sensitive to penetrating shortwave radiation on interseasonal time scales. However, the actual dependence of the OBL on shortwave radiation is not fully understood. Recall that GA09 and Anderson et al. (2007) find that the tropics cool when penetrating shortwave radiation depends on surface chlorophyll, while M05 found tropical cooling for one parameterization of light extinction and warming for another.

In this chapter, we extend portions of the analysis carried out in the previous chapter to two-dimensions. This will allow us to, at least partially, assess the dependence of the tropical ocean circulation on zonal variations in surface chlorophyll. Prior to discussing the simulations, we discuss the discretization of advection and the pressure gradient force.

6.1 Two-Dimensional Framework

We will retain the coordinate defined in equation (3.3). The equations of motion and thermodynamics in this coordinate system are given in Appendix D. They are

$$\frac{Du}{Dt} - fv = -\frac{1}{\rho_o} \left(\frac{\partial p}{\partial x} \right)_\sigma + \frac{g\rho}{\rho_o} \left(\frac{\partial z}{\partial x} \right)_\sigma - \frac{\partial \sigma}{\partial z} \frac{\partial \overline{u'w'}}{\partial \sigma} \quad (6.1)$$

$$\frac{Dv}{Dt} + fu = -\frac{\partial \sigma}{\partial z} \frac{\partial \overline{v'w'}}{\partial \sigma} \quad (6.2)$$

$$\frac{D\theta}{Dt} = -\frac{\partial \sigma}{\partial z} \frac{\partial \overline{w'\theta'}}{\partial \sigma} + \frac{1}{\rho_o C_p} \frac{\partial \sigma}{\partial z} \frac{\partial I}{\partial \sigma} \quad (6.3)$$

$$\frac{DS}{Dt} = -\frac{\partial \sigma}{\partial z} \frac{\partial \overline{w'S'}}{\partial \sigma} \quad (6.4)$$

$$\frac{1}{m} \frac{Dm}{Dt} + \left(\frac{\partial u}{\partial x} \right)_\sigma + \frac{\partial \dot{\sigma}}{\partial \sigma} = 0 \quad (6.5)$$

$$\frac{D}{Dt} ()_\sigma \equiv \frac{\partial}{\partial t} ()_\sigma + u \frac{\partial}{\partial x} ()_\sigma + \dot{\sigma} \frac{\partial}{\partial \sigma} ()_\sigma. \quad (6.6)$$

The vertical velocity $\left(\dot{\sigma} \right)$ is calculated as described in Section 3.1. The turbulent fluxes are predicted via the TKE method outlined in Chapter 3. The remaining numerical details to discuss are the horizontal and vertical advective terms and the pressure gradient force.

The advective terms are discretized using the van Leer (1974) flux limiter. The necessary boundary conditions to discretize the vertical advection are a simple linear extrapolation with the limits suggested by Thuburn (1993). The discretization of the pressure gradient force in our normalized height coordinate is trickier. It is discussed in the following section.

6.1.1 Pressure gradient force

The two-term pressure gradient force is a well known bane to ocean and atmosphere models (e.g. Janjic 1977, Messinger 1982, Haney 1991, Mellor et al. 1994, Song 1998). The two terms can become large and of opposite sign whenever the σ surfaces are sufficiently tilted. In our coordinate system this can occur without topography. If the boundary layer depth becomes strongly tilted, the corresponding σ surfaces become tilted as well. For this reason we must address this issue in our two-dimensional model.

Janjic (1977) and Messinger (1982) have shown that this problem can be reduced with sufficiently high horizontal resolution relative to the vertical resolution. However, this can be a very large burden for large scale ocean models (Mellor et al. 1994).

Two different remedies have been proposed to alleviate this problem. Some propose calculating a horizontally averaged background density and subtracting this from the density field (e.g. Gary 1973). This can be effective at removing the error when the deviation from the computed reference state is small, such as in small domain simulations. At the global scale, the departure from the reference state is much larger and more of the error remains.

Others propose reformulating the pressure gradient force as a Jacobian (e.g. Song and Haidvogel 1994, Song 1998, Shchepetkin and McWilliams 2003; SW03). In crude terms, this reformulation increases the order of accuracy of the discretized pressure force.

In our model, we have chosen to follow the work of SW03. SW03 derive the pressure gradient as would be done from first principles. The pressure force is the sum of the forces across all the faces of a control volume.

In this system of SW03, as in all hydrostatic models, the pressure at a depth z is given by

$$P(x, y, z) = g \int_z^\zeta \rho(x, y, z') dz'.$$

Where ζ is the free surface height. Utilizing this definition, we can now rewrite the pressure gradient force as

$$-\frac{1}{\rho_o} \left(\frac{\partial p}{\partial x} \right)_z = -\frac{g\rho(\zeta)}{\rho_o} \frac{\partial \zeta}{\partial x} - \frac{g}{\rho_o} \int_z^\zeta \frac{\partial z}{\partial \sigma} \left(\frac{\partial \rho}{\partial x} \right)_\sigma - \frac{\partial \rho}{\partial \sigma} \left(\frac{\partial z}{\partial x} \right)_\sigma ds.$$

In this equation, the integrand is the Jacobian $\left\{ J(A, B) \equiv \left(\frac{\partial A}{\partial x} \right)_\sigma \frac{\partial B}{\partial \sigma} - \frac{\partial A}{\partial \sigma} \left(\frac{\partial B}{\partial x} \right)_\sigma \right\}$ in our

σ -coordinate. Using Green's theorem, the pressure gradient force is equivalent to a contour integral around the shaded area in Figure 6.1 (adapted from SW03, their Figure 7). In this figure, a new horizontal and vertical coordinate (ξ, s) has been introduced.

The vertical (horizontal) coordinate is zero on the bottom (at the left) edge of the cell and one on the top (right) edge of the cell. The pressure gradient force is now rewritten as the sum of the fluxes across each wall or

$$PGF = FX_{i, k+\frac{1}{2}} + FC_{i+\frac{1}{2}, k+1} - FX_{i+1, k+\frac{1}{2}} - FC_{i+\frac{1}{2}, k}.$$

In this equation, FX is the horizontal flux and FC is the vertical flux. These terms are written as

$$FX_{i,k+\frac{1}{2}} = \int_{s_{i,k}}^{s_{i,k+1}} \rho \frac{\partial z}{\partial s} ds; \quad FC_{i+\frac{1}{2},k} = \int_{\xi_{i,k}}^{\xi_{i+1,k}} \rho \frac{\partial z}{\partial \xi} d\xi \quad .$$

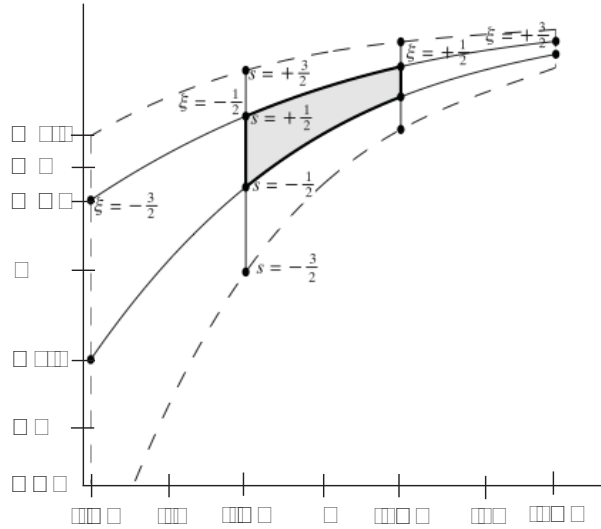


Figure 6.1 - Schematic of the contour interval to be evaluated in the model pressure gradient force. The solid curved lines represent constant σ surfaces. This figure has been adapted from SW03, their Figure 7

Both of these terms are line integrals.

From here, it is assumed that z and ρ can be represented by monotone cubic polynomials, which increases the accuracy of the pressure force. Use of cubic polynomials requires the knowledge of vertical and horizontal derivatives of the mid layer depth (z) and density (ρ). SW03 discretize the horizontal and vertical derivatives as

$$\left. \frac{\partial}{\partial \xi} \right|_{\xi=\pm 1/2} = \frac{2\Delta^+ \Delta^-}{\Delta^+ + \Delta^-}; \quad \left. \frac{\partial}{\partial s} \right|_{s=\pm 1/2} = \frac{2\Delta_v^+ \Delta_v^-}{\Delta_v^+ + \Delta_v^-} \quad .$$

In these equations, we have defined four elementary differences, they are given for a general function f as

$$\Delta^+ = f_{i+3/2,k} - f_{i+1/2,k}; \quad \Delta^- = f_{i+1/2,k} - f_{i-1/2,k}; \quad \Delta_v^+ = f_{i,k+3/2} - f_{i,k+1/2}; \quad \Delta_v^- = f_{i,k+1/2} - f_{i,k-1/2}.$$

If Δ^+ and Δ^- are of opposite sign, the derivative is set to zero. Using these new definitions, the fluxes are given by

$$FC_{i+1/2,k} = \frac{\rho_{i+1,k} + \rho_{i,k}}{2} (z_{i+1,k} - z_{i,k}) - \frac{1}{10} \left\{ (d\rho_{i+1,k} - d\rho_{i,k}) \left[z_{i+1,k} - z_{i,k} - \frac{dz_{i+1,k} + dz_{i,k}}{12} \right] - (dz_{i+1,k} - dz_{i,k}) \left[\rho_{i+1,k} - \rho_{i,k} - \frac{d\rho_{i+1,k} + d\rho_{i,k}}{12} \right] \right\}$$

and

$$FX_{i,k+1/2} = \frac{\rho_{i,k+1} + \rho_{i,k}}{2} (z_{i,k+1} - z_{i,k}) - \frac{1}{10} \left\{ (d\rho'_{i,k+1} - d\rho'_{i,k}) \left[z_{i,k+1} - z_{i,k} - \frac{dz'_{i,k+1} + dz'_{i,k}}{12} \right] - (dz'_{i,k+1} - dz'_{i,k}) \left[\rho_{i,k+1} - \rho_{i,k} - \frac{d\rho'_{i,k+1} + d\rho'_{i,k}}{12} \right] \right\}.$$

In these equations, $d\rho$ and dz are the horizontal derivatives of density and layer depth and $d\rho'$ and dz' are the corresponding vertical derivatives.

At the topmost grid box, FX is given by

$$FX_{i,1/2} = \left[\rho_{i,1} + \frac{1}{2} (\zeta_i - z_{i,1}) \frac{\rho_{i,1} - \rho_{i,2}}{z_{i,1} - z_{i,2}} \right] (\zeta_i - z_{i,1}).$$

The FC and FX terms complete the PGF. SW03 also derived a simpler, but equivalent version of the PGF. If the pressure in the first layer is computed by

$$P_{i,1} = g \left[\rho_{i,1} + \frac{1}{2} (\zeta_i - z_{i,1}) \frac{\rho_{i,1} - \rho_{i,2}}{z_{i,1} - z_{i,2}} \right] (\zeta_i - z_{i,1})$$

and the pressure in the middle of the remaining layers is calculated following

$$P_{i,k} = P_{i,k-1} + g \frac{\rho_{i,k-1} - \rho_{i,k}}{2} (z_{i,k-1} - z_{i,k}) - \frac{g}{10} \left\{ (d\rho'_{i,k-1} - d\rho'_{i,k}) \left[z_{i,k-1} - z_{i,k} - \frac{dz'_{i,k-1} + dz'_{i,k}}{12} \right] - (dz'_{i,k-1} - dz'_{i,k}) \left[\rho_{i,k-1} - \rho_{i,k} - \frac{d\rho'_{i,k-1} + d\rho'_{i,k}}{12} \right] \right\}.$$

The pressure gradient force at each momentum point, which is defined on the grid given in Figure 3.1, is given by

$$\left(\frac{\partial P}{\partial x} \right)_{i+\frac{1}{2},k} = \frac{P_{i+1,k} - P_{i,k}}{\Delta x} + g \frac{FC_{i+\frac{1}{2},k}}{\Delta x}.$$

This is the form of the PGF used in our model.

The final addition we make to the two-dimensional model is to allow for user defined mass sources and sinks in the continuity equation (6.5). Currently, this is simply set as a constant. For example, if we blow a easterly wind over our ocean, we need a way to remove mass from the OBL on the western boundary. A negative constant, which represents column integrated divergence, is added to the continuity equation (6.5). Whenever this option is used, we must have compensating convergence. We choose to have this occur at the eastern boundary, in the deep ocean.

As a final note, we use the PCM for the virtual mass flux in all the simulations in this chapter. The only reason for this is computational speed, but we do not expect there to be very large and quick movements of the boundary layer depth in these simulations.

6.2 Simple Tests of the Pressure Gradient Force.

In this section, a very simple test is conducted to evaluate the model pressure gradient force. The constant mass source/sink option is not used in these runs. In these two simulations, the temperature profile is uniform ($\theta = 20^{\circ}\text{C}$) in the upper 20 meters. Below this mixed layer the temperature decreases at a constant rate of $0.04^{\circ}\text{Cm}^{-1}$. There is no initial velocity and the initial surface is flat.

In the first test, we use a constant seven meter resolution, with three layers in the boundary layer. In the second test, the resolution is increased to 2.5 meters and the number of layers in the boundary layer is increased to eight. In both runs, the horizontal resolution is 2° . The surface is forced by a constant easterly forcing ($u_* = -0.0064 \text{ ms}^{-1}$), which is similar to observed wind stresses in the tropical Pacific. In addition to a surface momentum forcing, we impose a very idealized surface temperature restoring. On the western boundary, the restoring temperature is set to 21°C and we assume there is a linear decrease to 19.5°C on the eastern boundary. A restoring timescale of 30 days^{-1} is used. The simulation is run for two years.

The temperature and velocity fields at the end of year two for both tests, are shown in Figure 6.2. Superimposed on top of these figures is the boundary layer depth predicted by the model. The longitude-depth profiles of temperature are qualitatively similar between the low (Figure 6.2a) and high (Figure 6.2b) resolution runs. The thermocline is deeper in the west and shallower in the east. However, as we move away

from the western boundary, the temperatures cool much more quickly in the high

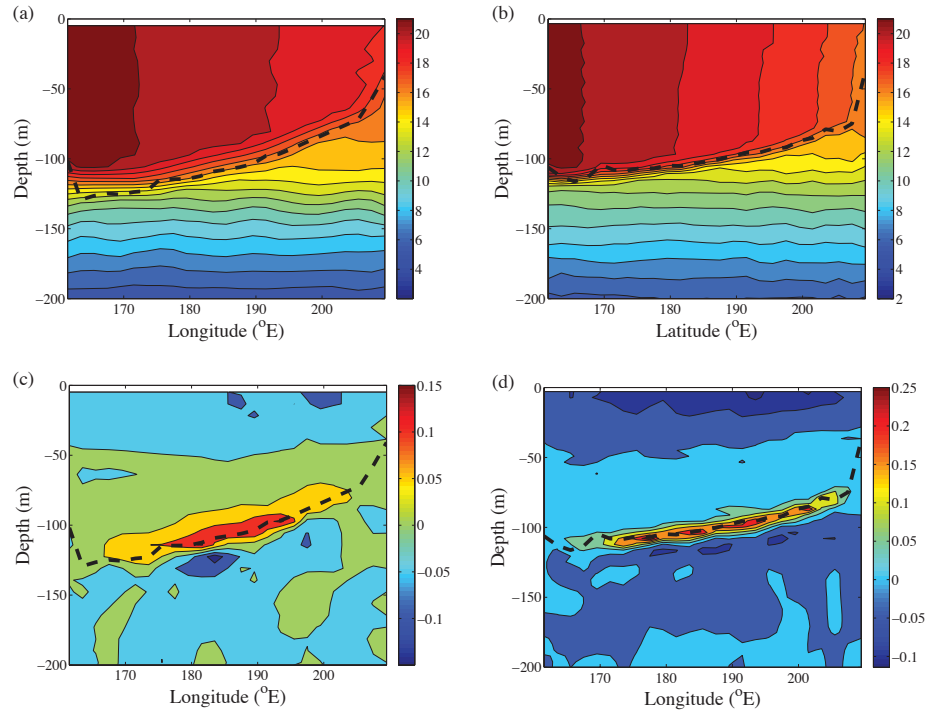


Figure 6.2 - Longitude-Depth plots of Temperature at (a) seven meter resolution and (b) 2.5 meter resolution (b). Plotted in (c) is the zonal velocity at seven meter resolution. In (d) is the zonal velocity at 2.5 meter resolution. The contour intervals for the temperature plots is 1°C and is 0.05 ms^{-1} for velocity.

resolution run.

We can see in the velocity plots, which are given in Figure 6.2c for the coarse resolution run and Figure 6.2d for the high resolution run, that the surface velocity is stronger in the high resolution run compared to the low resolution run. The stronger easterly current pulls isotherms up toward the surface more effectively in the high resolution simulation. In addition, the mixing is stronger in the high resolution run, leading to a slightly weaker gradient in boundary layer depth than seen in the coarse run.

The EUC simulated in the coarse resolution simulation (Figure 6.2c) is spread out more in the vertical than what is seen in the Figure 6.2d. Further, the high resolution EUC is nearly double the strength of the coarse simulation.

Since we are not using the mass source/sink terms, the boundary layer in both runs will continue to deepen, but the rate of deepening is very small (not shown). Despite the continued OBL deepening, the surface height is nearly steady after six months (see Figure 6.3). Using Figure 6.3, we can explain a small portion of the difference in the strength of the EUC between the two tests. The final surface height is slightly higher

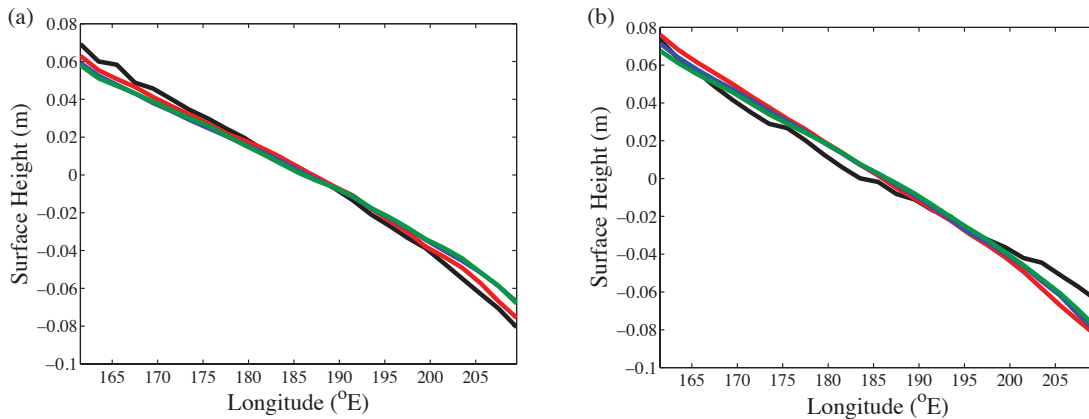


Figure 6.3 - Sea surface height in the coarse resolution simulation (a) and the simulation with 2.5 meter resolution (b). In both models, the black line is one quarter the way through the run, the red line is one half through the run, blue is three quarters through the run, and green is at the end of the run.

near the boundaries in the high resolution simulation (Figure 6.3b) than the low resolution run (Figure 6.3a). This creates a slightly stronger pressure gradient force at the surface, which must be balanced by a slightly stronger EUC.

These two tests have shown us that the model PGF is behaving appropriately. The results are encouraging and we feel confident in using this model framework to evaluate how the predicted temperature and velocity responds to the spatial and temporal variability of chlorophyll.

6.3 More Realism

In the remaining simulations, we have chosen to initialize the model using data from Levitus and Boyer (1994, LB94). The annually averaged equatorial Tropical Pacific temperature is shown in Figure 6.4a (160 to 275°E). The initial temperature field is taken as the zonal average of this section, and is shown in Figure 6.4b. In these runs, salinity is

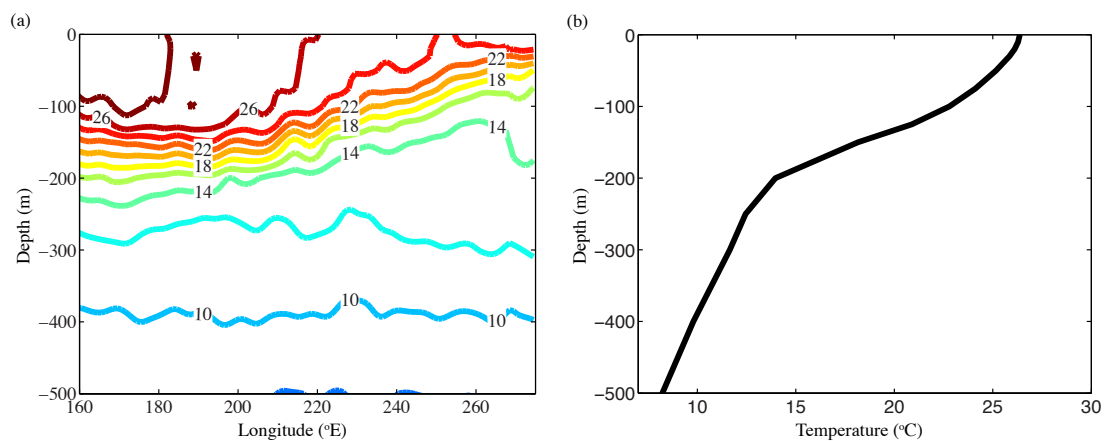


Figure 6.4 - (a) Annually averaged temperature from LB94 at the equator. (b) the initial temperature profile used in the simulations, which is a zonal average of (a).

fixed, and there is no initial motion.

We cannot feasibly use the high resolution from the previous section. Further, since we are now extending our domain to 6000 meters, we cannot use a constant thickness throughout a model column. Thus, in the remainder of this chapter, we use the thicknesses from LB94; (see Table 6.1). The top three layers are taken as the initial boundary layer thickness.

The model is forced in two ways. First, the surface friction velocity used in the previous test is included. The temperature field is again restored, but here the model temperature is restored to the annually averaged LB94 SST. Instead of restoring directly

to data (black line in Figure 6.5), we fit a third order polynomial through the data, which is the blue line in Figure 6.3. The functional form is given by

$$T_{\text{Restore}} = -62.98 + 1.468\lambda - 7.55 \times 10^{-3} \lambda^2 + 1.23 \times 10^{-5} \lambda^3.$$

For all of the runs, the restoring time scale is set to 30 days⁻¹.

When solar forcing is included, we are including a large input of heat to the system that is not easily dissipated. Therefore, we include a cooling of 100 Wm⁻² at the surface to represent the influence of evaporation. This cooling is also included in the run

Layer Number	Thickness (m)	Layer Number	Thickness (m)	Layer Number	Thickness (m)
1	10	12	100	23	100
2	10	13	100	24	250
3	10	14	100	25	250
4	20	15	100	26	500
5	25	16	100	27	500
6	25	17	100	28	500
7	25	18	100	29	500
8	25	19	100	30	500
9	50	20	100	31	500
10	50	21	100	32	500
11	50	22	100	33	500

Table 6.1 - Thickness of model layers used in the simulations conducted in this chapter.

without solar forcing.

The pressure gradient formulation outlined in Section 6.1.1 will require a short time step, due to surface gravity waves. In the previous section, we had to use a 60 second time step, even at 2° resolution.

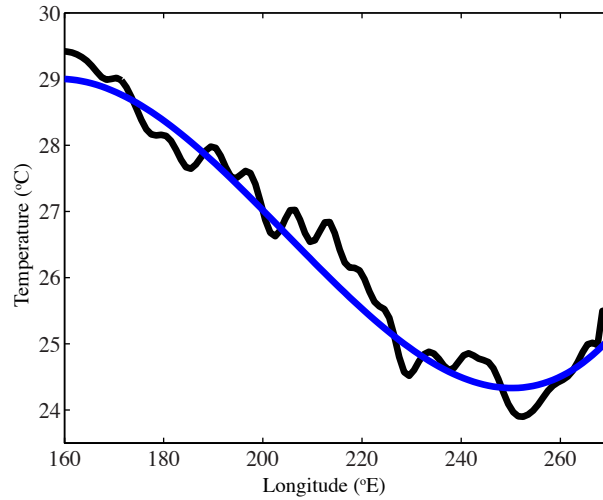


Figure 6.5 - Levitus (1994) SST along the section in Figure 6.4a (solid black), and the restoring function used in the model simulations (blue line).

Many ocean models predict the barotropic and baroclinic components of the flow separately. While this would allow a much longer time step, the complexity of this endeavor is beyond the scope of this dissertation. Instead, we pursue a middle ground. The pressure gradient force in this model can be written in a crude sense as

$$\left(\frac{\partial P}{\partial x} \right)_z = \frac{\partial \zeta}{\partial x} + B.$$

Where B is the baroclinic contribution and ζ is the free surface height. The most straightforward, explicit discretization is given as

$$\frac{P_{i+1,k}^n - P_{i,k}^n}{\Delta x} = \frac{\zeta_{i+1,k}^n - \zeta_{i,k}^n}{\Delta x} + B_{i+\frac{1}{2},k}^n.$$

If we compute the pressure gradient force at the end of the time step, we can use a partially implicit surface height field (e.g. Haltiner and Williams 1984). With this change, we are able to increase the time step by roughly a factor of two.

At the end of each time step, the sigma levels are remapped such that the value of

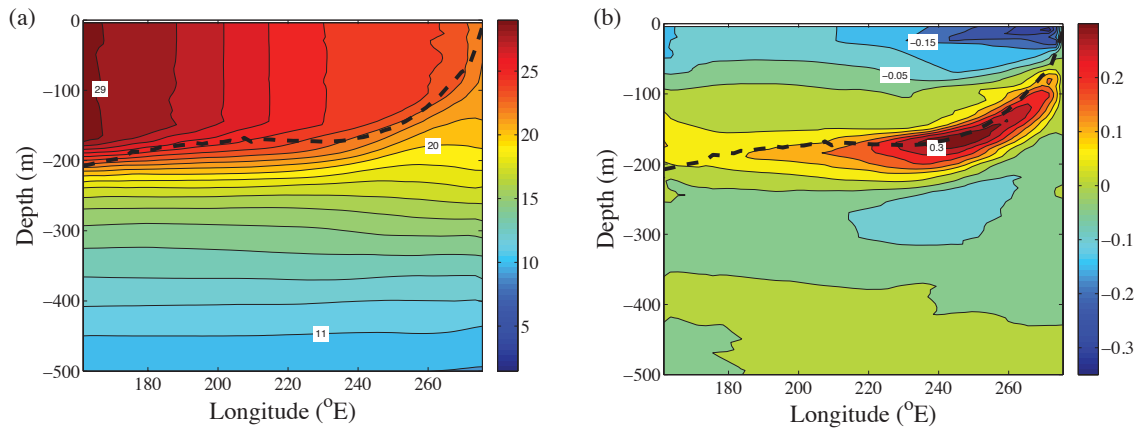


Figure 6.6 - Time averaged longitude-depth profiles of temperature (a) and zonal velocity (b) for the baseline Levitus simulation. On both plots, the modeled boundary layer depth is plotted as a dashed line. As in the previous plots, the output from the model has been interpolated to a uniformly spaced vertical grid. The contour intervals are as in Figure 6.2.

sigma at a given model level remains constant in longitude. The model is run at 2° resolution.

The model is run for 10 years. The temperature and velocity fields, which are averaged over the final month of the run, are shown in Figures 6.6a and 6.6b respectively. The near surface temperature is very similar to the Levitus SST due to the restoring included in the model. The longitude-depth section of temperature looks similar to the LB94 data (Figure 6.4a). Some of the surface features in the Levitus result are missing here, most notably the slight increase in temperature from about 250°W to the eastern

boundary. The model predicted thermocline (dashed line in Figure 6.6) is flatter than what is observed in LB94.

The EUC in this model is weaker than observations, most likely due to missing three-dimensional processes. A portion of the EUC strength is due to the two-dimensional ocean attempting to balance the surface height gradient. In reality, a significant portion of the EUC is fed by waters that originate in the extratropics (Blanke and Raynaud 1997, Sloyan et al. 2003, Goodman et al. 2005). In this framework we rely on water returning at depth, since it cannot move down from the surface. For this reason, we expect that the EUC in two-dimensions will be significantly weaker than its three-dimensional counterpart without some additional ad hoc forcing.

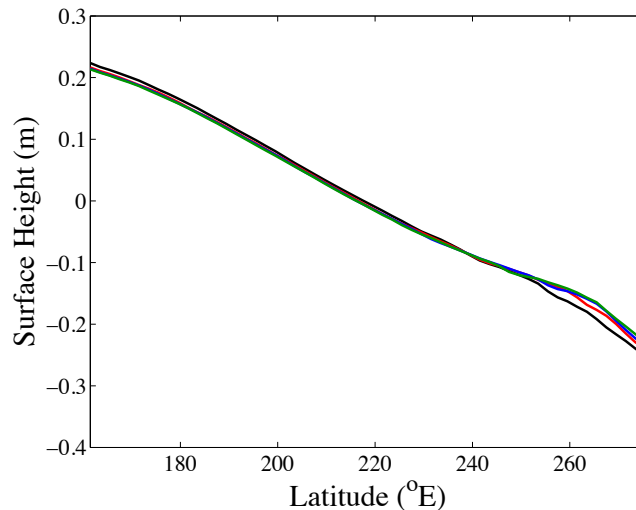


Figure 6.7 - Surface height predicted by the new model at 2.5 years (black), 5 years (red), 7.5 years (blue), and 10 years (green).

Despite some departures from observations, the new model is doing many things correctly. The observed temperature structure is close to LB94. The surface height gradient predicted by the model, which is plotted in Figure 6.7 at four separate times, is similar to what is seen in TOPEX-Poseidon data (not shown). This confirms that our

choice of wind stress in these simulations is similar to observations. We are also able to simulate a stable EUC in basically the right spot, although it is weaker than observed.

6.3.1 Diurnal cycle

We now add a diurnal cycle that is more complex than what was used in the previous chapter. Since longitudinal variations are allowed, the sun will rise at different times at different model locations. In these runs, we have borrowed the solar forcing routine from the CSU-OGCM. This is only a minor detail and does not influence the results.

The maximum surface shortwave radiation is set to 900 Wm^{-2} . The shortwave radiation is allowed to penetrate following the dual band exponential profile used throughout this work. In this first simulation, the extinction coefficients for infrared and visible bands are set to 1 m^{-1} and 0.05 m^{-1} respectively. A part from the addition of solar

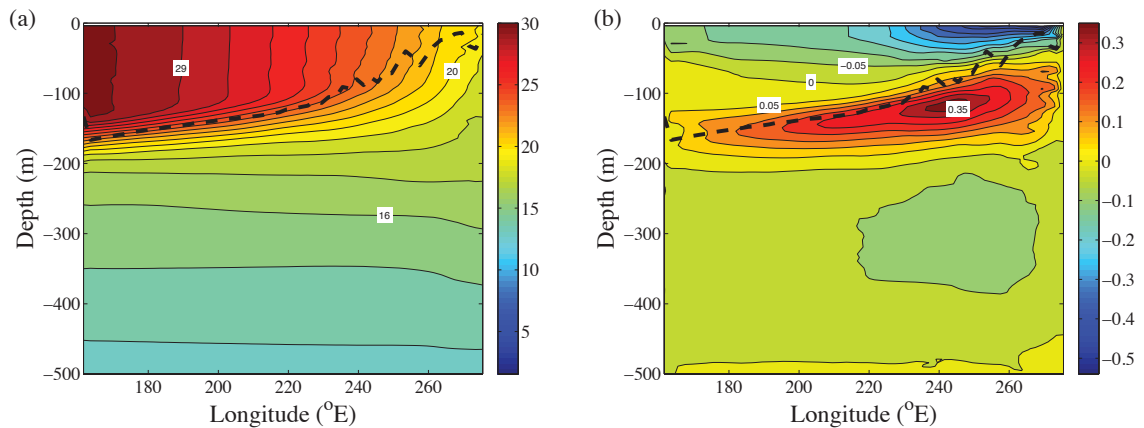


Figure 6.8 - Time averaged (year 10) latitude-depth plots of temperature (a) and zonal velocity (b). The contour intervals are as in Figure 6.2.

forcing, this simulation is identical to the one we have just conducted.

The longitude depth cross sections, which have been averaged over the final year of the run, for temperature and zonal velocity are shown in Figure 6.8a and 6.8b

respectively. When we add surface heating, the depth of the boundary layer is shallower in general than the OBL depth in Figure 6.6. With solar radiation, the upper ocean is not as easily mixed. Convection occurs constantly in the base simulation, which increases the mixing.

In this simulation, the east to west gradient of the thermocline is stronger. The depth of the thermocline near the western boundary is nearly 50 meters shallower in the run with solar forcing. The depth right next to the eastern boundary is similar between the two runs. The ocean is also much colder (the 11°C isotherm is above 500 meters in the no-solar simulation).

The boundary layer velocity near the eastern boundary is much stronger in the solar forcing run. Since there is less mixing in this simulation, more of the momentum input near the eastern boundary is confined near the surface than in the run without solar forcing. The maximum strength of the EUC is greater in this simulation, most likely due to the increased thermocline gradient. This also causes the EUC to spread through more of the domain.

In this simulation, the surface height field, which is plotted at four separate times in Figure 6.9, is not quite as steady as that in the simulation without solar forcing. In the previous simulation, the surface height gradient was nearly fixed after the first three years. In this simulation, the surface height is essentially constant in the first half of the simulation (black and red curves) and then the circulation is able to smooth the strong height gradient on the western boundary. In the second half of the run, the profile of surface height has changed slightly and the gradient is now smoother.

Despite the lack of a number of three-dimensional processes, the model is behaving quite well. In runs without solar heating, the upper ocean is more mixed, as

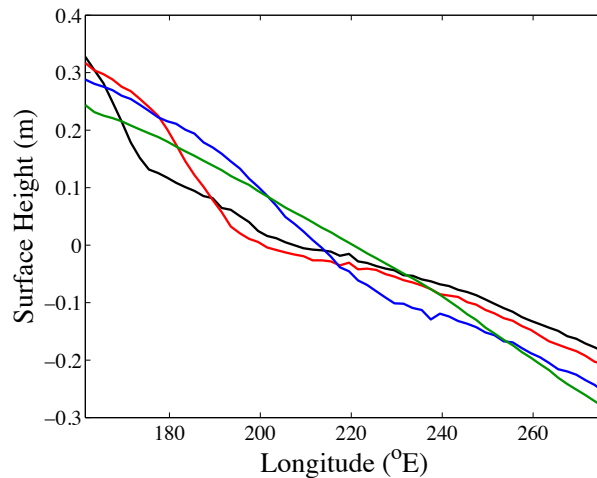


Figure 6.9 - Surface height predicted by the model in the run with constant coefficient solar forcing. The colors of the curves are as in Figure 6.7.

would be expected with no heating to prohibit strong night time mixing. The position of the EUC looks appropriate, despite the weaker strength.

Prior to examining the influence of surface chlorophyll on the modeled circulation and temperature, we have repeated this solar forcing run with the simple large scale convergence terms switched on. In this run, we add a constant divergence (10^{-6} s^{-1}) on the western boundary in the boundary layer, and a compensating convergence at the bottom of the ocean on the eastern boundary. The strength of the divergence chosen is similar to what is found from output of the global ocean data assimilation system near the surface in the vicinity of 160°E .

The change in the temperature and velocity fields relative to the previous simulation are shown in Figure 6.10a and 6.10b respectively. The fields have again been averaged over the final year of the run and interpolated to a uniform grid. The upper

ocean temperature (Figure 6.10a) is slightly warmer when upwelling is included. This may be due to less mixing in this run. The negative anomalies below the warm anomalies are the result of a shallower thermocline in the upwelling run. In the raw fields, colder isotherms outcrop when upwelling is strengthened, as expected. The included upwelling has decreased the rate of deepening during year 10. On the western boundary, the thermocline deepens by about 12 meters during the final year without upwelling. When our very simple parameterization is included, the deepening decreases to five meters during the year. This is what was desired. Unfortunately, there are some undesirable effects. The strength of the EUC with parameterized convergences is smaller

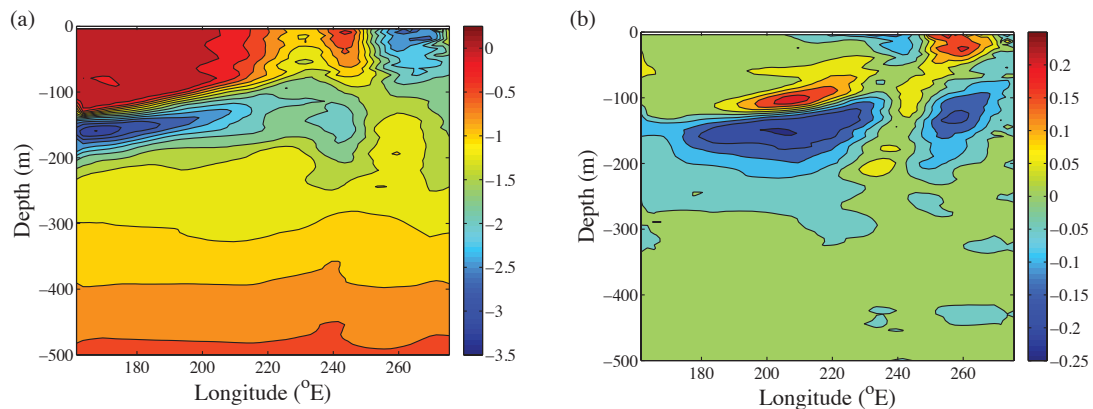


Figure 6.10 - Time averaged (year 10) latitude-depth plots of the change in temperature (a) and zonal velocity (b) relative to the previous simulation (Figure 6.8). The contour interval in (a) is 0.25°C and is 0.05 ms^{-1} in (b).

than the previous run, hence the negative anomaly in the depth range of the EUC in Figure 6.10b. The positive velocity anomalies result from a shift in the EUC to shallower depths in this test.

In this simulation, the final surface height gradient, as well as the eastern and western boundary heights, are very similar to the run without convergences (not shown).

As suggested by the previous research, our parameterization of convergences and divergences should be redesigned. It is observed that water diverges near the western boundary of the tropical Pacific. This is what we have included in our parameterization. Instead of having the compensating convergence in the deep ocean next to the eastern boundary, we should have convergence over a larger zonal extent, beginning near the

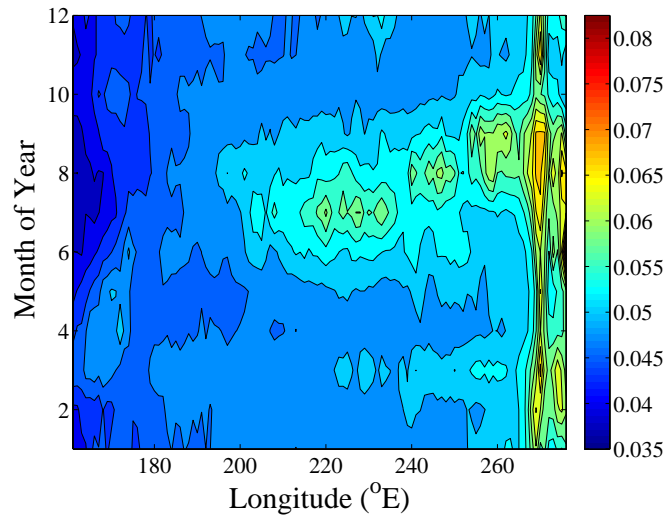


Figure 6.11 - Attenuation coefficients resulting from the GA09 optical parameterization. The chlorophyll is from a SeaWIFS monthly climatology.

western boundary. This would feed the EUC, similar to what is seen in observations. Refinement of this condition is left for future work.

6.3.2 Sensitivity to monthly varying surface chlorophyll.

Due to the uncertainty in the chosen parameterization of unrepresented sources and sinks of mass, we conduct this simulation without those terms. This simulation is similar to the baseline Levitus run with solar forcing in every way except for the parameterization of the extinction coefficient of the visible band of solar radiation.

In this section, we utilize the parameterization of GA09. The chlorophyll is taken from a monthly climatology of sea-viewing wide field of view sensor (SeaWIFS) data.

The resulting extinction coefficients are shown in Figure 6.11, where the contour interval is 0.0025 m^{-1} . In general, there is more chlorophyll in the cold tongue region (see Figure 5.1) and there is a decrease toward the west. In this framework, we will trap more shortwave radiation near the surface in the cold tongue region than near the western boundary. In this simulation the chlorophyll resets every year for the entire 10 years.

In Figure 6.12, we have plotted the differences in temperature and velocity, e.g.

$\Delta\theta_{\text{Fig 6.12}} = \theta_{\text{Chl}} - \theta_{\text{nochl}}$ averaged over year ten. The temperature change near the surface

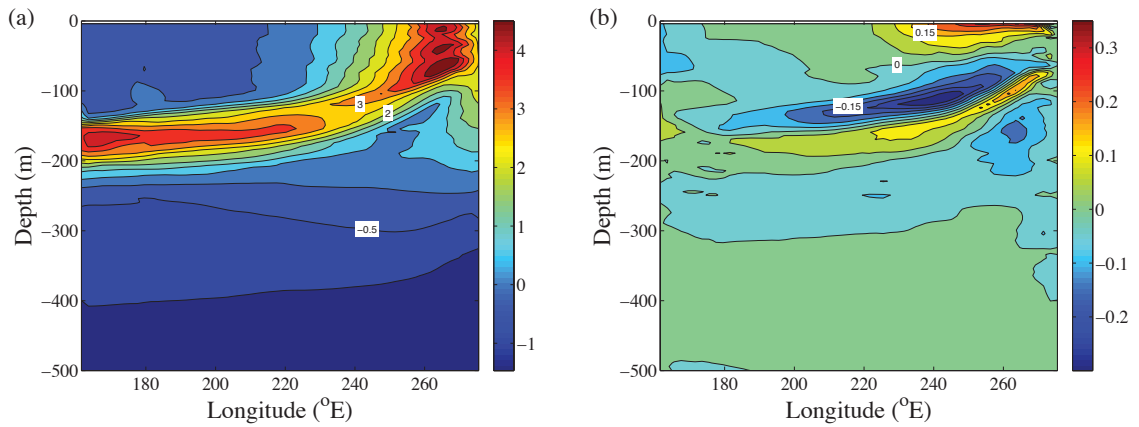


Figure 6.12 - Time averaged (year 10) latitude-depth plots of the change in temperature (a) and zonal velocity (b) due to the addition of surface chlorophyll relative to the previous simulation (Figure 6.8). The contour interval in (a) is 0.5°C and is 0.05 ms^{-1} in (b).

(Figure 6.12a) is positive near the eastern boundary and becomes negative on the western boundary. If we refer to Figure 6.11, the extinction coefficient is larger than that used in the simulation without chlorophyll ($k_{\text{vis}} \equiv 0.05 \text{ m}^{-1}$) on the eastern boundary and is smaller on the western boundary. Over the course of the simulation, the difference in surface extinction coefficients could cause the difference in surface temperature seen in Figure 6.12a. The warm anomaly seen near the surface is similar to what is expected in a one

dimensional heat balance. This is opposite to what is seen in GA09, where the cold tongue region cools. This suggests that it is the clarity of the water in the extratropics that influences the surface temperature of the eastern tropical Pacific (cold tongue).

The deeper ocean (near 500 meters depth) is colder when chlorophyll is included. This result is consistent with increased convection (as seen in Figure 6.6a), most likely due to weaker shortwave absorption near the western boundary.

The zonal velocity differences (Figure 6.12b) near the surface are very strong near the eastern boundary. The strong easterly velocity seen in Figure 6.8b is not seen in the run with chlorophyll included. Instead, the velocity is much more uniform in the upper ocean. The equatorial undercurrent is shallower and broader in the run without chlorophyll, but the maximum magnitude is similar in each run. The shallower thermocline in the run without chlorophyll results in a negative velocity anomaly about 150 meters below the surface. The deeper EUC in the chlorophyll run gives the positive anomaly below the negative anomaly.

The increased breadth and strength of the EUC in the run without chlorophyll seems to be a result of the stronger thermocline and surface height gradient. In the run with chlorophyll, the surface height gradient is weaker than the run without surface chlorophyll (not shown).

6.4 Conclusions

In this chapter we have constructed a two-dimensional model in a normalized height coordinate. This is a large step toward a fully three-dimensional model. The

pressure gradient in the meridional direction is simply a rotation of what was discretized in this chapter.

The flux limited advection scheme used in the horizontal in this chapter does not translate to two dimensions very well. Use of a one-dimensional limiter in two coordinate directions leads to biases in the advected field (e.g. Thuburn 1996).

The modeled temperature and velocity fields have many qualitative similarities to the observed fields. We simulate an EUC directly below the thermocline, although it is weaker than observed. To achieve the correct strength in this framework, we need to parameterize extratropical sources of water flowing into the EUC. The surface height gradient simulated in the two-dimensional model is similar to what is observed.

When a diurnal cycle is imposed, the thermocline gradient increases due to the decrease in convection. The sharpening of the thermocline increases the strength and size of the EUC, which is what we would expect.

When monthly averaged surface chlorophyll is included, the surface temperature near the eastern boundary warms relative to the run without chlorophyll. The opposite is true near the western boundary. The EUC becomes narrower in this test, even though the maximum strength remains the same as in the run without chlorophyll. This may be due to a decrease in the surface height gradient in the run with surface chlorophyll.

The general behavior agrees with what is expected from a one-dimensional heat balance. As seen in Chapter 5, an increase in turbidity warms the surface and decreasing the turbidity cools the surface. This was seen in the chlorophyll simulation conducted in this chapter.

The results found in this chapter confirm the results of Anderson et al. (2009) and GA09. These studies found that the water clarity near the equator is not as important in determining the surface temperature of the eastern tropical Pacific as the shortwave penetration depths in the extratropical regions. With a local heat balance imposed, we found a warmer cold tongue compared to the run without chlorophyll.

The upwelling condition used for the simulation, which is shown in Figure 6.10, could be used with surface chlorophyll. We have found this condition to be imperfect. Instead, we should allow the convergence to happen over most of the western portion of our domain. To implement this, we would not only need to know the flow strength at depth as a function of longitude, but also the temperature of the water flowing toward the equator. Once we specify the temperature of the water flowing into the EUC, we should see a cooler cold tongue when chlorophyll is included (assuming the EUC temperature is adjusted appropriately).

Chapter 7:

Regulation of Intraseasonal SST

Variability in the East Pacific

Warm Pool by Vertical Mixing

7.1 Introduction

A number of recent studies have shown significant intraseasonal variability of sea surface temperature (SST) in the east Pacific warm pool during boreal summer (e.g. Maloney and Kiehl 2002ab, Maloney et al. 2008). These studies, using the Reynolds and Smith (1994) SST product, TRMM Microwave imager SSTs, and buoy SSTs found regular oscillations with a time scale of about 50 days in most boreal summers. Maloney et al. (2008) have also shown that the variability is maximized near the Costa Rica Dome (CRD) region and in the northern portion of the eastern Pacific warm pool. In these areas, the amplitude of the SST oscillations can reach 1°C in a given event. Approximately 30 - 40% of this variance can be explained by the Madden-Julian oscillation (Maloney and Kiehl 2002a). Examination of SST, precipitation, and wind

anomalies lead to the conclusion that enhanced west winds and precipitation lead SST by about 7 - 10 days (e.g. Maloney et al. 2008).

The heightened SST variability in the region of the CRD is associated with a shallow annual mean thermocline and mixed layer depth. The thermocline depth is dominated by Ekman suction, driven by a positive wind stress curl. Figure 3 of Xie et al. (2005) shows that the positive wind stress curl is associated with small scale wind jets (e.g. Gulf of Papagayo) during the winter. In boreal summer, the CRD is near the northern edge of the monsoon westerlies, which would also input a positive wind stress curl.

Observed thermocline depths near the center of the CRD in northern hemisphere summer are less than 30 meters. Maloney and Kiehl (2002a), utilizing a slab ocean model forced by NCEP reanalysis with a fixed mixed layer depth, which was set to the annual mean, found that the variability in the slab model is overestimated relative to the Reynolds and Smith SST. This suggests that a more physical representation of the oceanic mixed layer is necessary. It should be noted that the quality of the Reynolds and Smith product may be suspect (Maloney et al. 2008).

A number of studies have been conducted using one-dimensional and more complex models to simulate intraseasonal SST variability in the western Pacific (e.g. Anderson et al. 1996, Shinoda and Hendon 1998). These studies have documented that strong OML variability occurs during intraseasonal oscillations. For example, anomalous precipitation (perhaps associated with the MJO) and its freshening effect on the upper ocean could limit the diurnal penetration of the MLD (described in Anderson et al. 1996). Also, in times of weak wind and strong insolation the thermal stratification is increased,

limiting the depth of the OML base. This suggests that correct simulation of the insolation, the solar heating profile, and surface stress is important to accurately simulate of ocean MLDs (Shinoda and Hendon 1998).

Finally, Bernie et al. (2005) suggest that nighttime deep mixing can enhance mixing across the thermocline, altering the MLD. This implies a model with nonlocal convective fluxes should more accurately simulate ocean MLDs, especially in regions where the diurnal cycle is important.

As in previous chapters, we utilize the newly developed model framework and the KPP model. The models are driven by surface forcing derived from 8°N 95°W TAO buoy observations during the boreal summer of 2002 (Figure 7.1). Strong and regular

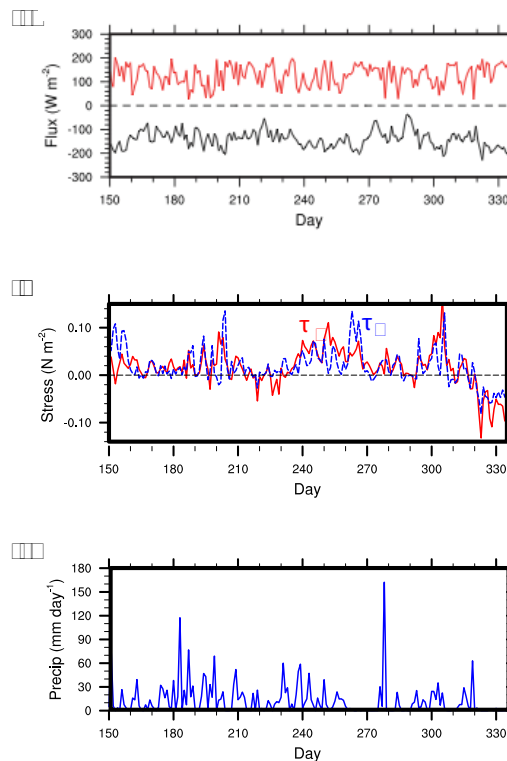


Figure 7.1 - Surface forcing derived from observations at the 8°N 95°W TAO buoy from 2002. (a) Surface heat flux (Black) and Surface Shortwave radiation (Red). (b) Zonal (red) and Meridional (blue) wind stress. (c) Precipitation.

SST oscillations are evident with a period of about 50 days (Maloney et al. 2008).

The summer of 2002 also featured a nearly continuous surface meteorology and radiative flux data set, associated with the East Pacific Investigation of Climate experiment (EPIC2001; e.g. Raymond et al. 2004).

7.2 Model Details

In the model, the long-wave radiative, sensible, and latent heat fluxes are applied to the top model layer, while the shortwave radiation penetrates to depths given by Jerlov type IB water (Paulson and Simpson 1977). The attenuation coefficients for the infrared and visible bands of shortwave radiation are 0.5 m^{-1} and 20 m^{-1} respectively.

The fluxes have been computed from TAO buoy surface radiation and meteorology data using the COARE algorithm (Fairall et al. 2003). During the summer of 2002, much of the buoy data was of low quality or missing. When the data was of low quality, the air temperature was set to 1.3°C below the SST, representing the average June - October air-sea temperature difference from 2001, 2003, and 2004. The relative humidity is set to 85% in these circumstances as well. These conditions are similar to that used by Shinoda and Hendon 1998.

The model is initialized from interpolated T and S buoy profiles with two meter resolution. A one hour time step will be used for the KPP simulations. The new model framework requires a 15 minute time step.

7.2.1 GCM tendencies

Two sets of initial runs will be conducted. First, the model will be tested in a configuration that only considers one-dimensional atmosphere and ocean physics. In the second, vertical and advective tendencies (for temperature and salinity) from the coupled Colorado State model (CCoSM) will be added to the model, which represent processes like Ekman pumping. Although there is some evidence that horizontal advective tendencies are weak (McPhadden et al. 2008), the cumulative effective over the length of the simulation may be non-negligible.

CCoSM is the general circulation model from Colorado State University. Unlike other models, the grid structure is geodesic (Dazlich et al. 2010). This model can be run with a fully interactive atmosphere, ocean, land surface, and sea ice. For this study, the ocean and sea ice are dynamic. The dynamic model components are driven by ERA-Interim reanalysis surface forcing fields (2001-2005). The resolution of the model is approximately 2.25° .

The advective tendencies used in these experiments are taken as the average of the eight nearest grid points to 8°N , 95°W . We then average over the final four years of the run (2002 - 2005), the first year is ignored as spin up⁸.

7.3 Results

In our results, the one-dimensional model results and buoy data will be de-trended (using a 59 day running mean) for an easier comparison. Small errors in the calculation

⁸ While it takes many centuries for the deep ocean to spin up, the surface circulation is nearly fully developed after one year.

of the fluxes or the neglect of large scale forcing can cause a model drift relative to observations, especially given the shallow mixed layer depths in this region. Figure 7.2a shows the raw, daily averaged SST fields for KPP (blue), the new model (black), and the buoy data (dashed red). There is some drift in the new model near the beginning of the simulation (~day 120), but KPP follows the observed data well. The drift in the new model may be the result of diffusion associated with the virtual mass flux scheme. To

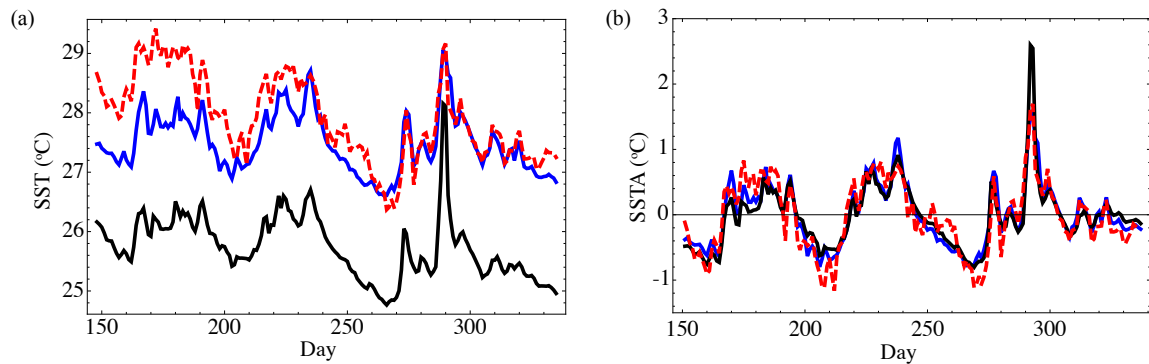


Figure 7.2 - Raw (a) and 59-day running mean filtered SST (b) for TAO data (dashed red), KPP (blue), and the new model (Black). In this plot and all others, the Day refers to days since January 1, 2002.

allow for an easier comparison, the data is filtered with a 59-day running mean (Figure 7.2b).

The SST anomalies for the new model and KPP compare well to the observations and to each other. The major structure of the intraseasonal SST oscillations are captured. There are a few times (especially near day 250) where the modeled SST deviates from the observed value. In the new model, there is a noticeable warm bias near day 290. We will return to this anomaly later.

The daily averaged MLDs for the new model and KPP versus observations are plotted in Figures 7.3a and 7.3b respectively. In Figure 7.3 the modeled MLDs are red

and the diagnosed buoy MLD is black. In general, the new model predicts an overly deep mixed layer and the KPP result is a bit better. Near day 250, the average MLD is deeper

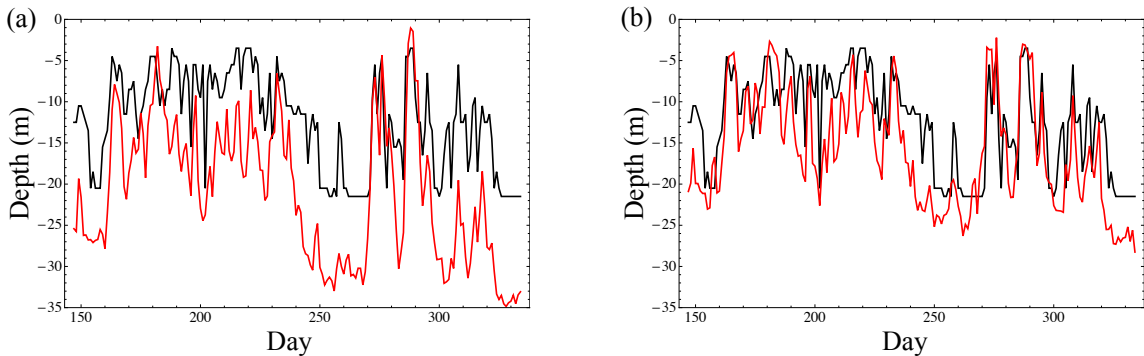


Figure 7.3 - (a) MLD predicted by the new model (red) versus observations (black) (b) MLD predicted by KPP (red) versus observations (black)

in the new model (and to a lesser extent KPP) compared to observations. It is possible that part of the model bias in SST near day 250 (Figure 7.2b) could be explained by an overly deep ML, as a shallower ML can be heated more effectively. If this were true, it is surprising that the SST simulated by the new model and KPP are so close despite the seven meter discrepancy in MLDs.

In these comparisons against buoy data, caution is required. Ideally, the MLD should be determined by a maximum density gradient criterion (as in Anderson et al 1996). The coarseness of the observed temperature and salinity profiles does not allow this method to be used, since buoy observations are only available at one, five, 10, 20, and 40 meters depth in the upper ocean. Instead the daily averaged buoy temperature and salinity profiles are interpolated to one-meter resolution and then the MLD is defined as the depth where there is a density increase from the surface value equivalent to a 0.5°C change in temperature, holding salinity fixed. Given the coarseness of the profiles, this method may introduce non-negligible errors in the MLD. To test this method, the

monthly averaged buoy MLD from Figure 7.3 is compared to the monthly averaged Monterey and Levitus (1997) data set. This comparison shows biases on the order of four to five meters an error of nearly 25% in some months.

Near day 290, the simulated MLDs agree fairly well with the TAO diagnosed value. However, the SST anomaly in the new model is approximately 1°C higher than observed. This is a time of weak wind stress and a stabilizing buoyancy flux. Little mixing near the surface is expected, but our model may not be representing all the sources of mixing (e.g. shear instability, breaking internal waves, etc...). Though shear instability is included in the new model through shear production of TKE, breaking internal waves are not included. To include the influence of breaking internal waves, KPP enforces a minimum value for the mixing coefficient. The minimum diffusivity is $10^{-5} \text{ m}^2\text{s}^{-1}$ and the minimum viscosity is $10^{-4} \text{ m}^2\text{s}^{-1}$. To this point we have not enforced a minimum viscosity or diffusivity in the new model framework. Figure 7.4 repeats the

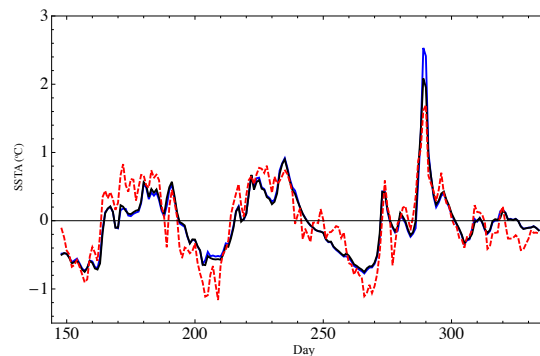


Figure 7.4 - Sensitivity to a minimum mixing coefficient in the new model. The simulated SST anomaly is in black. The result from Figure 7.2b has been replotted (blue). Again the TAO observation is the dashed red line.

initial simulation, but we have now included the KPP minimum mixing coefficients. In Figure 7.4, the initial result from Figure 7.2b is replotted in blue. The new model

framework with the inclusion of background mixing is plotted in black (the buoy data is

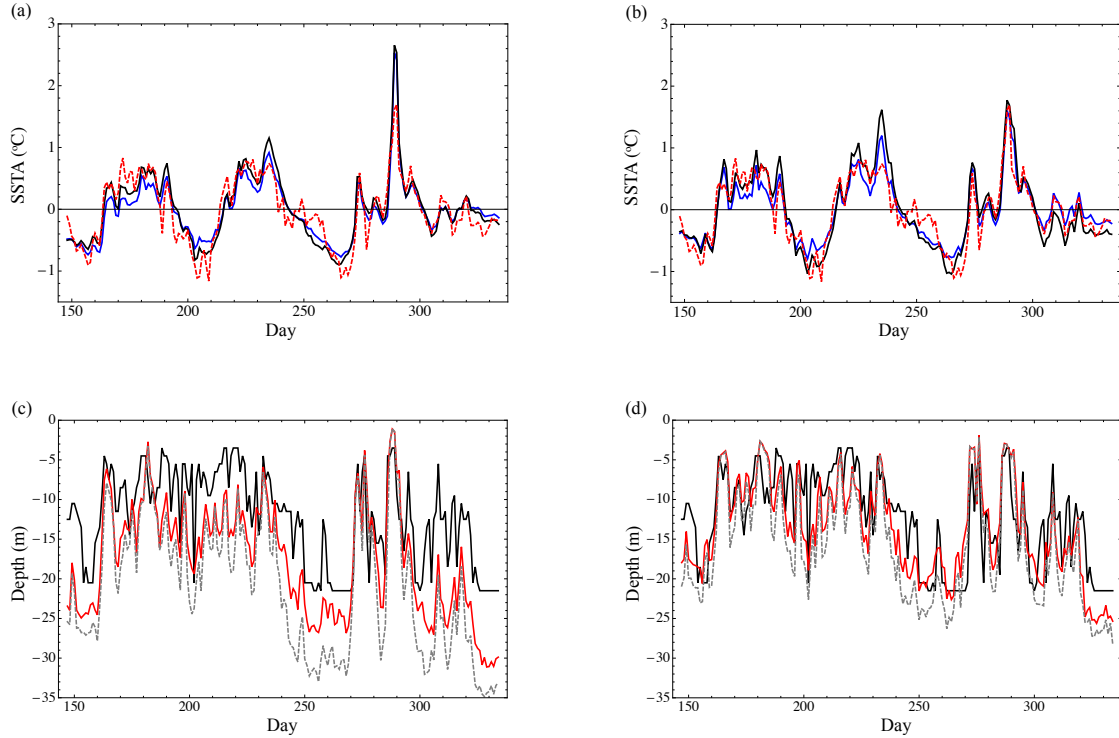


Figure 7.5 - Sensitivity of the simulated SST anomalies to advective tendencies diagnosed from CCoSM. (a) New model framework, (b) KPP. In (a)-(b), the baseline result is plotted in black, the run with advective tendencies in blue, and the dashed red line is from the TAO buoy. (c) OML depths simulated in the new model and (d) KPP. In (c)-(d), the observations are plotted in black, the control simulation is dashed gray, and the sensitivity test is in red.

again dashed red). The inclusion of the new mixing terms has decreased the amplitude of the warm anomaly near day 290 by nearly $0.5\text{ }^{\circ}\text{C}$. Apart from day 290, the minimum mixing coefficients have little effect on the intraseasonal SST variability.

The sensitivity of the SST anomalies to advective tendencies from CCoSM in the new model and KPP are plotted in Figures 7.5a and 7.5b respectively. In these figures, the initial test is plotted in blue for comparison. Overall, the pattern remains relatively unchanged. However, KPP seems to be slightly more sensitive to the tendencies than the new model framework (Figure 7.b). The simulation improves slightly near days 200 and 260, but degrades near day 225. In the new model (Figure 7.5a), there is a slight

improvement during the initial warm anomaly (day 170) and the cold anomalies at days 200 and 250. The overall conclusion is that the influence of large scale advective tendencies on intraseasonal SST variability is minor.

The sensitivity of the modeled mixed layer to advective tendencies are shown for KPP and the new model in Figure 7.5c and 7.5d. In both of these figures, the mixed layer depth from the control run is plotted as the dashed gray line and the new result is red. The tendency is a shallowing in both models. This makes physical sense as the large scale vertical advection tends to be upwelling in this region, which counteracts the downward diffusion of heat and salt.

7.4 Sensitivity Tests

We now conduct tests to determine how: shortwave and latent heat flux, wind stress, diurnal, and surface salinity flux variability influences the intraseasonal SST. Further, the influence of surface intensified diffusivity and the non-local KPP fluxes on the SST variability are examined. In the remaining tests, we now compress the result of the KPP model and new model onto a single plot. In these plots, KPP is plotted in blue and the new model is plotted in black (the data is again a dashed red line).

The first test fixes the latent heat flux to the summer time average. The resulting SST is plotted in Figure 7.6a. In both models, the magnitude of intraseasonal SST variability is greatly reduced. The warm anomaly near day 290 is almost non-existent. The cold anomaly near day 250 has also disappeared. Overall, there are very few times during the simulation where the SST remains similar to the initial test. This suggests that intraseasonal variability of latent and sensible heat fluxes strongly influence the SST near the CRD.

The simulated mixed layer depth for the new model (Figure 7.6b) and KPP

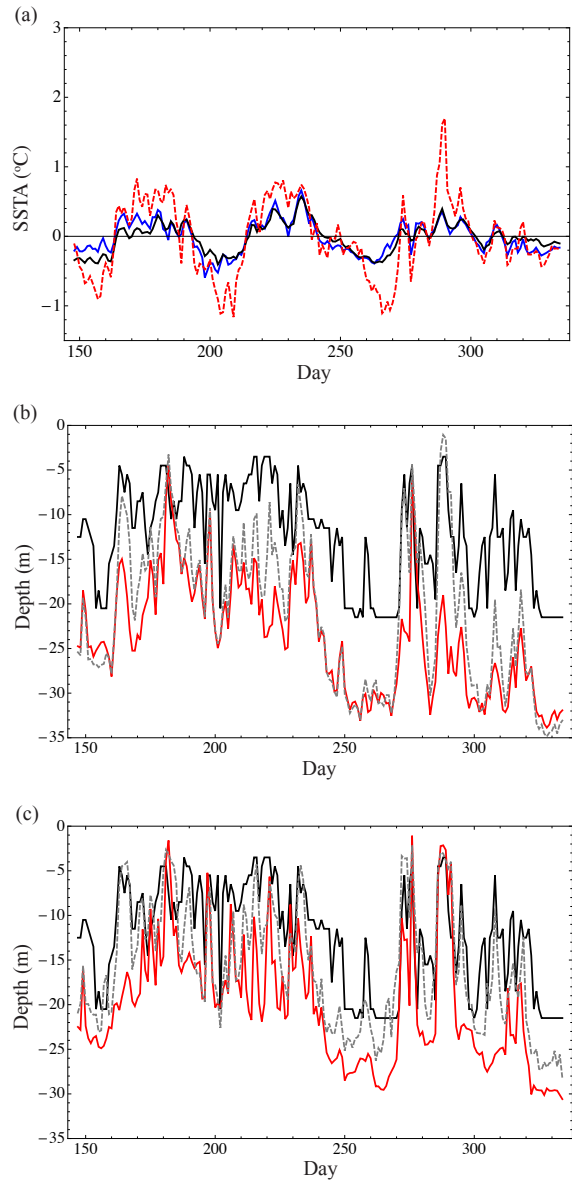


Figure 7.6 - Sensitivity to fixing the surface heat flux (Sensible plus Latent) to the summer time average. (a) SST anomaly, (b) OML depths simulated by the new model, (c) OML depths simulated by KPP. The colors are as in Figure 7.5.

(Figure 7.6c) is nearly identical to the original result (dashed gray). It seems that in this case, the MLD is not dependent on variations in the surface heat flux.

The next test fixes the incoming solar radiation to the summer average. As in the previous sensitivity test, there are some dramatic changes in the modeled SST (Figure

7.7a). Referencing Figure 7.2b, the magnitude of the cold event near day 170 is reduced in this run. The warm anomaly at day 290 is partially reduced in both models. In this

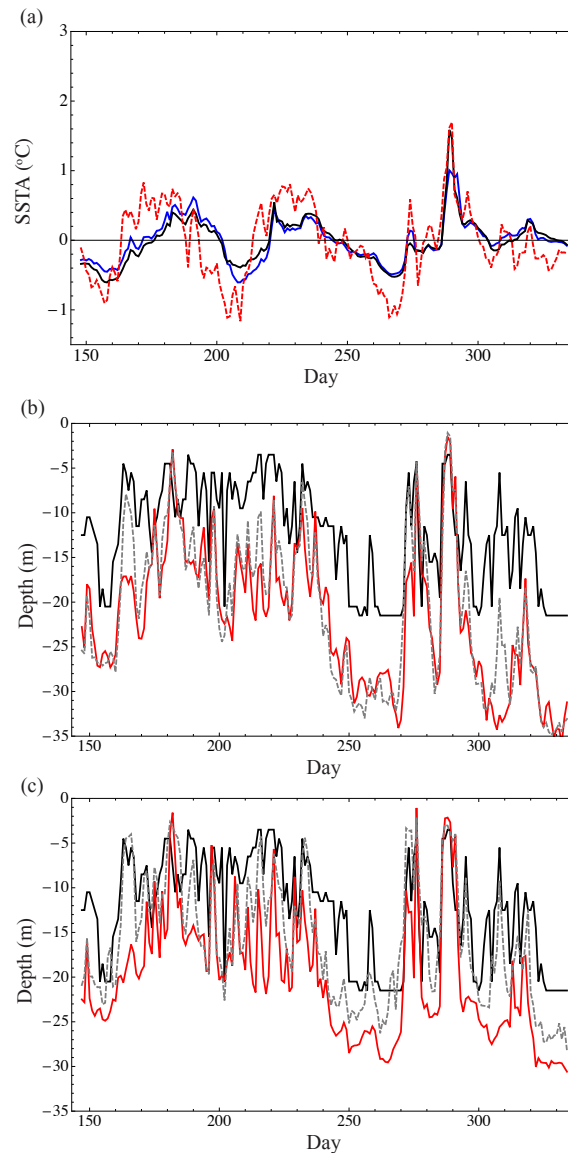


Figure 7.7 - Sensitivity to fixing the surface shortwave radiation to the summer time average. (a) SST anomaly, (b) OML depths simulated by the new model, (c) OML depths simulated by KPP. The colors are as in Figure 7.5.

test, an increased warm bias is noted at the end of the run in KPP and the new model. Again, the modeled mixed layer depths (Figures 7.7bc) stay relatively close in most instances (with the notable exceptions near days 160 and 305).

The most extreme test is to fix all fluxes to their summertime average. When this test is run (not shown), the resulting SST variability in both models is essentially non-

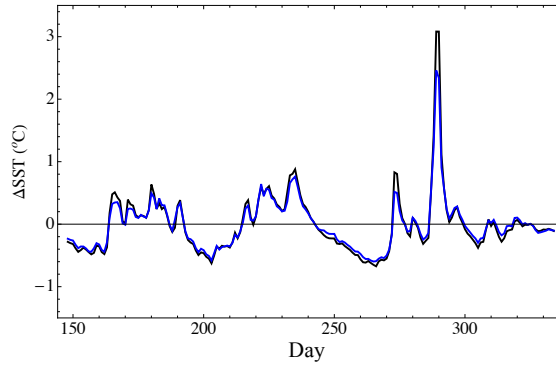


Figure 7.8 - Sum of SST changes due to fixing all fluxes to the summertime average (black). The blue line is the sum of SST changes due to fixing the surface heat flux and shortwave radiation to the summer average.

existent. If we then subtract the simulated SST anomalies from this test from the simulated SST in the baseline run, we obtain the blue line in Figure 7.8 (in this figure we have only plotted the output from the new model framework). If we now subtract the SST simulated in the fixed heat flux test from the baseline and add it to the SST difference from the fixed shortwave test relative to the baseline, we obtain the black curve in Figure 7.8. Schematically, these lines are defined as

$$\text{Blue Line} = SST_{control} - SST_{All\ Fixed}$$

$$\text{Black Line} = SST_{control} - \left(SST_{LH/SH\ Fixed} + SST_{SW\ Fixed} \right).$$

These two curves are nearly identical, suggesting that intraseasonal variations in surface heat fluxes and shortwave radiation are the primary control on intraseasonal SST variability near the CRD during boreal summer 2002. In KPP and the new model, intraseasonal variability in the surface heat flux and surface shortwave radiation do not control the variability of the OML base.

In the previous tests we have allowed shortwave radiation to penetrate with a dual

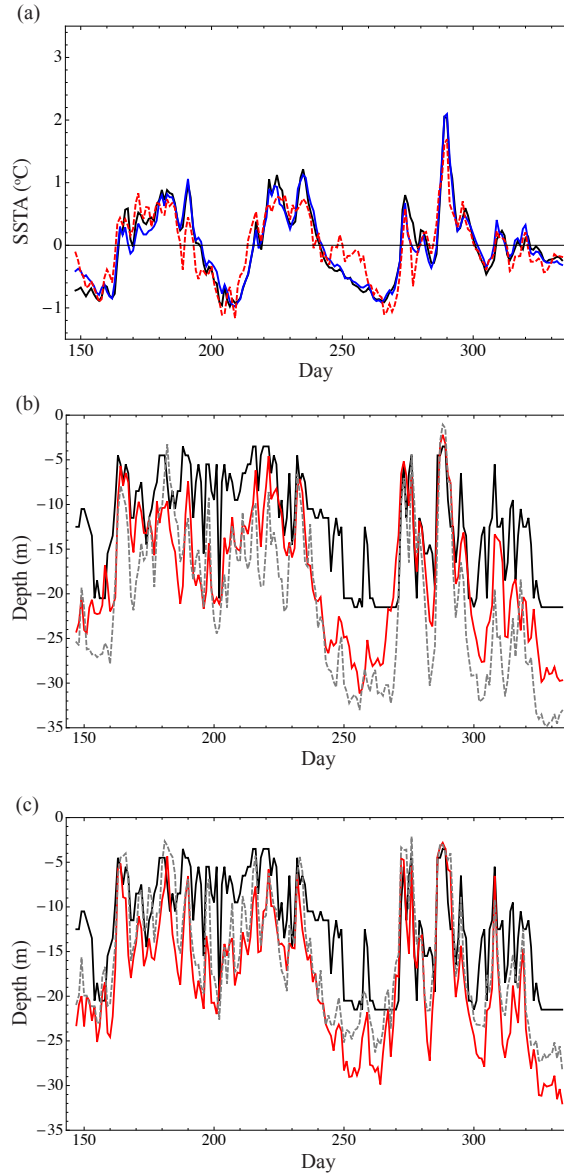


Figure 7.9 - Sensitivity to increasing the absorption of the visible component of shortwave radiation ($k = 5m^{-1}$). (a) SST anomaly, (b) OML depths simulated by the new model, (c) OML depths simulated by KPP. The colors are as in Figure 7.5.

band exponential profile, with a visible band extinction coefficient of $20 m^{-1}$. In this test, we increase the absorption coefficient such that 99% of the incoming solar radiation is

absorbed in the top 20 meters (previously it was 85%), which is equivalent to setting the extinction coefficient for visible light to 5 m^{-1} .

Figure 7.9 shows the resulting SST anomalies and MLDs for this sensitivity test. Qualitatively, the SST variability is similar to the control run (Figure 7.9a). The most common trend is for the SST anomalies to be greater in this test case than those in the control run. The modeled mixed layer depths simulated by the new model (Figure 7.9b) are slightly shallower in this sensitivity test. There are a few places where the modeled mixed layer base is deeper (e.g. near day 150). In KPP (Figure 7.9c), the mixed layer is relatively unchanged, except for a few place where it is slightly deeper.

Shallower mixed layer depths and warmer temperatures are expected. The places where the mixed layer base is deeper and SST cooler (e.g. near days 200 and 290) are counterintuitive. We believe that this result can also be explained by increased heat

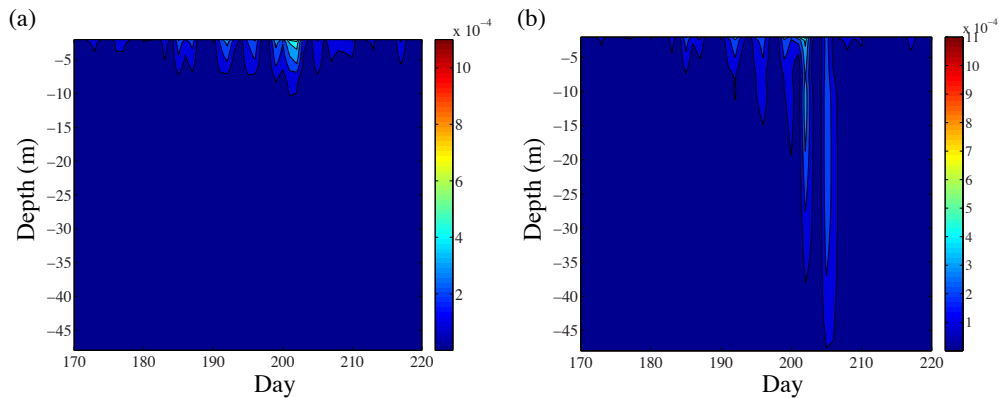


Figure 7.10 - Profiles of TKE near day 200 for (a) Baseline simulation, (b) and increased absorption test. The units are m^2s^{-2} .

absorbed at the surface. With limited solar heating at depth, there is less destruction of TKE. Therefore, there is more TKE available for mixing. This is seen in the new model output. Figure 7.10a shows the TKE near day 200 for the baseline run and Figure 7.10b shows the TKE for this sensitivity test. We see some bursts of TKE in this sensitivity

test, most likely associated with wind stress at the surface. It is possible that these fingers of TKE help mix the temperature and cool the SST.

Figure 7.11a shows the influence of fixing the surface stress to a summer average.

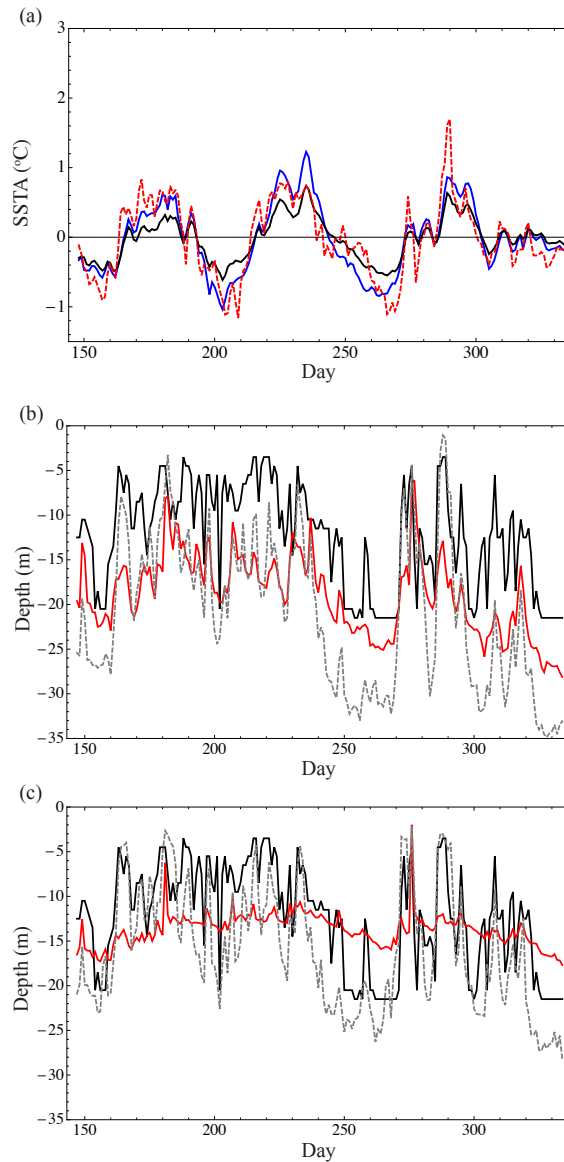


Figure 7.11 - Sensitivity to fixing the surface wind stress to the summer time average. (a) SST anomaly, (b) OML depths simulated by the new model, (c) OML depths simulated by KPP. The colors are as in Figure 7.5.

Overall the effect is minimal. The only readily observable changes are evident near days 200 and 290. Near day 200, the strength of the cold anomaly in the model is significantly

increased in the new model framework. The amplitude of the warm anomaly near day 290 is greatly reduced in KPP and the new model. The changes in intraseasonal variability is understood by comparing the summer average of surface stress to the stress at a given time. For example, day 290 is characterized by weak wind stress and a strong heat flux into the ocean. When we replace this weak stress with the summer average, we add a new source of TKE and hence mixing.

Conversely, near day 190, the wind stress is strong and the summertime average is weaker. Further, the heat flux is strongly out of the ocean (reference Figure 7.1). It seems that near day 290 the mixing was shear driven in the baseline run, but has become convective in this test.

The simulated mixed layer depths for the new model (Figure 7.11b) tend to be shallower, especially in regions where the summertime average of wind stress is smaller than the actual observed wind stress. The change in modeled mixed layer depths is far more dramatic in KPP (Figure 7.11c). The intraseasonal variability in the depth of the OML base is greatly reduced. It seems that KPP is very sensitive to the strength and variability of the wind stress.

Since changing the wind forcing alters the Richardson number, the lack of mixed layer depth variability could be tied directly to the intrinsic parameterization. As a check, this test has been run with the PWP model (not shown), and strong mixed layer variability remains. Since both of these models determine the boundary layer depth by a critical Richardson number, we do not believe that the lack of variability in KPP is directly tied to the boundary layer depth scheme.

Instead, we hypothesize that the cause is indirect and is a result of the internal mixing scheme. This parameterization is designed to represent unresolved shear instabilities and is known to be a model deficiency. As discussed in Chapter 1, mixing at the base of the boundary layer influences mixing through the upper ocean. This implies that stronger shear at depth will increase mixing in the boundary layer. It is possible that less shear (and less variability in the shear) changes the mixing through the upper ocean.

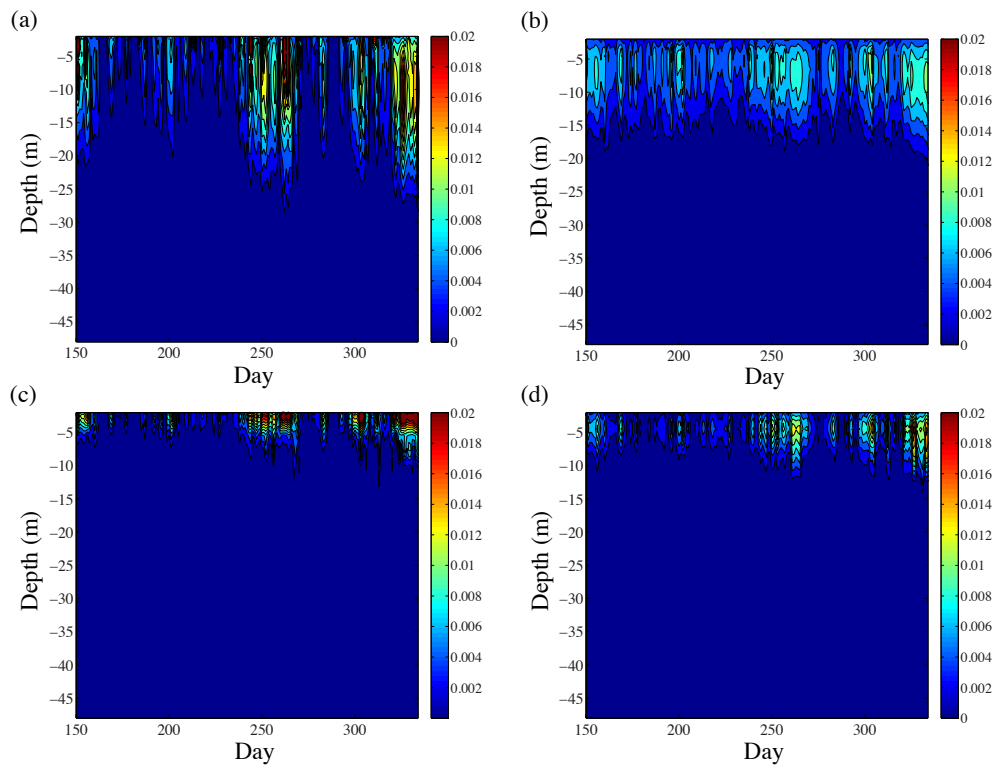


Figure 7.12 - Modeled viscosity for the baseline run (a) and (c) and the sensitivity test fixing wind stress to the summertime average (b) and (d). The top row is for KPP and the bottom is the new model framework. The units are m^2s^{-1} .

This changes the profile of momentum, temperature, and salinity, which amplifies the changes in Richardson number. This in turn would influence the mixed layer depth.

To better illustrate this mechanism, we have plotted the model predicted viscosity for the KPP baseline run and wind stress sensitivity test in Figures 7.12a and 7.12b respectively. The companion results for the new model are given in Figure 7.12cd.

As seen in previous chapters, the mixing predicted by KPP extends through a larger depth than the new model, however, the maximum magnitude is roughly equivalent. In this sensitivity test, both models predict less mixing. The striking difference is the difference in variability of mixing between the two models. In KPP, the viscosity remains fairly constant through the entire run. On the other hand, the new model retains more of the variability evident in the control simulation. As we have seen throughout this work, KPP is very sensitive to the amount of shear.

7.4.1 Sensitivity to model design

In the next test the mixing between the first and second model layers is artificially increased by a factor of five for the entire run. This increase is intended to represent missing model processes, such as wave breaking. Kantha and Clayson (1994) conducted a similar sensitivity test in their simulation of the western Pacific warm pool (Section 4.8 of Kantha and Clayson 1994). They found that an increased diffusivity improved the model simulation of MLDs.

Figure 7.13a shows the intraseasonal SST variability for this test. The only significant change in this run is at day 290. If we are thinking of the artificially elevated mixing as a representation of wave breaking, it seems that breaking would not occur near day 290. As previously mentioned, day 290 is a period of weak surface stress, so local wave generation is unlikely. This does not preclude the possibility of waves entering the region from afar and breaking locally.

The results of this test confirm the hypothesis explaining the reduction of the warm anomaly at day 290 in the previous sensitivity test.. The constant wind stress value

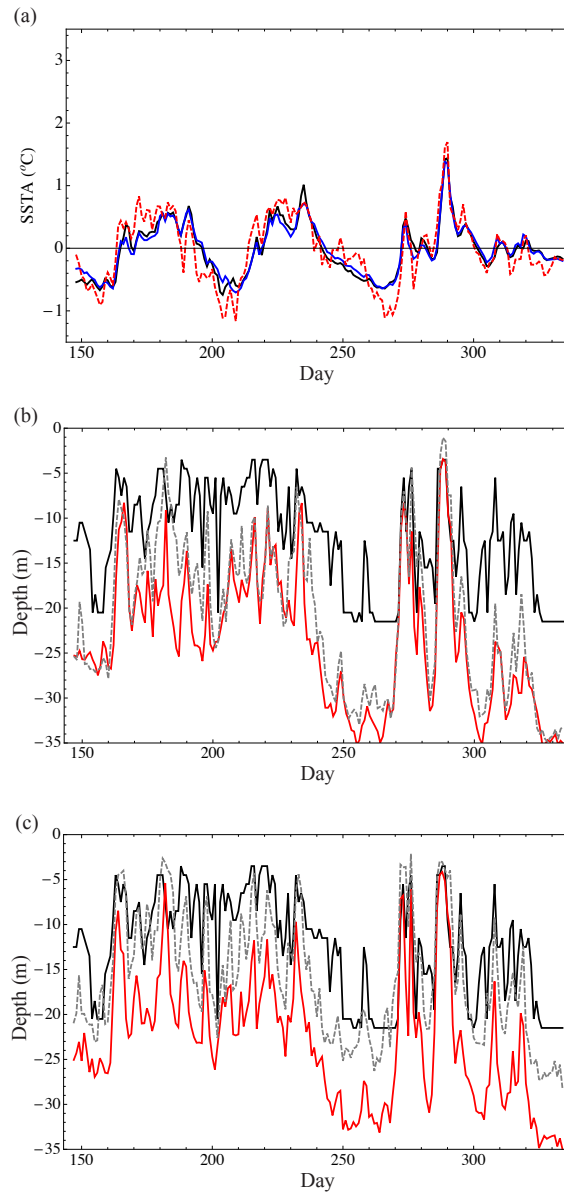


Figure 7.13 - Sensitivity to fixing the artificially increasing the diffusivity in the top model layer. (a) SST anomaly, (b) OML depths simulated by the new model, (c) OML depths simulated by KPP. The colors are as in Figure 7.5.

is greater than the actual forcing near day 290. This elevated wind stress increases the mixing strength, similar to what was artificially done in Figure 7.13a. In general the

modeled mixed layer depths (Figures 7.13bc) are either unchanged or deeper, which is what we would expect when extra mixing is introduced.

We have also assessed the influence of the non-local source term on the KPP simulated SST anomalies. In this test, we use the forcing from the control simulation. Without the nonlocal forcing, KPP should behave similarly to PWP or Pacanowski and Philander (1981). The result (Figure 7.14) is nearly identical to the control run. We do not want suggest that non-local effects are not significant. The subsurface temperature is

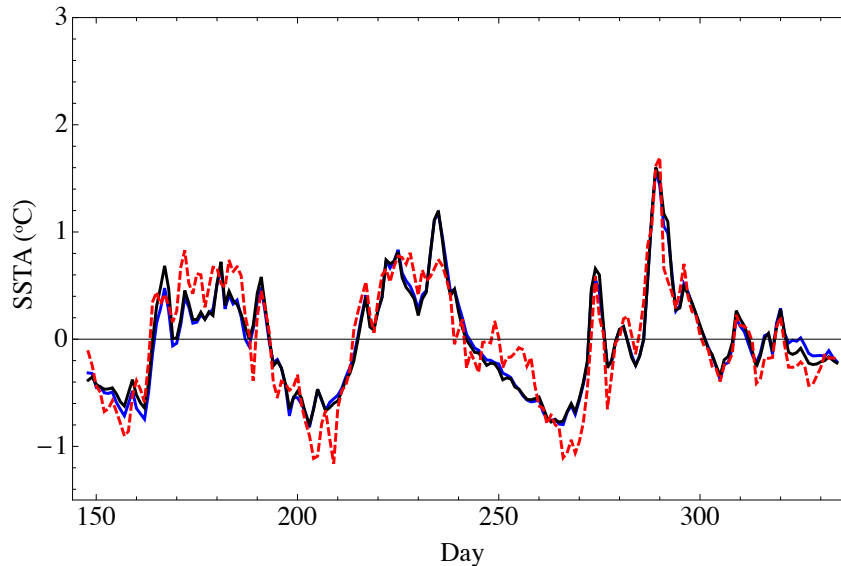


Figure 7.14 - Evaluation of the impact of non-local effects on KPP simulated SST. Black is the control run and Blue is the result from the test.

better mixed when the non-local terms are included (see Figure 4.10).

In addition to the test shown to this point, the impact of diurnal variability of the surface forcing was evaluated. The change in the simulated SST anomalies was minimal (not shown). The influence of salinity flux variability was also examined. While other studies have shown that intense precipitation can form barrier layers, which limit the diurnal penetration of the mixed layer base (e.g. Anderson et al. 1996), our sensitivity test

shows very little change from the control run. It may be possible that the precipitation is too weak in the vicinity of the CRD to initiate a barrier layer or that the MLDs are shallow enough to minimize the effect of barrier layers.

We have evaluated intraseasonal SST variability in two fairly complex vertical mixing models. Further, similar results were obtained in a less complex mixing model (PWP)⁹. A logical question would be, how much complexity can we strip out of the model while retaining the observed variability? To answer this question, we have constructed two different slab models, the first assumes an annual mean mixed layer

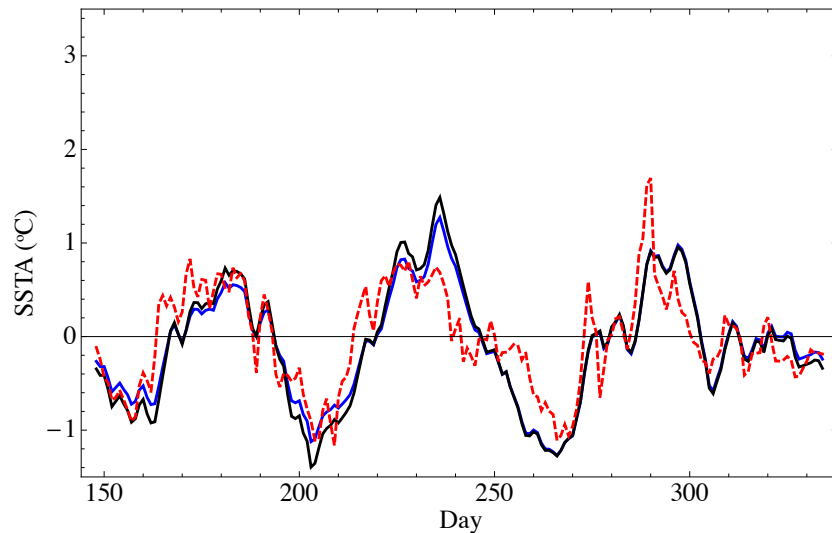


Figure 7.15 - SST anomalies simulated by a slab model. The black line is for a constant mixed layer depth. The blue line allows the mixed layer to vary according to the value given by the Monterrey and Levitus dataset.

depth of 11 meters. The second allows for some variability of the mixed layer depth. This is accomplished by changing the mixed layer depth monthly according to the Monterrey and Levitus (1997) dataset.

⁹ These runs were conducted by Dr. Eric Maloney

The results from the control case are shown in Figure 7.15. In this figure, the black line uses the constant mixed layer depth. The initial observation is that the slab model does a decent job capturing the SST variability. There are some strong biases, especially between days 240 and 270 and during the last warm anomaly. The bias in the vicinity of the strong warm event is not surprising as previous tests have shown that the simulated SST is sensitive to the mixing parameterization.

Allowing the mixed layer to change monthly does slightly improve the result (most notably near day 200), but the change is minor. It is possible that the slab model could be improved by a mixed layer depth data set with higher temporal resolution.

7.5 Conclusions

Three intraseasonal SST oscillations with a magnitude of about 1°C were observed during boreal summer of 2002 in the data. One dimensional simulations using the KPP model, and the newly developed mixing model, forced by the observed fluxes at an eastern Pacific TAO buoy (8°N 95°W) show that intraseasonal variability in the latent heat fluxes and shortwave heating are primarily responsible for the SST variability observed during boreal summer of 2002. Variations in surface stress are occasionally important to SST variability. This effect is most notable near the warm peak at day 290. When wind stress variability is neglected, the amplitude of this warm anomaly is reduced by about 50%. We again find that KPP is very sensitive to the model shear, and mixes momentum more rapidly than the new model and PWP.

A test where diffusion is artificially increased between layers one and two has a similar impact as fixing the wind stress to the summertime average on the third warm anomaly. Since the averaged value of wind stress used in the sensitivity test is greater

than that observed at day 290, an increased wind stress will also increase the amount of mixing near the surface.

To account for large scale processes that are missing in a one-dimensional run, advective tendencies derived from monthly mean output of CCoSM, a coupled geodesic ocean sea-ice model driven by ERA-Interim reanalysis, are added to the simulation. Including advection improves the SST field slightly, validating the use of one-dimensional models to study SST variability in the vicinity of the CRD.

There are a few potential caveats that should be mentioned in association with the GCM results. First, there may be issues with the reanalysis itself. There are a number of assumptions inherent in the reanalysis. For example, there must be some parameterization of how clouds interact with radiation to produce a shortwave forcing. Second, it is important to note that the resolution of the run is quite coarse ($2.5^\circ \times 2.5^\circ$). It is possible that small scale fluctuations in wind jets (e.g. the Gulf of Papagayo) may not be resolved. Since the reanalysis resolution is $1.25^\circ \times 1.25^\circ$, repeating the OGCM simulation at this resolution may improve the tendencies used in the one-dimensional models. Finally, we are also neglecting a negative feedback in our one-dimensional simulations. When the thermocline in an OGCM deepens to much, the pressure gradient changes. The depth anomaly is smoothed in a three-dimensional model. Any anomalous deepening in the one-dimensional model proceeds without this correction.

The CRD is associated with mean upwelling and shallow MLDs. It is possible that mechanisms for intraseasonal variability are different in other portions of the eastern Pacific warm pool, especially to the northwest where mean MLDs are deeper and ocean dynamics are less prominent. This, along with the caveats associated with the advective

GCM tendencies lead to the conclusion that a broader, regional, study is warranted to determine if the proposed mechanism for intraseasonal SST variability is evident in other portions of the eastern Pacific.

Chapter 8:

General Conclusions and Future

Work

The upper ocean is very important to many coupled processes. It is responsible for the transmission of fluxes between the atmosphere and the deep ocean. Accurate simulation of the depth of the boundary layer is integral to processes such as the meridional overturning circulation (Mohammad and Nilsson 2004) and El Niño. Further, hurricanes create an intense local coupling between the atmosphere and ocean. It is hypothesized that the maximum potential intensity of hurricanes is dependent on the SST (Emmanuel 1988). This implies that accurate simulation of the upper ocean is important for hurricane studies.

A wide variety of processes influence the dynamics of the mixed layer; such as surface fluxes, wave induced effects (i.e. Langmuir Cells), and entrainment at the base of the boundary layer. In this work, we have focused in on one of the processes influencing the upper ocean, the penetrating component of short wave radiation.

Studies of how penetrating short wave radiation influences the three-dimensional ocean circulation began with Schneider and Zhou (1998). Schneider and Zhou (1998) found that the simulated distribution and depths of the annually averaged mixed layer depths was greatly improved when the solar radiation was allowed to penetrate beyond the top model layer.

In this past decade, attention has shifted to how spatially variable attenuation coefficients influence the properties of the large scale ocean. The coefficients vary according to the amount of chlorophyll at a given location. The tropical response is not robust in previous work. Some, such as GA09 and Nakamoto et al (2001), find that the tropical Pacific cools relative to a chlorophyll free ocean. While others, such as Murtugudde et al. (2001), find the tropical Pacific warms. Manizza et al. (2005) found tropical Pacific cooling for one bio-optical parameterization and warming for another.

Most of the prior work has neglected vertically variable attenuation, with a few exceptions (e.g. Ohlmann et al. 1998). In addition, the focus has been on the interseasonal response of the ocean to spatially variable chlorophyll. Here we examined the response on shorter time scale.

Previous mixed layer models have some very well known biases. For example, models that predict the mixed layer depth by a critical Richardson number (e.g. KPP) have a deep bias for coarse resolution and shallow mixed layers (as seen in Chapter 4). The interior mixing scheme in KPP is far from perfect (e.g. Zaron and Moum 2009, Jackson et al. 2008). Since the mixed layer diffusivity is assumed to fit to the interior predicted value, the deficiencies in the interior scheme can affect the result in the upper

ocean. KPP is also more sensitive to resolution than other mixed layer models (e.g. Durski et al. 2004, Acreman and Jeffery 2007).

Bulk mixed layer models (e.g. KT) do not exhibit as strong of a resolution dependence as KPP. However, assumption of perfectly mixed properties in the upper ocean is not confirmed in observations and precludes potentially important processes. The entrainment rate predicted by these models is dependent on the layer integrated TKE. Physically, we expect that the entrainment should depend on energy at the boundary layer base and not throughout the entire layer.

To address some of these issues, we have developed a new mixing model that explicitly predicts the depth of the boundary layer base, like bulk models. Unlike bulk models, the entrainment rate is dependent on energy at the boundary layer base. The specific form of entrainment follows L10, but has been extended to include shear at the base of the boundary layer. The new model does not require the boundary layer to coincide with the mixed layer, as is assumed by bulk mixed models. The unrepresented mixing follows Canuto et al. (2002, 2008). This model is also easily adaptable to any coordinate system, unlike KPP.

To evaluate the model, we have developed VVM-Aqua, which follows Jung and Arakawa (2008). This model naturally incorporates the CLII mechanism for Langmuir Cell generation. Currently the model utilizes a linear equation of state and the sub-grid mixing scheme follows Noh et al. (1999). This model was evaluated by shear turbulence and Langmuir turbulence simulations that have been conducted by many previous authors (e.g. M97, Li et al. 2005, Polton et al. 2005, Harcourt and D'Asaro 2008). The general

conclusion is that VVM-Aqua is slightly more diffusive than previous results. We also find that the shear turbulence results matched well, but the Langmuir turbulence simulation did not.

In our initial evaluations, KPP outperforms the new model in pure convective situations. This is due to the lack of a counter gradient fluxes in the new model. In shear dominated regimes, the new model behaves as well, and sometimes better, than KPP.

In the simulations that followed W98, we found that the simulated temperature and velocity fields are sensitive to the chosen attenuation coefficient. If the short wave radiation is confined to the top level the thermocline depth is much shallower than the baseline run. For lower values of k_{VIS} , the near surface stratification is diminished and the velocity is more easily mixed. The surface pressure gradient is able to overwhelm the momentum input.

When observed chlorophyll profiles were utilized, there was little change relative to the baseline simulation. The irradiance profile that resulted from the optical parameterization of GA09 was nearly identical to that obtained when using a constant k_{VIS} of 20 m^{-1} .

The second chlorophyll profile was designed such that the necessary condition for instability derived in Lewis et al. (1983) is satisfied near seven meters depth. This profile did result in velocity and temperature changes relative to the baseline simulation, but the resulting behavior was similar to the runs with high extinction coefficients. Repeating the test at one, four, and ten meter resolution did not significantly alter the result relative

to the baseline simulation at those resolutions. This may be expected given the similarities in the results of Manizza et al. (2005) and GA09. Using a full ecosystem model slightly modulated the tropical ocean response.

When spatial (and temporal) variability of surface chlorophyll was considered, we found that surface temperature near the eastern boundary is warmer when compared to the baseline run. This is consistent with previous one-dimensional results. When chlorophyll is included, the two-dimensional model behaves similar to what is expected from a purely local heat balance. In other words, where the chlorophyll is increased, the temperature is warmer, and the temperature is cooler when there is less chlorophyll. This validates the result of GA09 and Anderson et al. (2009) that the water clarity in the subtropical gyres is more important to the temperature of waters in the EUC and the cold tongue than water clarity at the equator.

In the final test, all the different pieces were brought together to determine what controls the intraseasonal SST variability in the eastern pacific. Since the large scale terms were small, both in our companion GCM simulation and some observations (McPhadden et al. 2008), we were able to accurately simulate the intraseasonal SST variability. We found that the intraseasonal (not diurnal) variability of surface heat fluxes and shortwave radiation dominate the SST variability near the Costa Rica dome. When the attenuation coefficients were changed, the basic picture remained the same, although some of the variability is slightly reduced.

8.1 Future Work

The new model designed in this research behaves well, but as with many models, there are things to change. First and foremost is the inclusion of non-local terms in the turbulent fluxes of tracer. Currently, we parameterize the turbulent flux of theta as

$$\overline{w'\theta'} = -K \frac{\partial \theta}{\partial z}. \quad \text{With a non-local term, the heat flux becomes } \overline{w'\theta'} = -K^* \left(\frac{\partial \theta}{\partial z} - \gamma \right).$$

Kantha and Clayson (1994) use a form of γ suggested by Deardorff (1972). This form is used in KPP. However, implementing a non-local forcing in this manner does not seem correct. Change of the algebraic equation for the heat flux would change the structure function. This is why we include an asterisk on the mixing coefficient.

Instead, we believe that counter gradient effects are best added when we implement the algebraic model as a level 3 model. In this framework, the variance of temperature and salinity would be prognostic. This was done in Cheng et al. (2002) for atmospheric applications (i.e. no salinity). It seems reasonable to assume that a similar method could be followed when salinity is included.

In addition to non-local forcing, we would like to rework how the layers expand and contract for a given virtual mass flux. Currently the number of layers in the boundary layer and the deep ocean are fixed through the length of the run. This would imply that as we entrain, the resolution in the boundary layer decreases and the resolution in the deep ocean increases. Take the two-dimensional simulations as an example. With wind only, the western boundary will continue to entrain unchecked. In Figure 8.1 we

have plotted the initial model layer thicknesses (top 15 layers) in black circles. At the

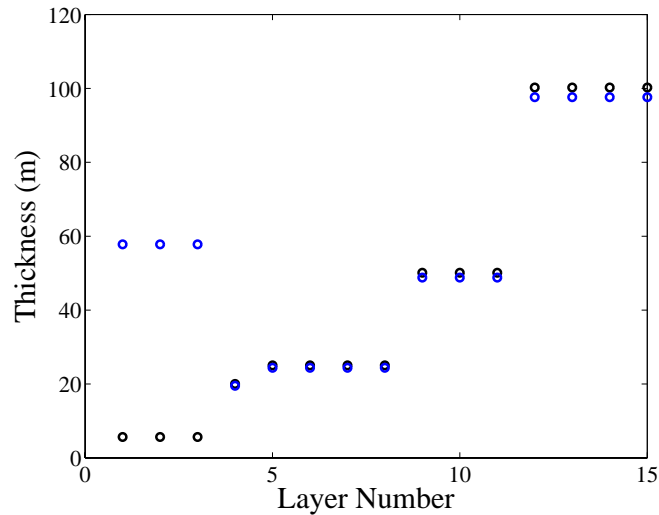


Figure 8.1 - Layer thicknesses, of the top 15 layers, adjacent to the western boundary for the baseline two dimensional run. The black circles are the initial thicknesses and the blue circles are thicknesses at the end of the ten year run.

end of the 10 year run (blue circles), the three layers in the boundary layer have gone from five meters in thickness to nearly 60. In the deep ocean, the layers thin. In most cases we would prefer that the resolution within the boundary layer to be higher than the deep ocean.

Instead of the current implementation, we could “absorb” some of the layers from the deep ocean into the boundary layer. When the boundary layer thins, the extra layers would be moved back to the deep ocean. On the other hand, when the boundary layer collapses there is a lot of variation in a small thickness and high resolution could be important. The proposed method of moving layers in and out of the boundary layer may not improve the simulation relative to our original scheme.

In addition to model improvements, there are many remaining physical questions. We have only examined a single bio-optical parameterization, many more remain. Manizza et al. (2005) found a completely opposite response with a new parameterization.

Without interactive biology, we are unable to examine some critical questions. As more nutrient rich water is injected into the upper ocean by entrainment or mesoscale eddies, phytoplankton populations increase and more heat is trapped near the surface. This could shut off the entrainment and kill the phytoplankton. On the other hand, if the population is concentrated, secondary circulations could develop that enhance entrainment. The influence of bio-optical parameterization and the possible stabilizing feedback could be examined in one-dimension. The influence of secondary circulations require an extension to three dimensions.

When studying the influence of vertical variations of chlorophyll on the model temperature and velocity, we assumed a one-way interaction between the vertical mixing model and the large scale forcing. To relax this assumption there are two requirements. First, we need to use the two-dimensional framework developed in this work, or move the model to three dimensions. The easiest option is the former. However, the physical mechanism that maintains the EUC is different than what is observed and may be difficult to accurately parameterize. Use of the two dimensional framework also ignores the important influence of extratropical water clarity.

The second requirement is independent of the first. To simulate the distribution of phytoplankton beyond more than two weeks, an ecosystem model is required. The most straightforward option is to couple a NPZD ecosystem model to the two-dimensional framework developed in this dissertation, but the eventual goal would be a move to three-dimensions.

In addition to simply simulating the vertical distribution of phytoplankton, and hence chlorophyll, it would also be interesting to take up the question of how sensitive the ocean is to the bio-optical parameterization.

It has been hypothesized by Anderson et al. (2007) that variability in penetrating shortwave radiation associated with surface chlorophyll influences the period and magnitude of El Niño Southern Oscillation (ENSO). To accurately simulate ENSO, it is important for a model to capture the boundary layer deepening and shoaling associated with wave propagation. The depth of the thermocline is essential to the discharge-recharge mechanism proposed by Jin (1997) to explain an ENSO cycle. We believe that the model developed in this work is very well suited to simulate the movement of the thermocline associated with wave propagation. Simulation of ENSO would require a coupled atmosphere. This could be accomplished in our two-dimensional framework by coupling to an atmospheric model similar to what is described in Sobel et al. (2003).

Appendix A:

Derivation of the Vorticity

Equations with CLII Forcing

The derivation of the equation describing the x-component of vorticity (ξ) begins as suggested in Table 2.1. Performing $\frac{\partial}{\partial y}(2.3) - \frac{\partial}{\partial z}(2.2)$ yields

$$\begin{aligned} \frac{\partial}{\partial y} \left(\frac{\partial w}{\partial t} + u \frac{\partial w}{\partial x} + v \frac{\partial w}{\partial y} + w \frac{\partial w}{\partial z} \right) - \frac{\partial}{\partial z} \left(\frac{\partial v}{\partial t} + u \frac{\partial v}{\partial x} + v \frac{\partial v}{\partial y} + w \frac{\partial v}{\partial z} \right) &= \frac{\partial B}{\partial y} \\ - \frac{\partial u_s \eta}{\partial y} - \frac{\partial v_s \xi}{\partial y} + \frac{\partial F_w}{\partial y} + f \frac{\partial}{\partial z} (u + u_s) + \frac{\partial u_s \zeta}{\partial z} - \frac{\partial F_v}{\partial z} \end{aligned}$$

Where we have again defined

$$\begin{aligned} F_v &\equiv - \frac{\partial \overline{u'v'}}{\partial x} - \frac{\partial \overline{v'v'}}{\partial y} - \frac{\partial \overline{v'w'}}{\partial z} \\ F_w &\equiv - \frac{\partial \overline{u'w'}}{\partial x} - \frac{\partial \overline{v'w'}}{\partial y} - \frac{\partial \overline{w'w'}}{\partial z} \\ B &\equiv g \frac{\rho}{\rho_o}. \end{aligned}$$

For the moment, we turn our attention to the left hand side only. When the derivative operation is performed, we obtain

$$\begin{aligned} \frac{\partial}{\partial t} \left(\frac{\partial w}{\partial y} - \frac{\partial v}{\partial z} \right) + \frac{\partial u}{\partial y} \frac{\partial w}{\partial x} + u \frac{\partial^2 w}{\partial x \partial y} - \frac{\partial u}{\partial z} \frac{\partial v}{\partial x} - u \frac{\partial^2 v}{\partial x \partial z} + \frac{\partial v}{\partial y} \frac{\partial w}{\partial y} + v \frac{\partial^2 w}{\partial y^2} - \frac{\partial v}{\partial z} \frac{\partial v}{\partial y} \\ - v \frac{\partial^2 v}{\partial y \partial z} + \frac{\partial w}{\partial y} \frac{\partial w}{\partial z} + w \frac{\partial^2 w}{\partial y \partial z} - \frac{\partial w}{\partial z} \frac{\partial v}{\partial z} - w \frac{\partial^2 v}{\partial z^2} = RHS. \end{aligned}$$

Rearranging, we obtain

$$\begin{aligned} \frac{\partial}{\partial t} \left(\frac{\partial w}{\partial y} - \frac{\partial v}{\partial z} \right) + u \frac{\partial}{\partial x} \left(\frac{\partial w}{\partial y} - \frac{\partial v}{\partial z} \right) + v \frac{\partial}{\partial y} \left(\frac{\partial w}{\partial y} - \frac{\partial v}{\partial z} \right) + w \frac{\partial}{\partial z} \left(\frac{\partial w}{\partial y} - \frac{\partial v}{\partial z} \right) + \frac{\partial u}{\partial y} \frac{\partial w}{\partial x} \\ - \frac{\partial u}{\partial z} \frac{\partial v}{\partial x} + \left(\frac{\partial w}{\partial y} - \frac{\partial v}{\partial z} \right) \frac{\partial v}{\partial y} + \left(\frac{\partial w}{\partial y} - \frac{\partial v}{\partial z} \right) \frac{\partial w}{\partial z} = RHS. \end{aligned}$$

Using the definitions of vorticity and adding and subtracting $\frac{\partial u}{\partial z} \frac{\partial u}{\partial y}$ yields

$$\frac{\partial \xi}{\partial t} + u \frac{\partial \xi}{\partial x} + \frac{\partial v \xi}{\partial y} + \frac{\partial w \xi}{\partial z} - \eta \frac{\partial u}{\partial y} - \zeta \frac{\partial u}{\partial z} = RHS$$

Next, we add and subtract $\xi \frac{\partial u}{\partial x}$, which gives

$$\frac{\partial \xi}{\partial t} + \frac{\partial u \xi}{\partial x} + \frac{\partial v \xi}{\partial y} + \frac{\partial w \xi}{\partial z} - \xi \frac{\partial u}{\partial x} - \eta \frac{\partial u}{\partial y} - \zeta \frac{\partial u}{\partial z} = RHS.$$

Now we return to the RHS

$$\begin{aligned} LHS &= \frac{\partial B}{\partial y} + \frac{\partial u_s \eta}{\partial y} + \frac{\partial u_s \zeta}{\partial z} - \frac{\partial v_s \xi}{\partial y} + \frac{\partial F_w}{\partial y} - \frac{\partial F_v}{\partial z} + f \frac{\partial}{\partial z} (u + u_s) \\ LHS &= \frac{\partial B}{\partial y} + \eta \frac{\partial u_s}{\partial y} + u_s \frac{\partial \eta}{\partial y} + u_s \frac{\partial \zeta}{\partial z} + \zeta \frac{\partial u_s}{\partial z} - \frac{\partial v_s \xi}{\partial y} + \frac{\partial F_w}{\partial y} - \frac{\partial F_v}{\partial z} + f \frac{\partial}{\partial z} (u + u_s) \end{aligned}$$

Using equation (2.6), we can write

$$\begin{aligned} LHS &= \frac{\partial B}{\partial y} + \eta \frac{\partial u_s}{\partial y} - u_s \left(\frac{\partial \xi}{\partial x} + \frac{\partial \zeta'}{\partial z} \right) + u_s \frac{\partial \zeta}{\partial z} + \zeta \frac{\partial u_s}{\partial z} - \frac{\partial v_s \xi}{\partial y} + \frac{\partial F_w}{\partial y} - \frac{\partial F_v}{\partial z} + f \frac{\partial}{\partial z} (u + u_s) \\ LHS &= \frac{\partial B}{\partial y} + \eta \frac{\partial u_s}{\partial y} - \frac{\partial u_s \xi}{\partial x} + \xi \frac{\partial u_s}{\partial x} + u_s \frac{\partial \zeta}{\partial z} - \frac{\partial v_s \xi}{\partial y} + \frac{\partial F_w}{\partial y} - \frac{\partial F_v}{\partial z} + f \frac{\partial}{\partial z} (u + u_s) \end{aligned}$$

We are now ready to reinstate both sides of the equation. After rearranging terms our equation becomes

$$\begin{aligned} \frac{\partial \xi}{\partial t} + \frac{\partial u \xi}{\partial x} + \frac{\partial u_s \xi}{\partial x} + \frac{\partial v \xi}{\partial y} + \frac{\partial v_s \xi}{\partial y} + \frac{\partial w \xi}{\partial z} - \xi \frac{\partial u}{\partial x} - \xi \frac{\partial u_s}{\partial x} - \eta \frac{\partial u}{\partial y} - \eta \frac{\partial u_s}{\partial y} - \zeta \frac{\partial u}{\partial z} \\ - \zeta \frac{\partial u_s}{\partial z} = \frac{\partial B}{\partial y} + \frac{\partial F_w}{\partial y} - \frac{\partial F_v}{\partial z} + f \frac{\partial}{\partial z} (u + u_s) \end{aligned}$$

$$\frac{\partial \xi}{\partial t} + \frac{\partial u_* \xi}{\partial x} + \frac{\partial v_* \xi}{\partial y} + \frac{\partial w \xi}{\partial z} - \xi \frac{\partial u_*}{\partial x} - \eta \frac{\partial u_*}{\partial y} - \zeta \frac{\partial u_*}{\partial z} - f \frac{\partial u_*}{\partial z} = \frac{\partial B}{\partial y} + \frac{\partial F_w}{\partial y} - \frac{\partial F_v}{\partial z}.$$

This is a similar form to that used in the atmospheric version of the VVM, except the u and v velocities are modified to include the Stokes drift. The derivations of the η and ζ equations are similar and thus they are not presented.

Appendix B:

Higher Order Moments

B.1 Second Moment Equations

The momentum, temperature, salinity and passive tracer equations to be considered are given by

$$\frac{\partial u_i}{\partial t} + u_j \frac{\partial u_i}{\partial x_j} - 2\varepsilon_{ijk} u_j \Omega_k = -\frac{1}{\rho_o} \frac{\partial P}{\partial x_i} + g_i (\alpha\theta - \beta S) + \frac{\partial F_{i,j}}{\partial x_j} \quad (\text{B.1})$$

$$\frac{\partial \theta}{\partial t} + u_j \frac{\partial \theta}{\partial x_j} + \frac{\partial V_j^\theta}{\partial x_j} = Q_\theta \quad (\text{B.2})$$

$$\frac{\partial S}{\partial t} + u_j \frac{\partial S}{\partial x_j} + \frac{\partial V_j^S}{\partial x_j} = Q_S \quad (\text{B.3})$$

$$\frac{\partial P}{\partial t} + u_j \frac{\partial P}{\partial x_j} + \frac{\partial V_j^P}{\partial x_j} = 0. \quad (\text{B.4})$$

In the ocean, the continuity equation can be written as $\frac{\partial u_j}{\partial x_j} = 0$. In these equations we

have assume that the buoyancy term can be approximated as follows

$$g_i \frac{\rho - \rho_o}{\rho_o} \cong g_i (\alpha\theta - \beta S).$$

In other words, a linear equation of state has been used. $F_{i,j}$ is the viscous stress tensor,

and is approximated as $F_{i,j} = \nu \left(\frac{\partial u_i}{\partial x_j} + \frac{\partial u_j}{\partial x_i} \right)$. In the ocean, we can simplify this

expression further. Consider the last term in (B.1).

$$\frac{\partial F_{i,j}}{\partial x_j} = \frac{\partial}{\partial x_j} \left\{ \nu \left(\frac{\partial u_i}{\partial x_j} + \frac{\partial u_j}{\partial x_i} \right) \right\} = \nu \left(\frac{\partial^2 u_i}{\partial x_j^2} + \frac{\partial^2 u_j}{\partial x_i \partial x_j} \right) = \nu \frac{\partial^2 u_i}{\partial x_j^2}$$

Where we have used the continuity equation in the last equality. This suggests that $F_{i,j}$

can approximately be written as

$$F_{i,j} \cong \nu \frac{\partial u_i}{\partial x_j}.$$

In the tracer equations, V_j^Z represent the molecular diffusion of that tracer. It is given by

$$V_j^Z = \kappa_Z \frac{\partial Z}{\partial x_j}.$$

If (B.1) - (B.4) are averaged, we obtain

$$\frac{\partial \bar{u}_i}{\partial t} + \bar{u}_j \frac{\partial \bar{u}_i}{\partial x_j} - 2\varepsilon_{ijk} \bar{u}_j \bar{\Omega}_k = -\frac{\partial}{\partial x_j} \left(\overline{u_i u_j} - F_{i,j} \right) - \frac{1}{\rho_o} \frac{\partial \bar{p}}{\partial x_i} + g_i (\alpha \bar{\theta} - \beta \bar{S}) \quad (\text{B.5})$$

$$\frac{\partial \bar{\theta}}{\partial t} + \bar{u}_j \frac{\partial \bar{\theta}}{\partial x_j} = - \frac{\partial \overline{u_j' \theta'}}{\partial x_j} - \frac{\partial V_j^\theta}{\partial x_j} \quad (\text{B.6})$$

$$\frac{\partial \bar{S}}{\partial t} + \bar{u}_j \frac{\partial \bar{S}}{\partial x_j} = - \frac{\partial \overline{u_j' S'}}{\partial x_j} - \frac{\partial V_j^S}{\partial x_j} \quad (\text{B.7})$$

$$\frac{\partial \bar{P}}{\partial t} + \bar{u}_j \frac{\partial \bar{P}}{\partial x_j} = - \frac{\partial \overline{u_j' P'}}{\partial x_j} - \frac{\partial V_j^P}{\partial x_j} \quad (\text{B.8})$$

Subtraction of the mean equations from their respective counterparts in (B.1) - (B.4) yields

$$\begin{aligned} \frac{\partial u_i'}{\partial t} + \bar{u}_j \frac{\partial u_i'}{\partial x_j} + u_j' \frac{\partial \bar{u}_i}{\partial x_j} + u_j' \frac{\partial u_i'}{\partial x_j} - 2\varepsilon_{ijk} u_j' \Omega_k = - \frac{1}{\rho_o} \frac{\partial p'}{\partial x_i} + g_i (\alpha \theta' - \beta S') \\ - \frac{\partial}{\partial x_j} (\overline{u_i' u_j'} - F_{i,j}) \end{aligned} \quad (\text{B.9})$$

$$\frac{\partial \theta'}{\partial t} = - u_j' \frac{\partial \theta'}{\partial x_j} - \frac{\partial \overline{u_j' \theta'}}{\partial x_j} - \bar{u}_j \frac{\partial \theta'}{\partial x_j} - u_j' \frac{\partial \bar{\theta}}{\partial x_j} - \frac{\partial V_j^\theta}{\partial x_j} \quad (\text{B.10})$$

$$\frac{\partial S'}{\partial t} = - u_j' \frac{\partial S'}{\partial x_j} - \frac{\partial \overline{u_j' S'}}{\partial x_j} - \bar{u}_j \frac{\partial S'}{\partial x_j} - u_j' \frac{\partial \bar{S}}{\partial x_j} - \frac{\partial V_j^S}{\partial x_j} \quad (\text{B.11})$$

$$\frac{\partial P'}{\partial t} = - u_j' \frac{\partial P'}{\partial x_j} - \frac{\partial \overline{u_j' P'}}{\partial x_j} - \bar{u}_j \frac{\partial P'}{\partial x_j} - u_j' \frac{\partial \bar{P}}{\partial x_j} - \frac{\partial V_j^P}{\partial x_j} \quad (\text{B.12})$$

There are two more useful equations for the derivations to follow. Equation (B.9) is equally valid if the i index is swapped for another value (not j or k as they are present in the equation already).

$$\begin{aligned} \frac{\partial u_l'}{\partial t} + \bar{u}_j \frac{\partial u_l'}{\partial x_j} + u_j' \frac{\partial \bar{u}_l}{\partial x_j} + u_j' \frac{\partial u_l'}{\partial x_j} = - \frac{1}{\rho_o} \frac{\partial p'}{\partial x_l} + g_l (\alpha \delta \theta' - \beta \delta S') \\ - \frac{\partial}{\partial x_j} (\overline{u_l' u_j'} - F_{l,j}) \end{aligned} \quad (\text{B.13})$$

$$\begin{aligned} \frac{\partial \dot{u}_m}{\partial t} + \dot{u}_j \frac{\partial \dot{u}_m}{\partial x_j} + \dot{u}_j \frac{\partial \overline{\dot{u}_m}}{\partial x_j} + \dot{u}_j \frac{\partial \dot{u}_m}{\partial x_j} = -\frac{1}{\rho_o} \frac{\partial p'}{\partial x_m} + g_m (\alpha \delta \theta' - \beta \delta S') \\ - \frac{\partial}{\partial x_j} (\overline{\dot{u}_m \dot{u}_j} - F_{m,j}') \end{aligned} \quad (\text{B.14})$$

To derive the equation describing the Reynolds stress, equation (B.9) is multiplied by \dot{u}_i

and equation (B.13) is multiplied by \dot{u}_i , then the resulting equation are summed. This

yields

$$\begin{aligned} \dot{u}_i \frac{\partial \dot{u}_i}{\partial t} + \dot{u}_i \frac{\partial \dot{u}_i}{\partial t} + \dot{u}_i \dot{u}_j \frac{\partial \dot{u}_i}{\partial x_j} + \dot{u}_i \dot{u}_j \frac{\partial \dot{u}_i}{\partial x_j} + \dot{u}_i \dot{u}_j \frac{\partial \overline{\dot{u}_i}}{\partial x_j} + \dot{u}_i \dot{u}_j \frac{\partial \overline{\dot{u}_i}}{\partial x_j} + \dot{u}_i \dot{u}_j \frac{\partial \dot{u}_i}{\partial x_j} + \dot{u}_i \dot{u}_j \frac{\partial \dot{u}_i}{\partial x_j} \\ = -\frac{\dot{u}_i}{\rho_o} \frac{\partial p'}{\partial x_i} - \frac{\dot{u}_i}{\rho_o} \frac{\partial p'}{\partial x_i} + \dot{u}_i g_i (\alpha \theta' - \beta S') + \dot{u}_i g_i (\alpha \theta' - \beta S') - \\ \dot{u}_i \frac{\partial}{\partial x_j} (\overline{\dot{u}_i \dot{u}_j} - F_{i,j}') - \dot{u}_i \frac{\partial}{\partial x_j} (\overline{\dot{u}_i \dot{u}_j} - F_{i,j}') \end{aligned}$$

After some manipulation, this equation is can be written as

$$\begin{aligned} \frac{\partial \dot{u}_i \dot{u}_i}{\partial t} + \frac{\partial}{\partial x_j} (\dot{u}_i \dot{u}_j \dot{u}_k + \overline{\dot{u}_i \dot{u}_j \dot{u}_k} - \dot{u}_i F_{l,j}' - \dot{u}_l F_{i,j}') = -\dot{u}_j \dot{u}_l \frac{\partial \overline{\dot{u}_i}}{\partial x_j} - \dot{u}_j \dot{u}_l \frac{\partial \overline{\dot{u}_i}}{\partial x_j} \\ + g_i (\alpha \dot{u}_i \theta' - \beta \dot{u}_i S') + g_l (\alpha \dot{u}_l \theta' - \beta \dot{u}_l S') - \left(F_{i,j}' \frac{\partial \dot{u}_i}{\partial x_j} + F_{l,j}' \frac{\partial \dot{u}_i}{\partial x_j} \right) \\ - \frac{\dot{u}_i}{\rho_o} \frac{\partial p'}{\partial x_i} - \frac{\dot{u}_i}{\rho_o} \frac{\partial p'}{\partial x_i} + \dot{u}_i \frac{\partial \overline{\dot{u}_i \dot{u}_j}}{\partial x_j} + \dot{u}_i \frac{\partial \overline{\dot{u}_i \dot{u}_j}}{\partial x_j} \end{aligned} \quad (\text{B.15})$$

Averaging (B.15) yields the Reynolds stress equation, which is given by

$$\begin{aligned}
\frac{\partial \overline{u_i' u_i'}}{\partial t} + \frac{\partial}{\partial x_j} \left(\overline{u_i' u_j' u_k'} + \overline{u_j' u_i' u_l'} - \overline{u_i' F_{l,j}'} - \overline{u_l' F_{i,j}'} \right) &= -\overline{u_j' u_i'} \frac{\partial \overline{u_i'}}{\partial x_j} - \overline{u_j' u_i'} \frac{\partial \overline{u_i'}}{\partial x_j} \\
&+ g_i \left(\overline{\alpha u_i' \theta'} - \overline{\beta u_i' S'} \right) + g_l \left(\overline{\alpha u_i' \theta'} - \overline{\beta u_i' S'} \right) \\
&- \frac{\overline{u_l' \partial p'}}{\rho_o \partial x_i} - \frac{\overline{u_i' \partial p'}}{\rho_o \partial x_l} - \left(\overline{F_{i,j}'} \frac{\partial \overline{u_i'}}{\partial x_j} + \overline{F_{l,j}'} \frac{\partial \overline{u_i'}}{\partial x_j} \right)
\end{aligned} \tag{B.16}$$

To derive the expression for the turbulent heat flux, we first multiply (B.10) by u_i' and

(B.9) by θ' . The resulting equations are summed, yielding

$$\begin{aligned}
\frac{\partial \overline{u_i' \theta'}}{\partial t} + \frac{\partial \overline{u_i' u_j' \theta'}}{\partial x_j} &= -\overline{u_j' \theta'} \frac{\partial \overline{u_i'}}{\partial x_j} - \overline{u_j' \theta'} \frac{\partial \overline{u_i'}}{\partial x_j} - \overline{u_j' u_i'} \frac{\partial \overline{\theta}}{\partial x_j} - \frac{\overline{\theta'} \partial p'}{\rho_o \partial x_i} \\
&+ g_i \left(\overline{\alpha \theta'^2} - \overline{\beta \theta' S'} \right) - \overline{u_i' \frac{\partial \overline{u_j' \theta'}}{\partial x_j}} - \overline{\theta' \frac{\partial}{\partial x_j} \left(\overline{u_i' u_j'} - F_{i,j}' \right)} - \overline{u_i' \frac{\partial V_j^{\theta'}}{\partial x_j}}
\end{aligned} \tag{B.17}$$

After rearranging and averaging, we obtain

$$\begin{aligned}
\frac{\partial \overline{u_i' \theta'}}{\partial t} + \frac{\partial \overline{u_i' u_j' \theta'}}{\partial x_j} &= -\overline{u_j' \theta'} \frac{\partial \overline{u_i'}}{\partial x_j} - \overline{u_i' u_j'} \frac{\partial \overline{\theta}}{\partial x_j} - \overline{u_j' \frac{\partial \overline{u_i' \theta'}}{\partial x_j}} + g_i \left(\overline{\alpha \theta'^2} - \overline{\beta \theta' S'} \right) \\
&- \overline{u_i' \frac{\partial V_j^{\theta'}}{\partial x_j}} + \overline{\theta' \frac{\partial F_{i,j}'}{\partial x_j}} - \frac{\overline{\theta'} \partial p'}{\rho_o \partial x_i}
\end{aligned} \tag{B.18}$$

The derivation of the turbulent fluxes of salt and passive tracer proceed identically. The unaveraged equations are

$$\begin{aligned}
\frac{\partial \overline{u_i' S'}}{\partial t} + \frac{\partial \overline{u_i' u_j' S'}}{\partial x_j} &= -\overline{u_j' S'} \frac{\partial \overline{u_i'}}{\partial x_j} - \overline{u_j' S'} \frac{\partial \overline{u_i'}}{\partial x_j} - \overline{u_j' u_i'} \frac{\partial \overline{S}}{\partial x_j} - \frac{\overline{S'} \partial p'}{\rho_o \partial x_i} \\
&+ g_i \left(\overline{\alpha \theta' S'} - \overline{\beta S'^2} \right) - \overline{u_i' \frac{\partial \overline{u_j' S'}}{\partial x_j}} - \overline{S' \frac{\partial}{\partial x_j} \left(\overline{u_i' u_j'} - F_{i,j}' \right)} - \overline{u_i' \frac{\partial V_j^{S'}}{\partial x_j}}
\end{aligned} \tag{B.19}$$

$$\begin{aligned}
\frac{\partial \overline{u_i' P'}}{\partial t} + \frac{\partial \overline{u_i' u_j' P'}}{\partial x_j} &= -\overline{u_j} \frac{\partial \overline{u_i' P'}}{\partial x_j} - \overline{u_j' P'} \frac{\partial \overline{u_i}}{\partial x_j} - \overline{u_j' u_i'} \frac{\partial \overline{P}}{\partial x_j} - \frac{P'}{\rho_o} \frac{\partial p'}{\partial x_i} \\
&+ g_i (\alpha \theta' P' - \beta S' P') - \overline{u_i} \frac{\partial \overline{u_j' P'}}{\partial x_j} - P' \frac{\partial}{\partial x_j} (\overline{u_i' u_j'} - F_{i,j}') - \overline{u_i} \frac{\partial V_j^{P'}}{\partial x_j}
\end{aligned} \tag{B.20}$$

Averaging these equations yields

$$\begin{aligned}
\frac{\partial \overline{u_i' S'}}{\partial t} + \frac{\partial \overline{u_i' u_j' S'}}{\partial x_j} &= -\overline{u_j S'} \frac{\partial \overline{u_i}}{\partial x_j} - \overline{u_i' u_j'} \frac{\partial \overline{S}}{\partial x_j} - \overline{u_j} \frac{\partial \overline{u_i' S'}}{\partial x_j} + g_i (\alpha \overline{\theta' S'} - \beta \overline{S'^2}) \\
&- \overline{u_i} \frac{\partial \overline{V_j^{S'}}}{\partial x_j} + \overline{S'} \frac{\partial \overline{F_{i,j}'}}{\partial x_j} - \frac{\overline{S'}}{\rho_o} \frac{\partial p'}{\partial x_i}
\end{aligned} \tag{B.21}$$

$$\begin{aligned}
\frac{\partial \overline{u_i' P'}}{\partial t} + \frac{\partial \overline{u_i' u_j' P'}}{\partial x_j} &= -\overline{u_j P'} \frac{\partial \overline{u_i}}{\partial x_j} - \overline{u_i' u_j'} \frac{\partial \overline{P}}{\partial x_j} - \overline{u_j} \frac{\partial \overline{u_i' P'}}{\partial x_j} + g_i (\alpha \overline{\theta' P'} - \beta \overline{P' S'}) \\
&- \overline{u_i} \frac{\partial \overline{V_j^{P'}}}{\partial x_j} + \overline{P'} \frac{\partial \overline{F_{i,j}'}}{\partial x_j} - \frac{\overline{P'}}{\rho_o} \frac{\partial p'}{\partial x_i}
\end{aligned} \tag{B.22}$$

The equations for tracer variance are derived by multiplying the respective tracer equation by twice that tracer. For example, consider potential temperature variance.

Multiplying (B.10) by yields

$$\frac{\partial \overline{\theta'^2}}{\partial t} + \frac{\partial \overline{u_j' \theta'^2}}{\partial x_j} = -\overline{u_j} \frac{\partial \overline{\theta'^2}}{\partial x_j} - 2\overline{u_j' \theta'} \frac{\partial \overline{\theta}}{\partial x_j} - 2\overline{\theta'} \frac{\partial \overline{u_j' \theta'}}{\partial x_j} - 2\overline{\theta'} \frac{\partial V_j^\theta}{\partial x_j} \tag{B.23}$$

The equations for S'^2 and P'^2 can be written as

$$\frac{\partial \overline{S'^2}}{\partial t} + \frac{\partial \overline{u_j' S'^2}}{\partial x_j} = -\overline{u_j} \frac{\partial \overline{S'^2}}{\partial x_j} - 2\overline{u_j' S'} \frac{\partial \overline{S}}{\partial x_j} - 2\overline{S'} \frac{\partial \overline{u_j' S'}}{\partial x_j} - 2\overline{S'} \frac{\partial V_j^S}{\partial x_j} \tag{B.24}$$

$$\frac{\partial \overline{P'^2}}{\partial t} + \frac{\partial \overline{u'_j P'^2}}{\partial x_j} = -\overline{u'_j} \frac{\partial \overline{P'^2}}{\partial x_j} - 2\overline{u'_j P'} \frac{\partial \overline{P}}{\partial x_j} - 2\overline{P'} \frac{\partial \overline{u'_j P'}}{\partial x_j} - 2\overline{P'} \frac{\partial \overline{V'_j P'}}{\partial x_j} \quad (\text{B.25})$$

The final variance equations are

$$\frac{\partial \overline{\theta'^2}}{\partial t} + \frac{\partial \overline{u'_j \theta'^2}}{\partial x_j} = -\overline{u'_j} \frac{\partial \overline{\theta'^2}}{\partial x_j} - 2\overline{u'_j \theta'} \frac{\partial \overline{\theta}}{\partial x_j} - 2\overline{\theta'} \frac{\partial \overline{V'_j \theta'}}{\partial x_j} \quad (\text{B.26})$$

$$\frac{\partial \overline{S'^2}}{\partial t} + \frac{\partial \overline{u'_j S'^2}}{\partial x_j} = -\overline{u'_j} \frac{\partial \overline{S'^2}}{\partial x_j} - 2\overline{u'_j S'} \frac{\partial \overline{S}}{\partial x_j} - 2\overline{S'} \frac{\partial \overline{V'_j S'}}{\partial x_j} \quad (\text{B.27})$$

$$\frac{\partial \overline{P'^2}}{\partial t} + \frac{\partial \overline{u'_j P'^2}}{\partial x_j} = -\overline{u'_j} \frac{\partial \overline{P'^2}}{\partial x_j} - 2\overline{u'_j P'} \frac{\partial \overline{P}}{\partial x_j} - 2\overline{P'} \frac{\partial \overline{V'_j P'}}{\partial x_j} \quad (\text{B.28})$$

The equations derived to this point have introduced the need for three cross correlations $(\overline{\theta' S'}, \overline{S' P'}, \overline{\theta' P'})$. The operations necessary to derive these moments are summarized in

Table B.1.

Moment Equation	Operation Performed
$\overline{\theta' S'}$	$\overline{\theta'^* (B.11)} + \overline{S'^* (B.10)}$
$\overline{\theta' P'}$	$\overline{\theta'^* (B.12)} + \overline{P'^* (B.10)}$
$\overline{S' P'}$	$\overline{S'^* (B.12)} + \overline{P'^* (B.11)}$

Table B.1: Operations performed to derive the cross correlations

The unaveraged equations are

$$\begin{aligned} \frac{\partial \theta' S'}{\partial t} + \frac{\partial u_j' \theta' S'}{\partial x_j} = & -u_j \frac{\partial \theta' S'}{\partial x_j} - \overline{u_j' \theta'} \frac{\partial \bar{S}}{\partial x_j} - \overline{u_j' S'} \frac{\partial \bar{\theta}}{\partial x_j} - \overline{\theta'} \frac{\partial V_j^{S'}}{\partial x_j} - \overline{S'} \frac{\partial V_j^{\theta'}}{\partial x_j} \\ & - \overline{S'} \frac{\partial u_j' \theta'}{\partial x_j} - \overline{\theta'} \frac{\partial u_j' S'}{\partial x_j} \end{aligned} \quad (\text{B.29})$$

$$\begin{aligned} \frac{\partial \theta' P'}{\partial t} + \frac{\partial u_j' \theta' P'}{\partial x_j} = & -u_j \frac{\partial \theta' P'}{\partial x_j} - \overline{u_j' \theta'} \frac{\partial \bar{P}}{\partial x_j} - \overline{u_j' P'} \frac{\partial \bar{\theta}}{\partial x_j} - \overline{\theta'} \frac{\partial V_j^{P'}}{\partial x_j} - \overline{P'} \frac{\partial V_j^{\theta'}}{\partial x_j} \\ & - \overline{P'} \frac{\partial u_j' \theta'}{\partial x_j} - \overline{\theta'} \frac{\partial u_j' P'}{\partial x_j} \end{aligned} \quad (\text{B.30})$$

$$\begin{aligned} \frac{\partial S' P'}{\partial t} + \frac{\partial u_j' S' P'}{\partial x_j} = & -u_j \frac{\partial S' P'}{\partial x_j} - \overline{u_j' S'} \frac{\partial \bar{P}}{\partial x_j} - \overline{u_j' P'} \frac{\partial \bar{S}}{\partial x_j} - \overline{S'} \frac{\partial V_j^{P'}}{\partial x_j} - \overline{P'} \frac{\partial V_j^{S'}}{\partial x_j} \\ & - \overline{P'} \frac{\partial u_j' S'}{\partial x_j} - \overline{S'} \frac{\partial u_j' P'}{\partial x_j} \end{aligned} \quad (\text{B.31})$$

The final equations are given by

$$\frac{\partial \overline{\theta' S'}}{\partial t} + \frac{\partial \overline{u_j' \theta' S'}}{\partial x_j} = -\overline{u_j} \frac{\partial \overline{\theta' S'}}{\partial x_j} - \overline{u_j' \theta'} \frac{\partial \bar{S}}{\partial x_j} - \overline{u_j' S'} \frac{\partial \bar{\theta}}{\partial x_j} - \overline{\theta'} \frac{\partial \overline{V_j^{S'}}}{\partial x_j} - \overline{S'} \frac{\partial \overline{V_j^{\theta'}}}{\partial x_j} \quad (\text{B.32})$$

$$\frac{\partial \overline{\theta' P'}}{\partial t} + \frac{\partial \overline{u_j' \theta' P'}}{\partial x_j} = -\overline{u_j} \frac{\partial \overline{\theta' P'}}{\partial x_j} - \overline{u_j' \theta'} \frac{\partial \bar{P}}{\partial x_j} - \overline{u_j' P'} \frac{\partial \bar{\theta}}{\partial x_j} - \overline{\theta'} \frac{\partial \overline{V_j^{P'}}}{\partial x_j} - \overline{P'} \frac{\partial \overline{V_j^{\theta'}}}{\partial x_j} \quad (\text{B.33})$$

$$\frac{\partial \overline{S' P'}}{\partial t} + \frac{\partial \overline{u_j' S' P'}}{\partial x_j} = -\overline{u_j} \frac{\partial \overline{S' P'}}{\partial x_j} - \overline{u_j' S'} \frac{\partial \bar{P}}{\partial x_j} - \overline{u_j' P'} \frac{\partial \bar{S}}{\partial x_j} - \overline{S'} \frac{\partial \overline{V_j^{P'}}}{\partial x_j} - \overline{P'} \frac{\partial \overline{V_j^{S'}}}{\partial x_j} \quad (\text{B.34})$$

Equations (B.5) - (B.8) and (B.15) - (B.34) describe the mean fields and second order moments for momentum, theta, salinity, and a passive tracer. There are a total of 21 equations. However, the equations are not completely closed, third order moments have appeared in the equations and must be determined. Further, assumptions must be made

about certain terms, such as pressure correlation, rotation, and viscosity. We return to the third order moments after a discussion of some model assumptions.

B.2 Simplifying Assumptions

The closures for the second moment equations follow directly from Canuto et al. (2001,2002). The pressure correlation terms contain three parts: the slow (or return-to-isotropy), a fast term, which acts to damp the moments described by the equation they appear in. Finally, a buoyancy contribution is included. The viscous terms all have the

form $\overline{\kappa B' \frac{\partial^2 C'}{\partial x_j^2}} + \overline{\kappa B' \frac{\partial^2 C'}{\partial x_j^2}}$, and can be rewritten using the product rule as

$\kappa \frac{\overline{\partial^2 B' C'}}{\partial x_j^2} - 2\kappa \frac{\overline{\partial B'}}{\partial x_j} \frac{\overline{\partial C'}}{\partial x_j}$. The first term represents molecular diffusion and is assumed

small compared to the second (dissipation) term (Stull 1988). The parameterization for the dissipation terms follow Canuto et al. (2001,2002) for momentum, temperature, and salinity. In the case of a passive tracer, the pressure correlation terms are found by analogy to those for salinity.

Finally, we limit our focus to vertical variations in turbulence. To this end, where the index 'j' appears in equations (B.5) - (B.8) and (B.15) - (B.34), it is set to 3. Terms involving advection by the mean horizontal flow are also neglected. The resulting second moment equations are given by

$$\begin{aligned} \frac{\partial \overline{u_i u_i'}}{\partial t} + \frac{\partial \overline{w u_i u_i'}}{\partial z} &= -\overline{w u_i} \frac{\partial \overline{u_i}}{\partial z} - \overline{w' u_i'} \frac{\partial \overline{u_i}}{\partial z} + g_i \left(\alpha \overline{u_i \theta'} - \beta \overline{u_i' S'} \right) + g_l \left(\alpha \overline{u_i \theta} - \beta \overline{u_i S} \right) \\ &\quad - \left\{ 2\tau_{pv}^{-1} \left(\overline{u_i u_i'} - \frac{2}{3} k \delta_{ii} \right) - \frac{4}{5} k S_{i,l} + (1 - \beta_s) B_{i,l} - c_1 \Sigma_{i,l} - c_2 Z_{i,l} \right\} - \frac{2}{3} \varepsilon \delta_{ii} \end{aligned} \quad (\text{B.35})$$

$$\begin{aligned} \frac{\partial \overline{u_i \theta'}}{\partial t} + \frac{\partial \overline{w u_i \theta'}}{\partial z} &= -\overline{w \theta'} \frac{\partial \overline{u_i}}{\partial z} - \overline{u_i w'} \frac{\partial \overline{\theta}}{\partial z} + g_i \left(\alpha \overline{\theta'^2} - \beta \overline{\theta' S'} \right) \\ &\quad - \left\{ \tau_{p\theta}^{-1} \overline{u_i \theta'} + d_1 g_i \left(\alpha \overline{\theta'^2} - \beta \overline{\theta' S'} \right) - \frac{3}{4} c_3 \left(S_{i,m} + \frac{5}{3} V_{i,m} \right) \overline{u_m \theta'} \right\} \end{aligned} \quad (\text{B.36})$$

$$\begin{aligned} \frac{\partial \overline{u_i S'}}{\partial t} + \frac{\partial \overline{w u_i S'}}{\partial z} &= -\overline{w S'} \frac{\partial \overline{u_i}}{\partial z} - \overline{u_i w'} \frac{\partial \overline{S}}{\partial z} + g \left(\alpha \overline{\theta' S'} - \beta \overline{S'^2} \right) \\ &\quad - \left\{ \tau_{ps}^{-1} \overline{u_i S'} + d_1 g_i \left(\alpha \overline{\theta' S'} - \beta \overline{S'^2} \right) - \frac{3}{4} c_3 \left(S_{i,m} + \frac{5}{3} V_{i,m} \right) \overline{u_m S'} \right\} \end{aligned} \quad (\text{B.37})$$

$$\begin{aligned} \frac{\partial \overline{u_i P'}}{\partial t} + \frac{\partial \overline{w u_i P'}}{\partial z} &= -\overline{w P'} \frac{\partial \overline{u_i}}{\partial z} - \overline{u_i w'} \frac{\partial \overline{\theta}}{\partial z} + g \left(\alpha \overline{\theta' P'} - \beta \overline{S' P'} \right) \\ &\quad - \left\{ \tau_{pP}^{-1} \overline{u_i P'} + d_1 g_i \left(\alpha \overline{\theta' P'} - \beta \overline{S' P'} \right) - \frac{3}{4} c_3 \left(S_{i,m} + \frac{5}{3} V_{i,m} \right) \overline{u_m P'} \right\} \end{aligned} \quad (\text{B.38})$$

$$\frac{\partial \overline{\theta'^2}}{\partial t} + \frac{\partial \overline{w \theta'^2}}{\partial z} = -2 \overline{w \theta'} \frac{\partial \overline{\theta}}{\partial z} - 2 \tau_{\theta}^{-1} \overline{\theta'^2} \quad (\text{B.39})$$

$$\frac{\partial \overline{S'^2}}{\partial t} + \frac{\partial \overline{w S'^2}}{\partial z} = -2 \overline{w S'} \frac{\partial \overline{S}}{\partial z} - 2 \tau_s^{-1} \overline{S'^2} \quad (\text{B.40})$$

$$\frac{\partial \overline{P'^2}}{\partial t} + \frac{\partial \overline{w P'^2}}{\partial z} = -2 \overline{w P'} \frac{\partial \overline{P}}{\partial z} - 2 \tau_p^{-1} \overline{P'^2} \quad (\text{B.41})$$

$$\frac{\partial \overline{\theta' S'}}{\partial t} + \frac{\partial \overline{w \theta' S'}}{\partial x_j} = -\overline{w \theta'} \frac{\partial \overline{S}}{\partial z} - \overline{w' S'} \frac{\partial \overline{\theta}}{\partial z} - \tau_{\theta S}^{-1} \overline{\theta' S'} \quad (\text{B.42})$$

$$\frac{\partial \overline{\theta' P'}}{\partial t} + \frac{\partial \overline{w \theta' P'}}{\partial x_j} = -\overline{w \theta'} \frac{\partial \overline{P}}{\partial z} - \overline{w' P'} \frac{\partial \overline{\theta}}{\partial z} - \tau_{\theta P}^{-1} \overline{\theta' P'} \quad (\text{B.43})$$

$$\frac{\partial \overline{S' P'}}{\partial t} + \frac{\partial \overline{w S' P'}}{\partial x_j} = -\overline{w S'} \frac{\partial \overline{P}}{\partial z} - \overline{w' P'} \frac{\partial \overline{S}}{\partial z} - \tau_{SP}^{-1} \overline{S' P'} \quad (\text{B.44})$$

In these equations, we have introduced the turbulence kinetic energy $\left(k \equiv 0.5 \left\{ \overline{u'^2} + \overline{v'^2} + \overline{w'^2} \right\}\right)$, and the eddy turnover time $\left(\tau \equiv 2k/\varepsilon\right)$, where ε is the dissipation rate of k . The definition of the remaining tensors are summarized in Table B.2 (in these definitions, δ_{ij} is the Kroenicker delta).

Term	Definition
$S_{i,j}$	$S_{i,l} \equiv \frac{1}{2} \left(\frac{\partial \overline{u}_i}{\partial x_l} + \frac{\partial \overline{u}_l}{\partial x_i} \right)$
$B_{i,l}$	$B_{i,l} \equiv g_i \left(\alpha \overline{u'_i \theta'} - \beta \overline{u'_i S'} \right) + g_l \left(\alpha \overline{u'_l \theta'} - \beta \overline{u'_l S'} \right) - \frac{2}{3} \delta_{il} g_k \left(\alpha \overline{u'_k \theta'} - \beta \overline{u'_k S'} \right)$
$\Sigma_{i,l}$	$\Sigma_{i,l} \equiv S_{ik} \left(\overline{u'_k u'_i} - \frac{2}{3} \delta_{ik} k \right) + S_{lk} \left(\overline{u'_i u'_k} - \frac{2}{3} \delta_{ik} k \right) - \frac{2}{3} \delta_{il} S_{km} \left(\overline{u'_m u'_k} - \frac{2}{3} \delta_{km} k \right)$
$Z_{i,l}$	$Z_{i,l} \equiv V_{i,k} \left(\overline{u'_k u'_i} - \frac{2}{3} k \delta_{ki} \right) + V_{lk} \left(\overline{u'_i u'_k} - \frac{2}{3} k \delta_{ik} \right)$
$V_{i,l}$	$V_{i,l} \equiv \frac{1}{2} \left(\frac{\partial u_i}{\partial x_j} - \frac{\partial u_j}{\partial x_i} \right)$

Table B.2 - Tensor forms of functions introduced in equations (B.35) - (B.44)

We are also going to assume that the equations describing the second moments of passive tracer (equations (B.38), (B.41), (B.43), and (B.44)) can be treated algebraically. In other

words, the time derivative and third order moment terms are neglected. Under this assumption the vertical flux of passive tracer is given by

$$\overline{w'P'} = -\tau_{pP} \frac{\partial \overline{P}}{\partial z} \left[\frac{\overline{w'^2} + (1-d_1)\tau_{\theta p} g (\alpha \overline{w'\theta'} - \beta \overline{w'S'}) - \frac{c_3}{4} \tau_{pP} \left(\overline{u'w'} \frac{\partial \overline{u}}{\partial z} - \overline{v'w'} \frac{\partial \overline{v}}{\partial z} \right)}{1 + \pi_4 \tau^2 \left\{ \left(\frac{\partial \overline{u}}{\partial z} \right)^2 + \left(\frac{\partial \overline{v}}{\partial z} \right)^2 \right\} \left((1-d_1)\pi_2 Ri - \frac{c_3}{4} \pi_4 (1-c_3) \right)} \right] \quad (\text{B.45})$$

The constants introduced in equations (B.35) - (B.44), including the values of τ_{pv} , $\tau_{p\theta}$, τ_{pS} , τ_{θ} , τ_S , $\tau_{\theta S}$, and τ_{pP} are discussed in Appendix B.

B.3 Third Order Moments

The third order moments can be derived in a similar manner to that used in Section B.1. However, in this derivation fourth order moments will emerge. The equations for fourth order moments will contain fifth order moments. At some point, a closure must be invoked. We will invoke a closure similar to that presented in Cheng et al. (2005). A complete discussion of this closure follows a presentation of the prognostic equations for the third order moments. The necessary operations for the derivation of the third order moments (TOMs) are given in Table B.3. Recall that we are assuming production equals dissipation for the passive tracer in the second moment equations. Therefore equations for the TOMs of passive tracer are not derived.

Moment Equation	Operation Performed
$\overline{u_i' u_l' u_m'}$	$\overline{u_i' u_l' * (B.14) + u_m' * (B.13)}$
$\overline{u_i' u_l' \theta'}$	$\overline{\theta' * (B.13) + u_i' u_l' * (B.10)}$
$\overline{u_i' u_l' S'}$	$\overline{S' * (B.13) + u_i' u_l' * (B.11)}$
$\overline{u_i' S'^2}$	$\overline{u_i' S' * (B.11) + S' * (B.19)}$
$\overline{u_i' \theta'^2}$	$\overline{u_i' \theta' * (B.10) + \theta' * (B.17)}$
$\overline{u_i' \theta' S'}$	$\overline{u_i' \theta' * (B.11) + S' * (B.17)}$
$\overline{\theta'^3}$	$\overline{3\theta' * (B.23)}$
$\overline{S'^3}$	$\overline{3S' * (B.24)}$
$\overline{\theta'^2 S'}$	$\overline{\theta' S' * (B.10) + \theta' * (B.22)}$
$\overline{\theta' S'^2}$	$\overline{\theta' S' * (B.11) + S' * (B.22)}$

Table B.3 - Operations performed to derive the third order moments.

The resulting equations are

$$\begin{aligned}
\frac{\partial \overline{u_i' u_l' u_m'}}{\partial t} + \frac{\partial \overline{u_j' u_l' u_m'}}{\partial x_j} &= -\overline{u_j u_l u_m} \frac{\partial \overline{u_i}}{\partial x_j} - \overline{u_j u_l u_m} \frac{\partial \overline{u_l}}{\partial x_j} - \overline{u_j u_l u_l} \frac{\partial \overline{u_m}}{\partial x_j} - \overline{u_l u_m} \frac{\partial \overline{u_i}}{\partial x_j} \\
&\quad - \overline{u_i u_m} \frac{\partial \overline{u_j}}{\partial x_j} - \overline{u_i u_l} \frac{\partial \overline{u_m}}{\partial x_j} + g \left(\overline{\alpha u_i u_l \theta'} - \overline{\beta u_i u_l S'} \right) + g \left(\overline{\alpha u_i u_m \theta'} - \overline{\beta u_i u_m S'} \right) \\
&\quad + g \left(\overline{\alpha u_m u_l \theta'} - \overline{\beta u_m u_l S'} \right) - \frac{1}{\rho_o} \left(\overline{u_i u_l} \frac{\partial p'}{\partial x_m} + \overline{u_i u_m} \frac{\partial p'}{\partial x_l} + \overline{u_l u_m} \frac{\partial p'}{\partial x_i} \right) \\
&\quad + \overline{u_i u_l} \frac{\partial F'_{m,j}}{\partial x_j} + \overline{u_i u_m} \frac{\partial F'_{l,j}}{\partial x_j} + \overline{u_l u_m} \frac{\partial F'_{i,j}}{\partial x_j}
\end{aligned} \tag{B.46}$$

$$\begin{aligned}
\frac{\partial \overline{u_i u_i \theta}}{\partial t} + \frac{\partial \overline{u_i u_j u_i \theta}}{\partial x_j} &= -\overline{u_i u_j u_i} \frac{\partial \overline{\theta}}{\partial x_j} - \overline{u_i u_j \theta} \frac{\partial \overline{u_i}}{\partial x_j} - \overline{u_i u_j \theta} \frac{\partial \overline{u_i}}{\partial x_j} - \overline{u_i \theta} \frac{\partial \overline{u_i u_j}}{\partial x_j} - \overline{u_i \theta} \frac{\partial \overline{u_i u_j}}{\partial x_j} \\
&\quad - \overline{u_i u_i} \frac{\partial \overline{u_j \theta}}{\partial x_j} - \overline{u_i u_i} \frac{\partial \overline{V_j^{\theta'}}}{\partial x_j} + \overline{u_i \theta} \frac{\partial \overline{F_{i,j}'}}{\partial x_j} + \overline{u_i \theta} \frac{\partial \overline{F_{i,j}'}}{\partial x_j} + g \left(\overline{\alpha u_i \theta'^2} - \overline{\beta u_i \theta' S'} \right) \\
&\quad + g \left(\overline{\alpha u_i \theta'^2} - \overline{\beta u_i \theta' S'} \right) - \frac{\overline{u_i \theta'}}{\rho_o} \frac{\partial \overline{p'}}{\partial x_i} - \frac{\overline{u_i \theta'}}{\rho_o} \frac{\partial \overline{p'}}{\partial x_i}
\end{aligned} \tag{B.47}$$

$$\begin{aligned}
\frac{\partial \overline{u_i u_i S'}}{\partial t} + \frac{\partial \overline{u_i u_j u_i S'}}{\partial x_j} &= -\overline{u_i u_j u_i} \frac{\partial \overline{S'}}{\partial x_j} - \overline{u_i u_j S'} \frac{\partial \overline{u_i}}{\partial x_j} - \overline{u_i u_j S'} \frac{\partial \overline{u_i}}{\partial x_j} - \overline{u_i S'} \frac{\partial \overline{u_i u_j}}{\partial x_j} - \overline{u_i S'} \frac{\partial \overline{u_i u_j}}{\partial x_j} \\
&\quad - \overline{u_i u_i} \frac{\partial \overline{u_j S'}}{\partial x_j} - \overline{u_i u_i} \frac{\partial \overline{V_j^{S'}}}{\partial x_j} + \overline{u_i S'} \frac{\partial \overline{F_{i,j}'}}{\partial x_j} + \overline{u_i S'} \frac{\partial \overline{F_{i,j}'}}{\partial x_j} + g \left(\overline{\alpha u_i \theta' S'} - \overline{\beta u_i S'^2} \right) \\
&\quad + g \left(\overline{\alpha u_i \theta' S'} - \overline{\beta u_i S'^2} \right) - \frac{\overline{u_i S'}}{\rho_o} \frac{\partial \overline{p'}}{\partial x_i} - \frac{\overline{u_i S'}}{\rho_o} \frac{\partial \overline{p'}}{\partial x_i}
\end{aligned} \tag{B.48}$$

$$\begin{aligned}
\frac{\partial \overline{u_i S'^2}}{\partial t} + \frac{\partial \overline{u_i u_j S'^2}}{\partial x_j} &= \overline{u_j S'^2} \frac{\partial \overline{u_i}}{\partial x_j} - 2 \overline{u_i u_j S'} \frac{\partial \overline{S'}}{\partial x_j} - 2 \frac{\overline{u_i S'}}{\rho_o} \frac{\partial \overline{u_j S'}}{\partial x_j} - \frac{\overline{S'^2}}{\rho_o} \frac{\partial \overline{u_i u_j}}{\partial x_j} + g \left(\overline{\alpha \theta' S'^2} - \overline{\beta S'^3} \right) \\
&\quad - \frac{\overline{S'^2}}{\rho_o} \frac{\partial \overline{p'}}{\partial x_i} - \overline{S'^2} \frac{\partial \overline{F_{i,j}'}}{\partial x_j} - 2 \overline{u_i S'} \frac{\partial \overline{V_j^{S'}}}{\partial x_j}
\end{aligned} \tag{B.49}$$

$$\begin{aligned}
\frac{\partial \overline{u_i \theta'^2}}{\partial t} + \frac{\partial \overline{u_i u_j \theta'^2}}{\partial x_j} &= \overline{u_j \theta'^2} \frac{\partial \overline{u_i}}{\partial x_j} - 2 \overline{u_i u_j \theta'} \frac{\partial \overline{\theta}}{\partial x_j} - 2 \frac{\overline{u_i \theta'}}{\rho_o} \frac{\partial \overline{u_j \theta'}}{\partial x_j} - \frac{\overline{\theta'^2}}{\rho_o} \frac{\partial \overline{u_i u_j}}{\partial x_j} + g \left(\overline{\alpha \theta'^3} - \overline{\beta \theta'^2 S'} \right) \\
&\quad - \frac{\overline{\theta'^2}}{\rho_o} \frac{\partial \overline{p'}}{\partial x_i} - \overline{\theta'^2} \frac{\partial \overline{F_{i,j}'}}{\partial x_j} - 2 \overline{u_i \theta'} \frac{\partial \overline{V_j^{\theta'}}}{\partial x_j}
\end{aligned} \tag{B.50}$$

$$\begin{aligned}
\frac{\partial \overline{u_i \theta' S'}}{\partial t} + \frac{\partial \overline{u_i u_j \theta' S'}}{\partial x_j} &= -\overline{u_i u_j \theta'} \frac{\partial \overline{S'}}{\partial x_j} - \overline{u_i u_j S'} \frac{\partial \overline{\theta}}{\partial x_j} - \overline{u_j \theta' S'} \frac{\partial \overline{u_i}}{\partial x_j} - \frac{\overline{u_i \theta'}}{\rho_o} \frac{\partial \overline{u_j S'}}{\partial x_j} - \frac{\overline{u_i S'}}{\rho_o} \frac{\partial \overline{u_j \theta'}}{\partial x_j} \\
&\quad - \frac{\overline{\theta' S'}}{\rho_o} \frac{\partial \overline{u_i u_j}}{\partial x_j} + \overline{\theta' S'} \frac{\partial \overline{F_{i,j}'}}{\partial x_j} - \frac{\overline{\theta' S'}}{\rho_o} \frac{\partial \overline{p'}}{\partial x_i} + g \left(\overline{\alpha \theta'^2 S'} - \overline{\beta \theta' S'^2} \right) - \overline{u_i S'} \frac{\partial \overline{V_j^{\theta'}}}{\partial x_j} \\
&\quad - \overline{u_i \theta'} \frac{\partial \overline{V_j^{S'}}}{\partial x_j}
\end{aligned} \tag{B.51}$$

$$\frac{\partial \overline{\theta'^3}}{\partial t} + \frac{\partial \overline{u_j \theta'^3}}{\partial x_j} = -\overline{u_j} \frac{\partial \overline{\theta'^3}}{\partial x_j} - 3 \overline{u_j \theta'^2} \frac{\partial \overline{\theta}}{\partial x_j} - 3 \overline{\theta'^2} \frac{\partial \overline{u_j \theta'}}{\partial x_j} - 3 \overline{\theta'^2} \frac{\partial \overline{V_j^{\theta'}}}{\partial x_j} \tag{B.52}$$

$$\frac{\overline{\partial S'^3}}{\partial t} + \frac{\overline{\partial u'_j S'^3}}{\partial x_j} = -\overline{u'_j \frac{\partial S'^3}{\partial x_j}} - 3\overline{u'_j S'^2} \frac{\partial \overline{S}}{\partial x_j} - 3\overline{S'^2} \frac{\partial \overline{u'_j S'}}{\partial x_j} - 3\overline{S'^2} \frac{\partial \overline{V_j^{S'}}}{\partial x_j} \quad (\text{B.53})$$

$$\begin{aligned} \frac{\overline{\partial \theta'^2 S'}}{\partial t} + \frac{\overline{\partial u'_j \theta'^2 S'}}{\partial x_j} = & -2\overline{u'_j} \frac{\partial \overline{\theta'^2 S'}}{\partial x_j} - 2\overline{u'_j S' \theta'} \frac{\partial \overline{\theta}}{\partial x_j} - 2\overline{\theta' S'} \frac{\partial \overline{V_j^{\theta'}}}{\partial x_j} - 2\overline{\theta' S'} \frac{\partial \overline{u'_j \theta'}}{\partial x_j} \\ & - \overline{u'_j \theta'^2} \frac{\partial \overline{S}}{\partial x_j} - \overline{\theta'^2} \frac{\partial \overline{V_j^{S'}}}{\partial x_j} - \overline{\theta'^2} \frac{\partial \overline{u'_j S'}}{\partial x_j} \end{aligned} \quad (\text{B.54})$$

$$\begin{aligned} \frac{\overline{\partial \theta' S'^2}}{\partial t} + \frac{\overline{\partial u'_j \theta' S'^2}}{\partial x_j} = & -\overline{u'_j} \frac{\partial \overline{\theta' S'^2}}{\partial x_j} - 2\overline{u'_j \theta' S'} \frac{\partial \overline{S}}{\partial x_j} - \overline{u'_j S'^2} \frac{\partial \overline{\theta}}{\partial x_j} - 2\overline{\theta' S'} \frac{\partial \overline{V_j^{S'}}}{\partial x_j} \\ & - \overline{S'^2} \frac{\partial \overline{V_j^{\theta'}}}{\partial x_j} - \overline{S'^2} \frac{\partial \overline{u'_j \theta'}}{\partial x_j} - 2\overline{\theta' S'} \frac{\partial \overline{u'_j S'}}{\partial x_j} \end{aligned} \quad (\text{B.55})$$

Limiting ourselves to the vertical only is equivalent to setting $j = 3$ in equations (B.46) -

(B.55). Utilizing the pressure correlation and dissipation parameterizations from Canuto

et al. (2007) and Cheng et al. (2005), the TOM equations are

$$\begin{aligned} \frac{\overline{\partial u'_i u'_i u'_m}}{\partial t} + \frac{\overline{\partial w'_i u'_i u'_m}}{\partial z} = & -\frac{2c_8}{\tau} \overline{u'_i u'_i w'} + \lambda_\theta \left(\overline{u'_i u'_i \theta'} \delta_{3m} + \overline{u'_i w' \theta'} \delta_{3l} + \overline{u'_i w' \theta'} \delta_{3i} \right) \\ & - \lambda_S \left(\overline{u'_i u'_i S'} \delta_{3m} + \overline{u'_i w' S'} \delta_{3l} + \overline{u'_i w' S'} \delta_{3i} \right) - \overline{u'_m u'_i w'} \frac{\partial \overline{u'_i}}{\partial z} - \overline{u'_m u'_i w'} \frac{\partial \overline{u'_l}}{\partial z} \\ & - \overline{u'_i u'_i w'} \frac{\partial \overline{u'_m}}{\partial z} \end{aligned} \quad (\text{B.56})$$

$$\begin{aligned} \frac{\overline{\partial u'_i u'_i \theta'}}{\partial t} + \frac{\overline{\partial w'_i u'_i u'_i \theta'}}{\partial z} = & -\overline{w'_i u'_i} \frac{\partial \overline{\theta}}{\partial z} - \overline{w'_i \theta'} \frac{\partial \overline{u'_i}}{\partial z} - \overline{w'_i \theta'} \frac{\partial \overline{u'_l}}{\partial z} - \frac{2c_8}{\tau} \overline{u'_i u'_i \theta'} \\ & + g_i \left(\overline{\alpha u'_i \theta'^2} - \overline{\beta u'_i \theta' S'} \right) + g_l \left(\overline{\alpha u'_i \theta'^2} - \overline{\beta u'_i \theta' S'} \right) \\ & - c_{11} g \alpha \left(\overline{u'_i \theta'^2} \delta_{3l} + \overline{u'_i \theta'^2} \delta_{3i} \right) + \overline{u'_i u'_i} \frac{\partial \overline{w' \theta'}}{\partial z} + \overline{u'_i \theta'} \frac{\partial \overline{u'_i w'}}{\partial z} \\ & + \overline{u'_i \theta'} \frac{\partial \overline{u'_i w'}}{\partial z} - \frac{c_{10}}{3\tau} \delta_{il} \overline{u'_k u'_k \theta'} \end{aligned} \quad (\text{B.57})$$

$$\begin{aligned}
\frac{\partial \overline{u_i u_i S'}}{\partial t} + \frac{\partial \overline{w u_i u_i S'}}{\partial z} &= -\overline{w u_i u_i} \frac{\partial \overline{S}}{\partial z} - \overline{w u_i S'} \frac{\partial \overline{u_i}}{\partial z} - \overline{w u_i S'} \frac{\partial \overline{u_i}}{\partial z} - \overline{u_i S'} \frac{\partial \overline{w u_i}}{\partial z} - \overline{u_i S'} \frac{\partial \overline{w u_i}}{\partial z} \\
&\quad - \overline{u_i u_i} \frac{\partial \overline{w S'}}{\partial z} + g_i \left(\overline{\alpha u_i \theta' S'} - \overline{\beta u_i S'^2} \right) + g_i \left(\overline{\alpha u_i \theta' S'} - \overline{\beta u_i S'^2} \right) - \frac{2c_8}{\tau} \overline{u_i u_i S'} \\
&\quad - c_{11} g \beta \left(\overline{u_i S'^2} \delta_{3i} + \overline{u_i S'^2} \delta_{3i} \right) - \frac{c_{10}}{3\tau} \delta_{il} \overline{u_k u_k S'}
\end{aligned} \tag{B.58}$$

$$\begin{aligned}
\frac{\partial \overline{u_i S'^2}}{\partial t} + \frac{\partial \overline{w u_i S'^2}}{\partial z} &= \overline{w S'^2} \frac{\partial \overline{u_i}}{\partial z} - 2\overline{w u_i S'} \frac{\partial \overline{S}}{\partial z} - 2\frac{\overline{u_i S'}}{\rho_o} \frac{\partial \overline{w S'}}{\partial z} - \frac{\overline{S'^2}}{\rho_o} \frac{\partial \overline{w u_i}}{\partial z} + g \left(\overline{\alpha \theta' S'^2} - \overline{\beta S'^3} \right) \\
&\quad - \frac{2c_8}{\tau} \overline{u_i S'^2} - c_{11} g \beta \overline{S'^3} \delta_{3i}
\end{aligned} \tag{B.59}$$

$$\begin{aligned}
\frac{\partial \overline{u_i \theta'^2}}{\partial t} + \frac{\partial \overline{w u_i \theta'^2}}{\partial x_j} &= \overline{w \theta'^2} \frac{\partial \overline{u_i}}{\partial z} - 2\overline{w u_i \theta'} \frac{\partial \overline{\theta}}{\partial z} - 2\frac{\overline{u_i \theta'}}{\rho_o} \frac{\partial \overline{w \theta'}}{\partial z} - \frac{\overline{\theta'^2}}{\rho_o} \frac{\partial \overline{w u_i}}{\partial z} + g_i \left(\overline{\alpha \theta'^3} - \overline{\beta \theta'^2 S'} \right) \\
&\quad - \frac{2c_8}{\tau} \overline{u_i \theta'^2} - c_{11} g \alpha \overline{\theta'^3} \delta_{3i}
\end{aligned} \tag{B.60}$$

$$\begin{aligned}
\frac{\partial \overline{u_i \theta' S'}}{\partial t} + \frac{\partial \overline{w u_i \theta' S'}}{\partial z} &= -\overline{w u_i \theta'} \frac{\partial \overline{S}}{\partial z} - \overline{w u_i S'} \frac{\partial \overline{\theta}}{\partial z} - \overline{w \theta' S'} \frac{\partial \overline{u_i}}{\partial z} - \frac{\overline{u_i \theta'}}{\rho_o} \frac{\partial \overline{w S'}}{\partial z} - \frac{\overline{u_i S'}}{\rho_o} \frac{\partial \overline{w \theta'}}{\partial z} \\
&\quad - \frac{\overline{\theta' S'}}{\rho_o} \frac{\partial \overline{w u_i}}{\partial z} + g_i \left(\overline{\alpha \theta'^2 S'} - \overline{\beta \theta' S'^2} \right) - \frac{2c_8}{\tau} \overline{u_i \theta' S'} - c_{11} g \alpha \overline{\theta'^3} \delta_{3i} - c_{11} g \beta \overline{S'^3} \delta_{3i}
\end{aligned} \tag{B.61}$$

$$\frac{\partial \overline{\theta'^3}}{\partial t} + \frac{\partial \overline{w \theta'^3}}{\partial z} = -3\overline{w \theta'^2} \frac{\partial \overline{\theta}}{\partial z} + 3\overline{\theta'^2} \frac{\partial \overline{w \theta'}}{\partial z} - \frac{2c_{10}}{\tau} \overline{\theta'^3} \tag{B.62}$$

$$\frac{\partial \overline{S'^3}}{\partial t} + \frac{\partial \overline{w S'^3}}{\partial z} = -3\overline{w S'^2} \frac{\partial \overline{S}}{\partial z} - 3\overline{S'^2} \frac{\partial \overline{w S'}}{\partial z} - \frac{2c_{10}}{\tau} \overline{S'^3} \tag{B.63}$$

$$\begin{aligned}
\frac{\partial \overline{\theta'^2 S'}}{\partial t} + \frac{\partial \overline{w \theta'^2 S'}}{\partial z} &= -2\overline{w \theta' S'} \frac{\partial \overline{\theta}}{\partial z} + 2\frac{\overline{\theta' S'}}{\rho_o} \frac{\partial \overline{w \theta'}}{\partial z} - \frac{c_{10}}{\tau} \overline{\theta'^2 S'} - \overline{w \theta'^2} \frac{\partial \overline{S}}{\partial z} \\
&\quad + \frac{\overline{\theta'^2}}{\rho_o} \frac{\partial \overline{w S'}}{\partial z}
\end{aligned} \tag{B.64}$$

$$\frac{\partial \overline{\theta' S'^2}}{\partial t} + \frac{\partial \overline{w \theta' S'^2}}{\partial z} = -2\overline{w \theta' S'} \frac{\partial \overline{S}}{\partial z} - \overline{w S'^2} \frac{\partial \overline{\theta}}{\partial z} - \overline{S'^2} \frac{\partial \overline{w \theta'}}{\partial z} - 2\overline{\theta' S'} \frac{\partial \overline{w S'}}{\partial z} - \frac{c_{10}}{\tau} \overline{\theta' S'^2} \tag{B.65}$$

At this point, the system is closed, except for the fourth order moments. Here we choose to follow the framework discussed in Cheng et al. (2005) and Canuto et al. (2007). The commonly used quasi-normal approximation (e.g. Andre et al. 1976, Moeng and Randall 1984, Canuto et al. 1994), which can cause unphysical behavior in buoyancy driven regimes, is abandoned. Instead, each fourth order moment is assumed to be the sum of a quasi-normal contribution and a non-gaussian contribution. Further, the time change terms in equations (B.56) - (B.65) are ignored. This yields a system of coupled linear equations. The resulting matrix can be solved to yield the algebraic third order moments. The missing TOMs needed in equations (B.35) - (B.37), (B.39) - (B.40), and (B.42) are given by

$$\begin{aligned}
\overline{w'^3} = & - \left(\frac{\overline{3w'^2}}{f_1} + \frac{3\lambda_\theta \overline{w'\theta'}}{f_1 f_{26}} - \frac{3\lambda_s \overline{w'S'}}{f_1 f_{20}} \right) \frac{\partial \overline{w'^2}}{\partial z} \\
& - \left(\frac{6\lambda_\theta \overline{w'^2}}{f_1 f_{26}} + \frac{12\lambda_\theta^2 \overline{w'\theta'}}{f_1 f_{11} f_{26}} - \frac{6g\alpha\lambda_s \overline{w'S'}}{f_1 f_{14} f_{20}} - \frac{6g\beta\lambda_\theta \overline{w'\theta'}}{f_1 f_{14} f_{26}} \right) \frac{\partial \overline{w'\theta'}}{\partial z} \\
& - \left(-\frac{6\lambda_s \overline{w'^2}}{f_1 f_{20}} + \frac{12\lambda_s^2 \overline{w'S'}}{f_1 f_8 f_{20}} - \frac{6g\alpha\lambda_s \overline{w'\theta'}}{f_1 f_{14} f_{20}} - \frac{6g\beta\lambda_\theta \overline{w'\theta'}}{f_1 f_{14} f_{26}} \right) \frac{\partial \overline{w'S'}}{\partial z} \\
& - \left(\frac{6\lambda_\theta^2 \overline{w'^2}}{f_1 f_{11} f_{26}} + \frac{18\lambda_\theta^3 \overline{w'\theta'}}{f_1 f_{11} f_{16} f_{26}} - \frac{6g\beta\lambda_\theta^2 \overline{w'S'}}{f_1 f_{11} f_{17} f_{26}} \right) \frac{\partial \overline{\theta'^2}}{\partial z} \\
& - \left(\frac{6\lambda_s^2 \overline{w'^2}}{f_1 f_8 f_{20}} + \frac{6g\alpha\lambda_s^2 \overline{w'\theta'}}{f_1 f_8 f_{20} f_{23}} - \frac{18\lambda_\theta^3 \overline{w'\theta'}}{f_1 f_8 f_{15} f_{20}} \right) \frac{\partial \overline{S'^2}}{\partial z} \\
& - \left(\frac{12g\alpha\lambda_s^2 \overline{w'S'}}{f_1 f_8 f_{20} f_{23}} - \frac{12g\beta\lambda_\theta^2 \overline{w'\theta'}}{f_1 f_{11} f_{17} f_{26}} - \frac{6g\alpha\lambda_s \overline{w'^2}}{f_1 f_{14} f_{20}} - \frac{6g\beta\lambda_\theta \overline{w'^2}}{f_1 f_{14} f_{26}} \right) \frac{\partial \overline{\theta'S'}}{\partial z}
\end{aligned} \tag{B.66}$$

$$\begin{aligned}
\overline{u'^2 w'} = & - \frac{\overline{2u'w'}}{f_2} \frac{\partial \overline{u'w'}}{\partial z} - \left(\frac{\lambda_\theta \overline{w'\theta'}}{f_2 f_{24}} + \frac{\overline{w'^2}}{f_2} - \frac{\lambda_s \overline{w'S'}}{f_2 f_{18}} \right) \frac{\partial \overline{u'^2}}{\partial z} + \frac{2\lambda_s \overline{u'w'}}{f_2 f_{18}} \frac{\partial \overline{u'S'}}{\partial z} \\
& - \frac{2\lambda_\theta \overline{u'w'}}{f_2 f_{24}} \frac{\partial \overline{u'\theta'}}{\partial z}
\end{aligned} \tag{B.67}$$

$$\begin{aligned} \overline{v'^2 w'} = & -\frac{2\overline{v' w'} \partial \overline{v' w'}}{f_3 \partial z} + \frac{2\lambda_s \overline{v' w'} \partial \overline{v' S'}}{f_3 f_{19} \partial z} - \frac{2\lambda_\theta \overline{v' w'} \partial \overline{v' \theta'}}{f_3 f_{25} \partial z} \\ & - \left(\frac{\overline{w'^2}}{f_3} + \frac{\lambda_\theta \overline{w' \theta'}}{f_3 f_{25}} - \frac{\lambda_s \overline{w' S'}}{f_3 f_{19}} \right) \frac{\partial \overline{v'^2}}{\partial z} \end{aligned} \quad (\text{B.68})$$

$$\begin{aligned} \overline{u' w'^2} = & -\frac{\overline{u' w'} \partial \overline{w'^2}}{f_4 \partial z} + \frac{2\lambda_s \overline{u' w'} \partial \overline{w' S'}}{f_4 f_{21} \partial z} - \frac{2\lambda_\theta \overline{u' w'} \partial \overline{w' \theta'}}{f_4 f_{27} \partial z} + \frac{2\lambda_s^2 \overline{u' w'} \partial \overline{S'^2}}{f_4 f_6 f_{21} \partial z} - \frac{2\lambda_\theta^2 \overline{u' w'} \partial \overline{\theta'^2}}{f_4 f_9 f_{27} \partial z} \\ & - \left(\frac{2\overline{w'^2}}{f_4} + \frac{2\lambda_\theta \overline{w' \theta'}}{f_4 f_{27}} - \frac{2\lambda_s \overline{w' S'}}{f_4 f_{21}} \right) \frac{\partial \overline{u' w'}}{\partial z} + \left(\frac{2g\alpha\lambda_s \overline{u' w'}}{f_4 f_{12} f_{21}} + \frac{2g\beta\lambda_\theta \overline{u' w'}}{f_4 f_{12} f_{27}} \right) \frac{\partial \overline{\theta' S'}}{\partial z} \\ & - \left(\frac{4\lambda_\theta^2 \overline{w' \theta'}}{f_4 f_9 f_{27}} + \frac{2\lambda_\theta \overline{w'^2}}{f_4 f_{27}} - \frac{2g\alpha\lambda_s \overline{w' S'}}{f_4 f_{12} f_{21}} - \frac{2g\beta\lambda_\theta \overline{w' \theta'}}{f_4 f_{12} f_{27}} \right) \frac{\partial \overline{u' \theta'}}{\partial z} \\ & - \left(\frac{4\lambda_s^2 \overline{w' S'}}{f_4 f_6 f_{21}} - \frac{2\lambda_s \overline{w'^2}}{f_4 f_{21}} - \frac{2g\alpha\lambda_s \overline{w' \theta'}}{f_4 f_{12} f_{21}} - \frac{2g\beta\lambda_\theta \overline{w' S'}}{f_4 f_{12} f_{27}} \right) \frac{\partial \overline{u' S'}}{\partial z} \end{aligned} \quad (\text{B.69})$$

$$\begin{aligned} \overline{v' w'^2} = & -\frac{\overline{v' w'} \partial \overline{w'^2}}{f_5 \partial z} + \frac{2\lambda_s \overline{v' w'} \partial \overline{w' S'}}{f_5 f_{22} \partial z} - \frac{2\lambda_\theta \overline{v' w'} \partial \overline{w' \theta'}}{f_5 f_{28} \partial z} + \frac{2\lambda_s^2 \overline{v' w'} \partial \overline{S'^2}}{f_5 f_7 f_{22} \partial z} - \frac{2\lambda_\theta^2 \overline{v' w'} \partial \overline{\theta'^2}}{f_5 f_{10} f_{28} \partial z} \\ & - \left(\frac{2\overline{w'^2}}{f_5} + \frac{2\lambda_\theta \overline{w' \theta'}}{f_5 f_{28}} - \frac{2\lambda_s \overline{w' S'}}{f_5 f_{22}} \right) \frac{\partial \overline{v' w'}}{\partial z} + \left(\frac{2g\alpha\lambda_s \overline{v' w'}}{f_5 f_{13} f_{22}} + \frac{2g\beta\lambda_\theta \overline{v' w'}}{f_5 f_{13} f_{28}} \right) \frac{\partial \overline{\theta' S'}}{\partial z} \\ & - \left(\frac{2\lambda_\theta \overline{w'^2}}{f_5 f_{28}} + \frac{4\lambda_\theta^2 \overline{w' \theta'}}{f_5 f_{10} f_{28}} - \frac{2g\alpha\lambda_s \overline{w' S'}}{f_5 f_{13} f_{22}} - \frac{2g\beta\lambda_\theta \overline{w' S'}}{f_5 f_{13} f_{28}} \right) \frac{\partial \overline{v' \theta'}}{\partial z} \\ & - \left(-\frac{2\lambda_s \overline{w'^2}}{f_5 f_{22}} + \frac{4\lambda_s^2 \overline{w' S'}}{f_5 f_7 f_{22}} - \frac{2g\alpha\lambda_s \overline{w' \theta'}}{f_5 f_{13} f_{22}} - \frac{2g\beta\lambda_\theta \overline{w' \theta'}}{f_5 f_{13} f_{28}} \right) \frac{\partial \overline{v' S'}}{\partial z} \end{aligned} \quad (\text{B.70})$$

$$\overline{u' v' w'} = -\overline{v' w'} \frac{\partial \overline{u' w'}}{\partial z} - \overline{u' w'} \frac{\partial \overline{v' w'}}{\partial z} - \overline{w'^2} \frac{\partial \overline{u' v'}}{\partial z} - (1 - c_{11}) \left(\overline{u' w'^2} \frac{\partial \overline{v'}}{\partial z} + \overline{v' w'^2} \frac{\partial \overline{u'}}{\partial z} \right) \quad (\text{B.71})$$

$$\begin{aligned} \overline{w'^2 \theta'} = & - \left(\frac{2\overline{w'^2}}{f_{26}} + \frac{4\lambda_\theta \overline{w' \theta'}}{f_{11} f_{26}} - \frac{2g\beta \overline{w' S'}}{f_{14} f_{26}} \right) \frac{\partial \overline{w' \theta'}}{\partial z} + \frac{2g\beta \overline{w' \theta'} \partial \overline{w' S'}}{f_{14} f_{26} \partial z} - \frac{\overline{w' \theta'} \partial \overline{w'^2}}{f_{26} \partial z} \\ & - \left(\frac{2\lambda_\theta \overline{w'^2}}{f_{11} f_{26}} + \frac{6\lambda_\theta^2 \overline{w' \theta'}}{f_{11} f_{16} f_{26}} - \frac{2g\beta \lambda_\theta \overline{w' \theta'}}{f_{11} f_{17} f_{26}} \right) \frac{\partial \overline{\theta'^2}}{\partial z} + \left(\frac{2g\beta \overline{w'^2}}{f_{14} f_{26}} + \frac{4g\beta \lambda_\theta \overline{w' \theta'}}{f_{11} f_{17} f_{26}} \right) \frac{\partial \overline{\theta' S'}}{\partial z} \end{aligned} \quad (\text{B.72})$$

$$\overline{w' \theta'^2} = -\frac{2\overline{w' \theta'} \partial \overline{w' \theta'}}{f_{11} \partial z} + \frac{2g\beta \overline{w' \theta'} \partial \overline{\theta' S'}}{f_{11} f_{17} \partial z} - \left(\frac{3\lambda_\theta \overline{w' \theta'}}{f_{11} f_{16}} + \frac{\overline{w'^2}}{f_{11}} - \frac{g\beta \overline{w' S'}}{f_{11} f_{17}} \right) \frac{\partial \overline{\theta'^2}}{\partial z} \quad (\text{B.73})$$

$$\begin{aligned} \overline{w'^2 S'} = & -\frac{\overline{w' S'} \partial \overline{w'^2}}{f_{20} \partial z} - \frac{2g\alpha \overline{w' S'} \partial \overline{w' \theta'}}{f_{14} f_{20} \partial z} - \left(\frac{2\overline{w'^2}}{f_{20}} + \frac{2g\alpha \overline{w' \theta'}}{f_{14} f_{20}} - \frac{4\lambda_s \overline{w' S'}}{f_8 f_{20}} \right) \frac{\partial \overline{w' S'}}{\partial z} \\ & - \left(\frac{6\lambda_s^2 \overline{w' S'}}{f_8 f_{15} f_{20}} - \frac{2g\alpha \lambda_s \overline{w' \theta'}}{f_8 f_{20} f_{23}} - \frac{2\lambda_s \overline{w'^2}}{f_8 f_{20}} \right) \frac{\partial \overline{S'^2}}{\partial z} + \left(\frac{4g\alpha \lambda_s \overline{w' S'}}{f_8 f_{20} f_{23}} - \frac{2g\alpha \overline{w'^2}}{f_{14} f_{20}} \right) \frac{\partial \overline{\theta' S'}}{\partial z} \end{aligned} \quad (\text{B.74})$$

$$\overline{w' S'^2} = -\frac{2\overline{w' S'} \partial \overline{w' S'}}{f_8 \partial z} - \left(\frac{g\alpha \overline{w' \theta'}}{f_8 f_{23}} + \frac{\overline{w'^2}}{f_8} - \frac{3\lambda_s \overline{w' S'}}{f_8 f_{15}} \right) \frac{\partial \overline{S'^2}}{\partial z} - \frac{2g\alpha \overline{w' S'}}{f_8 f_{23}} \frac{\partial \overline{\theta' S'}}{\partial z} \quad (\text{B.75})$$

$$\begin{aligned} \overline{u' w' S'} = & -\frac{\partial \overline{u' S'}}{\partial z} \left(\frac{\overline{w'^2}}{f_{21}} - \frac{2\lambda_s \overline{w' S'}}{f_6 f_{21}} + \frac{g\alpha \overline{w' \theta'}}{f_{12} f_{21}} \right) - \frac{\overline{u' w'} \partial \overline{w' S'}}{f_{21} \partial z} - \frac{g\alpha \overline{u' w'}}{f_{12} f_{21}} \frac{\partial \overline{\theta' S'}}{\partial z} \\ & + \frac{\lambda_s \overline{u' w'}}{f_6 f_{21}} \frac{\partial \overline{S'^2}}{\partial z} - \frac{g\alpha \overline{w' S'}}{f_{12} f_{21}} \frac{\partial \overline{u' \theta'}}{\partial z} \end{aligned} \quad (\text{B.76})$$

$$\begin{aligned} \overline{v' w' S'} = & -\frac{\partial \overline{v' S'}}{\partial z} \left(\frac{\overline{w'^2}}{f_{22}} - \frac{2\lambda_s \overline{w' S'}}{f_7 f_{22}} + \frac{g\alpha \overline{w' \theta'}}{f_{13} f_{23}} \right) - \frac{\overline{v' w'} \partial \overline{w' S'}}{f_{22} \partial z} - \frac{g\alpha \overline{v' w'}}{f_{13} f_{22}} \frac{\partial \overline{\theta' S'}}{\partial z} \\ & + \frac{\lambda_s \overline{v' w'}}{f_7 f_{22}} \frac{\partial \overline{S'^2}}{\partial z} - \frac{g\alpha \overline{w' S'}}{f_{13} f_{22}} \frac{\partial \overline{v' \theta'}}{\partial z} \end{aligned} \quad (\text{B.77})$$

$$\begin{aligned} \overline{u' w' \theta'} = & -\frac{\partial \overline{u' \theta'}}{\partial z} \left(\frac{\overline{w'^2}}{f_{27}} - \frac{g\beta \overline{w' S'}}{f_{12} f_{27}} + \frac{2\lambda_\theta \overline{w' \theta'}}{f_9 f_{27}} \right) - \frac{\overline{u' w'} \partial \overline{w' \theta'}}{f_{27} \partial z} - \frac{g\beta \overline{u' w'}}{f_{12} f_{27}} \frac{\partial \overline{\theta' S'}}{\partial z} \\ & + \frac{\lambda_\theta \overline{u' w'}}{f_9 f_{27}} \frac{\partial \overline{\theta'^2}}{\partial z} - \frac{g\beta \overline{w' \theta'}}{f_{12} f_{27}} \frac{\partial \overline{u' \theta'}}{\partial z} \end{aligned} \quad (\text{B.78})$$

$$\begin{aligned} \overline{v' w' \theta'} = & -\frac{\partial \overline{v' \theta'}}{\partial z} \left(\frac{\overline{w'^2}}{f_{28}} - \frac{g\beta \overline{w' S'}}{f_{13} f_{28}} + \frac{2\lambda_\theta \overline{w' \theta'}}{f_{10} f_{28}} \right) - \frac{\overline{v' w'} \partial \overline{w' \theta'}}{f_{28} \partial z} - \frac{g\beta \overline{v' w'}}{f_{13} f_{28}} \frac{\partial \overline{\theta' S'}}{\partial z} \\ & + \frac{\lambda_\theta \overline{v' w'}}{f_{10} f_{28}} \frac{\partial \overline{\theta'^2}}{\partial z} - \frac{g\beta \overline{w' \theta'}}{f_{13} f_{28}} \frac{\partial \overline{v' \theta'}}{\partial z} \end{aligned} \quad (\text{B.79})$$

In these equations, the constants in the denominator (f_x) have the general form

$f_x = \frac{b_y}{\tau}$, where the values of b_y follow Cheng et al. (2005). The complete set of second

moment equations (with TOMs given by equations (B.66) - (B.79)) is now given by

$$\frac{\partial \bar{u}^{\cdot 2}}{\partial t} + \frac{\partial \bar{u}^{\cdot 2} \bar{w}^{\cdot}}{\partial z} = \left(\frac{1}{3} c_1 + c_2 - 2 \right) \bar{u}^{\cdot} \bar{w}^{\cdot} \frac{\partial \bar{u}}{\partial z} - \frac{2}{3} c_1 \bar{v}^{\cdot} \bar{w}^{\cdot} \frac{\partial \bar{v}}{\partial z} + \frac{g}{3} \left(\alpha \bar{w}^{\cdot} \bar{\theta}^{\cdot} - \beta \bar{w}^{\cdot} \bar{S}^{\cdot} \right) - \frac{2}{3} \varepsilon - 2 \tau_{pv}^{-1} \left(\bar{u}^{\cdot 2} - \frac{2}{3} k \right) \quad (\text{B.80})$$

$$\frac{\partial \bar{w}^{\cdot 2}}{\partial t} + \frac{\partial \bar{w}^{\cdot 3}}{\partial z} = \left(\frac{1}{3} c_1 - c_2 \right) \left(\bar{u}^{\cdot} \bar{w}^{\cdot} \frac{\partial \bar{u}}{\partial z} + \bar{v}^{\cdot} \bar{w}^{\cdot} \frac{\partial \bar{v}}{\partial z} \right) + \frac{4g}{3} \left(\alpha \bar{w}^{\cdot} \bar{\theta}^{\cdot} - \beta \bar{w}^{\cdot} \bar{S}^{\cdot} \right) - \frac{2}{3} \varepsilon - 2 \tau_{pv}^{-1} \left(\bar{w}^{\cdot 2} - \frac{2}{3} k \right) \quad (\text{B.81})$$

$$\frac{\partial \bar{u}^{\cdot} \bar{w}^{\cdot}}{\partial t} + \frac{\partial \bar{u}^{\cdot} \bar{w}^{\cdot 2}}{\partial z} = \frac{1}{2} \frac{\partial \bar{u}}{\partial z} \left[(c_1 + c_2 - 2) \bar{w}^{\cdot 2} + (c_1 - c_2) \bar{u}^{\cdot 2} + 4 \left(\frac{1}{5} - \frac{c_1}{3} \right) k \right] + \frac{c_1 - c_2}{2} \bar{u}^{\cdot} \bar{v}^{\cdot} \frac{\partial \bar{v}}{\partial z} + \frac{g}{2} \left(\alpha \bar{u}^{\cdot} \bar{\theta}^{\cdot} - \beta \bar{u}^{\cdot} \bar{S}^{\cdot} \right) - 2 \tau_{pv}^{-1} \bar{u}^{\cdot} \bar{w}^{\cdot} \quad (\text{B.82})$$

$$\frac{\partial \bar{v}^{\cdot} \bar{w}^{\cdot}}{\partial t} + \frac{\partial \bar{v}^{\cdot} \bar{w}^{\cdot 2}}{\partial z} = \frac{1}{2} \frac{\partial \bar{v}}{\partial z} \left[(c_1 - c_2 - 2) \bar{w}^{\cdot 2} + (c_1 - c_2) \bar{v}^{\cdot 2} + 4 \left(\frac{1}{5} - \frac{c_1}{3} \right) k \right] + \frac{c_1 - c_2}{2} \bar{u}^{\cdot} \bar{v}^{\cdot} \frac{\partial \bar{u}}{\partial z} + \frac{g}{2} \left(\alpha \bar{v}^{\cdot} \bar{\theta}^{\cdot} - \beta \bar{v}^{\cdot} \bar{S}^{\cdot} \right) - 2 \tau_{pv}^{-1} \bar{v}^{\cdot} \bar{w}^{\cdot} \quad (\text{B.83})$$

$$\frac{\partial \bar{u}^{\cdot} \bar{v}^{\cdot}}{\partial t} + \frac{\partial \bar{u}^{\cdot} \bar{v}^{\cdot} \bar{w}^{\cdot}}{\partial z} = - \left[1 - \frac{1}{2} (c_1 + c_2) \right] \left(\bar{u}^{\cdot} \bar{w}^{\cdot} \frac{\partial \bar{v}}{\partial z} + \bar{v}^{\cdot} \bar{w}^{\cdot} \frac{\partial \bar{u}}{\partial z} \right) - 2 \tau_{pv}^{-1} \bar{u}^{\cdot} \bar{v}^{\cdot} \quad (\text{B.84})$$

$$\frac{\partial k}{\partial t} + \frac{1}{2} \frac{\partial}{\partial z} \left(\bar{u}^{\cdot 2} \bar{w}^{\cdot} + \bar{v}^{\cdot 2} \bar{w}^{\cdot} + \bar{w}^{\cdot 3} \right) = - \left(\bar{u}^{\cdot} \bar{w}^{\cdot} \frac{\partial \bar{u}}{\partial z} + \bar{v}^{\cdot} \bar{w}^{\cdot} \frac{\partial \bar{v}}{\partial z} \right) + g \left(\alpha \bar{w}^{\cdot} \bar{\theta}^{\cdot} - \beta \bar{w}^{\cdot} \bar{S}^{\cdot} \right) - \varepsilon \quad (\text{B.85})$$

$$\frac{\partial \bar{u}^{\cdot} \bar{\theta}^{\cdot}}{\partial t} + \frac{\partial \bar{u}^{\cdot} \bar{w}^{\cdot} \bar{\theta}^{\cdot}}{\partial z} = - (1 + c_3) \bar{w}^{\cdot} \bar{\theta}^{\cdot} \frac{\partial \bar{u}}{\partial z} - \bar{u}^{\cdot} \bar{w}^{\cdot} \frac{\partial \bar{\theta}}{\partial z} - \tau_{p\theta}^{-1} \bar{u}^{\cdot} \bar{\theta}^{\cdot} \quad (\text{B.86})$$

$$\frac{\partial \bar{v}^{\cdot} \bar{\theta}^{\cdot}}{\partial t} + \frac{\partial \bar{v}^{\cdot} \bar{w}^{\cdot} \bar{\theta}^{\cdot}}{\partial z} = - (1 + c_3) \bar{w}^{\cdot} \bar{\theta}^{\cdot} \frac{\partial \bar{v}}{\partial z} - \bar{v}^{\cdot} \bar{w}^{\cdot} \frac{\partial \bar{\theta}}{\partial z} - \tau_{p\theta}^{-1} \bar{v}^{\cdot} \bar{\theta}^{\cdot} \quad (\text{B.87})$$

$$\frac{\partial \bar{w}^{\cdot} \bar{\theta}^{\cdot}}{\partial t} + \frac{\partial \bar{w}^{\cdot 2} \bar{\theta}^{\cdot}}{\partial z} = - (1 - d_1) g \left(\alpha \bar{\theta}^{\cdot 2} - \beta \bar{\theta}^{\cdot} \bar{S}^{\cdot} \right) - \bar{w}^{\cdot 2} \frac{\partial \bar{\theta}}{\partial z} - \frac{c_3}{4} \left(\bar{u}^{\cdot} \bar{\theta}^{\cdot} \frac{\partial \bar{u}}{\partial z} + \bar{v}^{\cdot} \bar{\theta}^{\cdot} \frac{\partial \bar{v}}{\partial z} \right) - \tau_{p\theta}^{-1} \bar{w}^{\cdot} \bar{\theta}^{\cdot} \quad (\text{B.88})$$

$$\frac{\partial \overline{u'S'}}{\partial t} + \frac{\partial \overline{u'w'S'}}{\partial z} = -(1+c_3)\overline{w'S'}\frac{\partial \overline{u}}{\partial z} - \overline{u'w'}\frac{\partial \overline{S}}{\partial z} - \tau_{p\theta}^{-1}\overline{u'S'} \quad (\text{B.89})$$

$$\frac{\partial \overline{v'S'}}{\partial t} + \frac{\partial \overline{v'w'S'}}{\partial z} = -(1+c_3)\overline{w'S'}\frac{\partial \overline{v}}{\partial z} - \overline{v'w'}\frac{\partial \overline{S}}{\partial z} - \tau_{p\theta}^{-1}\overline{v'S'} \quad (\text{B.90})$$

$$\frac{\partial \overline{w'S'}}{\partial t} + \frac{\partial \overline{w'^2S'}}{\partial z} = -(1-d_1)g\left(\alpha\overline{\theta'S'} - \beta\overline{S'^2}\right) - \overline{w'^2}\frac{\partial \overline{S}}{\partial z} - \frac{c_3}{4}\left(\overline{u'S'}\frac{\partial \overline{u}}{\partial z} + \overline{v'S'}\frac{\partial \overline{v}}{\partial z}\right) - \tau_{p\theta}^{-1}\overline{w'S'} \quad (\text{B.91})$$

$$\frac{\partial \overline{\theta'^2}}{\partial t} + \frac{\partial \overline{w'\theta'^2}}{\partial z} = -2\overline{w'\theta'}\frac{\partial \overline{\theta}}{\partial z} - 2\tau_{\theta}^{-1}\overline{\theta'^2} \quad (\text{B.92})$$

$$\frac{\partial \overline{S'^2}}{\partial t} + \frac{\partial \overline{w'S'^2}}{\partial z} = -2\overline{w'S'}\frac{\partial \overline{S}}{\partial z} - 2\tau_s^{-1}\overline{S'^2} . \quad (\text{B.93})$$

This closes the system, where the vertical flux of passive trace is given by equation (B.45).

Appendix C:

Model Parameters

The most important terms to discuss are the eddy turnover time scales $(\tau_{pv}, \tau_{p\theta}, \tau_{pS}, \tau_{pP}, \tau_{\theta}, \tau_S, \tau_P, \tau_{\theta S}, \tau_{\theta P}, \tau_{SP})$ and the values of $\pi_1, \pi_2, \pi_3, \pi_4$, and π_5 . The time scales follow directly from Canuto et al. (2007) and are given as

$$\begin{aligned} \tau_{pv} &= \frac{2}{5}\tau; & \tau_{p\theta} &= \pi_1\tau; & \tau_{pS} = \tau_{pP} &= \pi_4\tau; & \tau_{\theta} &= \pi_3\tau \\ \tau_S &= \pi_5\tau; & \tau_P &= \pi_5\tau; & \tau_{S\theta} = \tau_{\theta P} = \tau_{SP} &= \pi_2\tau; \end{aligned}$$

In the original models developed by Canuto and colleagues, the values of $\pi_1, \pi_2, \pi_3, \pi_4$,

and π_5 were defined as

$$\pi_1 = \pi_4 = 0.084226; \quad \pi_3 = \pi_5 = 0.72; \quad \pi_2 = 1/3$$

Using constant values would give mixing for all Richardson numbers (see Appendix F).

Canuto et al. (2001;2002) derived expressions for the critical Richardson number, above

which no mixing is allowed. To derive this value, the limit of the steady state TKE equation as the TKE goes to zero is taken. This results in a fairly complex equation for the case of variable salinity (see Appendix C of Canuto et al. 2002).

Canuto et al. (2008) tested the assumption of constant values π_x against laboratory and oceanic data. As expected, the assumption was not valid. A fit to this data gave the following relations

$$\begin{aligned} \pi_1 &= \pi_1^0 \left(1 + \frac{Ri}{1 + 10R_\rho^{-1}} \right)^{-1}; & \pi_4 &= \pi_4^0 \left(1 + \frac{Ri}{1 + 10R_\rho} \right)^{-1}; \\ \pi_2 &= \pi_2^0 \left(\frac{1}{2} [R_\rho + R_\rho^{-1}] \right)^{-1}; & \pi_{3,5} &= \pi_{3,5}^0. \end{aligned}$$

The functions are plotted in Figure C.1. Now as the Richardson number and diffusivity ratios change, the value of the constants defined above change as well. In general, as the Richardson number increases, the value of the constant decreases. As the diffusivity ratio increases, the decrease with increasing Richardson number is slowed. This is meant to mimic double diffusive convection. In this model, we will assume that the diffusion of the passive tracer will be limited in a way similar to salinity.

The remaining constant introduced in Appendix B are defined as

$$\begin{aligned} c_1 &= 0.984; & c_2 &= 0.568; & c_3 &= 0.29; & d_1 &= 1/3 \\ c_{11} &= 0.1; & c_8 &= 5. \end{aligned}$$

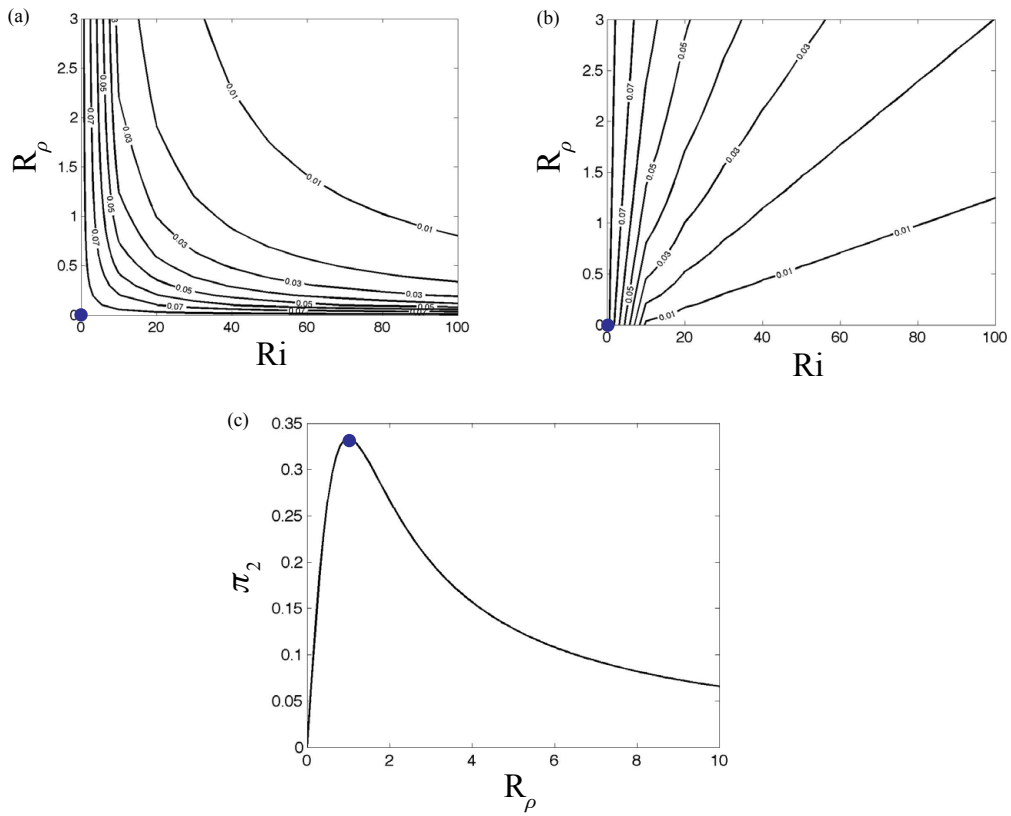


Figure C.1 - Plot of functions from Canuto et al. (2008) (a) π_1 , (b) π_4 , and (c) π_2 . In all of the plots, the constant value assumed in Canuto et al. (2002) is signified by a blue dot.

Appendix D:

Two-Dimensional Equations

The conversion to the coordinate given by equation (3.3) is easiest by first writing the model equations, which are given as

$$\frac{\partial u}{\partial t} + \frac{1}{2} \frac{\partial u^2}{\partial x} + w \frac{\partial u}{\partial z} - fv = -\frac{\partial \pi}{\partial x} - \frac{\partial \overline{u'w'}}{\partial z} \quad (\text{D.1})$$

$$\frac{\partial v}{\partial t} + u \frac{\partial v}{\partial x} + w \frac{\partial v}{\partial z} + fu = -\frac{\partial \overline{v'w'}}{\partial z} \quad (\text{D.2})$$

$$\frac{\partial \theta}{\partial t} + u \frac{\partial \theta}{\partial x} + w \frac{\partial \theta}{\partial z} = -\frac{\partial \overline{w'\theta'}}{\partial z} + \frac{1}{\rho_o C_p} \frac{\partial I}{\partial z} \quad (\text{D.3})$$

$$\frac{\partial S}{\partial t} + u \frac{\partial S}{\partial x} + w \frac{\partial S}{\partial z} = -\frac{\partial \overline{w'S'}}{\partial z} \quad (\text{D.4})$$

$$\frac{1}{\rho} \frac{D\rho}{Dt} + \frac{\partial u}{\partial x} + \frac{\partial w}{\partial z} = 0, \quad (\text{D.5})$$

in a generalized (η) coordinate. The first step is to transform the necessary derivatives to

the η -coordinate. These are given by

$$\left(\frac{\partial}{\partial t}\right)_z = \left(\frac{\partial}{\partial t}\right)_\eta + \left(\frac{\partial \eta}{\partial t}\right)_z \frac{\partial}{\partial \eta} \quad (\text{D.6})$$

$$\left(\frac{\partial}{\partial x}\right)_z = \left(\frac{\partial}{\partial x}\right)_\eta + \left(\frac{\partial \eta}{\partial x}\right)_z \frac{\partial}{\partial \eta} \quad (\text{D.7})$$

$$\frac{\partial}{\partial z} = \frac{\partial \eta}{\partial z} \frac{\partial}{\partial \eta}. \quad (\text{D.8})$$

To transform the vertical derivative in equation (D.5), we begin with

$$\frac{\partial \dot{\eta}}{\partial \eta} \equiv \frac{\partial}{\partial \eta} \frac{D\eta}{Dt} = \frac{\partial}{\partial \eta} \left[\frac{\partial \eta}{\partial t} + u \frac{\partial \eta}{\partial x} + w \frac{\partial \eta}{\partial z} \right] = \frac{\partial z}{\partial \eta} \frac{\partial}{\partial z} \left[\frac{\partial \eta}{\partial t} + u \frac{\partial \eta}{\partial x} + w \frac{\partial \eta}{\partial z} \right].$$

We now pull in the z-derivative, and rearrange the first derivative. This yields

$$\begin{aligned} \frac{\partial z}{\partial \eta} \frac{\partial}{\partial z} \left[\frac{\partial \eta}{\partial t} + u \frac{\partial \eta}{\partial x} + w \frac{\partial \eta}{\partial z} \right] &= \frac{\partial z}{\partial \eta} \frac{\partial}{\partial t} \frac{\partial \eta}{\partial z} + \frac{\partial z}{\partial \eta} \frac{\partial}{\partial z} \left(u \frac{\partial \eta}{\partial x} \right) + \frac{\partial z}{\partial \eta} \frac{\partial}{\partial z} \left(w \frac{\partial \eta}{\partial z} \right) \\ &= \frac{\partial z}{\partial \eta} \frac{D}{Dt} \left(\frac{\partial \eta}{\partial z} \right) + \frac{\partial z}{\partial \eta} \frac{\partial u}{\partial z} \frac{\partial \eta}{\partial x} + \frac{\partial z}{\partial \eta} \frac{\partial w}{\partial z} \frac{\partial \eta}{\partial z} \\ &= \frac{\partial z}{\partial \eta} \frac{D}{Dt} \left(\frac{\partial \eta}{\partial z} \right)_z + \frac{\partial u}{\partial \eta} \left(\frac{\partial \eta}{\partial x} \right)_z + \frac{\partial w}{\partial z}. \end{aligned}$$

This can be arranged to give

$$\frac{\partial w}{\partial z} = \frac{\partial \dot{\eta}}{\partial \eta} - \frac{\partial z}{\partial \eta} \frac{D}{Dt} \left(\frac{\partial \eta}{\partial z} \right)_\eta - \frac{\partial u}{\partial x} \left(\frac{\partial \eta}{\partial x} \right)_z. \quad (\text{D.9})$$

We now plug (D.7) and (D.9) into the continuity equation (D.5). This yields

$$\frac{1}{\rho} \frac{D\rho}{Dt} + \frac{\partial \dot{\eta}}{\partial \eta} - \frac{\partial z}{\partial \eta} \frac{D}{Dt} \left(\frac{\partial \eta}{\partial z} \right)_\eta - \frac{\partial u}{\partial \eta} \left(\frac{\partial \eta}{\partial x} \right)_z + \frac{\partial u}{\partial \eta} \left(\frac{\partial \eta}{\partial x} \right)_z + \left(\frac{\partial u}{\partial x} \right)_\eta = 0. \quad (\text{D.10})$$

The next step is to cast the first term on the left hand side in the generalized coordinate.

Using the hydrostatic approximation, we can write

$$\rho = -\frac{1}{g} \frac{\partial p}{\partial \eta} \frac{\partial \eta}{\partial z} = m \left| \frac{\partial \eta}{\partial z} \right|.$$

In the second equality, we have defined the pseudodensity $\left(m = \left| \frac{1}{g} \frac{\partial p}{\partial \eta} \right| \right)$. Using this, we

can write

$$\frac{1}{\rho} \frac{D\rho}{Dt} = \frac{1}{m} \frac{D}{Dt} \left(m \frac{\partial \eta}{\partial z} \right) = \frac{1}{m} \frac{Dm}{Dt} + \frac{1}{\frac{\partial \eta}{\partial z}} \frac{D}{Dt} \left(\frac{\partial \eta}{\partial z} \right).$$

This is then plugged into D.10 to yield the continuity equation in the η -coordinate, given

by

$$\frac{1}{m} \frac{Dm}{Dt} + \left(\frac{\partial u}{\partial x} \right)_\eta + \frac{\partial \dot{\eta}}{\partial \eta} = 0. \quad (\text{D.11})$$

The material derivative in (D.11) is given by $\frac{D}{Dt}(\)_{\eta} \equiv \frac{\partial}{\partial t}(\)_{\eta} + u \frac{\partial}{\partial x}(\)_{\eta} + \dot{\eta} \frac{\partial}{\partial \eta}(\)_{\eta}$.

The pressure gradient force in the zonal momentum equation is written in the general coordinate as

$$\frac{1}{\rho} \left(\frac{\partial p}{\partial x} \right)_z = \frac{1}{\rho} \left(\frac{\partial p}{\partial x} \right)_{\eta} - \frac{1}{\rho} \frac{\partial p}{\partial z} \left(\frac{\partial z}{\partial x} \right)_{\eta}.$$

The dynamic and thermodynamic equations in the η -coordinate are given by

$$\frac{Du}{Dt} - fv = - \left(\frac{\partial \pi}{\partial x} \right)_{\eta} + \frac{\partial \pi}{\partial z} \left(\frac{\partial z}{\partial x} \right)_{\eta} - \frac{\partial \eta}{\partial z} \frac{\partial \overline{u'w'}}{\partial \eta}$$

$$\frac{Dv}{Dt} + fu = - \frac{\partial \eta}{\partial z} \frac{\partial \overline{v'w'}}{\partial \eta}$$

$$\frac{D\theta}{Dt} = - \frac{\partial \eta}{\partial z} \frac{\partial \overline{w'\theta'}}{\partial \eta} + \frac{1}{\rho_o C_p} \frac{\partial \eta}{\partial z} \frac{\partial I}{\partial \eta}$$

$$\frac{DS}{Dt} = - \frac{\partial \eta}{\partial z} \frac{\partial \overline{w'S'}}{\partial \eta}$$

$$\frac{1}{m} \frac{Dm}{Dt} + \left(\frac{\partial u}{\partial x} \right)_{\eta} + \frac{\partial \dot{\eta}}{\partial \eta} = 0$$

$$\frac{D}{Dt}(\)_{\eta} \equiv \frac{\partial}{\partial t}(\)_{\eta} + u \frac{\partial}{\partial x}(\)_{\eta} + \dot{\eta} \frac{\partial}{\partial \eta}(\)_{\eta}$$

These equations can now be converted to our chosen coordinate. Using equation (3.3), m

and $\frac{\partial \eta}{\partial z}$ are defined as

$$m \equiv \begin{cases} \rho(z_{sfc} - z_{BL}) & z_{sfc} \geq z \geq z_{BL} \\ \rho(z_{BL} - z_{BOT}) & z_{BL} \geq z \geq z_{BOT} \end{cases}$$

and

$$\frac{\partial \eta}{\partial z} \equiv \frac{\partial \sigma}{\partial z} = \begin{cases} \frac{-1}{(z_{sfc} - z_{BL})} & z_{sfc} \geq z \geq z_{BL} \\ \frac{-1}{(z_{BL} - z_{BOT})} & z_{BL} \geq z \geq z_{BOT} \end{cases}$$

Using these definitions, the equations of motions in our coordinate are

$$\frac{Du}{Dt} - fv = -\frac{1}{\rho_o} \left(\frac{\partial p}{\partial x} \right)_\sigma + \frac{1}{\rho_o} \frac{\partial p}{\partial z} \left(\frac{\partial z}{\partial x} \right)_\sigma - \frac{\partial \sigma}{\partial z} \frac{\partial \overline{u'w'}}{\partial \sigma} \quad (\text{D.12})$$

$$\frac{Dv}{Dt} + fu = -\frac{\partial \sigma}{\partial z} \frac{\partial \overline{v'w'}}{\partial \sigma} \quad (\text{D.13})$$

$$\frac{D\theta}{Dt} = -\frac{\partial \sigma}{\partial z} \frac{\partial \overline{w'\theta'}}{\partial \sigma} + \frac{1}{\rho_o C_p} \frac{\partial \sigma}{\partial z} \frac{\partial I}{\partial \sigma} \quad (\text{D.14})$$

$$\frac{DS}{Dt} = -\frac{\partial \sigma}{\partial z} \frac{\partial \overline{w'S'}}{\partial \sigma} \quad (\text{D.15})$$

$$\frac{1}{m} \frac{Dm}{Dt} + \left(\frac{\partial u}{\partial x} \right)_\sigma + \frac{\partial \dot{\sigma}}{\partial \sigma} = 0 \quad (\text{D.16})$$

$$\frac{D}{Dt} ()_\sigma \equiv \frac{\partial}{\partial t} ()_\sigma + u \frac{\partial}{\partial x} ()_\sigma + \dot{\sigma} \frac{\partial}{\partial \sigma} ()_\sigma. \quad (\text{D.17})$$

Appendix E:

Equation Predicting the Inversion

Layer Thickness

As discussed in Chapter 3, the inversion layer thickness is determined by equating our expression for entrainment (equation 3.11) to the form given by Gaspar (1988).

Performing this operation gives

$$\frac{\overline{w'^2}^3}{\left\{ \overline{w'^2} - 3(1 - c_{11})\Delta b\delta z \right\} \left\{ \overline{w'^2} - \frac{4}{3}\Delta b\delta z - \left(\frac{1}{3}c_1 - c_2 \right) (\Delta u^2 + \Delta v^2) \right\}} - \frac{m_1^2 k_{avg}^2 \overline{w'^2}}{h^2 \Delta b^2} = 0. \quad (\text{E.1})$$

In these equations, we have defined

$$k_{avg} = \frac{1}{h} \int_{-h}^0 k dz; \quad \overline{w'^2} = \frac{1}{h} \int_{-h}^0 \overline{w'^2} dz,$$

where h is the boundary layer depth. If equation (E.1) is solved for δz , we obtain

$$\delta z = -\frac{9SP}{24\Delta b} + \frac{(13-9c_{11})\overline{w'^2}}{24(1-c_{11})\Delta b} \pm \frac{1}{24(1-c_{11})\Delta b m_1 k_{avg} \overline{w'^2}} \text{sqrt} \left(432\Delta b^2 h^2 \overline{w'^2}^3 (1-c_{11}) + \right. \\ \left. 81m_1^2 SP^2 k_{avg}^2 \overline{w'^2}^2 (1-c_{11})^2 - 18m_1^2 SP k_{avg}^2 \overline{w'^2} \overline{w'^2}^2 (1-c_{11})(5-9c_{11}) \right. \\ \left. + m_1^2 k_{avg}^2 \overline{w'^2}^2 \overline{w'^2}^2 (5-9c_{11})^2 \right)$$

In the previous equation, $SP \equiv \left(\frac{1}{3}c_1 - c_2 \right) (\Delta u^2 + \Delta v^2)$. If we plug in the values of the

three constants (c_1, c_2, c_{11}) given in Appendix C, the equation for inversion thickness is

now

$$\delta z = \frac{2.16(\Delta u^2 + \Delta v^2)}{24\Delta b} + \frac{13.44\overline{w'^2}}{24\Delta b} \pm \frac{1.11}{24\Delta b k_{avg} \overline{w'^2}} \text{sqrt} \left(388.8\Delta b^2 h^2 \overline{w'^2}^3 + \right. \\ \left. 3.78(\Delta u^2 + \Delta v^2)^2 k_{avg}^2 \overline{w'^2}^2 + 15.94(\Delta u^2 + \Delta v^2) k_{avg}^2 \overline{w'^2} \overline{w'^2}^2 + 16.81 k_{avg}^2 \overline{w'^2}^2 \overline{w'^2}^2 \right).$$

We make two brief observations. First the radical is guaranteed to be positive, precluding the possibility of imaginary numbers. Second, there are some dependencies we expect in this equation (e.g. Δb , Δu^2 , Δv^2 , and to a certain extent $\overline{w'^2}$). However, we have no *a priori* reason to expect that the inversion layer thickness is dependent on layer integrated TKE and vertical velocity variance.

Appendix F:

Structure Functions

The form of the structure functions (A_h , A_S , and A_m) are given by

$$A_h = \pi_4 \left\{ 1 + px + \pi_2 \pi_4 x (1 - \gamma^{-1}) \right\}^{-1}$$

$$A_S = \pi_1 \left\{ 1 + qx + x \pi_1 \pi_2 R_\rho (\gamma - 1) \right\}^{-1}$$

$$A_m = \frac{4}{75} (12 + a_1 n + a_2 n c + a_3 c^2 + a_4 n + a_5 c) / D.$$

$$D = 24 + d_1 y n^2 + d_2 y n c + d_3 y c^2 + d_4 n^3 + d_5 n^2 c + d_6 n c^2 + d_7 c^3 \\ + d_8 y n + d_9 y c + d_{10} n^2 + d_{11} n c + d_{12} c^2 + d_{13} y + d_{14} n + d_{15} c$$

Here, we have introduced seven new variables (p , q , x , n , c , y , and γ) they are written as

$$p \equiv \pi_4 \pi_5 - \pi_2 \pi_4 (1 + R_\rho)$$

$$q \equiv \pi_1 \pi_2 (1 + R_\rho) - \pi_1 \pi_3 R_\rho$$

$$x \equiv \frac{(\tau N)^2}{(1 - R_\rho)}$$

$$\gamma \equiv \frac{1}{R_\rho} \frac{\pi_4}{\pi_1} \frac{1 + qx}{1 + px}$$

$$y \equiv \frac{4}{25} x (1 - R_\rho) R_i^{-1}$$

$$n \equiv -\pi_2 \pi_3 x$$

$$c \equiv \pi_3^2 R_\rho x$$

where we have introduced the density ratio $R_\rho \equiv \frac{\beta \frac{\partial S}{\partial z}}{\alpha \frac{\partial \theta}{\partial z}}$. The values of the subscripted a 's and

d 's are given in Appendices A and B of Canuto et al. (2002). The remaining constants,

$(\pi_1, \pi_2, \pi_3, \pi_4, \pi_5)$ are defined in Appendix C.

Appendix G:

Implicit Treatment of the Discretized TKE Equation

In the simulations, the equation for TKE will be given as

$$\frac{\partial e}{\partial t} = -\overline{u'w'} \frac{\partial u}{\partial z} - \overline{v'w'} \frac{\partial v}{\partial z} + g \alpha_T \overline{w'\theta'} - g \alpha_S \overline{w'S'} - \frac{\partial}{\partial z} (\overline{w'u'u' + w'v'v' + w'w'w'}) - \varepsilon$$

In this model framework, we assume that the second moments can be written as

$$\begin{aligned} \overline{u'w'} &= -2\sqrt{e} \Lambda S_m \frac{\partial u}{\partial z}; & \overline{v'w'} &= -2\sqrt{e} \Lambda S_m \frac{\partial v}{\partial z}; \\ \overline{w'\theta'} &= -2\sqrt{e} \Lambda S_H \frac{\partial \theta}{\partial z}; & \overline{w'S'} &= -2\sqrt{e} \Lambda S_s \frac{\partial S}{\partial z}; \end{aligned}$$

where the $S_{m,H,s}$ are the structure functions given in Canuto et al. (2002, 2008) and Λ is the

dissipation length scale. Plugging in our relations, the TKE equation becomes,

$$\frac{\partial e}{\partial t} = 2\sqrt{e} \Lambda S_m \left\{ \left(\frac{\partial u}{\partial z} \right)^2 + \left(\frac{\partial v}{\partial z} \right)^2 \right\} - 2g\sqrt{e} \Lambda \left(\alpha_T S_H \frac{\partial \theta}{\partial z} - \alpha_S S_s \frac{\partial S}{\partial z} \right) - \frac{\partial}{\partial z} \left(\frac{\overline{w'u'u' + w'v'v' + w'w'w'}}{2} \right) - \frac{e^{3/2}}{\Lambda}$$

The next step is to write this in a finite difference form. For simplicity, I am going to only treat dissipation implicitly. Therefore, define the production terms as

$$P^n \equiv 2\sqrt{e} \Lambda S_m \left\{ \left(\frac{\partial u}{\partial z} \right)^2 + \left(\frac{\partial v}{\partial z} \right)^2 \right\} - 2g\sqrt{e} \Lambda \left(\alpha_T S_H \frac{\partial \theta}{\partial z} - \alpha_S S_S \frac{\partial S}{\partial z} \right) - \frac{\partial}{\partial z} \left(\frac{\overline{w'u'u'} + \overline{w'v'v'} + \overline{w'w'w'}}{2} \right)$$

where the n signifies the current time level. Using this, the TKE equation is discretized as

$$\frac{e^{n+1} - e^n}{\Delta t} = P^n - \frac{e^{n+1^{3/2}}}{\Lambda}.$$

Throughout this derivation, we keep the length scale in its general form, but will use the fact that it is always positive or zero. The TKE equation becomes

$$\begin{aligned} \frac{e^{n+1} - e^n}{\Delta t} &= P^n - \frac{e^{n+1^{3/2}}}{\Lambda} \\ \Lambda \frac{e^{n+1} - e^n}{\Delta t} &= \Lambda P^n - e^{n+1^{3/2}} \\ e^{n+1^{3/2}} + \frac{\Lambda}{\Delta t} e^{n+1} - \left(\frac{\Lambda}{\Delta t} e^n + \Lambda P^n \right) &= 0 \quad (\text{G.1}) \\ \sqrt{e^{n+1}}^3 + \frac{\Lambda}{\Delta t} \sqrt{e^{n+1}}^2 + C &= 0 \\ q^3 + \frac{\Lambda}{\Delta t} q^2 + C &= 0 \end{aligned}$$

In these equations, we have made the following definitions

$$C = -\left(\frac{\Lambda}{\Delta t} e^n + \Lambda P^n \right); \quad q = \sqrt{e^{n+1}}$$

Updating the TKE involves the solution of a cubic equation. There are three possible situations that can occur based on the sign of the polynomial discriminant, which in this case is given as

$$D = \left(\frac{\Lambda}{\Delta t} \right)^3 \frac{C}{27} + \frac{C^2}{4}. \quad \text{If } D > 0, \text{ there is one real root and two imaginary roots. If } D = 0, \text{ then}$$

there are three real roots with at least two being equal, and if $D < 0$ then all roots are real and

unequal. The hope is that D is greater than zero at all times, however, efforts to prove this is true for the TKE equation (G.1) have been unsuccessful.

A different approach must be taken. To have three real roots of a cubic equation, the plot of the function will be similar to one of the four cases in Figure G.1.

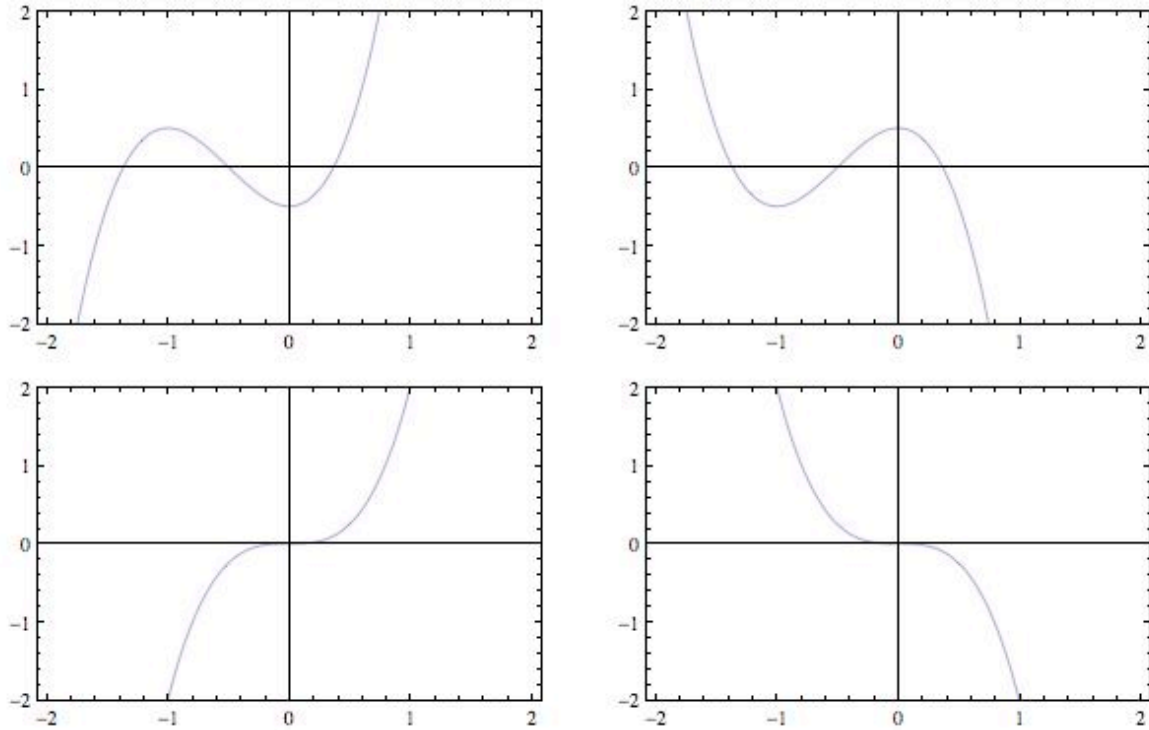


Figure G.1 - Four different cases of a cubic function defined by equation G.1

Of course these plots could shift in different directions. Since we are predicting TKE, in particular the square root of TKE, we can add an extra realizability requirement that the root is greater than or equal to zero. The question that must be answered is whether or not, the cubic can shift such that the roots are realistic.

We wish to argue from the reconstruction of the cubic from the location of maximums and minimums. The location of the local maximums and minimums are given by where the first derivative is equal to zero. The local maximums and minimums of equation (G.1) will be

$$f(q) = q^3 + \frac{\Lambda}{\Delta t} q^2 + C$$

$$f'(q) = 3q^2 + \frac{2\Lambda}{\Delta t} q = 0$$

$$q \left(3q + \frac{2\Lambda}{\Delta t} \right) = 0$$

$$q_1 = 0 \text{ or } q_2 = -\frac{2\Lambda}{3\Delta t}$$

In this problem, the cubic will have a maximum or minimum at zero regardless of the value of production or past value of TKE. Also, q_2 will always be negative, since the length scale is greater or equal to zero and the denominator is also positive. Therefore the cubic equation will have one positive (or zero) root. There will not be any cases that will give two positive real roots. In order for this to happen, a local maximum or minimum would have to occur at a value greater than zero. For this problem, there is an extremum at zero and a negative number. Further, the concavity (or the location where the second derivative is equal to zero) changes at a negative value as well.

In this situation, the solution of the equation (G.1) can be computed with closed form equations (Cardano's Formula).. The physically appropriate solution will be the lone positive (or zero) root.

REFERENCES

Acreman, D. M., and C. D. Jeffery, 2007: The use of Argo for validation and tuning of mixed layer models. *Ocean Model.*, **19**, 53-69.

Anderson, S. P., R. A. Weller, and R. B. Lukas, 1996: Surface buoyancy forcing and the mixed layer of the western pacific warm pool: Observations and 1D model results. *J. Clim.*, **9**, 3056-3085.

Anderson, W. G., A. Gnanadesikan, R. Hallberg, J. Dunne, and B. L. Samuels, 2007: Impact of ocean color on the maintenance of the Pacific cold tongue. *Geophys. Res. Lett.*, **34**.

——, ——, and A. Wittenberg, 2009: Regional impacts of ocean color on tropical Pacific variability. *Ocean Sci.*, **5**, 313-327.

Andre, J. C., G. D. Moor, P. Lacarrere, and R. D. Vachat, 1976: Turbulence approximation for inhomogeneous flows .1. Clipping approximation. *J. Atmos. Sci.*, **33**, 476-481.

——, ——, ——, G. Therry, and R. Duvachat, 1978: Modeling 24-hour evolution of mean and turbulent structures of planetary boundary-layer. *J. Atmos. Sci.*, **35**, 1861-1883.

——, and P. Lacarrere, 1985: Mean and turbulent structures of the oceanic surface-layer as determined from one-dimensional, third-order simulations *J. Phys. Oceanogr.*, **15**, 121-132.

Arakawa, A., and C. S. Konor, 1996: Vertical differencing of the primitive equations based on the Charney-Phillips grid in hybrid sigma-p vertical coordinates. *Mon. Wea. Rev.*, **124**, 511-528.

Bernie, D. J., S. J. Woolnough, J. M. Slingo, and E. Guilyardi, 2005: Modeling diurnal and intraseasonal variability of the ocean mixed layer. *J. Clim.*, **18**, 1190-1202.

Blanke, B., and S. Raynaud, 1997: Kinematics of the Pacific equatorial undercurrent: An Eulerian and Lagrangian approach from GCM results. *J. Phys. Oceanogr.*, **27**, 1038-1053.

- Bleck, R., R. Onken, and J.D. Woods, 1988: A two-dimensional model of mesoscale frontogenesis in the ocean. *Quart. J. Roy. Meteor. Soc.*, **114**, 347-371.
- Boyer, T. P., J.I. Antonov, H.E. Garcia, D.R. Johnson, R.A. Locarnini, A.V. Mishonov, M.T. Pitcher, O.K. Baranova, I.V. Smolyar, Ed., 2006: *World ocean database 2005, NOAA Atlas NESDIS 60*. U.S. Government Printing Office, 190 pp.
- Bretherton, C. S., and A. H. Sobel, 2002: A simple model of a convectively coupled Walker circulation using the weak temperature gradient approximation. *J. Clim.*, **15**, 2907-2920.
- Bryan, K., 1969: A numerical method for the study of the circulation of the world ocean. *J. Comput. Phys.*, **4**, 347-376.
- Burchard, H., O. Petersen, and T. P. Rippeth, 1998: Comparing the performance of the Mellor-Yamada and the k-epsilon two-equation turbulence models. *J. Geophys. Res.*, **C103**, 10543-10554.
- Canuto, V. M., F. Minotti, C. Ronchi, R. M. Ypma, and O. Zeman, 1994: 2nd-order closure PBL model with new 3rd-order moments - comparison with LES data. *J. Atmos. Sci.*, **51**, 1605-1618.
- , and M. Dubovikov, 1998: Stellar turbulent convection. I. Theory. *Astrophys. J.*, **493**, 834-847.
- , A. Howard, Y. Cheng, and M. S. Dubovikov, 2001: Ocean turbulence. Part I: One-point closure model; momentum and heat vertical diffusivities. *J. Phys. Oceanogr.*, **31**, 1413-1426.
- , ———, ———, 2002: Ocean turbulence. Part II: Vertical diffusivities of momentum, heat, salt, mass, and passive scalars. *J. Phys. Oceanogr.*, **32**, 240-264.
- , ——— P. Hogan, Y. Cheng, M. S. Dubovikov, and L. M. Montenegro, 2004: Modeling ocean deep convection. *Ocean Model.*, **7**, 75-95.
- , Y. Cheng, and A. M. Howard, 2007: Non-local ocean mixing model and a new plume model for deep convection. *Ocean Model.*, **16**, 28-46.
- , ———, ———, 2008: A new model for double diffusion plus turbulence. *Geophys. Res. Lett.*, **35**.
- Cheng, Y., V. M. Canuto, and A. M. Howard, 2002: An improved model for the turbulent PBL. *J. Atmos. Sci.*, **59**, 1550-1565.

——, ——, ——, 2005: Nonlocal convective PBL model based on new third- and fourth-order moments. *J. Atmos. Sci.*, **62**, 2189-2204.

Colella, P., and P. R. Woodward, 1984: The piecewise parabolic method (ppm) for gas-dynamical simulations. *J. Comput. Phys.*, **54**, 174-201.

Craik, A. D. D., 1977: Generation of Langmuir circulations by an instability mechanism. *J. Fluid Mech.*, **81**, 209-223.

Cunningham, S. A., S. G. Alderson, B. A. King, and M. A. Brandon, 2003: Transport and variability of the Antarctic circumpolar current in Drake Passage. *J. Geophys. Res.*, **C108**.

Danabasoglu, G., W.G. Large, 2003: Changes to the KPP vertical mixing parameterization. *CCSM Ocen Model Working Group*, Boulder, CO.

——, ——, J. J. Tribbia, P. R. Gent, B. P. Briegleb, and J. C. McWilliams, 2006: Diurnal coupling in the tropical oceans of CCSM3. *J. Clim.*, **19**, 2347-2365.

Dazlich, D., D.A. Randall, T. Ringler, and L.P. Van Roekel, 2010: A coupled model constructed using geodesic grids. *Manuscript in preparation*.

Deardorff, J. W., 1983: A multi-limit mixed-layer entrainment formulation. *J. Phys. Oceanogr.*, **13**, 988-1002.

Denman, K. L., 1973: A time-dependent model of the upper ocean. *J. Phys. Oceanogr.*, **3**, 173-184.

Durski, S. M., S. M. Glenn, and D. B. Haidvogel, 2004: Vertical mixing schemes in the coastal ocean: Comparison of the level 2.5 Mellor-Yamada scheme with an enhanced version of the K profile parameterization. *J. Geophys. Res.*, **C109**.

Emanuel, K. A., 1988: The maximum intensity of hurricanes. *J. Atmos. Sci.*, **45**, 1143-1155.

Fairall, C. W., E. F. Bradley, J. E. Hare, A. A. Grachev, and J. B. Edson, 2003: Bulk parameterization of air-sea fluxes: Updates and verification for the COARE algorithm. *J. Clim.*, **16**, 571-591.

Gary, J. M., 1973: Estimate of truncation error in transformed coordinate, primitive equation atmospheric models. *J. Atmos. Sci.*, **30**, 223-233.

Gaspar, P., 1988: Modeling the seasonal cycle of the upper ocean. *J. Phys. Oceanogr.*, **18**, 161-180.

- Gent, P. R., 1991: The heat-budget of the TOGA-COARE domain in an ocean model. *J. Geophys. Res.*, **C96**, 3323-3330.
- Gibson, M. M., and B. E. Launder, 1976: Calculation of horizontal, turbulent, free shear flows under gravitational influence. *J. Heat Transf.-Trans. ASME*, **98**, 81-87.
- Gnanadesikan, A., and W. G. Anderson, 2009: Ocean water clarity and the ocean general circulation in a coupled climate model. *J. Phys. Oceanogr.*, **39**, 314-332.
- Goodman, P. J., W. Hazeleger, P. De Vries, and M. Cane, 2005: Pathways into the Pacific equatorial undercurrent: A trajectory analysis. *J. Phys. Oceanogr.*, **35**, 2134-2151.
- Grant, A. L. M., and S. E. Belcher, 2009: Characteristics of Langmuir turbulence in the ocean mixed layer. *J. Phys. Oceanogr.*, **39**, 1871-1887.
- Griffies, S. M., R. C. Pacanowski, and R. W. Hallberg, 2000: Spurious diapycnal mixing associated with advection in a z-coordinate ocean model. *Mon. Wea. Rev.*, **128**, 538-564.
- Hallberg, R., and A. Adcroft, 2009: Comparison of GFDL's CM2G coupled climate model with CM2.1 and CM2M. *Layered Ocean Modelling Workshop*, Miami, FL.
- Halliwel, G. R., R. Bleck, and E. Chassignet, 1998: Atlantic ocean simulations performed using a new hybrid-coordinate ocean model. *AGU Fall Meeting*, San Francisco, CA.
- , 2004: Evaluation of vertical coordinate and vertical mixing algorithms in the hybrid-coordinate ocean model (HYCOM). *Ocean Model.*, **7**, 285-322.
- Haltiner, G.J., and R.T. Williams, 1980: *Numerical Prediction and Dynamic Meteorology*. John Wiley and Sons, 477 pp.
- Haney, R. L., 1991: On the pressure-gradient force over steep topography in sigma coordinate ocean models. *J. Phys. Oceanogr.*, **21**, 610-619.
- Harcourt, R. R., and E. A. D'Asaro, 2008: Large-eddy simulation of Langmuir turbulence in pure wind seas. *J. Phys. Oceanogr.*, **38**, 1542-1562.
- Holtslag, A. A. M., E. I. F. Debruijn, and H. L. Pan, 1990: A high-resolution air-mass transformation model for short-range weather forecasting. *Mon. Wea. Rev.*, **118**, 1561-1575.

- Jackson, L., R. Hallberg, and S. Legg, 2008: A parameterization of shear-driven turbulence for ocean climate models. *J. Phys. Oceanogr.*, **38**, 1033-1053.
- Jacob, S. D., L. K. Shay, A. J. Mariano, and P. G. Black, 2000: The 3D oceanic mixed layer response to hurricane gilbert. *J. Phys. Oceanogr.*, **30**, 1407-1429.
- , D.M. Levine, L.K. Shay, G.R. Halliwell, C. Lozano, and A. Mehra, 2006: Evaluation of upper ocean mixing parameterizations for use in coupled models. *27th Conference on Hurricanes and Tropical Meteorology*, Monterey, CA.
- Janjic, Z., and A. Wiinnelsen, 1977: Geostrophic adjustment and numerical procedures in a rotating fluid. *J. Atmos. Sci.*, **34**, 297-310.
- Jerlov, N. G., 1968: *Optical Oceanography*. American Elsevier Publ. Co., 194 pp.
- Jin, F. F., 1997: An equatorial ocean recharge paradigm for ENSO .1. Conceptual model. *J. Atmos. Sci.*, **54**, 811-829.
- Jung, J. H., and A. Arakawa, 2008: A three-dimensional anelastic model based on the vorticity equation. *Mon. Wea. Rev.*, **136**, 276-294.
- Kalnay, E., and M. Kanamitsu, 1988: Time schemes for strongly nonlinear damping equations. *Mon. Wea. Rev.*, **116**, 1945-1958.
- Kantha, L. H., and C. A. Clayson, 1994: An improved mixed-layer model for geophysical applications. *J. Geophys. Res.*, **C99**, 25235-25266.
- , —, 2004: On the effect of surface gravity waves on mixing in the oceanic mixed layer. *Ocean Model.*, **6**, 101-124.
- Kirk, J. T. O., 1988: Solar heating of water bodies as influenced by their inherent optical-properties. *J. Geophys. Res.*, **D93**, 10897-10908.
- Kraus, E. B., and J. S. Turner, 1967: A one-dimensional model of seasonal thermocline .2. General theory and its consequences. *Tellus*, **19**, 98-&.
- Langmuir, I., 1938: Surface motion of water induced by wind. *Science*, **87**, 119-123.
- Lappen, C. L., D. Randall, and T. Yamaguchi, 2010: A higher-order closure model with an explicit PBL top. *J. Atmos. Sci.*, **67**, 834-850.

- Large, W. G., J. C. McWilliams, and S. C. Doney, 1994: Oceanic vertical mixing - a review and a model with a nonlocal boundary-layer parameterization. *Rev. Geophys.*, **32**, 363-403.
- , and P. R. Gent, 1999: Validation of vertical mixing in an equatorial ocean model using large eddy simulations and observations. *J. Phys. Oceanogr.*, **29**, 449-464.
- Leibovich, S., 1977: Evolution of a system of wind drift currents and langmuir circulations in the ocean. 1. Theory and averaged current. *J. Fluid Mech.*, **79**, 715-743.
- , 1983: The form and dynamics of langmuir circulations. *Ann. Rev. Fluid Mech.*, **15**, 391-427.
- Levitus, S. a. T. P. B., 1994: World ocean atlas 1994. Volume 4. Temperature, 132 pp.
- Lewis, M. R., J. J. Cullen, and T. Platt, 1983: Phytoplankton and thermal structure in the upper ocean - consequences of nonuniformity in chlorophyll profile. *J. Geophys. Res.*, **NC88**, 2565-2570.
- Li, M., and C. Garrett, 1997: Mixed layer deepening due to Langmuir circulation. *J. Phys. Oceanogr.*, **27**, 121-132.
- , —, and E. Skillingstad, 2005: A regime diagram for classifying turbulent large eddies in the upper ocean. *Deep-Sea Res.*, **52**, 259-278.
- Lilly, D. K., 1968: Models of cloud-topped mixed layers under a strong inversion. *Quart. J. Roy. Meteor. Soc.*, **94**, 292-&.
- Maloney, E. D., and J. T. Kiehl, 2002: Intraseasonal eastern Pacific precipitation and SST variations in a GCM coupled to a slab ocean model. *J. Clim.*, **15**, 2989-3007.
- , —, 2002: MJO-related SST variations over the tropical eastern Pacific during northern hemisphere summer. *J. Clim.*, **15**, 675-689.
- , D. B. Chelton, and S. K. Esbensen, 2008: Subseasonal SST variability in the tropical eastern north Pacific during boreal summer. *J. Clim.*, **21**, 4149-4167.
- Manizza, M., C. Le Quere, A. J. Watson, and E. T. Buitenhuis, 2005: Bio-optical feedbacks among phytoplankton, upper ocean physics and sea-ice in a global model. *Geophys. Res. Lett.*, **32**.
- Martin, P. J., 1985: Simulation of the mixed layer at OWS November and Papa with several models. *J. Geophys. Res.*, **C90**, 903-916.

- Mason, P. J., 1989: Large-eddy simulation of the convective atmospheric boundary-layer. *J. Atmos. Sci.*, **46**, 1492-1516.
- McGillicuddy, D.J., A.R. Robinson, D.A. Siegel, H.W. Jannasch, R. Johnson, T.D. Dickey, J. McNeil, A.F. Michaels, and A.H. Knap, 1998: Influence of mesoscale eddies on new production in the Sargasso Sea. *Nature*, **394**, 263 - 266.
- , and coauthors, 2007: Eddy/Wind interaction stimulate extraordinary mid-ocean plankton blooms. *Science*, **316**, 1021-1026.
- McWilliams, J. C., P. P. Sullivan, and C. H. Moeng, 1997: Langmuir turbulence in the ocean. *J. Fluid Mech.*, **334**, 1-30.
- , ——, 2000: Vertical mixing by Langmuir circulations. *Spill Sci. Tech. Bull.*, **6**, 225-237.
- Mellor, G. L., and T. Yamada, 1982: Development of a turbulence closure-model for geophysical fluid problems. *Rev. Geophys.*, **20**, 851-875.
- , T. Ezer, and L. Y. Oey, 1994: The pressure-gradient conundrum of sigma coordinate ocean models. *J. Atmos. Ocean. Technol.*, **11**, 1126-1134.
- Mesinger, F., 1982: On the convergence and error problems of the calculation of the pressure-gradient force in sigma coordinate models. *Geophys. Astrophys. Fluid Dyn.*, **19**, 105-117.
- Moeng, C. H., and D. A. Randall, 1984: Problems in simulating the stratocumulus-topped boundary-layer with a 3rd-order closure-model. *J. Atmos. Sci.*, **41**, 1588-1600.
- Mohammad, R., and J. Nilsson, 2004: The role of diapycnal mixing for the equilibrium response of thermohaline circulation. *Ocean Dyn.*, **54**, 54-65.
- Montegut, C. D., G. Madec, A. S. Fischer, A. Lazar, and D. Iudicone, 2004: Mixed layer depth over the global ocean: An examination of profile data and a profile-based climatology. *J. Geophys. Res.*, **C109**.
- Monterey, G. I., and S. Levitus, 1997: Climatological cycle of mixed layer depth in the world ocean., U.S. Gov. Printing Office, NOAA NESDIS, 5pp.
- Morel, A., and D. Antoine, 1994: Heating rate within the upper ocean in relation to its biooptical state. *J. Phys. Oceanogr.*, **24**, 1652-1665.

——, and S. Maritorena, 2001: Bio-optical properties of oceanic waters: A reappraisal. *J. Geophys. Res.*, **C106**, 7163-7180.

Moum, J. N., D. R. Caldwell, and C. A. Paulson, 1989: Mixing in the equatorial surface-layer and thermocline. *J. Geophys. Res.*, **C94**, 2005-2021.

Murtugudde, R., J. Beauchamp, C. R. McClain, M. Lewis, and A. J. Busalacchi, 2002: Effects of penetrative radiation on the upper tropical ocean circulation. *J. Clim.*, **15**, 470-486.

Nakamoto, S., S. P. Kumar, J. M. Oberhuber, J. Ishizaka, K. Muneyama, and R. Frouin, 2001: Response of the equatorial Pacific to chlorophyll pigment in a mixed layer isopycnal ocean general circulation model. *Geophys. Res. Lett.*, **28**, 2021-2024.

Niiler, P. P., and E.B. Kraus, 1977: One-dimensional models of the upper ocean. *Modeling and Prediction of the Upper Layers of the Ocean*, E. B. Kraus, Ed., Pergamon, 143-177.

Noh, Y., C.J. Jang, and J.W. Kim, 1999: Large eddy simulation of open ocean deep convection with application to the deep water formation in the East sea (Japan sea). *J. Oceanogr.*, **55**, 347-367.

——, H. S. Min, and S. Raasch, 2004: Large eddy simulation of the ocean mixed layer: The effects of wave breaking and Langmuir circulation. *J. Phys. Oceanogr.*, **34**, 720-735.

Ohlmann, J. C., D. A. Siegel, and L. Washburn, 1998: Radiant heating of the western equatorial Pacific during TOGA-COARE. *J. Geophys. Res.*, **C103**, 5379-5395.

——, ——, and C.D. Mobley, 2000: Ocean Radiant Heating. Part I: Optical influences. *J. Phys. Oceanogr.*, **30**, 1833-1848.

Pacanowski, R. C., and S. G. H. Philander, 1981: Parameterization of vertical mixing in numerical-models of tropical oceans. *J. Phys. Oceanogr.*, **11**, 1443-1451.

Paulson, C. A., and J. J. Simpson, 1977: Irradiance measurements in upper ocean. *J. Phys. Oceanogr.*, **7**, 952-956.

Plueddemann, A. J., and Coauthors, 1996: Structure and variability of Langmuir circulation during the surface waves processes program. *J. Geophys. Res.*, **C101**, 3525-3543.

- Polton, J. A., J. A. Smith, J. A. MacKinnon, and A. E. Tejada-Martinez, 2008: Rapid generation of high-frequency internal waves beneath a wind and wave forced oceanic surface mixed layer. *Geophys. Res. Lett.*, **35**.
- Price, J. F., C. N. K. Mooers, and J. C. Vanleer, 1978: Observation and simulation of storm-induced mixed-layer deepening. *J. Phys. Oceanogr.*, **8**, 582-599.
- , R. A. Weller, and R. Pinkel, 1986: Diurnal cycling - observations and models of the upper ocean response to diurnal heating, cooling, and wind mixing. *J. Geophys. Res.*, **C91**, 8411-8427.
- Randall, D. A., 2010: An overview on the effects of radiation and convection. *An Introduction to the General Circulation of the Atmosphere*.
- Raymond, D. J., and Coauthors, 2004: Epic2001 and the coupled ocean-atmosphere system of the tropical east pacific. *Bull. Amer. Meteorol. Soc.*, **85**, 1341-1354.
- Reynolds, R. W., and T. M. Smith, 1994: Improved global sea-surface temperature analyses using optimum interpolation. *J. Clim.*, **7**, 929-948.
- Rodi, W., 1976: New algebraic relation for calculating Reynolds stresses. *Z. Angew. Math. Mech.*, **56**, T219-T221.
- Schneider, E. K., and Z. X. Zhu, 1998: Sensitivity of the simulated annual cycle of sea surface temperature in the equatorial Pacific to sunlight penetration. *J. Clim.*, **11**, 1932-1950.
- Shchepetkin, A. F., and J. C. McWilliams, 2003: A method for computing horizontal pressure-gradient force in an oceanic model with a nonaligned vertical coordinate. *J. Geophys. Res.*, **C108**.
- Shinoda, T., and H. H. Hendon, 1998: Mixed layer modeling of intraseasonal variability in the tropical western pacific and indian oceans. *J. Clim.*, **11**, 2668-2685.
- Siegel, D.A., 1998: Resource competition in a discrete environment: Why are plankton distributions paradoxical? *Limnol. Oceanogr.*, **43**, 1133-1146.
- , S. Maritorena, N.B. Nelson, and M.J. Behrenfeld, 2005: Independence and interdependencies among global ocean color properties: Reassessing the bio-optical assumption. *J. Geophys. Res.*, **110**, C07011, doi: 10.1029/2004JC002527.
- Simonot, J. Y., E. Dollinger, and H. Letreut, 1988: Thermodynamic-biological-optical coupling in the oceanic mixed layer. *J. Geophys. Res.*, **C93**, 8193-8202.

- Skyllingstad, E. D., and D. W. Denbo, 1995: An ocean Large-eddy simulation of Langmuir circulations and convection in the surface mixed-layer. *J. Geophys. Res.*, **C100**, 8501-8522.
- Sloyan, B. M., G. C. Johnson, and W. S. Kessler, 2003: The Pacific cold tongue: A pathway for interhemispheric exchange. *J. Phys. Oceanogr.*, **33**, 1027-1043.
- Smyth, W. D., E.D. Skyllingstad, G.B. Crawford, and H. Wijesekera, 2002: Nonlocal fluxes and Stokes drift effect in the K-profile parameterization. *Ocean Dyn.*, **52**, 104-115.
- Song, Y. H., and D. Haidvogel, 1994: A semi-implicit ocean circulation model using a generalized topography-following coordinate system. *J. Comput. Phys.*, **115**, 228-244.
- Song, Y. T., 1998: A general pressure gradient formulation for ocean models. Part I: Scheme design and diagnostic analysis. *Mon. Wea. Rev.*, **126**, 3213-3230.
- Strutton, P. G., and F. P. Chavez, 2004: Biological heating in the equatorial Pacific: Observed variability and potential for real-time calculation. *J. Clim.*, **17**, 1097-1109.
- Stull, R. B., 1988: *An Introduction to Boundary Layer Meteorology*. Kluwer Academic Publishers, 666 pp.
- Thuburn, J., 1993: Use of a flux-limited scheme for vertical advection in a GCM. *Quart. J. Roy. Meteor. Soc.*, **119**, 469-487.
- , 1996: Multidimensional flux-limited advection schemes. *J. Comput. Phys.*, **123**, 74-83.
- Troen, I., and L. Mahrt, 1986: A simple-model of the atmospheric boundary-layer - sensitivity to surface evaporation. *Bound.-Layer Meteor.*, **37**, 129-148.
- Vanleer, B., 1974: Towards ultimate conservative difference scheme .2. Monotonicity and conservation combined in a second-order scheme. *J. Comput. Phys.*, **14**, 361-370.
- Walker, R. T., and D. M. Holland, 2007: A two-dimensional coupled model for ice shelf-ocean interaction. *Ocean Model.*, **17**, 123-139.
- Wallace, J. M., E. M. Rasmusson, T. P. Mitchell, V. E. Kousky, E. S. Sarachik, and H. von Storch, 1998: The structure and evolution of ENSO-related climate variability in the tropical Pacific: Lessons from TOGA. *J. Geophys. Res.*, **C103**, 14241-14259.

Wang, D. L., J. C. McWilliams, and W. G. Large, 1998: Large-eddy simulation of the diurnal cycle of deep equatorial turbulence. *J. Phys. Oceanogr.*, **28**, 129-148.

Webster, P. J., and R. Lukas, 1992: TOGA-COARE - the coupled ocean atmosphere response experiment. *Bull. Amer. Meteorol. Soc.*, **73**, 1377-1416.

White, L., A. Adcroft, and R. Hallberg, 2009: High-order regridding-remapping schemes for continuous isopycnal and generalized coordinates in ocean models. *J. Comput. Phys.*, **228**, 8665-8692.

Xie, S. P., H. M. Xu, W. S. Kessler, and M. Nonaka, 2005: Air-sea interaction over the eastern pacific warm pool: Gap winds, thermocline dome, and atmospheric convection. *J. Clim.*, **18**, 5-20.

Zaron, E. D., and J. N. Moum, 2009: A new look at Richardson number mixing schemes for equatorial ocean modeling. *J. Phys. Oceanogr.*, **39**, 2652-2664.